

This file is part of the following work:

**Lawrence, Leigh (2021) *Geochemistry and origin of explosive alkaline volcanism in the early Rukwa Rift, southwestern Tanzania*. PhD Thesis, James Cook University.**

Access to this file is available from:

<https://doi.org/10.25903/r04r%2D5e25>

Copyright © 2021 Leigh Lawrence.

The author has certified to JCU that they have made a reasonable effort to gain permission and acknowledge the owners of any third party copyright material included in this document. If you believe that this is not the case, please email

[researchonline@jcu.edu.au](mailto:researchonline@jcu.edu.au)

---

Geochemistry and origin of explosive  
alkaline volcanism in the early Rukwa Rift,  
southwestern Tanzania.

Thesis submitted by

Leigh Lawrence

April 2021

For the Degree of Doctor of Philosophy

James Cook University



---

## Statement of Access

I, the undersigned author of this thesis, understand that James Cook University will make this thesis available for use within the university library and allow access in other approved libraries after its submission. All users consulting this thesis will have to sign the following statement:

*In consulting this thesis, I agree not to copy or closely paraphrase it in whole or in part without the written consent of the author; and to make proper public written acknowledgement for any assistance which I have obtained from it.*

Beyond this, I do not wish to place any restrictions on access to this thesis.

Leigh Lawrence

April 2021

---

## Declaration

I declare that this thesis is my own work and has not been submitted in any form for another degree or diploma at any university or other institute or tertiary education. Information derived from the published or unpublished work of others has been acknowledged in the text and a list of references is given.

Leigh Lawrence

April 2021

*Every reasonable effort has been made to gain permission and acknowledge the owners of copyright material. I would be pleased to hear from any copyright owner who has been omitted or incorrectly acknowledged.*

---

## Statement of the Contribution of Others

This thesis includes one original published paper in a peer-reviewed journal and three unpublished research chapters. The ideas, development and writing up of all the papers in this thesis were the principal responsibility of myself, the candidate, under the supervision of Carl Spandler and Eric Roberts

Nature of assistance	Contribution	Names & affiliations of co-contributors
Intellectual support	Supervision	Dr Carl Spandler, JCU/UofA Dr Eric Roberts, JCU
	Data analysis	Dr Carl Spandler, JCU/UofA Dr Eric Roberts, JCU Dr Hannah Hilbert-Wolf, JCU
	Editorial assistance	Dr Carl Spandler, JCU/UofA Dr Eric Roberts, JCU
Financial support	Research Funding	NSF (BCS-1638796 and EAR-1424892) JCU
	Stipend	JCU RTPS
External data collection	Zircon geochemistry	Isotope Geology Laboratory, BSU, USA.
	Experimental petrology facilities and materials	Research School of Earth Sciences, ANU.
	Bulk Rb-Sr and Sm-Nd isotopes	Mawson Analytical Spectrometry Services, UofA

### Statement of the Contribution for Chapter 2 (now published in Lithos)

Publication Title	Nature and % of student contribution	Nature and % of co-author C. Spandler contribution	Nature and % of co-author E. Roberts contribution	Nature and % of co-author H. Hilbert Wolf contribution
Mineralogy and origin of the alkaline Nsungwe Formation tuff of the Rukwa Rift Basin, south-western Tanzania Lithos, 380-381, 105885, 2021	80% Sample preparation, Project conceptualization, Data collection and interpretation, writing, editing figure drafting, manuscript preparation	10% data interpretation, manuscript editing	5% sample provision, logistical support manuscript editing	5% sample provision, field support

---

I confirm my contribution to the paper and consent to the inclusion of the paper in this thesis.

Name: Dr Carl Spandler

Signature:

Date: 27-03-2021

**Statement of the Contribution**

I confirm my contribution to the paper and consent to the inclusion of the paper in this thesis.

Name: Dr Eric Roberts

Signature:

Date: 27-03-2021

**Statement of the Contribution**

I confirm my contribution to the paper and consent to the inclusion of the paper in this thesis.

Name: Dr Hannah L. Hilbert-Wolf

Signature:

Date: 30-03-2021

---

## Acknowledgements

There are many people I would like to acknowledge that have contributed to my education, personal and intellectual growth, and character over the course of my life. Ironically, the majority will never read this page. But for those who do, please share this message with the many others that may not.

Thank you for challenging me, encouraging me, and inspiring me to find and follow my passions. Without this I would certainly not be who or where I am today, and for this I am extremely and forever grateful.

For my supervisor Dr Carl Spandler, I deeply appreciate your mentorship and guidance. Your calm, patience and encouragement has been unwavering and your example as a scientist and teacher has been invaluable. I have thoroughly enjoyed working and developing as a scientist under your supervision over the course of this project. Thank you.

For my supervisor Eric Roberts, since welcoming me onto the Rukwa Rift Basin Project you have been nothing but enthusiastic and supportive of everything I do. I am extremely grateful for the time spent and knowledge shared in the valleys of Tanzania and Malawi. I will cherish these field experiences for the rest of my life. Thank you.

I owe a debt of gratitude to Dr Hannah Hilbert-Wolf for her willingness to collaborate and share both samples and ideas concerning all things volcanic tuffs. To Pat, Nancy and all members of the Rukwa Rift Basin Project for the inspiring conversations and support throughout our field campaigns. Kevin Blake, Shane Askew and Yi Hu for all their analytical support and eclectic conversations we've had in the AAC over the years. All staff in the College of Science and Engineering, and colleagues past and present in the Geology department for their academic assistance, intellectual support, and comradery. Thank you.

For Madie, we have been on this wild ride together each step of the way. I am inspired daily by your resilience, kindness and intellect and am forever grateful for your support. Time to fuel up and restock – the next adventure awaits!

Mum and Robert. What can I say? Your unconditional love and support throughout my life has been instrumental in equipping me with the resilience and determination I possess today. None of the work presented in this thesis would have been possible without it. Thank you.

Dad, you have always had a seat at the table and an ear on the other end of the phone whenever I have needed it. Much like your form in our footy tipping, the last few years have not been any different. I'll always appreciate your support, 6pm music playlists and collect on your consistency. Thank you.

---

## Thesis Abstract

The East African Rift System is the archetypal and best-studied continental rift on Earth. Despite this, geological windows into the processes associated with the initiation of continental rifts are exceedingly rare and understudied. The earliest magmatic episodes associated with continental break-up not only provide key geological constraints regarding the onset of rifting and evolution of the local lithosphere, but they also represent some of the most exotic volcanic systems on Earth. Notwithstanding, their characteristically low-volume and short-lived nature means they are scarcely preserved for study at the Earth's surface. In contrast, sedimentary archives hosted within the tectonic basins of the East African Rift reliably record the processes that exemplify a continental rift environment including large magnitude earthquakes, debris flows and punctuated episodes of explosive volcanism. Where preserved in outcrop, these strata offer unprecedented insights into the dynamic nature of geological processes shaping the Earth's surface during continental rifting, including early-rift volcanism, and coincidentally the adaptations occurring within biologically diverse eco-systems in response.

A series of volcanic tuff horizons identified in ca. 25 – 26 Ma fossiliferous syn-rift sequences of the Rukwa Rift Basin (southwestern Tanzania) mark the initiatory stages of rifting in the lesser studied Western Branch. Despite challenging long-established models of rift development, these deposits offer a rare opportunity to study early rift-related magmatism and tectonics, particularly as it pertains to the complex terrains and magma-poor character of the Western Branch. The collection of work presented here includes a series of geochemical and mineralogical investigations into the nature and origin of the late-Oligocene volcanic tuff deposits, that by extension examine magma genesis and volcanism, formation and evolution of the lithospheric mantle, and the broader Cenozoic geodynamics of the Rukwa Rift Basin.

While the age and significance of the 25-26 Ma Nsungwe Formation tuff deposits is well recognised, their pervasively-altered state and lack of an appropriately aged volcanic vent or source in the region presents a considerable challenge to conventional methods of geochemical study. Therefore, the initial phases of this work successfully developed a 'single crystal approach' and highlights the wealth of extractable petrological information residing within individual primary igneous minerals and their inclusions. The petrographic relations carefully inferred via mineral inclusions are well supported by the major and trace element compositions of all phases analysed. Collectively, these tuffs are characterised by an alkaline-carbonatite igneous assemblage, the chemistry and partitioning behaviour of which, are consistent with derivation from a peralkaline phonolite melt. Revised spatial and temporal analysis indicates these tuffs are the earliest known products of the nearby Miocene – recent Rungwe Volcanic Province. Given the poor preservation capacity and scarcity of early rift volcanic rocks, the analysis of igneous crystals from volcanogenic basin sediments shown here may play an integral role in identifying and describing early rift volcanism elsewhere, particularly in the Western Branch.

---

Titanite is a common accessory mineral in alkaline rocks, including the Nsungwe Formation tuffs, however it is often overlooked and underutilised as a geochemical monitor of rift-related alkaline systems. Here, pristine titanite grains hosting large silicate glass inclusions are showcased for their geochemical potential and provide an extraordinary glimpse into the volcanic system from which they formed. Geochemical analysis and modelling of the magma evolution preserved in glass inclusions reveals that unmixing alkali-carbonatite melt from an evolved phonolite precursor (via isobaric cooling) capably produces volatile-rich silicic melt compositions within a closed fractionating magmatic system. These observations and the geological conditions inferred are well supported by existing and follow-up experimental work, as well as other melt inclusion studies of incipient rift volcanics. Together, this study presents an entirely new mechanism for generating silicic magmas of explosive constitution within developing continental rift zones.

A series of follow-up polythermal (1000 °C – 700 °C), isobaric (0.5 GPa), piston-cylinder experiments were performed to replicate magma evolution and mineralogy observed in natural rocks and more broadly to investigate the poorly-understood carbonatite-trachyte association of the East African Rift. The chemical evolution of carbonatite-phonolite conjugate liquid pairs produced at 1000 °C, 950 °C and 900 °C mimic the predicted expansion of the two-liquid solvus for the compositions and geological conditions specified. Additionally, the paragenetic sequence and overall mineralogy of run products between 900 °C and 800 °C support the magmatic P-T conditions previously estimated for the Nsungwe Formation tuffs. Although trachytic melts were not successfully generated, the principles demonstrated and assemblages produced support the observations presented for natural rocks.

The protracted accordion-like behaviour and episodic alkaline magmatism of the Rukwa Rift Basin reflect isolated periods of lithospheric response to geological stress. The magmatic products coinciding with episodes of basin reactivation and deposition during the Jurassic-Cretaceous, Paleogene, and Miocene – recent times may reliably sample, time-stamp and fingerprint the isotopic composition of the local lithosphere. Combining Sr-Nd-Hf isotope data from the ~165 Ma Panda Hill Carbonatite, the ~25 Ma Nsungwe Formation tuffs, and the 8.7 and 3.5 Ma Lake Beds volcanic tuffs, this work produces an isotopic record of magma genesis prior-to, and since, the onset of East African Rift development, filling a crucial gap at ~25 Ma. Remarkably, our data show that magmas generated prior to the Miocene are sourced from isotopically distinct components of the lithosphere and that the source of magmatism has become progressively enriched from the Oligocene – recent. Combined with recent geophysical and sedimentological data, a conceptual geodynamic model involving the destabilisation (lithospheric drip) of a compositionally layered lithosphere at the onset of East African Rift development (~30-25 Ma) considers both the isotopic and geodynamic history of the Rukwa-Malawi-Usangu junction. Such a model may have implications for the evolution of isolated volcanic provinces and magma-poor rifting elsewhere in the Western Branch.

---

## Table of Contents

Statement of Access .....	I
Declaration .....	II
Statement of the Contribution of Others.....	III
Acknowledgements .....	V
Thesis Abstract.....	VI
Table of Contents .....	VIII
List of Tables.....	XII
List of Figures.....	XIII
Chapter 1 Introduction to Thesis .....	1
Chapter 2 Mineralogy and origin of the alkaline Nsungwe Formation tuffs of the Rukwa Rift Basin, southwestern Tanzania .....	9
Abstract.....	9
2.1 Introduction.....	9
2.2 Background and regional geology .....	11
2.3 Sample description and preparation.....	13
2.4 In-situ analysis .....	15
2.5 Results.....	16
2.5.1 Titanite.....	17
2.5.2 Mica.....	17
2.5.3 Fluorapatite.....	19
2.5.4 Andradite .....	20
2.5.5 Pyrochlore.....	21
2.5.6 Sanidine .....	21
2.5.7 Clinopyroxene .....	23
2.5.8 Carbonates .....	25
2.5.9 Zircon .....	25
2.5.10 Silicate glass .....	25
2.5.11 Summary of micro-phenocryst inclusions and phases.....	25
2.6 Discussion.....	26
2.6.1 Identification of the igneous mineral assemblage for the NFT .....	26
2.6.1.1 Petrography and mineral chemistry .....	26
2.6.1.2 Mineral trace element composition and distribution.....	27
2.6.2 Contextualising the NFT mineral assemblage.....	31
2.6.3 Proximal sources.....	33
2.6.4 Identifying carbonatite volcanism .....	34
2.7 Conclusions.....	34

---

References .....	35
Chapter 3 Unmix and Erupt: Explosive early rift volcanism produced by magma immiscibility in the Western Branch of the East African Rift.....	41
Abstract.....	41
3.1 Introduction.....	41
3.2 Samples and analytical methods .....	43
3.2.1 Field relations and sample preparation.....	43
3.2.2 Petrography of titanite hosted primary inclusions .....	45
3.2.3 Analytical methods.....	46
3.2.3.1 Electron microprobe analysis.....	46
3.2.3.2 Trace element analysis.....	47
3.2.3.3 In-situ Sm-Nd isotope microanalysis.....	47
3.2.3.4 Raman Spectroscopy.....	47
3.3 Results.....	49
3.3.1 Major elements and volatile contents .....	49
3.3.2 Trace element and Sm-Nd isotope analysis.....	51
3.4 Discussion.....	51
3.4.1 Origin and source of the Nsungwe Formation Tuff deposits.....	51
3.4.2 Origin of glass inclusions .....	53
3.4.3 Melt evolution and a case for liquid immiscibility.....	54
3.4.4 Melt evolution modelling .....	56
3.4.5 Comparison to other EARS magma evolution models.....	58
3.4.6 Implications for explosive volcanism.....	59
3.4.7 Titanite as a monitor for alkaline magmatism .....	60
3.4.8 Alkaline volcanism and the ecological evolution of East Africa.....	60
3.5 Conclusions.....	61
References .....	61
Chapter 4 Experimental investigation of the carbonatite trachyte association: phase relations and liquid immiscibility in evolved carbonatite-phonolite magmas .....	67
Abstract.....	67
4.1 Introduction.....	67
4.2 Experimental and analytical methods .....	69
4.2.1 Starting materials.....	69
4.2.2 Experimental techniques.....	70
4.2.3 Microanalysis .....	71
4.3 Results.....	71
4.3.1 Run products.....	71
4.3.2 Liquid compositions .....	78
4.3.3 Solid phase compositions .....	79
4.4 Discussion.....	82

---

---

4.4.1 Crystallisation sequence for experimental CO <sub>2</sub> saturated nephelinite-phonolite GSR-CNK .....	82
4.4.2 Melt evolution, two-liquid solvus and the influence of H <sub>2</sub> O .....	83
4.4.3 Comparisons with natural peralkaline-carbonatite immiscible systems .....	86
4.4.4 Zirconium and fluorine in immiscible peralkaline igneous systems .....	87
4.5 Conclusions .....	88
References .....	89
Chapter 5 Radiogenic isotope record of magma genesis and lithospheric geodynamics of the Rukwa Rift, Tanzania: ca. 165 Ma to present .....	92
Abstract .....	92
5.1 Introduction .....	93
5.2 Geological setting .....	97
5.2.1 The East African Rift System .....	97
5.2.2 Local geology .....	98
5.2.3 Sample description and rationale .....	99
5.3 Analytical procedures .....	100
5.3.1 Sample Preparation .....	100
5.3.2 Bulk Sm-Nd and Rb-Sr isotope analysis .....	100
5.3.3 In-situ Sm-Nd isotope analysis .....	101
5.3.4 In-situ Lu-Hf isotope analysis .....	102
5.4 Results .....	102
5.4.1 Sm-Nd and Rb-Sr isotopes of bulk titanite separates .....	102
5.4.2 In-situ Sm-Nd isotopes .....	103
5.4.3 In-situ Lu-Hf isotopes of zircon .....	106
5.4.4 Model enrichment age calculations .....	106
5.5 Discussion .....	107
5.5.1 Isotopic constraints of the NFT .....	108
5.5.2 Isotopic evolution through time .....	110
5.5.3 Isotopic characteristics and possible lithospheric sources for the NFT .....	111
5.5.4 Model of the geological evolution of the Rukwa Rift Basin and Rungwe Volcanic Province .....	117
5.6 Conclusions .....	118
References .....	119
Chapter 6 Thesis summary and future work .....	124
Appendix A .....	128
A1 Major element and trace element analyses of NFT minerals .....	128
A2 REE+Y distribution and modelling .....	128
A3 Supplementary Figures .....	128
Appendix B .....	132
B1 Supplementary Data and Tables .....	132

---

---

referred to in text.....	132
B2 Additional analyses of Rukwa glass inclusions and host titanite.....	132
B3 Supplementary images of Rukwa glasses.....	132
B4 Supplementary figures and modelling details .....	132
Appendix C.....	139
C1 Synthesis of starting compositions and EDS analysis of run products.....	139
Appendix D .....	140
D1 Bulk Sm-Nd-Sr and in-situ Sm-Nd & Lu-Hf isotope analyses.....	140

---

## List of Tables

<b>Table 2.1</b> Representative analyses of igneous minerals by EMPA .....	18
<b>Table 2.2</b> Igneous mineral assemblage of the NFT .....	26
<b>Table 3.1</b> Normalised representative compositions of NFT glasses.....	49
<b>Table 4.1</b> Bulk composition of starting materials in wt. % .....	69
<b>Table 4.2</b> Experimental run conditions and products .....	71
<b>Table 4.3</b> Major element composition of silicate glass and quenched carbonate liquids .....	73
<b>Table 4.4</b> Average leucite compositions.....	79
<b>Table 4.5</b> Average nepheline compositions.....	79
<b>Table 4.6</b> Average sanidine compositions .....	80
<b>Table 4.7</b> Average titanite and clinopyroxene compositions.....	80
<b>Table 4.8</b> Representative analyses of Zr-rich phases.....	81
<b>Table 4.9</b> Representative analyses of cancrinite group minerals.....	82
<b>Table 5.1</b> Bulk Sm-Nd and Rb-Sr.....	102
<b>Table 5.2</b> In-situ Sm-Nd isotopes .....	105

---

## List of Figures

<b>Fig. 1.1.</b> The East African Rift system, Rukwa Rift Basin and Rungwe Volcanic Province.....	2
<b>Fig. 1.2.</b> Simplified stratigraphy and episodic alkaline volcanism of the Rukwa Rift Basin.....	3
<b>Fig. 1.3.</b> Regional basement map of the East African Rift system.....	6
<b>Fig. 2.1.</b> The Rukwa Rift Basin and Rungwe Volcanic Province. ....	12
<b>Fig. 2.2.</b> Field photos of the Songwe Member of the Nsungwe Formation and NFT.....	14
<b>Fig. 2.3.</b> Thin section microphotographs of the NFT.....	15
<b>Fig. 2.4.</b> Backscattered electron images of NFT minerals separates.....	19
<b>Fig. 2.5</b> C1 chondrite-normalised (mineral/C1 chondrite) REE+Y diagrams.....	20
<b>Fig. 2.6.</b> Na-REE-Carbonate imaging and analysis .....	22
<b>Fig. 2.7.</b> Examples of mineral inclusions observed in titanite and phlogopite.....	23
<b>Fig. 2.8.</b> Composition of clinopyroxene and associated alkaline silicate melts.....	24
<b>Fig. 2.9.</b> Trace element distribution and modelling .....	29
<b>Fig. 3.1</b> The Rukwa Rift Basin.....	42
<b>Fig. 3.2</b> Field photos of the Songwe Member of the Nsungwe Formation and NFT.....	44
<b>Fig. 3.3</b> Mineral and melt inclusions within NFT titanite.....	45
<b>Fig. 3.4 a)</b> Raman spectra of inclusion CS_BW4-2.....	48
<b>Fig. 3.5 a)</b> Total alkalis versus silica diagram.....	50
<b>Fig. 3.6</b> Chondrite normalised REE+Y plots of NFT titanite and glass inclusions .....	51
<b>Fig. 3.7 a)</b> Epsilon Nd (time = 25 Ma) versus SiO <sub>2</sub> content of NFT glass inclusions. ....	52
<b>Fig. 3.8</b> Comparison of the average titanite/melt trace element partition coefficients for the NFT and equilibrated titanite/melt pairs .....	54
<b>Fig. 3.9</b> Melt compositions projected into the SiO <sub>2</sub> -NaAlSiO <sub>4</sub> -KAlSiO <sub>4</sub> (quartz-nepheline-kalsilite, Q-Ne-Ks) ternary system. ....	55
<b>Fig. 3.10</b> Magma evolution via liquid immiscibility.....	57
<b>Fig. 3.11</b> Schematic cross section of a continental rift.....	59
<b>Fig. 4.1</b> Schematic cross section of assembly design.....	70
<b>Fig. 4.2</b> Run 1 (1000 °C) representative products and element maps.....	74
<b>Fig. 4.3</b> Run 2 (950 °C) representative products and element maps.....	74
<b>Fig. 4.4</b> Run 3 (900 °C) representative products and element maps.....	75
<b>Fig. 4.5</b> Run 4 (850 °C) representative products and element maps.....	76
<b>Fig. 4.6</b> Run 5 (800 °C) representative products and element maps.....	76
<b>Fig. 4.7</b> Run 6 (700 °C) representative products and element maps.....	77
<b>Fig. 4.8</b> Run 7 (800 °C; GSR-CNK-F) representative products and element maps.....	78
<b>Fig. 4.9</b> Paragenetic sequence T-X diagram .....	83

---

<b>Fig. 4.10</b> Hamilton projection of the experimentally derived silicate-carbonate conjugate liquid pairs .....	84
<b>Fig. 5.1</b> Image of the EARS showing rift segments, basement rocks and Cenozoic volcanic. ....	94
<b>Fig. 5.2</b> Regional map showing the approximate ages and distribution orogenic basement terrains surrounding the Tanzanian craton .....	96
<b>Fig. 5.3</b> The Rukwa-Malawi-USangu junction and simplified stratigraphy of the Rukwa Rift Basin.....	97
<b>Fig. 5.4</b> In-situ Sm-Nd isotopes of Panda Hill.....	103
<b>Fig. 5.5</b> In-situ Sm-Nd isotopes of NFT titanite .....	104
<b>Fig. 5.6</b> In-situ Sm-Nd isotopes of Lake Beds titanite .....	104
<b>Fig. 5.7</b> Epsilon Hf values of NFT and Lake Beds zircon. ....	106
<b>Fig. 5.8</b> Comparison between whole rock (WR) and in-situ Sm-Nd isotopes .....	108
<b>Fig. 5.9</b> $^{87}\text{Sr}/^{86}\text{Sr}$ vs initial $\epsilon\text{Nd}$ diagram.....	109
<b>Fig. 5.10</b> Epsilon Nd and Hf variation with time.....	112
<b>Fig. 5.11</b> $^{87}\text{Sr}/^{86}\text{Sr}$ - $^{143}\text{Nd}/^{144}\text{Nd}$ data of mafic Quaternary rocks throughout East Africa .....	113
<b>Fig. 5.12</b> Geological evolution of the Rukwa Rift and Rungwe Volcanic Province. ....	116
<b>Fig. 6.1</b> The emergence of active alkaline volcanism and fertile lake-shore environments in the Oligocene Rukwa Rift. ....	125

## Chapter 1

### Introduction to Thesis

The East African Rift System (EARS) serves as a natural laboratory for observing, describing and quantifying the dynamic geological processes of continental break-up. This includes active volcanism, tectonism and geologically rapid shifts in topography and surface expression of the landscape through geologic time. The several thousands of kilometres of inter-connected rift segments that comprise the Eastern and Western Branches of EARS have garnered considerable attention across the geosciences for over a century (Fig. 1.1a). Through the lens of uniformitarianism, the EARS not only provides a means to understand the geological evolution and break-up of eastern Africa but examines more deeply the fundamental aspects of plate tectonic theory and the prevalence of continental break-up throughout Earth's history. Extensive geochemical and geophysical studies have increasingly delved into the deeper lithospheric processes influencing the surficial and chemical expression of rift lavas, the structure and morphology of rift segments, and the presence of an anomalous deep mantle feature beneath the EARS (Bagley and Nyblade, 2013; Castillo et al., 2014; Furman et al., 2016; Hopper et al., 2020). This work continues to fuel long-standing debate between duelling plate vs plume centric models of continental rift development. In parallel, field-based research into the tectonic, volcanic, and depositional history of the EARS continues to redefine the temporal progression of rift development and reconstruct the diverse paleo-ecological past of Eastern Africa (Roberts et al., 2012; Stevens et al., 2013; Pouclet et al., 2016; Simon et al., 2017; Jess et al., 2020).

The research presented in this thesis has been carried out as an extension of the “Rukwa Rift Basin Project”, which is a combined geological and paleontological research effort focused on documenting the late Mesozoic-Quaternary records of faunal evolution in this section of the lesser studied Western Branch of the EARS. To date, this work has successfully uncovered a complex and long-lived history for the Western Branch of the EARS, with rift initiation and active volcanism commencing in the Rukwa Rift at ca. 25 Ma (Fig 1.1 & 1.2) (Roberts et al., 2012). Nearly two-decades of exploration in the late-Oligocene Nsungwe Formation of the Rukwa Rift Basin has described the only known continental Oligocene ecosystem from subequatorial Africa, including fossil evidence for the earliest divergence of Old World monkeys and apes (Roberts et al., 2010; Stevens et al., 2013). The Nsungwe Formation is significant in that it captures the Paleogene-Neogene transition, when major tectonic and magmatic events drastically impacted the landscape and the evolution of species by extension.

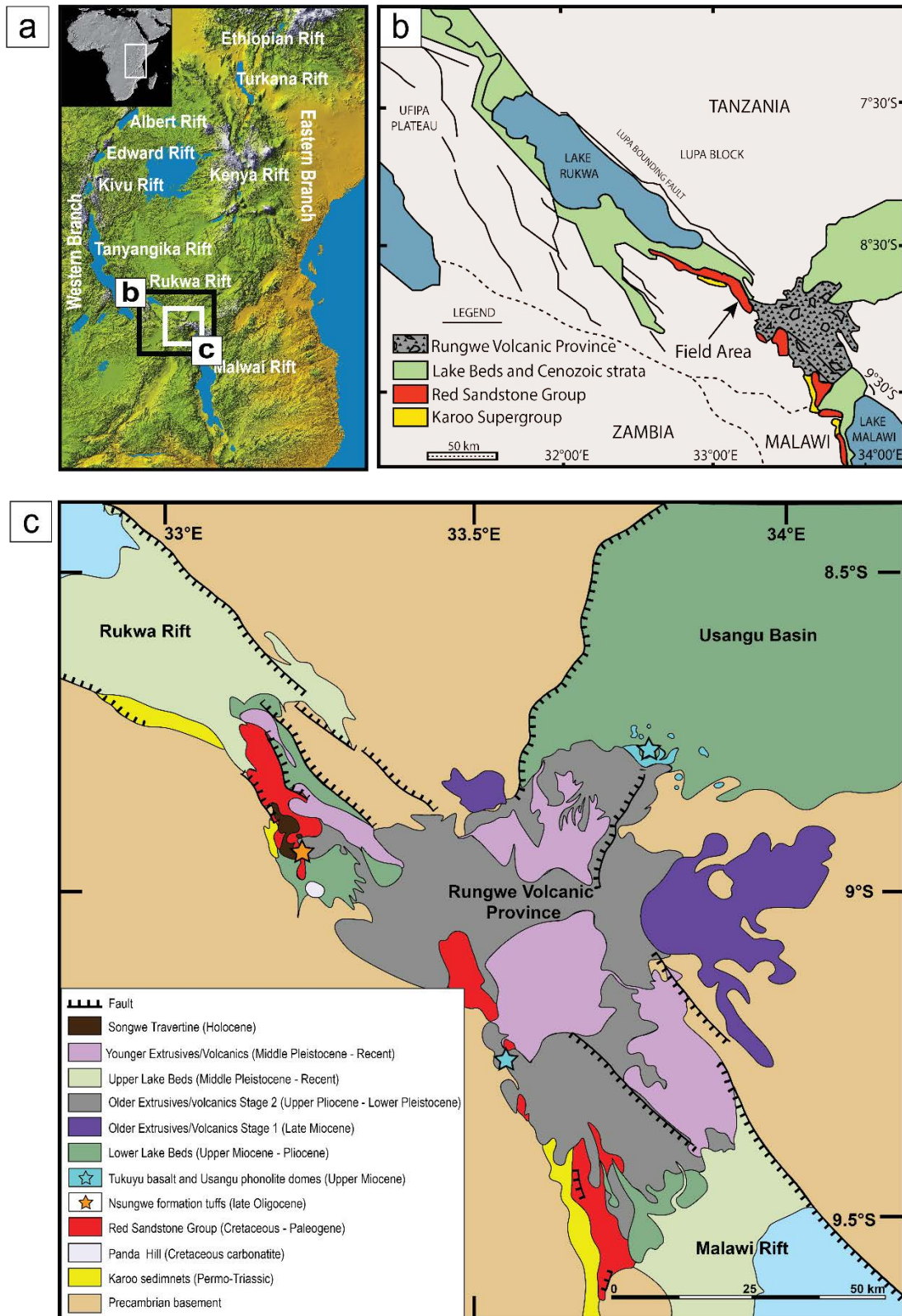


**Fig. 1.1.** The East African Rift system, Rukwa Rift Basin and Rungwe Volcanic Province a) Image of the EARS modified from the NASA Shuttle Radar Topography Mission collection. The black and white boxes indicate the location of panels b and c respectively. b) Simplified geological map of the Rukwa Rift Basin. c) Geological map of the Rungwe-Malawi-USangu junction and Rungwe Volcanic Province.

The rich history of alkaline volcanism preserved in a series of tuffs within the 25-26 Ma stratigraphy of the Nsungwe Formation (Nsungwe Formation tuffs; NFT) of the Rukwa Rift Basin, is the focus of this project, because they collectively represent the earliest and only known manifestation of Paleogene rifting and magmatism in the Western Branch of the EARS (Fig.1.2). As this is first comprehensive geochemical study of this enigmatic episode alkaline magmatism, the overarching aim of this work is to categorically describe the geochemical and petrological character of these volcanic deposits such that the data and insights gained offer meaningful contributions not only towards contemporary models of rift development and continental alkaline magmatism, but also to the broader scientific community.

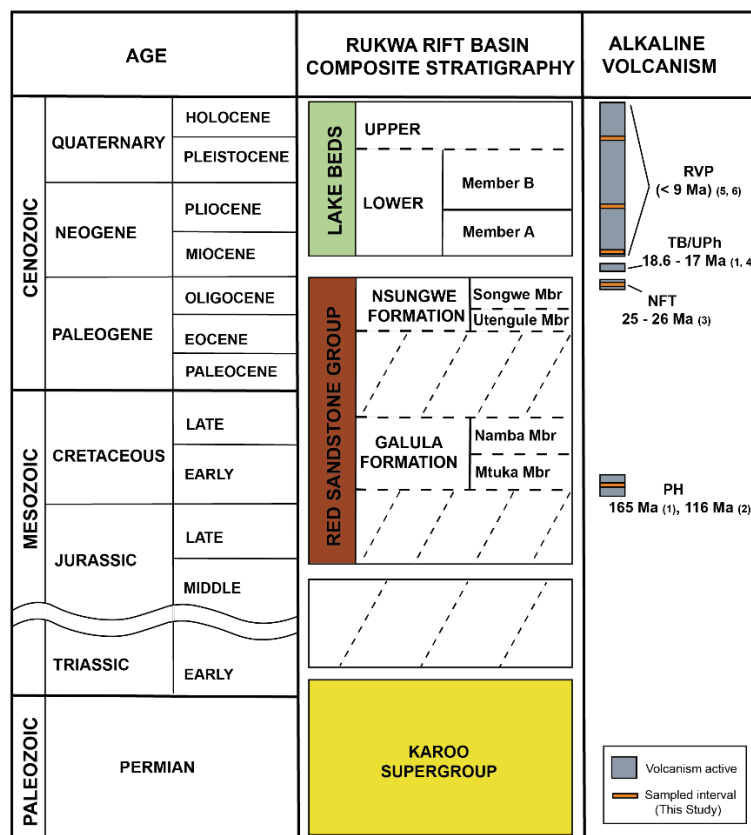


**Fig. 1.2.** Simplified stratigraphy and episodic alkaline volcanism of the Rukwa Rift Basin. Abbreviated volcanic episodes of the Rukwa-Malawi-Usangu Junction shown include PH = Panda Hill carbonatite, NFT = Nsungwe formation Tuffs, TB = Tikuyu Basalt, UPh = Usangu phonolites, RVP = Rungwe volcanic province. Reported ages are from: (1) Mesko et al. (2020); (2) Morisset (1993); (3) Roberts et al. (2012); (4) Rasskazov et al. (2003); (5) Ebinger et al. (1989); (6) Fontijn et al. (2012). The stratigraphy presented is from Mtelega et al. (2017).

This thesis consists of four individual research components (Chapters 2-5) bookended by an introductory chapter (Chapter 1) and conclusions chapter (Chapter 6). Chapters 2 to 5 each explore a fundamental aspect concerning the nature, source, and/or evolution of early rift volcanism in the Rukwa Rift. The thesis is structured such that each of the main research chapters are prepared as papers for publication. This format does lead to some repetition in description of geological background and

methodology, but has the advantage that each chapter can also be considered a stand-alone paper within the context of the broader thesis.

The first distinct element of this thesis (Chapter 2) addresses a long-standing challenge concerning the study of incipient rift volcanism in the global geological record – preservation. The innately low-volume, strongly alkaline and chemically susceptible nature of early rift lavas means they are prone to inundation and/or erosion from the landscape by later magmatic or geomorphological processes that typify a continental rift (Fig. 1.1c). The late-Oligocene NFT deposits of the early Rukwa Rift are a testament to the ‘preservation problem’ given they are the extensively altered, sole remnants of what was over a mega-annum of active explosive volcanism proximal to the southern Rukwa Rift Basin. Here, geochemical information locked within resistant igneous minerals presents an invaluable source of primary petrological information and the only opportunity to circumvent the pervasive secondary weathering processes inherent to volcanic deposits within continental rift basins. The careful acquisition of primary petrographic and geochemical data retained in igneous minerals and their inclusions provides a wealth of information regarding the composition, evolution, and approximate geological conditions implicated in the magma genesis and volcanism of the NFT. In first instance, this elucidates the nature and origin of these deposits and the advent of alkaline-carbonatite volcanism in the early Rukwa Rift. When combined with recent geochronological and geophysical data, this work offers renewed insights into the spatial and temporal distribution of volcanism for the Rungwe Volcanic Province. More broadly, the stepwise methodological approach presented is shown to be equally practical, broadly applicable, and, in this case, integral to the investigation of early rift volcanism of the Western Branch.

Despite the alkali-carbonatite volcanoes of the EARS accounting for the least-abundant low-volume occurrences of volcanism on Earth, their enigmatic nature, exotic mineralogy, and eminence in the silicate-carbonatite rock association have captivated petrologists for generations. During this time, both the study of melt inclusions and experimental petrology have played a vital role in understanding the genesis and evolution of carbonatite magmas globally (Wyllie and Tuttle, 1960; Brooker and Kjarsgaard, 2010; de Moor et al., 2013; Guzmics et al., 2015). This is in part because they too have the capacity to overcome the inherent ‘preservation problem’, but also because they reliably record/reproduce and preserve the conditions and complex processes (i.e. liquid immiscibility) involved in their formation. Accordingly, Chapter 3 of this thesis examines silicate glass inclusions hosted within NFT titanite to trace the composition and conditions of the pre-eruptive magmatic system. The resulting key principles and magma conditions derived from this study form a rational basis for the experimental investigation of silicate-carbonatite liquid immiscibility in evolved peralkaline systems (Chapter 4).

A distinctive feature of igneous titanite from the NFT is they frequently contain large silicate glass (formerly melt) inclusions. Geochemical analysis of pristine silicate glasses and host titanite

provide remarkable insights into the pre-eruptive alkali-carbonatite magmatic system and processes implicated in the formation of the NFT (Chapter 3). The melt evolution recorded in titanite shifts from silica-undersaturated to silica-saturated compositions and crosses the feldspar thermal divide. Such an evolution is unusual and is considered prohibitive within a closed magmatic system. However, geochemical modelling shows the observed shift from silica-undersaturated to silica-saturated compositions occurs via closed system unmixing of alkali-carbonatite magma from a CO<sub>2</sub>-rich phonolitic precursor, free of crustal assimilation. Existing experimental and melt inclusion data supports isobaric cooling as a viable mechanism for unmixing and crossing the feldspar thermal divide, estimated here to have occurred at mid-crustal conditions outlined for the Western Branch (Fadaie and Ranalli, 1990; Brooker and Kjarsgaard, 2010). Given the highly explosive, volatile-rich, silica-saturated melt compositions produced via this process, the data and modelling presented outlines an entirely new mode of explosive alkaline volcanism in developing continental rifts.

In-light of the unusual melt evolution recorded in NFT titanite and the poorly understood carbonatite-trachyte association of the EARS, a series of experiments focusing on the principle of isobaric cooling and expansion of the two-liquid solvus were performed, as outlined in Chapter 4. The overarching aim of this component was to investigate unmixing and liquid immiscibility as a viable mechanism for crossing the feldspar thermal divide by reproducing the magma compositions and geological conditions inferred from melt inclusions of the NFT (i.e. 1000 °C – 700 °C and 0.5 GPa). Although silica-saturated compositions were not generated in this series of experiments, expansion of the two-liquid solvus (as predicted) is shown to occur. Additionally, the mineral assemblages and overall paragenesis produced across the specified geological conditions are remarkably like those observed for the NFT and other alkaline-carbonatite systems elsewhere in nature. Collectively, this work provides renewed theoretical and petrological insights concerning the novel repercussions of liquid immiscibility in highly-evolved silica-undersaturated melt compositions and the trachyte-carbonatite association of the EARS.

The Rukwa Rift Basin is hosted within a structurally weakened Paleoproterozoic shear belt that connects the Tanganyika and Malawi rifts in southwestern Tanzania (Fig. 1.3.). Since the late Paleozoic, the Rukwa Rift has experienced multiple episodes of tectonic reactivation, many of which are associated with episodic alkaline magmatism (Fig 1.2) (Roberts et al., 2010; Delvaux et al., 2012; Mtelela et al., 2017). While Paleozoic and Mesozoic tectonic activity in the Rukwa Rift is attributed to shifts in far-field stress and global tectonics, the Cenozoic extension associated with EARS development purportedly stems from the interaction of an anomalous deep mantle upwelling with the relatively stagnant African continental lithosphere (Guiraud et al., 1992; O'Connor et al., 1999; Castillo et al., 2014). The isotopic character of local magmatism during Jurassic – Cretaceous times can be used to characterise the lithospheric source of melting prior to the onset of EARS development, whereas volcanic tuffs and their primary minerals from the late-Oligocene and Miocene-recent Rukwa Rift Basin strata may constrain

processes and source of lithospheric disturbance associated with the initiation and development of the EARS. Given the broad implications melt histories and lithospheric evolution have on the tectonic and crustal evolution of rift segments, establishing the lithospheric source of the NFT and re-examining the local record of magma evolution through a wider temporal lens is critically important in understanding the initiation and development of the Western Branch. The integrated geochemical data, combined with the available tectonic, magmatic and geophysical findings presented in Chapter 5 provides the basis of a new conceptual model for the geodynamic evolution of the Cenozoic Rukwa Rift. Such a model may be a useful consideration in describing amagmatic rift segments and isolated volcanic provinces elsewhere in the Western Branch.

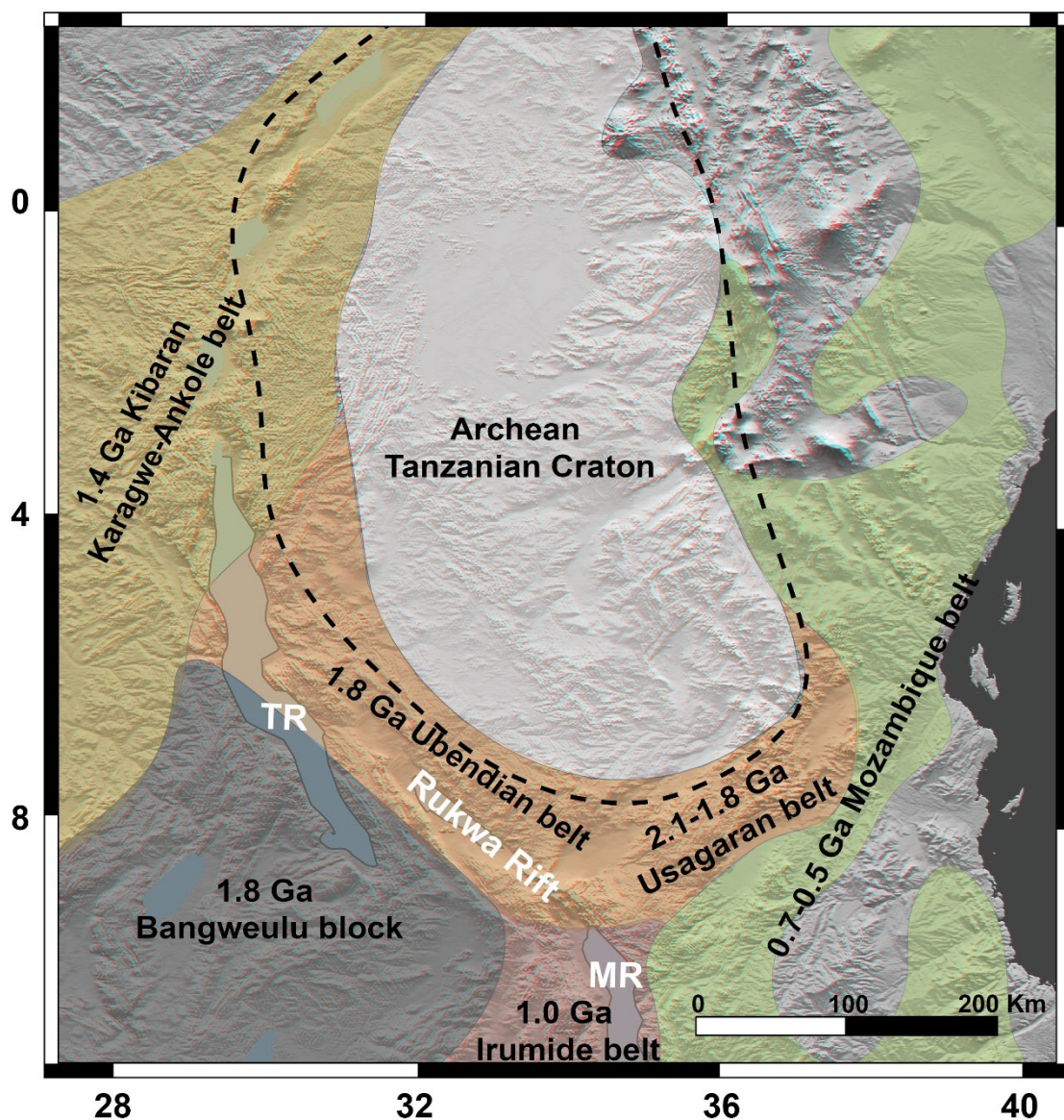


**Fig. 1.3.** Regional basement map of the East African Rift system showing the approximate ages and distribution of orogenic basement terrains surrounding the Tanzanian craton (adapted from Roberts et al. (2012)). Abbreviations refer to the Tanganyika Rift (TR), Malawi Rift (MR).

**References**

- Bagley, B., & Nyblade, A. A. (2013). Seismic anisotropy in eastern Africa, mantle flow, and the African superplume. *Geophysical Research Letters*, 40(8), 1500-1505.
- Brooker, R., & Kjarsgaard, B. (2010). Silicate–carbonate liquid immiscibility and phase relations in the system SiO<sub>2</sub>–Na<sub>2</sub>O–Al<sub>2</sub>O<sub>3</sub>–CaO–CO<sub>2</sub> at 0.1–2.5 GPa with applications to carbonatite genesis. *Journal of petrology*, 52(7-8), 1281-1305.
- Castillo, P. R., Hilton, D. R., & Halldórsson, S. A. (2014). Trace element and Sr-Nd-Pb isotope geochemistry of Rungwe Volcanic Province, Tanzania: implications for a superplume source for East Africa Rift magmatism. *Frontiers in Earth Science*, 2, 21.
- de Moor, J. M., Fischer, T. P., King, P. L., Botcharnikov, R. E., Hervig, R. L., Hilton, D. R., . . . Ramirez, C. (2013). Volatile-rich silicate melts from Oldoinyo Lengai volcano (Tanzania): Implications for carbonatite genesis and eruptive behavior. *Earth and Planetary Science Letters*, 361, 379-390.
- Delvaux, D., Kervyn, F., Macheyeke, A., & Temu, E. (2012). Geodynamic significance of the TRM segment in the East African Rift (W-Tanzania): Active tectonics and paleostress in the Ufipa plateau and Rukwa basin. *Journal of Structural Geology*, 37, 161-180.
- Ebinger, C.J., Deino, A.L., Drake, R., Tesha, A., 1989. Chronology of volcanism and rift basin propagation: Rungwe volcanic province, East Africa. *Journal of Geophysical Research: Solid Earth*, 94(B11): 15785-15803
- Fadaie, K. t., & Ranalli, G. (1990). Rheology of the lithosphere in the East African Rift System. *Geophysical Journal International*, 102(2), 445-453.
- Furman, T., Nelson, W. R., & Elkins-Tanton, L. T. (2016). Evolution of the East African rift: Drip magmatism, lithospheric thinning and mafic volcanism. *Geochimica et Cosmochimica Acta*, 185, 418-434.
- Guiraud, R., Binks, R., Fairhead, J., & Wilson, M. (1992). Chronology and geodynamic setting of Cretaceous-Cenozoic rifting in West and Central Africa. *Tectonophysics*, 213(1-2), 227-234.
- Guzmics, T., Zajacz, Z., Mitchell, R. H., Szabó, C., & Wälle, M. (2015). The role of liquid–liquid immiscibility and crystal fractionation in the genesis of carbonatite magmas: insights from Kerimasi melt inclusions. *Contributions to Mineralogy and Petrology*, 169(2), 17.
- Hopper, E., Gaherty, J. B., Shillington, D. J., Accardo, N. J., Nyblade, A. A., Holtzman, B. K., . . . Ferdinand, R. W. (2020). Preferential localized thinning of lithospheric mantle in the melt-poor Malawi Rift. *Nature Geoscience*, 13(8), 584-589.
- Jess, S., Koehn, D., Fox, M., Enkelmann, E., Sachau, T., & Aanyu, K. (2020). Paleogene initiation of the Western Branch of the East African Rift: The uplift history of the Rwenzori Mountains, Western Uganda. *Earth and Planetary Science Letters*, 552, 116593.
- Mesko, G.T., 2020. Magmatism at the southern end of the east african rift system: Origin and role during early stage rifting. Columbia University
-

- Morisset, N., 1993. Stable isotope and radioisotope geochemistry of the Panda Hill carbonatite, Tanzania.
- Mtelela, C., Roberts, E. M., Hilbert-Wolf, H. L., Downie, R., Hendrix, M. S., O'Connor, P. M., & Stevens, N. J. (2017). Sedimentology and paleoenvironments of a new fossiliferous late Miocene-Pliocene sedimentary succession in the Rukwa Rift Basin, Tanzania. *Journal of African Earth Sciences*, 129, 260-281.
- O'Connor, J., Stoffers, P., van den Bogaard, P., & McWilliams, M. (1999). First seamount age evidence for significantly slower African plate motion since 19 to 30 Ma. *Earth and Planetary Science Letters*, 171(4), 575-589.
- Pouclet, A., Bellon, H., & Bram, K. (2016). The Cenozoic volcanism in the Kivu rift: Assessment of the tectonic setting, geochemistry, and geochronology of the volcanic activity in the South-Kivu and Virunga regions. *Journal of African Earth Sciences*, 121, 219-246.
- Rasskazov, S. et al., 2003. A magmatic episode in the Western Rift of East Africa (19-17 Ma). *Geologiya i Geofizika*, 44(4): 317-324.
- Roberts, E. M., O'Connor, P. M., Stevens, N. J., Gottfried, M. D., Jinnah, Z. A., Ngasala, S., Armstrong, R. A. (2010). Sedimentology and depositional environments of the Red Sandstone Group, Rukwa Rift Basin, southwestern Tanzania: New insight into Cretaceous and Paleogene terrestrial ecosystems and tectonics in sub-equatorial Africa. *Journal of African Earth Sciences*, 57(3), 179-212.
- Roberts, E. M., Stevens, N., O'Connor, P. M., Dirks, P., Gottfried, M. D., Clyde, W., . . . Hemming, S. (2012). Initiation of the western branch of the East African Rift coeval with the eastern branch. *Nature Geoscience*, 5(4), 289.
- Simon, B., Guillocheau, F., Robin, C., Dauteuil, O., Nalpas, T., Pickford, M., . . . Bez, M. (2017). Deformation and sedimentary evolution of the Lake Albert rift (Uganda, east African rift system). *Marine and Petroleum Geology*, 86, 17-37.
- Stevens, N. J., Seiffert, E. R., O'Connor, P. M., Roberts, E. M., Schmitz, M. D., Krause, C., . . . Temu, J. (2013). Palaeontological evidence for an Oligocene divergence between Old World monkeys and apes. *Nature*, 497(7451), 611.
- Wyllie, P., & Tuttle, O. (1960). The System CaO-CO<sub>2</sub>-H<sub>2</sub>O and the Origin of Carbonatites. *Journal of petrology*, 1(1), 1-46

## Chapter 2

# **Mineralogy and origin of the alkaline Nsungwe Formation tuffs of the Rukwa Rift Basin, southwestern Tanzania**

### **Abstract**

The incipient phases of continental rift development remain enigmatic, as early rift sequences are rarely exposed, or poorly preserved in the geologic record. Here, we present petrographic and geochemical analyses of heavy mineral separates from pervasively weathered volcanic horizons intercalated within syn-rift sedimentary deposits from the Rukwa Rift Basin, southwestern Tanzania. These Oligocene (25-26 Ma) ashfalls represent the first magmatic products associated with the initiation of rifting in the Western Branch of the East African Rift System (EARS). In this work, we combine detailed single crystal petrography with in-situ geochemistry to characterise an alkaline volcanic mineral assemblage consisting of titanite, phlogopite, fluorapatite, clinopyroxene, Ti-rich andradite, sanidine, pyrochlore, nepheline, cancrinite, Fe-sulphide (pyrrhotite), calcite, Na-REE-carbonate and peralkaline silicate melt. These minerals are significantly enriched in trace elements particularly Ba, Sr and rare earth elements (REE), with REE+Y contents consistent with derivation from peralkaline phonolitic melts. Placed in context of EARS development, these tuffs display the hallmarks of explosive alkaline-carbonatite volcanism in their resistant minerals and inclusions; the nature and occurrence of which is consistent with early rift progression elsewhere in the EARS. Importantly, we showcase the depth of extractable petrographic information preserved in extensively weathered volcanic ash horizons deposited into an active continental rift basins. Such an approach may have significant implications for recognising early volcanogenic sequences in continental rift zones worldwide, but particularly in other segments of the Western branch of the EARS.

### **2.1 Introduction**

The East African Rift System (EARS) extends over 4000 km from the Red Sea in the north to Mozambique in the south. It is the archetypal continental rift zone. The onset and development of rifting and accompanying intra-plate magmatism of the EARS is attributed to a series of connected low-velocity seismic anomalies occurring ~400 km beneath Ethiopia, Kenya and Tanzania, defined as the African superswell (Nyblade, 2011). In the case of Eastern Africa, the arrival of the African superswell at 40-30

Ma and geomorphological transformations that occurred thereafter had profound effects on topography and climate, as well as the distribution and exchange of flora and fauna, including hominids within and beyond the African continent during a critical evolutionary time period (WoldeGabriel et al., 2000).

The EARS is often described as consisting of a much older, volcanically active and well exposed Eastern Branch, and a younger, less exposed Western Branch that is characterised deep rift lakes, dense vegetation and significant overburden that obscures its volcanic and sedimentary archives. The Rukwa Rift Basin is one of the few segments of the Western Branch receiving extensive geological attention in recent years (Roberts et al., 2010, 2012; Mtelela et al., 2016, 2017; Hilbert-Wolf et al., 2017; Grijalva et al., 2018; Njinju et al., 2019). Importantly, Roberts et al. (2010) described and dated one of the only fossiliferous Cretaceous-Palaeogene continental sedimentary sequences in sub-equatorial Africa – the Red Sandstone Group (Fig. 2.1). Within the Red Sandstone Group is the Oligocene-aged Nsungwe Formation, which is characterised by the presence of abundant vertebrate fossils (including two new species of primate) and intercalated weathered tuff units that have tentatively been assigned to be of alkaline, possibly carbonatitic, affinity (Roberts et al., 2012; Stevens et al., 2013).

The rift basins of the EARS have proven to be exceptional archives for rift-associated alkaline volcanism (WoldeGabriel et al., 2000; Fontijn et al., 2012; Greenwood, 2014; Mtelela et al., 2016, 2017). The ~25 Ma Nsungwe Formation tuffs (NFT hereafter) of the Rukwa Rift Basin are a prime example, as they represent the eruptive products of the earliest volcanic events in the Western Branch, and they are coeval with EARS development elsewhere in the eastern branch (Roberts et al., 2012). The age and geological significance of the NFT has challenged contemporary rift models by revealing that active volcanism, basin subsidence and sediment accumulation commenced in the Rukwa Rift Basin 14 m.y. earlier than previously recognised (Roberts et al., 2012). The relative timing and nature of these events is consistent with reports of Early Miocene tectono-magmatic development elsewhere in the Western Branch, such as ~21 Ma nephelinites of Idwige Island in the Kivu Rift (Poulet et al., 2016), the ~19-17 Ma phonolites and alkali basalts of the Usangu Basin and Tukuyu region of the Rungwe Volcanic Province (RVP) (Fig. 2.1b) (Rasskazov et al., 2003; Mesko et al., 2020), and deformation, basin subsidence and deposition reported for the Lake Albert Rift at ~17 Ma (Simon et al., 2017). In all cases, including the NFT presented here, these discoveries warrant further investigation to verify their nature and occurrence, and to consolidate these events for inclusion in continually evolving models of EARS development.

It has been well demonstrated, both in the EARS and elsewhere, that volcanic deposits formed at or during the initial stages of rifting can provide crucial information on the deeper magmatic and tectonic processes associated with continental breakup (Ernst and Bell, 2010; Kampunzu and Lubala, 2012; Baudouin et al., 2016, 2018). However, much of this potential utility hinges on the proviso that primary magmatic features of these often unusual volcanic products are preserved for study (Zaitsev and

Keller, 2006; Ernst and Bell, 2010; Baudouin et al., 2018; Guzmics et al., 2019). Herein lies the problem with the NFT and many other volcanic units formed in rift settings; their poor preservation and the dynamic nature of rift settings means that deciphering their original magmatic character using conventional petrographic approaches is inherently difficult (Veizer et al., 1992; Zaitsev and Keller, 2006; Ernst and Bell, 2010; Guzmics et al., 2019). Currently, no appropriately-aged volcanic vent or source of appropriate age is known in the region for the NFT, which presents a further challenge to understanding their nature and origin.

This study provides the first comprehensive petrographic and geochemical investigation of igneous minerals from the NFT deposits. Through this, we aim to decipher the magmatic character of this poorly-understood episode of volcanic activity in the Western Branch and place it in context of volcanic development of the greater EARS. This work not only highlights the utility of weathering-resistant igneous minerals in the investigation of enigmatic and poorly-preserved volcanic episodes, but also demonstrates what may become an integral and necessary approach in locating and deciphering early rift-related volcanism elsewhere in the EARS.

## **2.2 Background and regional geology**

The Rukwa Rift Basin lies between the Tanganyika and Nyasa (Malawi) rifts along the southern extension of the Western Branch of the EARS in southwestern Tanzania (Figs. 2.1a and 2.1b). It is a northwest-southeast trending half-graben basin approximately 360 km long and 40 km wide that is juxtaposed with the southwestern margin of the Tanzanian Craton. Basin geometry and subsidence are largely governed by the Lupa Bounding Fault that follows the northwest-southeast foliation trend of the underlying Paleoproterozoic Ubendian shear belt (Ebinger et al., 1989; Kilembe and Rosendahl, 1992). The Ubendian basement connects the Archean Tanzanian craton in the northeast to the Bangweulu block in the southwest. Elsewhere, the Rukwa Rift Basin is bound by the Ufipa Fault and Plateau to the west and southwest, and the Ubende Plateau to the north and northwest (Kilembe and Rosendahl, 1992). At its southernmost extent the Rukwa Rift Basin splits into the Msangano and Songwe troughs, which advance southward towards the Cenozoic RVP where well documented volcanic activity is recorded from ca. 9 Ma to present (Ebinger et al., 1989; Fontijn et al., 2012).

The Rukwa Rift initiated in response to Paleozoic sinistral shear zone development in the Ubendian Belt (Theunissen et al., 1996). Multiple reactivation events since the late Paleozoic have facilitated the accumulation of a remarkably thick (between 8-11 km) sedimentary package (Kilembe and Rosendahl, 1992; Morley et al., 1999; Delvaux et al., 2012). Comprehensive analysis of the seismic profiles, well data and surface geology identified at least four episodes of rifting in the RBB, which include; (1) a Permo-Triassic event, which resulted in the deposition of Karoo Supergroup equivalent strata (Kilembe and Rosendahl, 1992; Morley et al., 1999); (2) a Cretaceous rifting event that deposited the Galula Formation (dinosaur fossil bearing, fluvial, lower sequence of the Red Sandstone Group

(Roberts et al., 2010); (3) a late Oligocene event that deposited the Nsungwe Formation (upper sequence of the Red Sandstone Group (Roberts et al., 2010, 2012) and; (4) late Miocene to Recent rifting and deposition of the Lake Beds succession, accompanied by voluminous bimodal volcanism in the RVP (Ebinger et al., 1989; Mtelela et al., 2017).

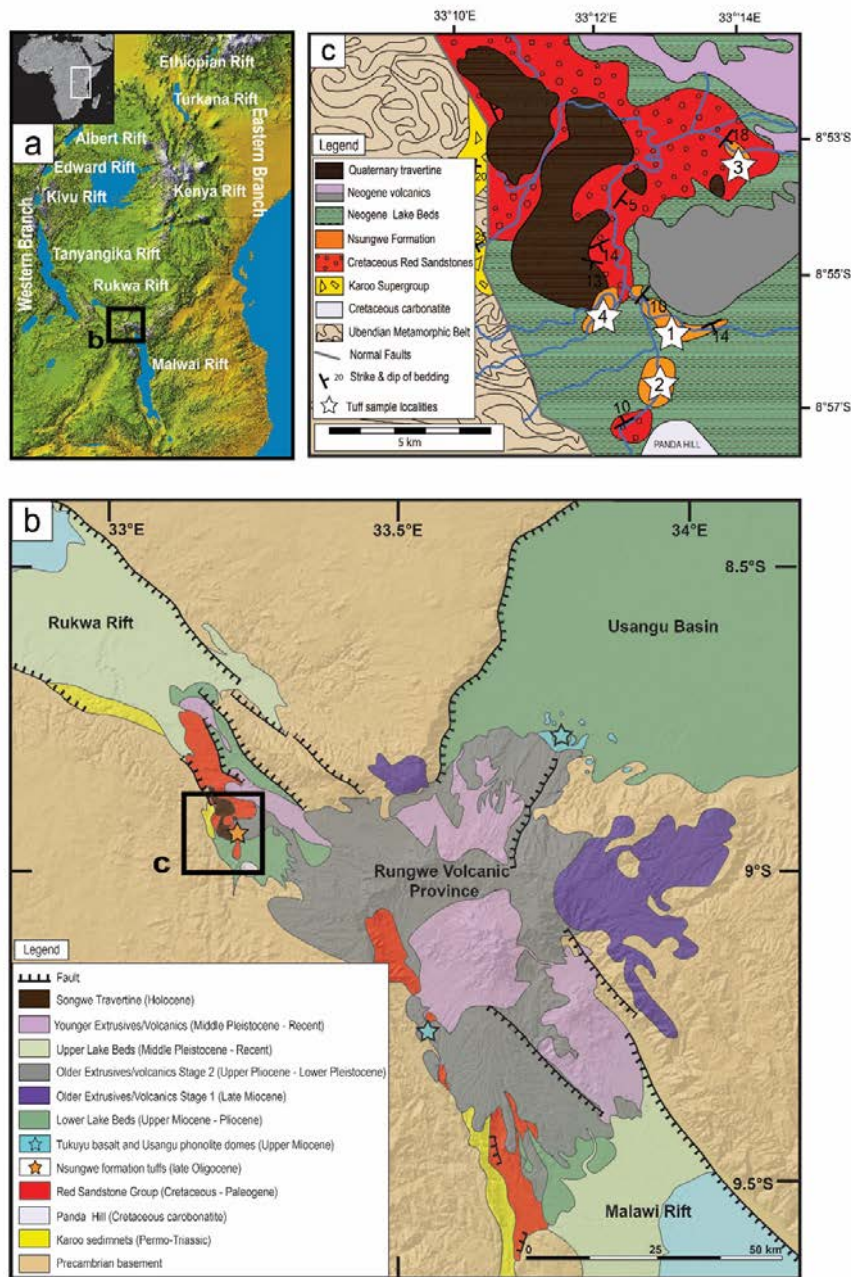


**Fig. 2.1.** The Rukwa Rift Basin and Rungwe Volcanic Province. a) Image of the EARS modified from the NASA Shuttle Radar Topography Mission collection. The black box indicates the location of the Rukwa Rift Basin of panel b. b) Geological map of the Rukwa-Malawi-Usangu basin junction and Rungwe Volcanic Province (adapted from Fontijn et al. (2012) and Rasskazov et al. (2003), using the Global Multi-Resolution Topography base map of Ryan et al. (2009). c) Local geological map of the field area in the Rukwa Rift Basin with the four Oligocene sample locations indicated by white stars (1 = Nsungwe; 2 = Songwe, 3 = Ikumbi and 4 = Nanyala river sections).

The southern Rukwa Rift region has experienced multiple phases of alkaline magmatism that coincide with periods of tectonic development. These include the Late Jurassic to Early Cretaceous (160-116 Ma) Panda Hill, Sengeri Hill, Mbalizi, Musensi and Songwe Scarp carbonatites (Van Straaten and Bell, 1989; Mesko et al., 2020), the Oligocene (25 Ma) NFT deposits (Roberts et al. 2010, 2012), Early Miocene (19-17 Ma) phonolites and alkali-basalt of the Usangu Basin and Tukuyu region (respectively) of the RVP (Rasskazov et al., 2003; Mesko et al., 2020), and Late Cenozoic to recent volcanism of the RVP (Ebinger et al., 1989; Fontijn et al., 2012). The Late Cenozoic to recent volcanism comprises a variety of alkaline to sub-alkaline rock types (including phonolites, nephelinites, trachytes, basanites, picrites and alkali basalts (Ebinger et al., 1989; Fontijn et al., 2012; Castillo et al., 2014) the formation of which have typically been grouped into three discrete episodes of increased activity; 9.4-5.4 Ma, 3.0-1.3 Ma and 0.6 Ma to present (Ebinger et al., 1989; Fontijn et al., 2012). However, analysis of detrital magmatic grains and tuffaceous deposits in drill core from the Cenozoic Lake Beds suggest this activity may have been more continuous than previously thought (Hilbert-Wolf et al., 2017).

The modern RVP notably lacks the ultra-potassic or hypersodic compositions observed elsewhere in the EARS. These lavas are nonetheless characterised by a high abundance and remarkable variance of incompatible trace elements, which is suggested to be the product of the degree of partial melting at the source and/or fractional crystallisation en-route to the surface (Castillo et al., 2014). The occurrence of strongly alkaline-carbonatite magmatism in the Rukwa Rift region (and EARS more broadly) has been attributed to a regional carbonatite metasomatic event that enriched the sub-continental lithospheric mantle beneath the Rukwa Rift and RVP c.a. 500-1000 Ma (Furman, 1995; Furman and Graham, 1999). Castillo et al. (2014) linked the source of this enrichment to the African Superplume. At a local scale, the contribution of long-lived metastable assemblages (mantle metasomes) has also been recognised in the EARS and are suggested to have formed during one or more of the ancient orogenic events that surround the Tanzanian Craton (Furman and Graham, 1999; Rooney, 2019).

### **2.3 Sample description and preparation**

The NFT are identified in outcrop as discrete, 3-10 cm-thick, laterally extensive mottled clay-rich horizons that are interbedded with the fossiliferous muddy sandstones and siltstones of the Songwe Member of the Nsungwe Formation (Roberts et al., 2010). They have been identified in four river sections (Nsungwe, Songwe, Ikumbi and now Nanyala) across the known exposed area of the Nsungwe Formation (Figs. 2.1c, 2.2a and b). These volcanic deposits consist almost entirely of montmorillonite ( $\pm$  saponite) clays, but also contain minor amounts of large (>1 cm) dark brown phlogopite mica, euhedral yellow titanite crystals (up to 0.5 cm), black Ti-andradite garnet (up to 0.5 cm) and translucent tabular sanidine crystals (up to 0.5 cm) (Figs. 2.2c and e). Phlogopite is often concentrated in the uppermost horizon of individual tuff units (Fig. 2.2e), while all minerals (including phlogopite) and occasional relict pumice clasts are dispersed throughout the tuffs (Figs. 2.2c-e). The NFT also contain

low proportions of bulk detrital minerals (i.e. quartz, metamorphic lithic fragments) and lack the vertebrate fossil material that characterise adjacent and interbedded lithologies.

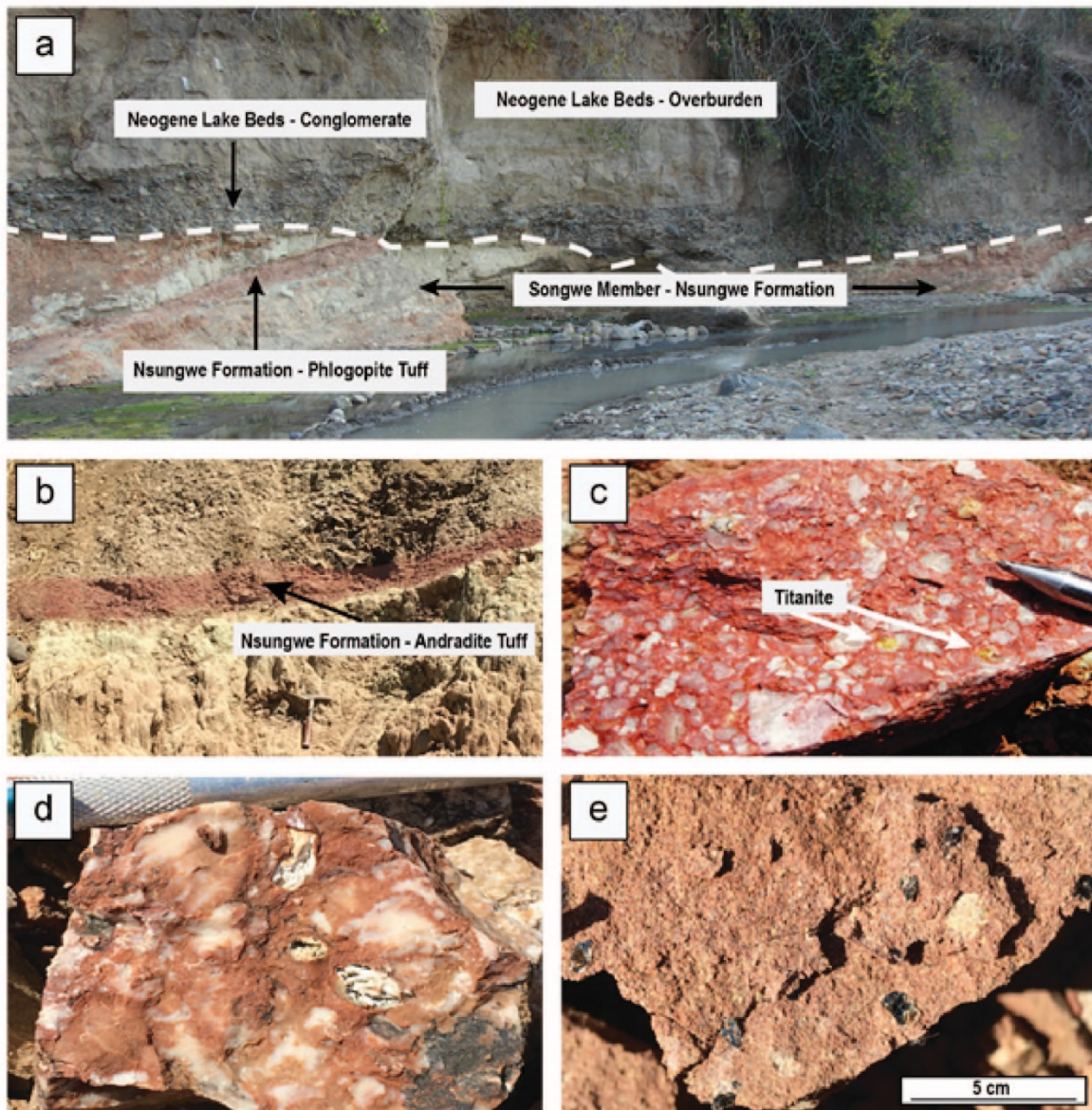


**Fig. 2.2.** Field photos of the Songwe Member of the Nsungwe Formation and NFT. a) Nsungwe River outcrop with the Songwe Member sitting below an erosional unconformity with the basal conglomerates of the overlying Neogene Lake Beds Group. b) Approximately 40 cm thick maroon tuff bed of the NFT deposit called the Andradite Tuff Bed (hand specimen shown in d). c) White relict tuffaceous textures of NFT in a maroon clay matrix with large yellow titanite. d) Altered pumice clasts within NFT hand sample. e) Top-down view showing multiple large phlogopite crystals (black) concentrated in the upper horizon of NFT.

Individual samples were collected across multiple field seasons (2015-2018) from the Nsungwe (AS18 and BW4), Songwe (TZ-1), Ikumbi (LL-05) and Nanyala (FT-1) river sections of the Nsungwe Formation (Fig. 2.1c). For this study, approximately 0.5-1 kg of each sample was soaked in water

overnight to saturate the clay matrix. Samples were then washed thoroughly to remove the clays prior to a combined multi-stage rinsing and ultra-sonic agitation procedure. The resulting crystal-rich sand was then subject to heavy-liquid separation followed by Franz magnetic separation of the heavy fraction to produce clean crystal separates. Pristine minerals were then picked and mounted in epoxy for geochemical analysis. Only euhedral minerals were selected to avoid any potential detrital contributions. An emphasis was placed on selecting minerals that contained inclusions of glass (melt) and other mineral phases to establish petrographic relationships between cogenetic phases. Samples AS18 and BW4 were selected to be the focus of the petrographic investigation presented here, based on the large volume of each sample, and the pristine nature and large crystal sizes of crystal-rich separates that were generated from these samples. Thin section blocks of BW4 and AS18 were also prepared to aid petrographic analysis. Once mineral phases were picked and mounted, samples were polished by hand and in a water-free environment to preserve any water-soluble phases (e.g. carbonates) that may be present as inclusions.

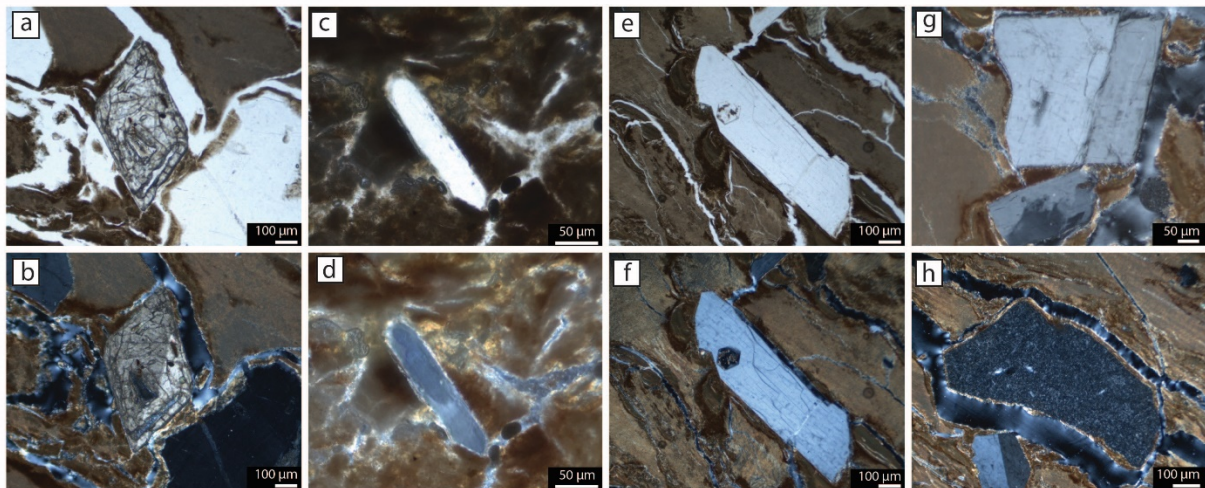


**Fig. 2.3.** Thin section microphotographs of the NFT. All grains are hosted in bentonite clay (devitrified volcanic ash) matrix. (a) Plane-polarised light (PPL) and, (b) Cross-polarised light (XPL) images of a euhedral titanite with simple twinning; (c) PPL and (d) XPL image of a euhedral apatite needle with patchy zonation; (e) PPL and (f) XPL image of tabular sanidine with a euhedral phlogopite inclusion; (g) XPL image of blocky sanidine with simple twinning and a smaller tabular sanidine with complex wavy zonation; (e) XPL image of a mafic volcanic clast dominated by fine-grained feldspar laths, and euhedral feldspar with simple twinning below.

## 2.4 In-situ analysis

Samples were studied in detail using an SU 5000 Hitachi field-emission gun scanning electron microscope at the Advanced Analytical Centre (AAC), James Cook University (JCU), Townsville, Australia. Imaging utilised secondary electron imaging, backscattered electron imaging and cathodoluminescence imaging, with careful attention paid to mineral inclusion assemblages (aided by energy dispersive spectrometry identification). Host grains and inclusions were examined in terms of

crystal geometry, zonation, signs of alteration, as well as the abundance and location of inclusions in the host. Euhedral crystals and inclusions with sharp unaltered grain boundaries were preferentially selected for quantitative major and trace element analysis.

Major element analyses of minerals were conducted by wavelength dispersive spectrometry using a JEOL JXA8200 superprobe at the AAC in Townsville. All analyses were conducted using a 20 nA and 15 kV electron beam defocused to 10  $\mu\text{m}$  diameter. Analyses were standardised using well-characterised oxide ( $\text{Fe}_2\text{O}_3$ ,  $\text{TiO}_2$ ,  $\text{ZrO}_2$ ,  $\text{LiNbO}_3$ ), silicate ( $\text{Mg}_2\text{SiO}_4$ ,  $\text{CaSiO}_3$ ,  $\text{NaAlSi}_3\text{O}_8$ ,  $\text{KAlSi}_3\text{O}_8$ ,  $\text{Mn}_3\text{Al}_2(\text{SiO}_4)_3$ ,  $\text{Na}_4\text{AlBeSi}_4\text{O}_{12}\text{Cl}$ ), sulphate ( $\text{BaSO}_4$ ), phosphate ( $\text{CePO}_4$ ,  $\text{P}_2\text{O}_5$ ) and fluoride ( $\text{SrF}$ ) mineral standards. Sodium and F were measured first in the analytical routine to minimise beam effects. For apatite analyses, F migration was investigated using the time-integrated methods presented by Slezak et al. (2018), however no significant affects were recorded for the analytical conditions and sample preparation methods used here.

Trace element analyses were conducted by laser ablation ICP-MS using a Geolas Pro 193 nm ArF excimer laser system coupled with a Bruker (formally Varian) 820-MS ICP-MS at the AAC, JCU, Townsville. Methods and instrumentation setup follow those outlined in Spandler et al. (2016). The largest possible spot size (between 30 and 125  $\mu\text{m}$ ) was selected for each mineral phase, with care taken to avoid analysis of mineral inclusions. All analyses were standardised using NIST SRM 610 reference glass using the reference values of Spandler et al. (2011). The MPI-DING glasses STHS and ML3B (Jochum et al., 2006) were used as secondary standards and analysed regularly throughout each session. Data reduction was carried out using the Iolite software.

Trace element analyses of zircon were conducted at the Boise State University Isotope Geology Laboratory. Zircons were ablated using a 25  $\mu\text{m}$  aperture spot, 5  $\text{J}/\text{cm}^2$  fluence, and 10 Hz firing repetition. The ablated material was carried by a 1 L/min He gas stream to the plasma. For concentration calculations, background-subtracted count rates for each analyte were internally normalized to  $^{29}\text{Si}$ , and calibrated with respect to NIST 610 and 612, or USGS BCR-2 and BIR-1 glasses as the primary standards.

## 2.5 Results

Thin section analysis reveals that the NFT samples are dominated by a fine clay matrix that forms a well-articulated fabric around euhedral igneous minerals (mostly titanite, apatite, phlogopite and sanidine; detailed below) and occasional angular mafic volcanic lithics (Fig. 2.3h). Clean mineral separates of the NFT samples contain euhedral titanite, phlogopite, apatite, andradite, sanidine, pyrochlore and anhedral zircon. Single crystal imaging and textural analysis (e.g., backscattered electron imaging, cathodoluminescence) reveals the presence of clinopyroxene, apatite, phlogopite, nepheline, cancrinite, calcite, pyrrhotite, peralkaline silicate glass and Na-REE-carbonates as primary inclusions in one or more the above phases. Detailed descriptions of these minerals, including major and trace element

---

analyses are presented below. Mineral abbreviations used in figures and tables adhere to those provided by Whitney and Evans (2010). Representative major element analyses of selected phases are presented in Table 2.1. Major and trace element data for all analyses (including secondary standards) are presented in Appendix A1 (Supplementary Data) along with stoichiometric formula calculations. Mineral classification diagrams are presented in Appendix A3 (Supplementary Figs. S1-S3).

### **2.5.1 Titanite**

Titanite crystals from all samples are distinctly yellow, have a prismatic tabular morphology (0.4 to 1.0 mm along the c-axis) and commonly host large (20 to >100  $\mu\text{m}$ ) rounded blobs or 3D wormy networks of primary silicate glass inclusions. Titanite compositions approach the end-member  $\text{CaTiSiO}_5$  with an average of 30 wt.%  $\text{SiO}_2$ , 37.5 wt.%  $\text{TiO}_2$ , 28.5 wt.%  $\text{CaO}$ , ~1.5 wt.%  $\text{FeO}$ , ~1 wt.% each of  $\text{Al}_2\text{O}_3$  and  $\text{Nb}_2\text{O}_5$ , and ~0.5 wt.% each of Ce and F (Table 2.1). These titanite compositions are comparable and consistent across all samples studied. Some titanite grains exhibit simple twinning (Fig. 2.3a-b). Secondary electron and BSE imaging of titanite grains reveals oscillatory zonation in many titanite grains (Fig. 2.4a), with more complex patchy zonation in others (Fig. 2.4b). The titanites are notably enriched (up to  $10^3$  times chondritic values) in REE+Y, with chondrite-normalised REE+Y patterns having slight concave downwards negative slope from La to Nd, flat negative slope through the MREE and HREE, and a distinct negative Y anomaly ( $Y/\text{Ho} = 19.8 - 27.9$ ; Fig. 2.5a). The titanites also have high concentrations of Sr (600-4000 ppm), Zr (1100-1550 ppm), Nb (2800-15000 ppm) and Ta (15-750 ppm).

### **2.5.2 Mica**

Mica grains are dark to medium brown (depending on thickness) hexagonal lamella prisms that are visible with the naked eye as they often exceed 500  $\mu\text{m}$  in diameter and 50  $\mu\text{m}$  in thickness. The NFT mica has some variance in composition, ranging from intermediate biotite ( $\text{Fe}/(\text{Mg}+\text{Fe}) = 0.6-0.4$ ) to phlogopite ( $\text{Fe}/(\text{Mg}+\text{Fe}) < 0.33$ ) in the phlogopite-annite (biotite) solid solution series (ternary mica classification diagram, Fig. S1). This variance in composition occurs across all samples as well as within individual zoned grains (Fig. 2.4d). Samples plotting in the phlogopite field contain <1 wt% BaO whereas BaO contents average between 2-4 wt.% in biotite compositions.  $\text{TiO}_2$  contents vary from 1.5-5.5 wt% across all compositions, with higher values recorded in biotite. Rubidium concentrations are higher in phlogopite (850-2500 ppm) than biotite (<850 ppm) and Sr concentrations across all mica range from 15- 400 ppm. Given the NFT mica range from intermediate biotite compositions towards phlogopite compositions in the phlogopite-annite (biotite) solid solution series, the term phlogopite will be used hereafter.

**Table 2.1** Representative analyses of igneous minerals by EMPA

Mineral	Titanite	Mica (Phl)	Mica (Bt)	Fluorapatite	Ti-Andradite	Pyrochlore	Sanidine (Ba-rich)	Sanidine (Na-rich)	Clinopyroxene	Cancrinite group	Nepheline	Calcite	Glass (in Ttn)
Sample ID	AS18-1-15	AS18-PIII-2-c	TZ-1-phl-1	As 18-ap-x2	AS18-grt-6	Py-10	bw4-san2-a	TZ1-San-1-a	AS18-cpx-5	AS18-3-BW4	BW4-neph1-inc	BW4-7-13	AS18-30
SiO <sub>2</sub>	29.98	33.66	39.23	0.83	32.78	0.00	59.44	64.69	46.42	35.55	43.42	-	51.37
TiO <sub>2</sub>	37.79	4.61	2.39	-	8.21	6.42	0.13	0.02	0.78	0.13	0.01	0.04	0.56
Al <sub>2</sub> O <sub>3</sub>	0.96	14.46	10.97	-	2.35	-	19.77	19.16	5.41	29.81	32.78	-	21.52
Fe <sub>2</sub> O <sub>3</sub>	1.06	-	-	-	24.55	-	0.27	0.20	-	0.35	1.00	-	-
FeO	-	19.22	14.56	0.03	-	0.01	-	-	14.10	-	-	0.21	4.15
MgO	-	10.74	17.01	-	0.42	-	0.01	-	8.15	-	-	0.11	0.18
MnO	-	0.47	0.66	0.04	0.75	-	-	-	0.35	-	-	0.21	0.23
CaO	28.52	-	-	54.10	32.52	19.25	0.04	0.43	22.17	4.66	0.23	53.73	2.35
BaO	-	3.26	0.16	-	-	-	6.77	0.59	-	-	0.03	-	-
SrO	-	-	-	1.40	-	-	-	-	-	-	-	-	-
Na <sub>2</sub> O	0.05	0.55	0.66	0.10	0.18	7.00	2.06	5.29	1.38	17.87	16.42	0.11	9.43
K <sub>2</sub> O	-	8.14	9.46	-	0.01	-	10.83	8.77	0.01	2.04	5.83	-	6.41
SO <sub>3</sub>	-	-	-	0.11	-	-	-	-	-	-	-	0.02	-
P <sub>2</sub> O <sub>5</sub>	-	-	-	40.47	-	-	-	-	-	-	-	-	-
ZrO <sub>2</sub>	0.23	-	-	-	0.31	1.59	-	-	-	-	-	-	-
Ce <sub>2</sub> O <sub>3</sub>	0.45	-	-	0.40	-	0.77	-	-	-	-	-	-	-
Nb <sub>2</sub> O <sub>5</sub>	0.83	-	-	-	-	60.43	-	-	-	-	-	-	-
F	0.26	0.42	1.94	0.98	-	5.12	-	-	-	0.20	-	-	-
Cl	-	0.02	0.01	0.01	-	-	0.02	0.02	-	1.24	-	0.02	0.32
<b>Total</b>	<b>99.87</b>	<b>95.37</b>	<b>96.23</b>	<b>99.86</b>	<b>99.58</b>	<b>100.59</b>	<b>99.48</b>	<b>99.17</b>	<b>98.82</b>	<b>91.91</b>	<b>99.74</b>	<b>54.47</b>	<b>96.57</b>
-O(F)		0.18	0.82	0.98									
-O(Cl)		-	-	0.01									
<i>New total (Mica, Ap)</i>		95.37	96.23	98.87									
<b>APFU</b>													
Si	0.99	5.32	5.90	0.14	2.63	0.00	2.86	2.96	1.78	5.76	4.19	-	-
Ti	0.94	0.55	0.27	-	0.50	0.27	0.00	0.00	0.02	0.02	0.00	-	-
Al	0.04	2.69	1.94	-	0.22	-	1.12	1.03	0.24	5.70	3.73	-	-
Fe <sup>3+</sup>	0.03	-	-	-	1.65	-	0.01	0.01	0.24	0.04	0.07	-	-
Fe <sup>2+</sup>	-	2.54	1.83	0.00	-	0.00	-	-	0.21	-	-	-	-
Mg	-	2.53	3.81	-	0.05	-	0.00	0.00	0.47	-	-	-	-
Mn	-	0.06	0.08	0.01	0.05	-	0.00	0.00	0.01	-	-	-	-
Ca	1.01	-	-	9.88	2.80	1.15	0.00	0.02	0.91	0.81	0.02	-	-
Ba	-	0.18	0.01	-	-	-	0.13	0.01	-	-	0.00	-	-
Sr	-	-	-	0.14	-	-	-	-	-	-	-	-	-
Na	0.00	0.17	0.19	0.03	0.01	0.76	0.19	0.47	0.10	5.62	3.07	-	-
K	-	1.64	1.82	-	0.00	-	0.67	0.51	0.00	0.42	0.72	-	-
P	-	-	-	5.84	-	-	-	-	-	-	-	-	-
Zr	0.00	-	-	-	0.01	0.04	-	-	-	-	-	-	-
Ce	0.01	0.01	0.01	0.03	-	0.03	-	-	-	-	-	-	-
Nb	0.01	0.01	0.01	-	-	1.52	-	-	-	-	-	-	-
<b>Cation total</b>	<b>3.02</b>	<b>15.69</b>	<b>15.86</b>	<b>15.93</b>	<b>7.93</b>	<b>3.77</b>	<b>4.99</b>	<b>5.01</b>	<b>4.00</b>	<b>17.56</b>	<b>11.78</b>	<b>-</b>	<b>-</b>

Mineral APFU were calculated for O = 5 (Titanite), 22 (Mica), 25 (Fluorapatite), 12 (Ti-Andradite), 6 (Pyrochlore), 8 (Sanidine), 6 (Clinopyroxene), 24 (Cancrinite), 16 (Nepheline).

Fe is assumed to be Fe<sup>2+</sup> for Mica, Fluorapatite, Pyrochlore and Fe<sup>3+</sup> for Titanite, Ti-Andradite, Sanidine, Cancrinite and Nepheline. Fe<sup>2+</sup> and Fe<sup>3+</sup> were calculated for clinopyroxene based on charge balance assuming a total number of cations = 4.

Analyses are presented in order of mineral description in the manuscript. For complete data and mineral formula see Appendix A.

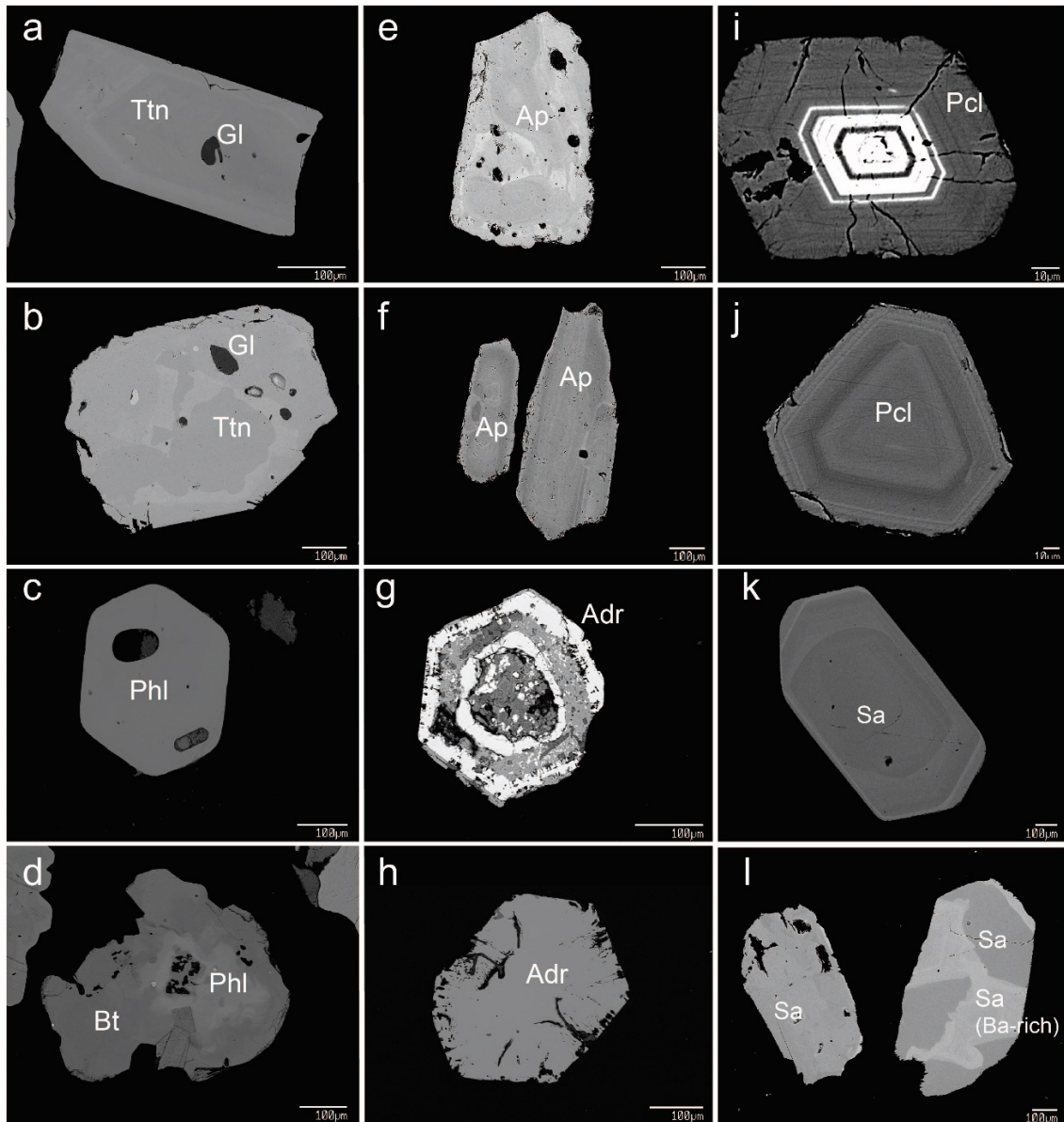


**Fig. 2.4.** Backscattered electron images of NFT minerals separates. a) Euhedral oscillatory-zoned titanite (Ttn) with a glass (Gl) inclusion; b) patchy complex zonation in titanite; c) euhedral homogenous phlogopite (Phl); d) zoned mica with phlogopite core and biotite (Bt) rim; e) complexly-zoned accretionary apatite (Ap); f) oscillatory-zoned apatite; g) strongly-altered, zoned andradite garnet (Adr) with replacement carbonate infill (dull grey zones) and visible skeletal texture (bright zones); (h) homogenous andradite with porosity and skeletal texture around the rim; i) high contrast (high-Th) oscillatory-zoned pyrochlore (Pcl) j) typical oscillatory-zoned pyrochlore; k) oscillatory-zoned sanidine (Sa); l) relatively-unzoned sanidine (*left*) and more complexly-zoned sanidine with bright zones corresponding to Ba enrichment (*right*).

### 2.5.3 Fluorapatite

Fluorapatite occurs as individual grains in the non-magnetic fraction (>1.5A) of the mineral separates. Large fluorapatite grains (typically 500 $\mu\text{m}$  along the c-axis) are transparent, colourless, euhedral, needle-like prisms (Fig. 2.3c-d). Individual grains and inclusions are compositionally similar

and can be defined as fluorapatite with ~53-54 wt.% CaO, 37-38 wt. % P<sub>2</sub>O<sub>5</sub>, 2-3 wt.%. F, up to 1.5 wt.% Sr and 0.7 wt.% Ce. Occasionally fluorapatite grains occur as micro-aggregates of 2-3 or more individual grains (Figs. 2.4e-f), although single crystals are most common. Many grains have both oscillatory and complex wavy zonation in BSE images (Figs. 2.4e-f). Fluorapatite grains occasionally contain spherical polyphase inclusions rich in alkali-REE carbonate (see below; Fig. 2. 6), but in most instances are pristine and free of inclusions and/or other notable defects. 10-200µm fluorapatites are present as primary inclusions in titanite and phlogopite. Chondrite-normalised REE+Y plots of fluorapatite display a steep negative slope and notable negative Y anomalies (Y/Ho = 22.5 – 27.9; Fig. 2.5b).

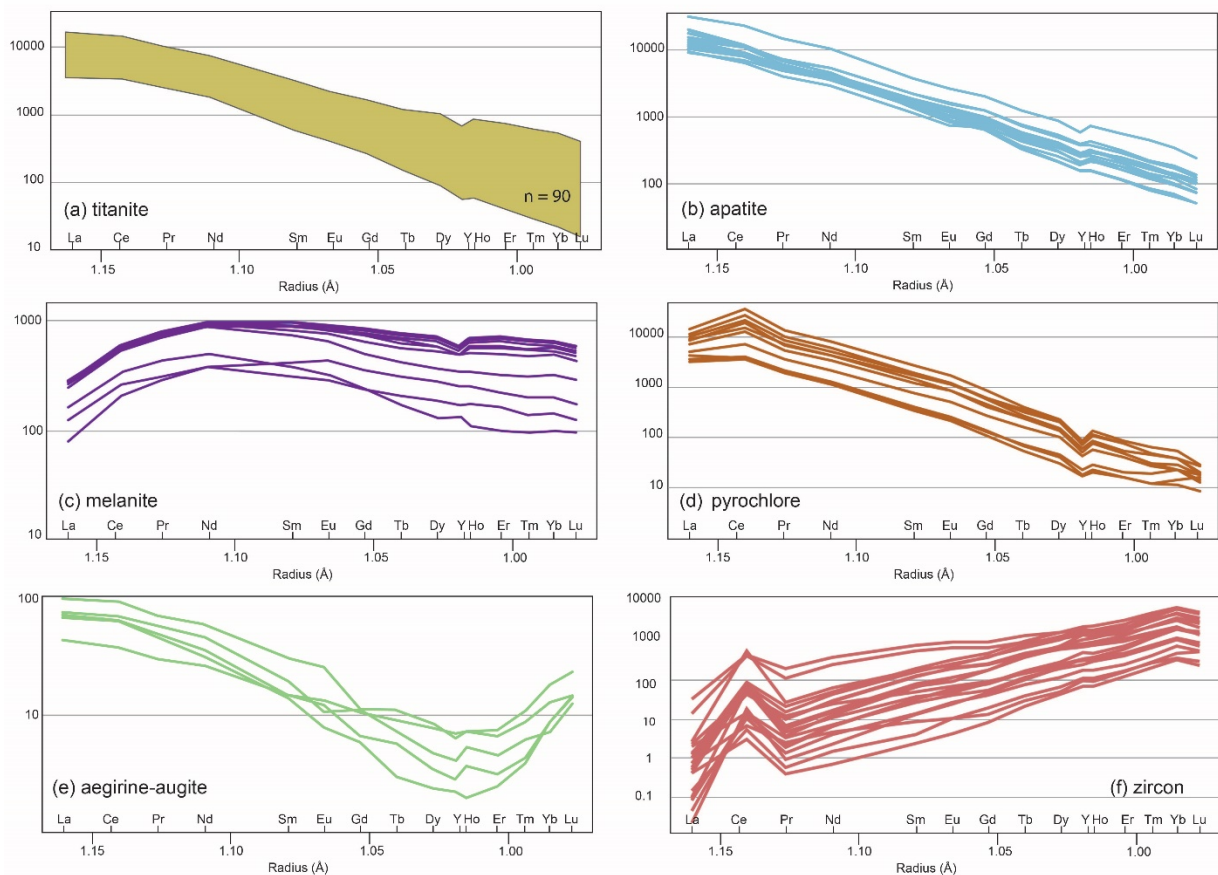


**Fig. 2.5** C1 chondrite-normalised (mineral/C1 chondrite) REE+Y diagrams (McDonough and Sun, 1995) of selected minerals with REE plotted according to their ionic radius in VII fold co-ordination; (Shannon and Prewitt, 1970). Note the significant Y anomalies in titanite, fluorapatite, Ti-andradite, pyrochlore and clinopyroxene, and the lack of Eu anomalies in zircon.

### 2.5.4 Andradite

Backscattered electron observations of NFT garnet reveal a degree of porosity, where relict skeletal textures can be seen along grain boundaries and between strongly zoned regions (Figs. 2.4g-h). Some grains are strongly zoned and pervasively altered, whereas others remain relatively unaltered (Fig.

2.4g-h). Many pore spaces and altered regions of garnet crystals are filled with secondary carbonate. Overall, NFT garnet lack the preservation quality observed for titanite, fluorapatite, phlogopite, sanidine and pyrochlore, making chemical analysis challenging. Nevertheless, all analysed garnets are Ti-rich andradite with 32-33 wt.% CaO and SiO<sub>2</sub>, 24 wt.% FeO, 7.5-8.5 wt.% TiO<sub>2</sub> and minor amounts of Al<sub>2</sub>O<sub>3</sub> (2-2.5 wt.%) MgO (0.4-0.5 wt.%) and MnO (0.6-0.7 wt.%). Garnet from all samples contain high concentrations of Zr (>2000 ppm). Chondrite-normalised REE+Y plots feature concave down patterns from the LREE to MREE (peaking at Nd) and a gentle negative slope across the MREE and HREE, albeit with a variable (mostly negative) Y anomaly (Y/Ho = 19.8 – 35.11; Fig. 2.5c).

### 2.5.5 Pyrochlore

Pyrochlore grains are rare and exceedingly small (50-100µm) in the NFT separates, and present as euhedral ‘diamond-like’ octahedral crystals that are translucent light brown to pale yellow in colour under plane-polarised light microscope view. In BSE images pyrochlore displays strong oscillatory zoning that, reflects variations in Nb (from WDS analysis) and Th (from EDS analysis) content. NFT pyrochlore compositions have between 58-62 wt.% Nb<sub>2</sub>O<sub>5</sub>, 18-20 wt.% CaO, 4-6 wt.% TiO<sub>2</sub>, 6-9 wt.% Na<sub>2</sub>O, 5-6 wt.% F and 1.5-2.5 wt.% ZrO<sub>2</sub> (Fig. S2). These pyrochlores typically contain >6000 ppm Sr, 1500-3000 ppm Th and are strongly enriched in LREE (up to 10<sup>4</sup> times chondritic values). Chondrite-normalised REE+Y patterns are similar to fluorapatite albeit with a notable positive Ce anomaly and a more pronounced negative Y anomaly (Y/Ho = 18.8 – 24.2; Fig. 2.5d).

### 2.5.6 Sanidine

Sanidine separates from the NFT are typically large (>300 µm) colourless, euhedral tabular crystals that display simple twinning and variable zonation (Fig. 2.3e-g). All analyses plot in the sanidine field of the feldspar classification diagram (Fig. S3a), with some crystals and zones in the sample TZ1 returning slightly more sodic compositions than those from samples AS18 and BW4. Backscattered electron imaging of sanidine reveals variable degrees of zonation with lighter regions returning elevated BaO concentrations (Table 2.1). Where present, zonation is typically complex patchy/wavy and irregular, although some sharp oscillatory zonations are also observed (Fig. 2.4k-l). Barium concentrations in NFT sanidine are negatively correlated with SiO<sub>2</sub> and positively correlated with Al<sub>2</sub>O<sub>3</sub> contents. Figure S3b shows this correlation as a function of Ba and Si substitution (a.p.f.u) in sanidine, where Ba<sup>2+</sup> is adhering to the typical substitution utilised by Ca<sup>2+</sup> to form anorthoclase (Ba+Al ↔ Na+Si). BaO concentrations overall range from 0.5 to 6.7 wt.%. Sanidine also has Rb and Sr concentrations of between 95-265 ppm and 2500-7500 ppm respectively (excluding a single anomalous Sr value of 318 ppm). Nepheline and pyrrhotite are found as tiny (<20 µm) inclusions in some sanidine grains. Overall sanidine is trace element poor with the majority of REE below detection limits. Where detected, Eu shows a strong positive correlation with Ba.

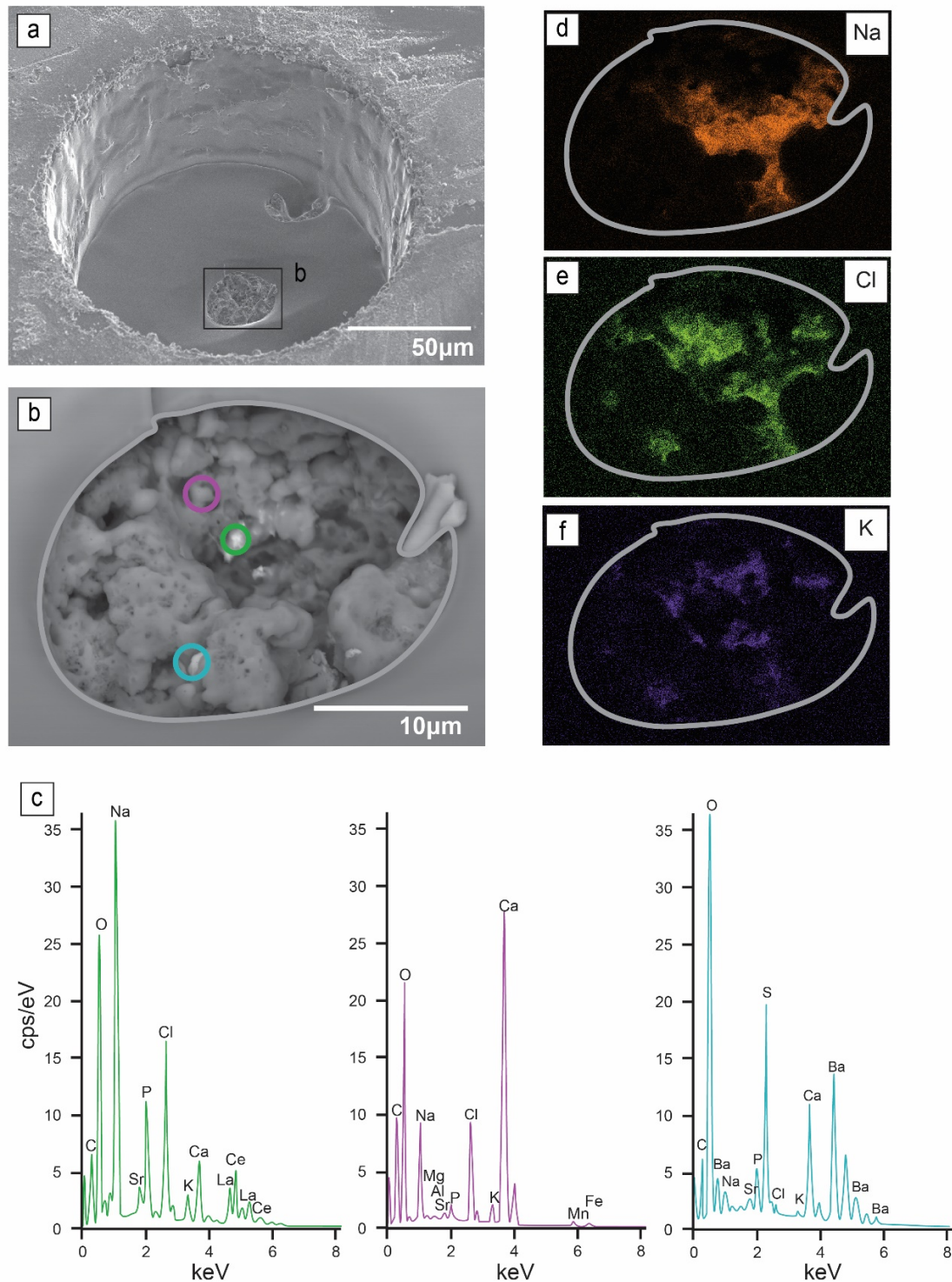


**Fig. 2.6.** Na-REE-Carbonate imaging and analysis . a) Secondary electron image of Na-REE-carbonate inclusion in fluorapatite (also shown in b-e) exposed via laser ablation (150  $\mu\text{m}$  spot size; approximately 60  $\mu\text{m}$  deep). b) Backscattered electron image of exposed inclusion with a porous spongy texture (grey outline of inclusion boundary shown in d-f). Coloured circles correspond to EDS analyses shown in (c). c) Semi-quantitative EDS analyses of regions of interest. Namely the presence of Na-REE-Cl components (green), Na-K-Ca-carbonate composition of low-contrast regions (purple) and presence of Ba and S. d-f) X-ray element maps highlighting the association and distribution of Na, K and Cl on internal surfaces of the inclusion that were possibly shielded during the ablation process.

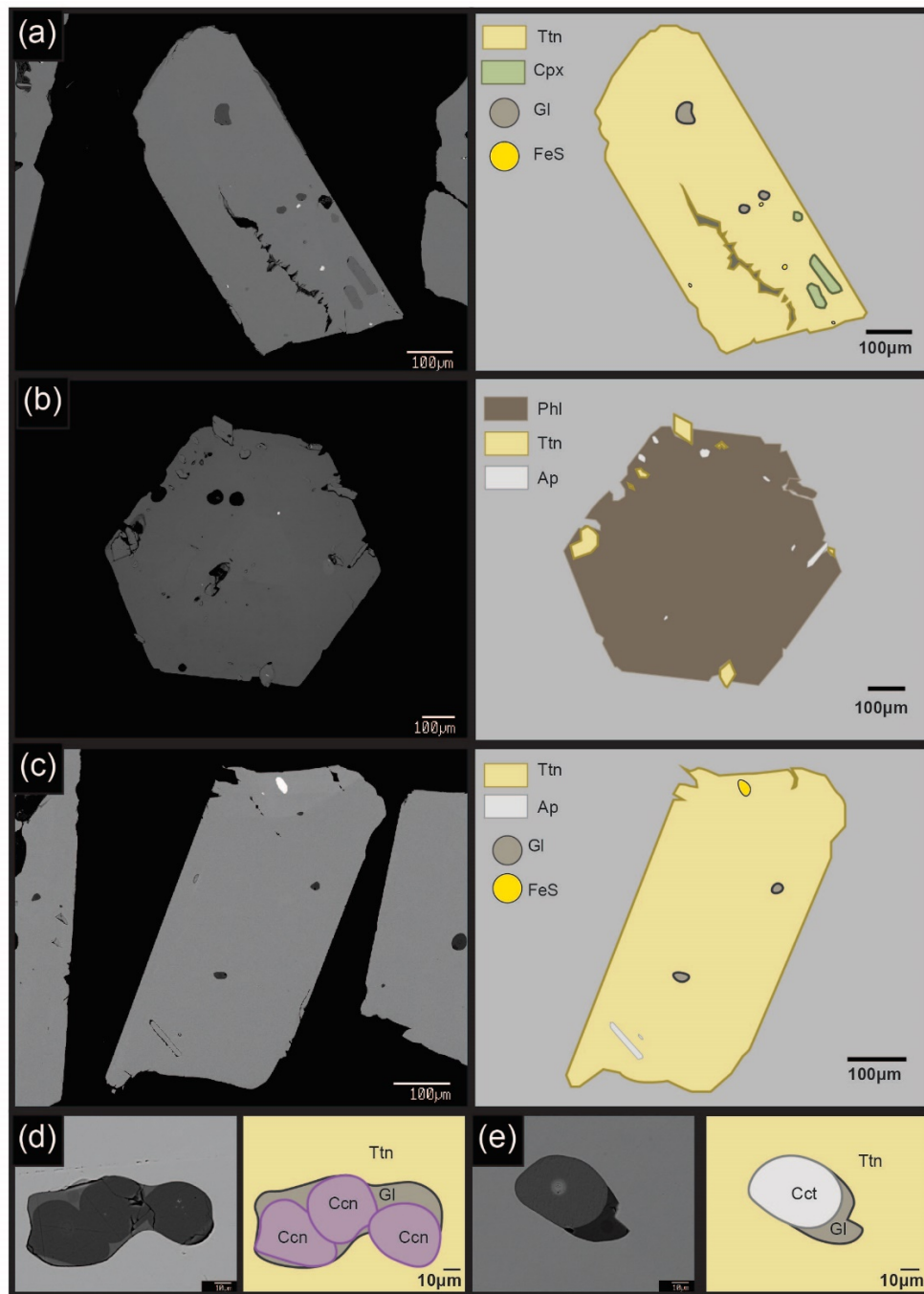


**Fig. 2.7.** Examples of mineral inclusions observed in titanite and phlogopite. a) titanite hosting clinopyroxene, silicate glass and Fe-sulphide (pyrrhotite); b) euhedral phlogopite hosting titanite and fluorapatite; c) titanite hosting fluorapatite, Fe-sulphide (pyrrhotite) and silicate glass; d) titanite hosting cancrinite and silicate glass; e) titanite hosting calcite and silicate glass.

### 2.5.7 Clinopyroxene

Clinopyroxene occurs as 10-100  $\mu\text{m}$  stout, prismatic inclusions within titanite grains, and within volcanic rock fragments identified in thin section (Fig. 2.3a and Fig. 2.7a). WDS analyses of clinopyroxene returned relatively high Fe contents, with compositions that cluster around the centre of the diopside-hedenbergite join in the En-Wo-Fs clinopyroxene ternary diagram (Fig. 2.8a).

Stoichiometric and charge balance requirements indicate that Fe exists in both  $\text{Fe}^{3+}$  and  $\text{Fe}^{2+}$  forms, where  $\text{Fe}^{3+}$  substitutes with  $\text{Al}^{3+}$  via Tschermaks essenite-type substitution and as a coupled substitution with  $\text{Na}^+$  ( $\text{Na}_2\text{O} = 1.3\text{--}2.4$  wt.%) as an aegirine-type substitution. These clinopyroxenes have  $\sim 1400$  ppm Sr and LREE enriched sinusoidal-shaped chondrite-normalised REE+Y patterns with inflections at Ce and Y ( $\text{Y}/\text{Ho} = 21.7 - 32.2$ ), and pronounced U shaped trough between Eu and Lu (Fig. 2.5e).

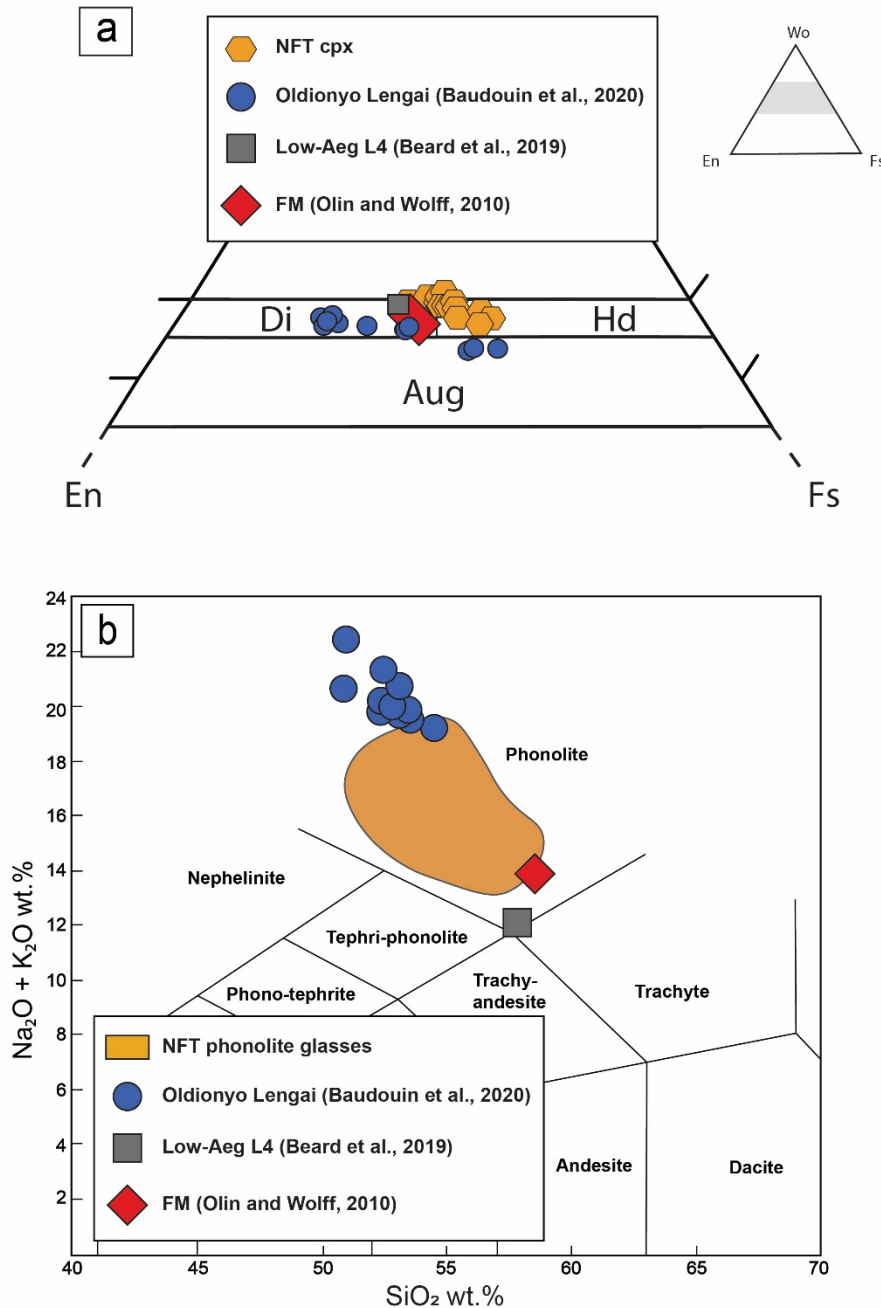


**Fig. 2.8.** Composition of clinopyroxene and associated alkaline silicate melts a) Natural (NFT (this study); Fasnja Member (FM; Olin and Wolff, 2010) and Oldionyo Lengai (Baudouin et al., 2020)) and experimental (Beard et al., 2019) clinopyroxene compositions projected as Wo-Fs-En endmembers (Morimoto, 1988). b) TAS classification diagram of associated natural and experimental glass compositions (n.b. orange field represents the range of phonolite glass compositions hosted in NFT titanite).

### **2.5.8 Carbonates**

Globular carbonate (calcite) typically forms discrete menisci with silicate glass in melt inclusions in titanite (Fig. 2.7e) although rare inclusions with only carbonate have also been recognised in both titanite and fluorapatite (Fig. 2.6). Trace element analyses of titanite hosted carbonate inclusions return ~20,000 ppm Sr, ~2000 ppm Ba and ~1800 ppm total REE. Chondrite-normalised REE+Y plots show a steep negative slope across the LREE with relatively depleted and flat MREE and HREE patterns (Appendix A1). Analyses of the carbonate inclusions in fluorapatite are limited due to their reactive nature during sample preparation and routine analytical conditions. Preliminary analysis of the carbonate inclusions (exposed via laser ablation) clearly show high contents of K, Na, Ba, Sr, S and LREE (Fig. 2.6c). Partial exposure and x-ray mapping of these inclusions reveals a spongy-textured carbonate network with variably distributed alkali elements adsorbed to internal carbonate surfaces. The alkali elements are associated with Cl and LREE (La, Ce), while Ba correlates with S (Fig. 2.6c-f).

### **2.5.9 Zircon**

Zircon is found as 100-200  $\mu\text{m}$  individual subhedral-anhedral crystals that show both complex and oscillatory zonation in cathodoluminescence imaging. Zircons from all samples show orders of magnitude variations in REE+Y concentrations. REE+Y plots display a smooth positive slope from LREE to HREE with a variably pronounced positive Ce anomaly. Notably, the negative Eu anomaly that is typical of most igneous zircons (Hoskin and Schaltegger, 2003) is absent in these grains (Fig. 2.5f).

### **2.5.10 Silicate glass**

Most silicate glass inclusions hosted within titanite (Fig. 2.7a and 2.7c-e) are of peralkaline phonolite composition and contain between ~7-10 wt. %  $\text{Na}_2\text{O}$ , 5.5-7.5 wt. %  $\text{K}_2\text{O}$ , 20-23 wt. %  $\text{Al}_2\text{O}_3$  and 51-56 wt.%  $\text{SiO}_2$  (Fig. 2.8b). These glasses are strongly enriched in Ba (2000-4000 ppm), Sr (1200-2000 ppm), and REE, with REE patterns showing LREE enrichment and relatively flat HREE contents. Details of the composition and evolution of these glass inclusions is the subject of a separate manuscript (Lawrence et al., Chapter 3, *in review*).

### **2.5.11 Summary of micro-phenocryst inclusions and phases**

The mineral inclusions and relationships are summarised in Table 2.2 and Fig. S4. Clinopyroxene and fluorapatite inclusions are common in titanite and occur as either small (<10  $\mu\text{m}$ ) prismatic crystals trapped alongside or within melt inclusions, or as larger (up to 100  $\mu\text{m}$ ) euhedral crystals found near the outer domains of titanite grains (Fig. 2.7a). Euhedral fluorapatite and titanite also occur as mineral inclusions in phlogopite grains, and reach up to 200  $\mu\text{m}$  and 100  $\mu\text{m}$  in size respectively (Fig. 2.7b). In all instances, fluorapatite and titanite inclusions exhibit the same morphology, optical properties and chemistry as those found as single crystals in mineral separates. The feldspathoid minerals nepheline and cancrinite are only rarely observed as small (<20  $\mu\text{m}$ ) inclusions hosted in

titanite (Fig. 2.7d) and, in the case of nepheline, in sanidine. Pyrrhotite is typically seen enclosed near to the outer boundary of large titanite grains (e.g. Fig. 2.7c), and more centrally in some fluorapatite and sanidine grains. Carbonate inclusions are found in both titanite (Fig. 2.7e) and fluorapatite.

**Table 2.2** Igenous mineral assemblage of the NFT

Summarised igneous mineral assemblage		
Phenocrysts	Microphenocryst inclusions	Other inclusions
Ttn	Ap, Cpx, Nph, Ccn, Cct	Gl, FeS
Phl	Ttn, Ap	-
Sa	nph	FeS
Ap	-	FeS, Na-REE-CO <sub>3</sub>
Adr	-	-
Pcl	-	-
Assemblage	Ttn, Ap, Phl, Sa, Adr, Pcl, Cpx, Nph, Ccn, Cct, Gl, FeS, Na-REE-CO <sub>3</sub>	

## 2.6 Discussion

### 2.6.1 Identification of the igneous mineral assemblage for the NFT

Previous work has successfully employed U-Pb and Ar-Ar geochronology to establish a temporal link between the igneous minerals titanite, phlogopite, pyrochlore and zircon across the series of volcanic tuffs investigated here (Roberts et al., 2010, 2012; Spandler et al., 2016). Building on this work, the petrographic geochemical investigation of resistant mineral phases and their inclusions from the NFT enables further genetic links to be made between the mineral phases presented and the formal identification of an igneous mineral assemblage (Table 2.2; Fig. S4).

#### 2.6.1.1 Petrography and mineral chemistry

Mineral phases, melts and fluids are commonly trapped as inclusions during periods of rapid crystal growth (Roedder, 1979). When preserved, primary igneous inclusions can be used as records of the magmatic conditions and processes from which they formed (Roedder, 1979; Sobolev, 1996; Putirka and Tepley, 2008). With this understanding, a genetic link can be made between titanite and the minerals fluorapatite, nepheline, augite, cancrinite, calcite, pyrrhotite and phonolite melt, as these all occur as unaltered primary phases in titanite. Additional links can be made via titanite found as inclusions in phlogopite, which is consistent with previous geochronological investigations (Roberts et al., 2010, 2012; Spandler et al., 2016). The presence of fluorapatite inclusions in both phlogopite and titanite ties fluorapatite to the aforementioned titanite assemblage, along with the Na-REE-carbonate inclusions hosted in fluorapatite. The composition of these inclusions and the presence of pyrochlore is distinctive and supportive of a carbonatite association for the NFT (Zaitsev et al., 2012), which is discussed further in a later section below.

The chemistry of igneous minerals may also reliably inherit and record key features of their magmatic environment of formation (Putirka and Tepley (2008) and references therein). The relationship between Ti-andradite and clinopyroxene with Tschermaks essenite-type substitution is a distinctive association of the NFT. Experimental work demonstrates that Ti-andradite compositions occur when primary garnet crystallises late in relation to clinopyroxene from low-temperature magmatic systems (Huckenholz, 1969). In nature, the coexistence of Ti-andradite and clinopyroxene with significant Tschermaks essenite component occurs almost exclusively in low-temperature alkali magmas such as nephelinites, phonolites (and their intrusive equivalents) and carbonatites (Huckenholz, 1969). Ti-andradite has been reported elsewhere for skarn deposits associated with alkaline (syenite) intrusions (i.e. Zippa Mountain, Canada; (Coulson et al., 2007)). Nonetheless, with the strong association between Ti-andradite and clinopyroxene (with Tschermaks essenite component) of the NFT, Ti-andradite is interpreted here to be a primary magmatic phase of the NFT assemblage.

### ***2.6.1.2 Mineral trace element composition and distribution***

Resistant minerals of the NFT are significantly enriched in incompatible trace elements, including Ba, Sr, Nb, Zr and REE; a feature that is interpreted to reflect the highly evolved nature of the parental melts and/or melts produced by low-degrees partial melting of enriched sources. High Ba concentrations feature in sanidine, phlogopite and calcite as well as the phonolite glass and Na-REE-carbonatite inclusions in titanite and fluorapatite, respectively. The size and incompatibility of Ba in most crystal lattices sees low degrees of partial melting and/or extensive crystal fractionation favour Ba enrichment in igneous systems. The euhedral morphology and presence of nepheline and pyrrhotite inclusions in NFT sanidine, coupled with variable zonation of BaO concentrations (up to 6.7 wt.%; also a feature of NFT phlogopite which has up to 4.5 wt.% BaO) supports a genetic link between sanidine and the NFT volcanic system as they are both effective scavengers of Ba in magmatic systems (Melluso et al., 2011). Experiments have shown that Ba and Sr increasingly partition into feldspar over the silicate melt with reducing temperature, increasing orthoclase content of feldspar, and increasing silica-undersaturation of the silicate melt (Henderson and Pierozynski, 2012). The compositions and complex zonation textures observed in the NFT sanidine (Figs. 2.3g and 2.4l) are consistent with experimental and natural sanidine derived from volatile-rich, low-temperature peralkaline igneous systems (Dawson et al., 1995; Ginibre et al., 2004; Melluso et al., 2011; Henderson and Pierozynski, 2012). The complex patchy or wavy textures in sanidine are considered artefacts of convective percolation of residual or replenishing liquids within the magma chamber; a process that is amplified in small-volume peralkaline systems (Dawson et al., 1995; Ginibre et al., 2004).

Clinopyroxene is a common and consequential mineral in alkaline magmatic systems (Olin and Wolff, 2010; Beard et al., 2019). As an early fractionating phase in these systems, the composition of clinopyroxene and the distribution of REE+Y between clinopyroxene, melt and successive crystallising

minerals are inherently linked. The incorporation of incompatible trivalent cations (i.e. REE+Y) in the crystal structure of clinopyroxene is described to be largely a function of variable cation occupation (in particular  $\text{Ca}^{2+}$ ,  $\text{Na}^{+}$  and  $\text{Fe}^{3+}$ ) of the M1 and M2 crystal sites (Olin and Wolff, 2010; Reguir et al., 2012; Beard et al., 2019; Baudouin et al., 2020). Beard et al. (2019) developed a predictive model for clinopyroxene/liquid partitioning between clinopyroxene and alkaline silicate melt (akin to those of the NFT) as a function of temperature, pressure, and major-element composition of clinopyroxene. Applying this model to the NFT clinopyroxenes, we can evaluate whether the clinopyroxene major-element and REE+Y composition is consistent with derivation from an alkaline silicate parental magma.

Clinopyroxene/melt distribution coefficients for REE+Y were calculated using the major element chemistry of NFT clinopyroxene, a pressure of 0.5 GPa, and temperatures of 850 °C (Fig. 2.9a). The chosen P-T conditions are based on the experimental assemblage of Kjarsgaard and Peterson (1991), which closely resembles our observations for the NFT spanning these conditions, as discussed in more detail below. The major element composition of our NFT clinopyroxene and predicted REE+Y partitioning behaviour are most similar to the “low-aegirine” population produced by experiments at 825 °C and 0.2 GPa by Beard et al. (2019) (Fig. 2.8; Fig. 2.9), which, incidentally, were reported to co-crystallise with titanite from a peralkaline phonolitic starting composition. A key feature of the major element composition of both experimental and NFT pyroxenes is the incorporation of  $\text{Fe}^{3+}$  on the M1 crystal site, which is shown to increase the compatibility of 6-fold coordinated  $\text{Yb}^{3+}$  and  $\text{Lu}^{3+}$  ions on this site via the lattice strain model described by Blundy and Wood (1994) (Olin and Wolff, 2010; Beard et al., 2019).

The REE+Y partition coefficients predicted for NFT clinopyroxene show an increase in compatibility from La-Sm, decreasing from Sm to Er and then sharply increasing for Tm, Yb and Lu (Fig. 2.9a). Based on the findings of Beard et al. (2019), Olin and Wolff (2010) and Baudouin et al. (2020), the deep trough registered between Sm and Lu in NFT clinopyroxene REE+Y patterns (Fig. 2.5e) can be explained as a function of both; 1) a significant reduction in compatibility for 8-fold coordinated Sm-Lu compatibility on the M2 crystal site; and 2) sharp increase in compatibility for 6-fold coordinated Tm, Yb and Lu ions on the M1 crystal site. This partitioning behaviour is most favourable in Fe-rich clinopyroxene compositions where sufficient  $\text{Fe}^{3+}$  is incorporated into the M1 site (Olin and Wolff, 2010; Beard et al., 2019). The characteristic sinusoidal REE pattern produced by this partitioning behaviour is in agreement with natural clinopyroxenes associated with peralkaline and carbonatite rocks elsewhere (Olin and Wolff, 2010; Reguir et al., 2012; Baudouin et al., 2016; Weidendorfer et al., 2016; Baudouin et al., 2020).

Taken to be reasonable model values, the predicted clinopyroxene partition coefficients can now be combined with the trace element composition of our NFT clinopyroxenes to calculate an estimated REE+Y composition for the crystallising silicate melt. This modelled melt composition can then be

compared to our measured titanite-hosted phonolite glasses from the NFT (i.e., a geochemical paternity test). Additionally, the calculated melt composition can be used with existing titanite/melt and apatite/melt distribution coefficients to calculate predicted REE+Y compositions for these minerals (Prowatke and Klemme, 2006; Olin and Wolff, 2012). Together, this allows for an independent evaluation of the genetic relationship between these minerals and the glass inclusions hosted in titanite from the NFT samples.

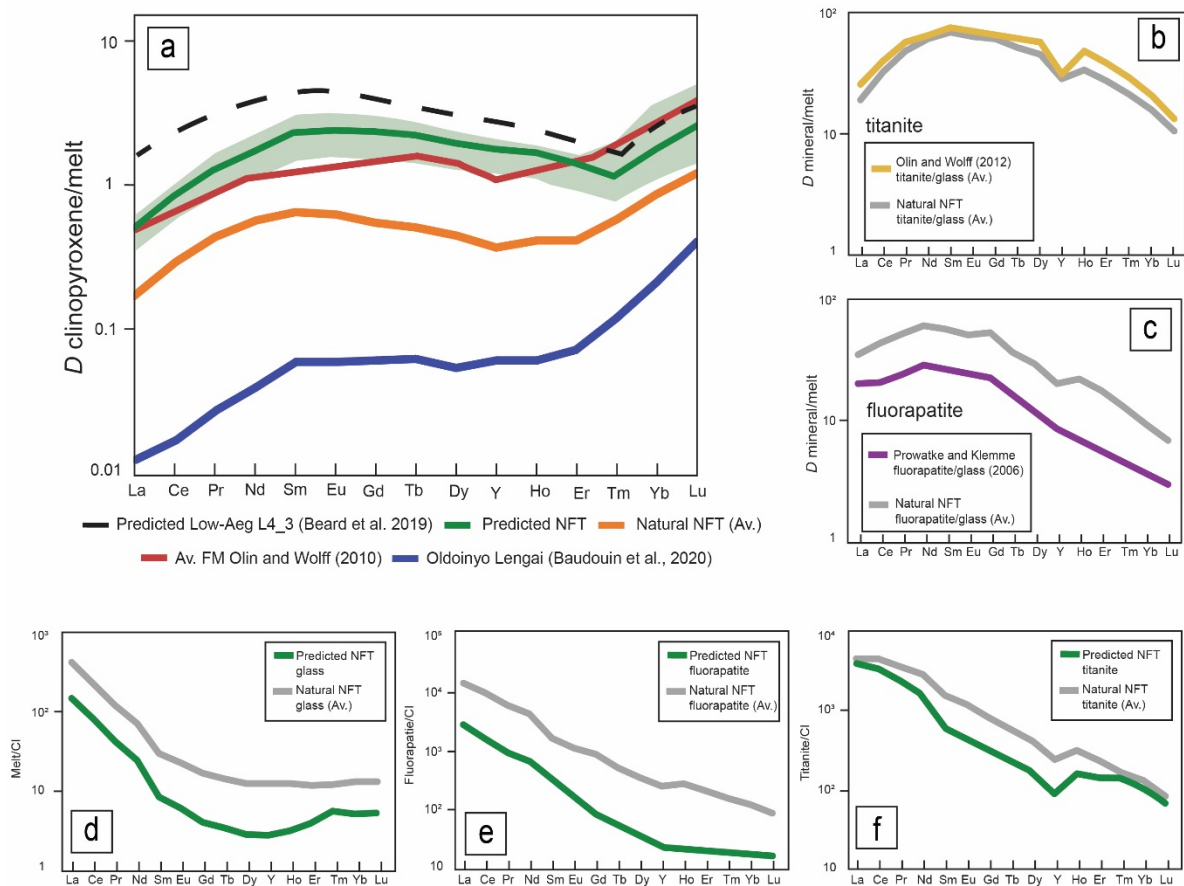


**Fig. 2.9.** Trace element distribution and modelling (Appendix A2). a) Distribution of rare earth elements between clinopyroxene and alkaline silicate melt. The green line represents the average (shaded area total range for individual NFT cpx) REE+Y distribution predicted by the model of Beard et al. (2019) for NFT clinopyroxene at 850°C and 0.5 GPa. The dashed black line represents the predicted partitioning behaviour for low-aegirine clinopyroxene formed from phonolite melt composition in Fig. 2.6 at 825 °C and 0.2 GPa. The orange line represents the REE+Y distribution between the average clinopyroxene-phonolite melt compositions of the NFT. The red and blue lines are the representative clinopyroxene/melt partition coefficients reported for the Fasia Member (FM) clinopyroxene-phonolite glass pairs at 825 °C and 0.1 GPa (Olin and Wolff, 2010) and Oldoinyo Lengai at 1050 °C and 0.3 GPa (Baudouin et al., 2020), respectively. Note the increase in compatibility (upward inflection) of Tm-Lu predicted by the model of Beard et al. 2019, is reflected in the natural NFT data. b) Distribution of REE+Y between titanite and phonolite glass. The grey line is the average titanite-phonolite REE+Y distribution reported in this study. The yellow line is the average REE+Y distribution reported by Olin and Wolff (2012) for equilibrated titanite-phonolite glass pairs from the Fasia Member (FM) phonolite at approximately

825 °C and 0.1 GPa. c) Distribution of REE+Y for fluorapatite-phonolite. The grey line represents the average REE+Y distribution for NFT fluorapatite-phonolite (hosted in titanite). The purple line represents the experimentally derived partition coefficients for fluorapatite-phonolite glass pairs reported by Prowatke and Klemme (2006) at 1GPa 1250 °C (run 54A). Note the general consistency in the slope of REE+Y distribution. d) Modelled REE+Y composition of the NFT silicate melt. Melt composition was derived using the trace element concentrations of NFT clinopyroxene and partition coefficients predicted for NFT clinopyroxene by the Beard et al. (2019) model. Note the similarity in slope and composition. e) Comparison of natural fluorapatite REE+Y compositions with those derived from the predicted melt composition (8d) and partition coefficients of Prowatke and Klemme (2006) run 54A (Fig. 2.8c). f) Comparison of natural titanite REE+Y compositions with those derived from the predicted melt composition of (2.8d) and partition coefficients of Olin and Wolff (2012) (Fig. 2.8b).

In general, the modelled REE+Y concentrations of melt, titanite and apatite compositions (Fig. 2.9d-e) are remarkably similar to—albeit slightly lower than—the concentration values measured for these phases in the NFT. This slight difference is consistent with the presence of fluorine in the NFT system, which has been shown to reduce the partitioning of La-Dy and Y (and to a lesser degree HREE) into clinopyroxene in favour of the residual melt (Beard et al., 2020). Additionally, our naturally-derived REE+Y mineral-melt distribution values for clinopyroxene, titanite and apatite are also in general agreement with published values provided by Olin and Wolff (2010; 2012) and Prowatke and Klemme (2006) (Fig. 2.9b-c). These data are in support of our petrographic observations and demonstrate a genetic link between these minerals and the silicate glass inclusions (interpreted to be primary magma) hosted in titanite.

Another noteworthy feature of REE+Y patterns of the NFT mineral phases is the lack of Eu anomalies, particularly in minerals such as zircon, and presence of a negative Y anomaly. The lack of Eu anomalies is interpreted to reflect conditions of feldspar fractionation dominated by sanidine, rather than plagioclase. While oxidation state will control  $\text{Eu}^{2+}$  availability for incorporation into feldspar,  $\text{Eu}^{2+}$  has been shown to be highly incompatible in low-Ca sanidine (Stix and Gorton, 1990). The majority of NFT sanidine contains very low Ca content (<0.03 wt% CaO), which will significantly limit the incorporation of  $\text{Eu}^{2+}$  into sanidine during crystallisation.

The fractionation of Y from Ho under typical magmatic conditions is unusual, and defies typical lattice strain and charge-radius-controlled partitioning behaviour given the similarity in size and charge of Y and Ho cations (Bau, 1996; Olin and Wolff, 2012). Yet, this feature is observed in minerals (e.g. pyroxene and titanite) associated with mantle-derived alkaline and carbonatite rocks (Olin and Wolff, 2012; Weidendorfer et al., 2016; Loges et al., 2019; Anenburg et al., 2020). The REE+Y patterns of titanite, clinopyroxene, fluorapatite, Ti-andradite and pyrochlore (Fig. 2.5) all display notable negative Y anomalies, which reflect non-chondritic Y/Ho ratios ( $\text{Y}/\text{Ho} \neq 28 \pm 4$ ; Bau, 1996).

Non-chondritic Y/Ho ratios are the suggested result of either mass fractionation (and may therefore be considered a proxy for low-temperatures; Olin and Wolff (2010)), and/or complexation

with F or other halogens in volatile-rich environments (observed as the tetrad effect; Bau (1996)), and/or reflect the composition of the lithospheric source that was modified during ancient subduction of ocean sediments with inherent non-chondritic Y/Ho (Loges et al., 2019; Anenburg et al., 2020). Currently, we can only speculate as to the precise cause of this feature (or that some analyses show a slight positive Y anomaly) in a given magmatic setting, however the probable causes outlined by the authors listed above are potentially applicable to the setting of the NFT. Notwithstanding, Y-Ho fractionation in conjunction with overall REE+Y enrichment is recognised here as geochemical link between the aforementioned NFT phases and as a meaningful artefact of the parental magmatic system.

The trace-element distribution described is consistent with the petrographic evidence (i.e. a co-genetic relationship between mineral and melt inclusions), and major element compositions of the mineral and glass phases. The unusual major and trace element composition of NFT clinopyroxene, the lack of appreciable Eu anomalies, and the decoupling of Y and Ho are distinctive features of the NFT assemblage. These features, together with the distinctive mineral assemblage of Table 2.2, are relatively uncommon globally, but, are consistent with observed alkaline-carbonatite sources both in the EARS and elsewhere (Dawson and Hill, 1998; Klaudius and Keller, 2006; Dawson, 2012; Zaitsev et al., 2012; Baudouin et al., 2016, 2018; Guzmics et al., 2019), as discussed in the following section.

### ***2.6.2 Contextualising the NFT mineral assemblage***

Roberts et al., (2010, 2012) proposed that the deposition of the Nsungwe Formation and accompanying punctuated volcanism of the NFT signifies the earliest manifestation (i.e., the initial phase) of rift development in the Western Branch. The volcanic character of early rift development is seldom preserved in the geological record, which is often attributed to one or more of the following factors; 1) early magmatic phases of rift development are isolated low-volume events and are thus less abundant in the available geologic record; 2) these products are typically strongly alkaline in nature and are often associated with carbonatites, and as a result have an inherently high chemical susceptibility to weathering at the surface; 3) subsequent rates of uplift and erosion in continental rift settings means that these early phases are easily eroded from the landscape; 4) the large volumes of bimodal volcanism that ensues in the succeeding stages of rifting may bury or otherwise obstruct any low-volume events that preceded it.

The EARS hosts some of the most well studied and spectacular expressions of alkaline magmatism on Earth; none more so than the only active natro-carbonatite volcano, Oldoinyo Lengai. Oldoinyo Lengai resides in one of the most concentrated occurrences of carbonatite magmatism known, the North Tanzanian Divergence zone (Fig. S6) at southernmost extent of the Gregory Rift (Klaudius and Keller, 2006; Dawson, 2012) and references therein). The North Tanzanian Divergence zone represents the youngest manifestations of rift development in the eastern branch of the EARS and is considered the natural laboratory for incipient rift processes (Dawson, 2012; Baudouin et al., 2016,

2018). This region is host to a number of young alkaline strata-volcanoes, including Oldoinyo Lengai, Kermasi, Sadiman and Hanang (<1.2 Ma), all of which are characterised by volumetrically-small, volatile-rich and highly-explosive alkaline-carbonatite magmatism (Dawson, 2012; Baudouin et al., 2016, 2018).

Striking similarities exist between the mineralogy of the incipient rift volcanic centres of the North Tanzanian Divergence zone in the eastern branch and those described here for the ~25 Ma NFT in the Western Branch. Namely, a diagnostic mineral assemblage of Fe-rich clinopyroxene, nepheline, Ti-rich andradite, titanite, fluorapatite and phlogopite in addition to carbonates and evolved alkaline (phonolite/nephelinite) silicate melts (Dawson and Hill, 1998; Klaudius and Keller, 2006; Dawson, 2012; Zaitsev et al., 2012; Baudouin et al., 2016, 2018). Indeed, in the EARS and elsewhere, this assemblage is common to both stand-alone nephelinites and phonolites, and those genetically linked with carbonatites. However, in cases where discrimination between the two is necessary, minerals such as pyrochlore and alkali-carbonates are considered reliable indicators of carbonatite-related occurrences specifically (Zaitsev et al., 2012). As both pyrochlore and Na-REE-carbonate (as inclusions in fluorapatite) are present in the NFT assemblage, a carbonatite association is implied for the NFT.

The abundance of sanidine in the NFT, along with phonolitic melt inclusions in NFT titanite is consistent with a strongly-alkaline system that has undergone extensive fractional crystallisation (Klaudius and Keller, 2006; Baudouin et al., 2020). Highly-evolved alkaline magmas have been the subject of ongoing experimental investigation in order to examine the role of silicate-carbonatite liquid immiscibility in the silicate-carbonatite rock association and, more specifically, the generation of the distinctive natro-carbonatite magmas observed at Oldoinyo Lengai (Freestone and Hamilton, 1980; Kjarsgaard and Peterson, 1991; Kjarsgaard et al., 1995; Brooker and Kjarsgaard, 2010). The isobaric silicate-carbonatite liquid immiscibility experiments of Kjarsgaard and Peterson (1991) record a paragenetic sequence for carbonated peralkaline bulk magma compositions subject to extensive crystallisation across a temperature range of 1025°C to 915°C at 0.5 GPa. The assemblage produced consists of clinopyroxene, nepheline, Ti-andradite, perovskite, titanite, magnetite and sanidine reported to be in equilibrium with both silicate and carbonate liquids. In these experiments, titanite is documented to crystallise and coexist with clinopyroxene and nepheline at temperatures below 960°C, followed by calcite and sanidine crystallisation at temperatures below 915°C (Kjarsgaard and Peterson, 1991). Given the well documented occurrence of this assemblage in the NFT and elsewhere in nature (Kjarsgaard and Peterson, 1991; Dawson and Hill, 1998; Klaudius and Keller, 2006; Dawson, 2012; Zaitsev et al., 2012; Greenwood, 2014; Baudouin et al., 2016, 2018; Weidendorfer et al., 2016; Balashova et al., 2018; Zaitsev et al., 2019), we may broadly infer similar geologic conditions and processes (i.e. low temperatures, high degrees of fractionation and liquid immiscibility) are relevant to the formation of NFT.

### 2.6.3 Proximal sources

The Rukwa Rift region has a rich history of alkaline magmatism with known volcanic centres dating to the Jurassic-Cretaceous (150-120 Ma Panda Hill) (Van Straaten and Bell, 1989; Mesko et al., 2020), the early Miocene (the 17 Ma Usangu phonolites and 19 Ma Tukuyu basalt) (Rasskazov et al., 2003; Mesko et al., 2020) and late-Miocene to recent (< 9 Ma) RVP (Ebinger et al., 1989; Fontijn et al., 2012; Hilbert-Wolf et al., 2017). Despite this record, a volcanic vent of appropriate age for the ca. 25-26 Ma NFT remains elusive.

The appreciable age discrepancy between the Cretaceous Panda Hill carbonatite and the Upper Oligocene NFT, and notable lack of associated silicate rocks and NFT assemblage minerals (e.g. titanite, pyroxene, Ti-andradite) at Panda Hill deem it an unrealistic source for the NFT. The central RVP approximately 30 km to the southeast of the NFT (Fig. 2.1b) comprises a thick pile of alkaline volcanic edifices, lava flows and pyroclastic deposits resulting from ongoing magmatic activity from ca. 9.2 Ma to present (Fontijn et al., 2012). While highly evolved phonolite and nephelinite lavas (as well as less evolved mafic compositions) are ubiquitous through the history of the RVP, there have been no reported instances of carbonatite magmas associated with these young rocks. Spatially, the RVP is a known source of sedimentary input for the Rukwa Rift Basin, with volcanic ash fallout and fluvially transported influx from the RVP featuring prominently in both the detrital and stratigraphic record of the upper and lower Lake Beds (Hilbert-Wolf et al., 2017; Mtelega et al., 2017). Nevertheless, a temporal discrepancy remains between these deposits and the NFT (Fontijn et al., 2012; Hilbert-Wolf et al., 2017; Mtelega et al., 2017)

The Usangu Basin on the north-eastern margin of the RVP contains 17 individual early Miocene phonolitic volcanic edifices (the earliest of which is dated via Ar/Ar to be 17.3 Ma); these are the oldest known volcanic centres associated with modern EARS development in the Rukwa region (Rasskazov et al., 2003). Follow-up geochronology of the Usangu phonolites has confirmed their age (Mesko et al., 2020), although their petrology remains largely undescribed and their relationship to the RVP is contentious (Fontijn et al., 2012). Nevertheless, there is an undoubted spatial association with the RVP. As seen in Figure 2.1a, the surface geology of the modern RVP features a prominent younging-inward trend, with the central zones inundated by recent volcanism. In this aspect, the peripheral distribution of both the NFT and Early Miocene volcanic rocks presented by Rasskazov et al. (2003) (Fig. 2.1b) adhere to the temporal and spatial distribution patterns of modern RVP magmatism.

An upsurge in intra-plate volcanism on the African continent and rifting in the eastern branch of the EARS is well documented between 30-25 Ma and coincides with a significant reduction in the northward motion of the African plate between 19 Ma and 30 Ma (O'Connor et al., 1999). The timing and nature of the NFT (ca. 25 Ma), Tukuyu basalt (18.6 Ma) and Usangu phonolites (17.3 Ma), coeval with rift development and magmatism in the eastern branch, suggests localised mantle melting beneath

the Rukwa-Malawi-USangu junction (Fig. 2.1b) during the Oligocene to Early Miocene may represent the southernmost expression of this broad-reaching tectonic shift. Geophysical studies of the upper mantle in the Rukwa-Malawi-USangu junction beneath the RVP suggest long-lived stagnation of mantle flow beneath the RVP (as a result of the deep-rooted Tanzanian Craton) could have induced localised magmatism in the RVP earlier than previously recognised (Tepp et al., 2018). The discovery of anomalously-thinned lithosphere beneath northern Malawi and the RVP (Njinju et al., 2019) also supports an episode of thermal perturbation and magmatism prior to modern rift development and volcanism in the RVP (Grijalva et al., 2018; Tepp et al., 2018; Njinju et al., 2019). The age and nature of the NFT presented here and the Early Miocene volcanism present by Rasskazov et al. (2003) is consistent with (and evidence of) this earlier magmatic episode in the broader RVP.

#### ***2.6.4 Identifying carbonatite volcanism***

New occurrences of abundant alkaline silicate-carbonatite volcanism are increasingly being recognised across the world (Bailey and Kearns, 2012; Campbell et al., 2012). Importantly, the key discovery criteria for this volcanism in the field relies on identifying and examining the widely-dispersed and variably-altered pyroclastic deposits these volcanic systems produce (Bailey and Kearns, 2012; Campbell et al., 2012). The crystal-scale petrographic approach utilised here to reveal the volcanic character of the NFT is a meaningful addition to those previously introduced by Bailey and Kearns (2012) and Campbell et al. (2012), as it does not require large sample volumes or whole-rock analytical techniques. Furthermore, it overcomes the extensive alteration that these volcanic materials undergo when deposited into the fluvio-lacustrine environments that typify continental rift basins (Zaitsev and Keller, 2006; Campbell et al., 2012). Given the diverse and often cryptic preservation exhibited by alkaline-carbonatite rocks in the geological record, our approach may have a critical role in the discovery of poorly-preserved early alkaline volcanism not only in the Rukwa Rift region and greater Western Branch of the EARS, but more broadly in continental rift zones worldwide. Such approaches will become increasingly valuable as economic interest in the critical metal ore potential of alkaline-carbonatite magmatic systems continues to grow.

### **2.7 Conclusions**

Careful petrographic observations and single crystal geochemistry of resistant mineral separates from weathered tuff samples has been instrumental in describing the magmatic character of the NFT. This study demonstrates that such an approach produces a wealth of diagnostic petrological and geochemical data that are otherwise unattainable using traditional whole rock methods.

With this data we conclude that:

- The NFT are characterised by an alkaline igneous mineral assemblage consisting of titanite, phlogopite, apatite, Ti-andradite, sanidine, pyrochlore, anhedral zircon and the primary mineral

inclusions clinopyroxene, fluorapatite, nepheline, cancrinite, calcite, pyrrhotite, peralkaline silicate glass and Na-REE-carbonates.

- The NFT assemblage is collectively enriched in alkalis, REE+Y, Ba and Sr, and represent the eruptive products of a phonolite-carbonatite magmatic system. This finding is well supported by natural and experimental data from the young volcanoes of the North Tanzanian Divergence zone.
- The NFT are interpreted to be the earliest manifestation of magmatism from what is now considered RVP. The volume and surface area of young RVP lavas likely obstructs their extrusive source.
- The sedimentary basins of the EARS remain reliable recorders of rift associated volcanic events capable of preserving those absent in surface outcrop. Further exploration of the stratigraphic record within Cenozoic rift basins and the petrographic approach presented here may provide renewed temporal insights into the tectono-magmatic development of the Western Branch of the EARS, and other rift sequences worldwide. This approach also presents a useful exploration tool for undiscovered and/or unrecognised carbonatites worldwide.

## References

- Anenburg, M., Mavrogenes, J.A. and Bennett, V.C., 2020. The fluorapatite P–REE–Th vein deposit at Nolans Bore: genesis by carbonatite metasomatism. *Journal of Petrology*, 61(1), p.egaa003.
- Bailey, D., Kearns, S., 2012. New forms of abundant carbonatite–silicate volcanism: recognition criteria and further target locations. *Mineralogical Magazine*, 76(2): 271-284.
- Balashova, A., Mattsson, H.B., Hirt, A.M., 2018. New tephrostratigraphic data from Lake Emakat (northern Tanzania): Implications for the eruptive history of the Oldoinyo Lengai volcano. *Journal of African Earth Sciences*, 147: 374-382.
- Bau, M., 1996. Controls on the fractionation of isovalent trace elements in magmatic and aqueous systems: evidence from Y/Ho, Zr/Hf, and lanthanide tetrad effect. *Contributions to Mineralogy and Petrology*, 123(3): 323-333.
- Baudouin, C., France, L., Boulanger, M., Dalou, C., Devidal, J.-L., 2020. Trace element partitioning between clinopyroxene and alkaline magmas: parametrization and role of M1 site on HREE enrichment in clinopyroxenes. *Contributions to Mineralogy and Petrology*, 175: 1-15.
- Baudouin, C., Parat, F., Denis, C.M., Mangasini, F., 2016. Nephelinite lavas at early stage of rift initiation (Hanang volcano, North Tanzanian Divergence). *Contributions to Mineralogy and Petrology*, 171(7): 64.
- Baudouin, C., Parat, F., Michel, T., 2018. CO<sub>2</sub>-rich phonolitic melt and carbonatite immiscibility in early stage of rifting: Melt inclusions from Hanang volcano (Tanzania). *Journal of Volcanology and Geothermal Research*, 358: 261-272.
-

- Beard, C.D., van Hinsberg, V.J., Stix, J., Wilke, M., 2019. Clinopyroxene/melt trace element partitioning in sodic alkaline magmas. *Journal of Petrology*, 60(9): 1797-1823.
- Beard, C.D., van Hinsberg, V.J., Stix, J., Wilke, M., 2020. The effect of fluorine on clinopyroxene/melt trace-element partitioning. *Contributions to Mineralogy and Petrology*, 175: 1-19.
- Blundy, J., Wood, B., 1994. Prediction of crystal–melt partition coefficients from elastic moduli. *Nature*, 372(6505): 452-454.
- Brooker, R., Kjarsgaard, B., 2010. Silicate–carbonate liquid immiscibility and phase relations in the system  $\text{SiO}_2\text{–Na}_2\text{O–Al}_2\text{O}_3\text{–CaO–CO}_2$  at 0–1–2–5 GPa with applications to carbonatite genesis. *Journal of Petrology*, 52(7-8): 1281-1305.
- Campbell, L., Dyer, A., Williams, C., Lythgoe, P., 2012. The masquerade of alkaline–carbonatitic tuffs by zeolites: a new global pathfinder hypothesis. *Mineralium Deposita*, 47(4): 371-382.
- Castillo, P.R., Hilton, D.R., Halldórsson, S.A., 2014. Trace element and Sr-Nd-Pb isotope geochemistry of Rungwe Volcanic Province, Tanzania: implications for a superplume source for East Africa Rift magmatism. *Frontiers in Earth Science*, 2: 21.
- Coulson, I.M., Westphal, M., Anderson, R., Kyser, T., 2007. Concomitant skarn and syenitic magma evolution at the margins of the Zippa Mountain pluton. *Mineralogy and Petrology*, 90(3-4): 199-221.
- Dawson, J., 2012. Nephelinite–melilitite–carbonatite relationships: Evidence from Pleistocene–recent volcanism in northern Tanzania. *Lithos*, 152: 3-10.
- Dawson, J., Hill, P., 1998. Mineral chemistry of a peralkaline combeitelamprophyllite nephelinite from Oldoinyo Lengai, Tanzania. *Mineralogical Magazine*, 62(2): 179-196.
- Dawson, J., Smith, J., Steele, I., 1995. Petrology and mineral chemistry of plutonic igneous xenoliths from the carbonatite volcano, Oldoinyo Lengai, Tanzania. *Journal of Petrology*, 36(3): 797-826.
- Delvaux, D., Kervyn, F., Macheyeke, A., Temu, E., 2012. Geodynamic significance of the TRM segment in the East African Rift (W-Tanzania): Active tectonics and paleostress in the Ufipa plateau and Rukwa basin. *Journal of Structural Geology*, 37: 161-180.
- Ebinger, C.J., Deino, A.L., Drake, R., Tesha, A., 1989. Chronology of volcanism and rift basin propagation: Rungwe volcanic province, East Africa. *Journal of Geophysical Research: Solid Earth*, 94(B11): 15785-15803.
- Ernst, R.E., Bell, K., 2010. Large igneous provinces (LIPs) and carbonatites. *Mineralogy and Petrology*, 98(1-4): 55-76.
- Fontijn, K., Williamson, D., Mbede, E., Ernst, G.G., 2012. The Rungwe volcanic province, Tanzania—a volcanological review. *Journal of African Earth Sciences*, 63: 12-31.
- Freestone, I., Hamilton, D., 1980. The role of liquid immiscibility in the genesis of carbonatites—an experimental study. *Contributions to Mineralogy and Petrology*, 73(2): 105-117.
- Furman, T., 1995. Melting of metasomatized subcontinental lithosphere: undersaturated mafic lavas from Rungwe, Tanzania. *Contributions to Mineralogy and Petrology*, 122(1-2): 97-115.

- Furman, T., Graham, D., 1999. Erosion of lithospheric mantle beneath the East African Rift system: geochemical evidence from the Kivu volcanic province, *Developments in Geotectonics*. Elsevier, pp. 237-262.
- Ginibre, C., Wörner, G., Kronz, A., 2004. Structure and dynamics of the Laacher See magma chamber (Eifel, Germany) from major and trace element zoning in sanidine: a cathodoluminescence and electron microprobe study. *Journal of Petrology*, 45(11): 2197-2223.
- Greenwood, S.M., 2014. Mineralogy and Geochemistry of Pleistocene Volcanics at Embagai Caldera and Natron Basin, Tanzania: Potential Constraints on the Stratigraphy of Olduvai Gorge.
- Grijalva, A., Nyblade, A.A., Homman, K., Accardo, N.J., Gaherty, J.B., Ebinger, C.J., Shillington, D.J., Chindandali, P.R., Mbogoni, G., Ferdinand, R.W. and Mulibo, G., 2018. Seismic evidence for plume-and craton-influenced upper mantle structure beneath the northern Malawi rift and the Rungwe volcanic province, East Africa. *Geochemistry, Geophysics, Geosystems*, 19(10): 3980-3994.
- Guzmics, T. et al., 2019. Natrocarbonatites: A hidden product of three-phase immiscibility. *Geology*, 47(6): 527-530.
- Henderson, C., Pierozynski, W., 2012. An experimental study of Sr, Ba and Rb partitioning between alkali feldspar and silicate liquid in the system nepheline–kalsilite–quartz at 0.1 GPa P (H<sub>2</sub>O): a revisitation and reassessment. *Mineralogical Magazine*, 76(1): 157-190.
- Hilbert-Wolf, H. et al., 2017. Application of U–Pb detrital zircon geochronology to drill cuttings for age control in hydrocarbon exploration wells: A case study from the Rukwa Rift Basin, Tanzania. *AAPG Bulletin*, 101(2): 143-159.
- Hogarth, D., 1977. Classification and nomenclature of the pyrochlore group. *American Mineralogist*, 62(5-6): 403-410.
- Hoskin, P.W., Schaltegger, U., 2003. The composition of zircon and igneous and metamorphic petrogenesis. *Reviews in mineralogy and geochemistry*, 53(1): 27-62.
- Huckenholz, H., 1969. Synthesis and stability of ferri-diopside. *Mineralogical Society of America Special Paper*, 2: 163-177.
- Kampunzu, A., Lubala, R., 2012. Magmatism in extensional structural settings: the Phanerozoic African plate. Springer Science & Business Media.
- Kilembe, E.A., Rosendahl, B.R., 1992. Structure and stratigraphy of the Rukwa rift. *Tectonophysics*, 209(1-4): 143-158.
- Kjarsgaard, B., Hamilton, D., Peterson, T., 1995. Peralkaline nephelinite/carbonatite liquid immiscibility: comparison of phase compositions in experiments and natural lavas from Oldoinyo Lengai, Carbonatite Volcanism. Springer, pp. 163-190.
- Kjarsgaard, B., Peterson, T., 1991. Nephelinite-carbonatite liquid immiscibility at Shombole volcano, East Africa: petrographic and experimental evidence. *Mineralogy and Petrology*, 43(4): 293-314.
-

- Klaudius, J., Keller, J., 2006. Peralkaline silicate lavas at Oldoinyo Lengai, Tanzania. *Lithos*, 91(1-4): 173-190.
- Le Gall, B. et al., 2008. Rift propagation at craton margin.: Distribution of faulting and volcanism in the North Tanzanian Divergence (East Africa) during Neogene times. *Tectonophysics*, 448(1-4): 1-19.
- Loges, A., Schultze, D., Klügel, A., Lucassen, F., 2019. Phonolitic melt production by carbonatite Mantle metasomatism: evidence from Eger Graben xenoliths. *Contributions to Mineralogy and Petrology*, 174(11): 93.
- McDonough, W.F., Sun, S.-S., 1995. The composition of the Earth. *Chemical geology*, 120(3-4): 223-253.
- Melluso, L., Morra, V., de'Gennaro, R., 2011. Coexisting Ba-feldspar and melilite in a melafoidite lava at Mt. Vulture, Italy: role of volatiles and alkaline earths in bridging a petrological incompatibility. *The Canadian Mineralogist*, 49(4): 983-1000.
- Mesko, G.T., 2020. Magmatism at the southern end of the east african rift system: Origin and role during early stage rifting. Columbia University.
- Mitchell, R., 1995. *Kimberlites, Orangeites and Related Rocks* Plenum Press, New York, pp. 410.
- Morimoto, N., 1988. Nomenclature of pyroxenes. *Mineralogy and Petrology*, 39(1): 55-76.
- Morley, C., Wescott, W., Harper, R., Cunningham, S., 1999. *Geology and geophysics of the Rukwa Rift*.
- Mtelela, C., Roberts, E.M., Downie, R., Hendrix, M.S., 2016. Interplay of structural, climatic, and volcanic controls on late quaternary lacustrine–deltaic sedimentation patterns in the Western Branch of the East African Rift System, Rukwa Rift Basin, Tanzania. *Journal of sedimentary research*, 86(10): 1179-1207.
- Mtelela, C. et al., 2017. Sedimentology and paleoenvironments of a new fossiliferous late Miocene-Pliocene sedimentary succession in the Rukwa Rift Basin, Tanzania. *Journal of African Earth Sciences*, 129: 260-281.
- Njinju, E.A. et al., 2019. Lithospheric Structure of the Malawi Rift: Implications for Magma-Poor Rifting Processes. *Tectonics*, 38(11): 3835-3853.
- Nyblade, A.A., 2011. The upper-mantle low-velocity anomaly beneath Ethiopia, Kenya, and Tanzania: Constraints on the origin of the African superswell in eastern Africa and plate versus plume models of mantle dynamics. *Geological Society of America Special Papers*, 478: 37-50.
- O'Connor, J., Stoffers, P., van den Bogaard, P., McWilliams, M., 1999. First seamount age evidence for significantly slower African plate motion since 19 to 30 Ma. *Earth and Planetary Science Letters*, 171(4): 575-589.
- Olin, P.H., Wolff, J.A., 2010. Rare earth and high field strength element partitioning between iron-rich clinopyroxenes and felsic liquids. *Contributions to Mineralogy and Petrology*, 160(5): 761-775.
-

- Olin, P.H., Wolff, J.A., 2012. Partitioning of rare earth and high field strength elements between titanite and phonolitic liquid. *Lithos*, 128: 46-54.
- Poucllet, A., Bellon, H., Bram, K., 2016. The Cenozoic volcanism in the Kivu rift: Assessment of the tectonic setting, geochemistry, and geochronology of the volcanic activity in the South-Kivu and Virunga regions. *Journal of African Earth Sciences*, 121: 219-246.
- Prowatke, S., Klemme, S., 2006. Trace element partitioning between apatite and silicate melts. *Geochimica et Cosmochimica Acta*, 70(17): 4513-4527.
- Putirka, K.D., Tepley, F.J., 2008. Minerals, inclusions and volcanic processes.
- Rasskazov, S. et al., 2003. A magmatic episode in the Western Rift of East Africa (19-17 Ma). *Geologiya i Geofizika*, 44(4): 317-324.
- Reguir, E.P. et al., 2012. Trace-element composition and zoning in clinopyroxene-and amphibole-group minerals: implications for element partitioning and evolution of carbonatites. *Lithos*, 128: 27-45.
- Roberts, E.M. et al., 2010. Sedimentology and depositional environments of the Red Sandstone Group, Rukwa Rift Basin, southwestern Tanzania: New insight into Cretaceous and Paleogene terrestrial ecosystems and tectonics in sub-equatorial Africa. *Journal of African Earth Sciences*, 57(3): 179-212.
- Roberts, E.M. et al., 2012. Initiation of the western branch of the East African Rift coeval with the eastern branch. *Nature Geoscience*, 5(4): 289.
- Roedder, E., 1979. Origin and significance of magmatic inclusions. *Bulletin de Mineralogie*, 102(5): 487-510.
- Rooney, T.O., 2019. The Cenozoic magmatism of East Africa: Part V—Magma sources and processes in the East African Rift. *Lithos*: 105296.
- Ryan, W.B. et al., 2009. Global multi-resolution topography synthesis. *Geochemistry, Geophysics, Geosystems*, 10(3).
- Shannon, R.t., Prewitt, C., 1970. Revised values of effective ionic radii. *Acta Crystallographica Section B: Structural Crystallography and Crystal Chemistry*, 26(7): 1046-1048.
- Simon, B. et al., 2017. Deformation and sedimentary evolution of the Lake Albert Rift (Uganda, East African rift system). *Marine and Petroleum Geology*, 86: 17-37.
- Slezak, P., Spandler, C., Blake, K., 2018. Ghosts of apatite past: using hyperspectral cathodoluminescence and micro-geochemical data to reveal multi-generational apatite in the Gifford Creek Carbonatite Complex, Australia. *The Canadian Mineralogist*, 56(5): 773-797.
- Sobolev, A., 1996. Melt inclusions in minerals as a source of principle petrological information. *Petrology*, 4(3): 209-220.
- Spandler, C. et al., 2016. MKED1: a new titanite standard for in situ analysis of Sm–Nd isotopes and U–Pb geochronology. *Chemical Geology*, 425: 110-126.
- Stevens, N.J. et al., 2013. Palaeontological evidence for an Oligocene divergence between Old World monkeys and apes. *Nature*, 497(7451): 611.

- Stix, J., Gorton, M.P., 1990. Variations in trace element partition coefficients in sanidine in the Cerro Toledo Rhyolite, Jemez Mountains, New Mexico: Effects of composition, temperature, and volatiles. *Geochimica et Cosmochimica Acta*, 54(10): 2697-2708.
- Tepp, G. et al., 2018. Seismic anisotropy of the upper mantle below the Western rift, East Africa. *Journal of Geophysical Research: Solid Earth*, 123(7): 5644-5660.
- Theunissen, K., Klerkx, J., Melnikov, A., Mruma, A., 1996. Mechanisms of inheritance of rift faulting in the western branch of the East African Rift, Tanzania. *Tectonics*, 15(4): 776-790.
- Van Straaten, P., Bell, K., 1989. Nature and structural relationships of carbonatites from Southwest and West Tanzania. *Carbonatites: Genesis and Evolution*. Unwin Hyman, London: 177-199.
- Veizer, J.n., Bell, K., Jansen, S.L., 1992. Temporal distribution of carbonatites. *Geology*, 20(12): 1147-1149.
- Weidendorfer, D., Schmidt, M.W., Mattsson, H.B., 2016. Fractional crystallization of Si-undersaturated alkaline magmas leading to unmixing of carbonatites on Brava Island (Cape Verde) and a general model of carbonatite genesis in alkaline magma suites. *Contributions to Mineralogy and Petrology*, 171(5): 43.
- Whitney, D.L., Evans, B.W., 2010. Abbreviations for names of rock-forming minerals. *American mineralogist*, 95(1): 185-187.
- WoldeGabriel, G. et al., 2000. Volcanism, tectonism, sedimentation, and the paleoanthropological record in the Ethiopian Rift System. *Special papers-geological society of america*: 83-99.
- Zaitsev, A. et al., 2012. Mineralogy, geochemistry and petrology of the phonolitic to nephelinitic Sadiman volcano, Crater Highlands, Tanzania. *Lithos*, 152: 66-83.
- Zaitsev, A.N., Keller, J., 2006. Mineralogical and chemical transformation of Oldoinyo Lengai natrocarbonatites, Tanzania. *Lithos*, 91(1-4): 191-207.
- Zaitsev, A.N. et al., 2019. Stratigraphy, mineralogy and geochemistry of the Upper Laetolil tuffs including a new tuff 7 site with footprints of *Australopithecus afarensis*, Laetoli, Tanzania. *Journal of African Earth Sciences*, 158: 103561.

## Chapter 3

# **Unmix and Erupt: Explosive early rift volcanism produced by magma immiscibility in the Western Branch of the East African Rift**

### **Abstract**

The earliest stages of continental rifting produce some of the most distinctive alkaline magmas on Earth. However, the rare exposure, poor chemical preservation and dynamic setting in which they occur sees these early volcanic rocks underrepresented in the geologic record. The ~25 Ma Nsungwe Formation airfall tuffs of the Rukwa Rift Basin (southwestern Tanzania) are the earliest known volcanic products associated with the initiation and development of the Western Branch of the East African Rift System. These devitrified ash deposits host a suite of alkaline accessory mineral phases, including euhedral titanite that host pristine magmatic glass (formerly melt) inclusions. Based on the chemical compositions of these glass inclusions, we describe the magmatic evolution of this early rift system from peralkaline phonolite to peraluminous dacitic compositions; a previously undescribed evolution that is incompatible with pure crystal fractionation or crustal contamination. Instead, this magma evolution is modelled using a combination of carbonatite liquid immiscibility and multi-stage crystal fractionation processes, which produces volatile-rich silicic magmas and, hence, describes a novel way to produce highly explosive, intermediate composition magmas. Magma evolution via this process may account for explosive intraplate volcanism elsewhere in the world, and in the geologic record. Our study also highlights the potential of titanite to record and archive the occurrence and chemical evolution of alkaline magmatic systems.

### **3.1 Introduction**

The East African Rift System (EARS) is the archetypal continental rift; it features active volcanism, tectonism and landscape evolution, and hosts some of the most important fossil sites in the world. The onset and development of rifting and accompanying intraplate alkaline magmatism at 30-40 Ma is commonly attributed to the African superswell (Bagley and Nyblade, 2013); a series of connected low-velocity seismic anomalies occurring ~400 km beneath Ethiopia, Kenya and Tanzania. Rift

development had profound effects on topography and climate (Sepulchre et al., 2006; Pik et al., 2008), as well as on the distribution and exchange of flora and fauna, within and beyond the African continent during this critical evolutionary time period (Chorowicz, 2005; Sepulchre et al., 2006; Roberts et al., 2012; Stevens et al., 2013).

Traditionally, the EARS has been described as consisting of a much older, volcanically-active eastern branch with extensive sedimentary exposures, and a younger, less volcanically-active Western Branch that is characterised by a series of deep rift lakes that mostly conceal its sedimentary archives (Chorowicz, 2005). The Rukwa Rift Basin (Fig. 3.1) is a northwest-southeast trending half-graben basin and comparatively small rift segment that links the Tanganyikan Rift (to the north) and Malawi Rifts (to the south) in the Western Branch of the EARS. It is a focus of geological attention in part, because it contains one of the only fossiliferous Cretaceous-Palaeogene continental sedimentary sequences in sub-equatorial Africa, but also since the discovery of the Nsungwe Formation airfall tuff deposits (NFT hereafter) that temporally constrain important primate fossil discoveries (Roberts et al., 2010, 2012; Stevens et al., 2013). Radiometric dating of igneous mineral phases from the NFT (including U-Pb of zircon, U-Pb of titanite and Ar/Ar of phlogopite) returned ages of 25 to 26 Ma (Roberts et al., 2010, 2012; Spandler et al., 2016), making these the earliest manifestations of magmatism associated with modern rifting in the Western Branch and indicating contemporaneous rift initiation in both the Eastern and Western Rift branches of the EARS (Roberts et al., 2012). Nevertheless, despite their significance, knowledge of the nature and origin of these volcanic deposits is limited due to their pervasively weathered state.

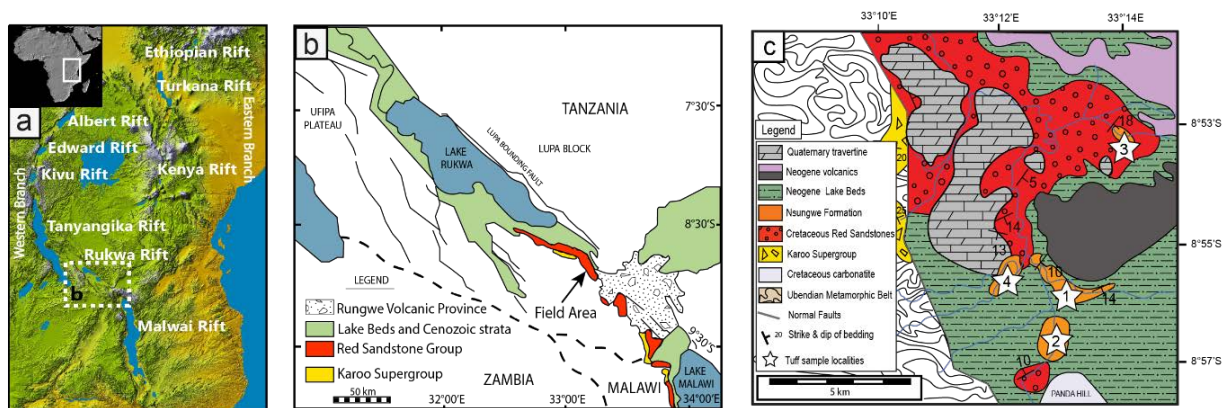


**Fig. 3.1** The Rukwa Rift Basin. a) Image of the EARS modified from the NASA Shuttle Radar Topography Mission collection. The dashed box indicates the location of the Rukwa Rift Basin study area of panel b. b) Geological map of the Rukwa Rift Basin. c) Local geological map of the field area with the three Oligocene sample locations indicated by white stars (1) Nsungwe; (2) Songwe; (3) Ikumbi and (4) Nanyala river sections.

Volcanic rocks formed during the incipient stages of continental rift development have the potential to provide crucial information on the tectonic, magmatic and temporal evolution of continental rift zones (Chorowicz, 2005; Woolley and Church, 2005; Ernst and Bell, 2010; Roberts et al., 2010, 2012; Kampunzu and Lubala, 2012; Baudouin et al., 2018). Because rift settings are typified by geologically rapid uplift and burial rates, large volumes of young mafic lavas, and formation of deep rift lakes, these early-formed alkaline volcanic units are rarely exposed, or are poorly preserved in the geologic record. This lack of exposure means that deciphering their original magmatic character is inherently difficult (Veizer et al., 1992; Woolley and Church, 2005; Zaitsev and Keller, 2006; Ernst and Bell, 2010).

Accessory igneous minerals that are resistant to weathering and alteration (e.g., zircon, apatite) are increasingly used to study volcanic rocks and processes (Guzmics et al., 2011; Garzanti et al., 2013; Bruand et al., 2016; Lawrence et al., 2020). If these minerals also contain preserved glass inclusions – small parcels of magma that are trapped within minerals during rapid crystal growth and subsequently quenched to glass upon magma eruption (Sobolev, 1996) – then they can provide insights into complex processes of magma generation, evolution and eruption (Sobolev, 1996; Guzmics et al., 2011, 2015; Sharygin et al., 2012; de Moor et al., 2013; Campeny et al., 2015). The study of glass inclusions in resistant mineral phases from rapidly-altered carbonatite or other alkaline magmatic rocks has been instrumental to advancing understanding of the complex magmatic processes, such as liquid immiscibility (Guzmics et al., 2011, 2012, 2015; Sharygin et al., 2012; de Moor et al., 2013), crystal fractionation (Guzmics et al., 2011, 2015), magma degassing (de Moor et al., 2013), and mantle source characteristics (Kamenetsky et al., 2004; Guzmics et al., 2015).

Currently, no volcanic vent or source for the NFT is known in the region, and their pervasively weathered state prohibits conventional petrographic study (Lawrence et al., 2020). Titanite (nominally  $\text{CaTiSiO}_5$ ) is a moderately robust and common accessory mineral of alkaline series volcanic rocks of the EARS (Garzanti et al., 2013; Lawrence et al., 2020), including the NFT. Therefore, our analysis focuses on magmatic titanite and their glass inclusions from four weathered NFT units (Fig. 3.2c, 3.3). Our dataset provides a crucial - and so far unique - record of the nature of magmatism in the early Rukwa Rift Basin. This record is important for understanding discrete explosive alkaline volcanic episodes and associated landscape evolution at the onset of continental rifting.

## **3.2 Samples and analytical methods**

### ***3.2.1 Field relations and sample preparation***

The NFT (previously described by Roberts et al., 2010 and Lawrence et al., 2020) typically crop out as stratigraphically thin (2.5 to 10 cm), laterally continuous, mottled maroon-white clay-rich horizons interbedded with the fossil-bearing muddy sandstones and siltstones of the Songwe Member of the Nsungwe Formation (Fig. 3.2a-b). These discrete horizons consist almost entirely of

montmorillonite  $\pm$  saponite clays, but do contain accessory titanite, phlogopite, fluorapatite, Ti-rich andradite, sanidine, zircon, pyrochlore and calcite. A high concentration of phlogopite often occurs in the uppermost horizon of individual tuff units, while all minerals (including phlogopite) and occasional relict pumice clasts are dispersed throughout the tuffs. The NFT contain notably low proportions of bulk detrital minerals (i.e. quartz, detrital zircon) and metamorphic lithic fragments, and lack the vertebrate fossil material that characterise adjacent and interbedded lithologies.

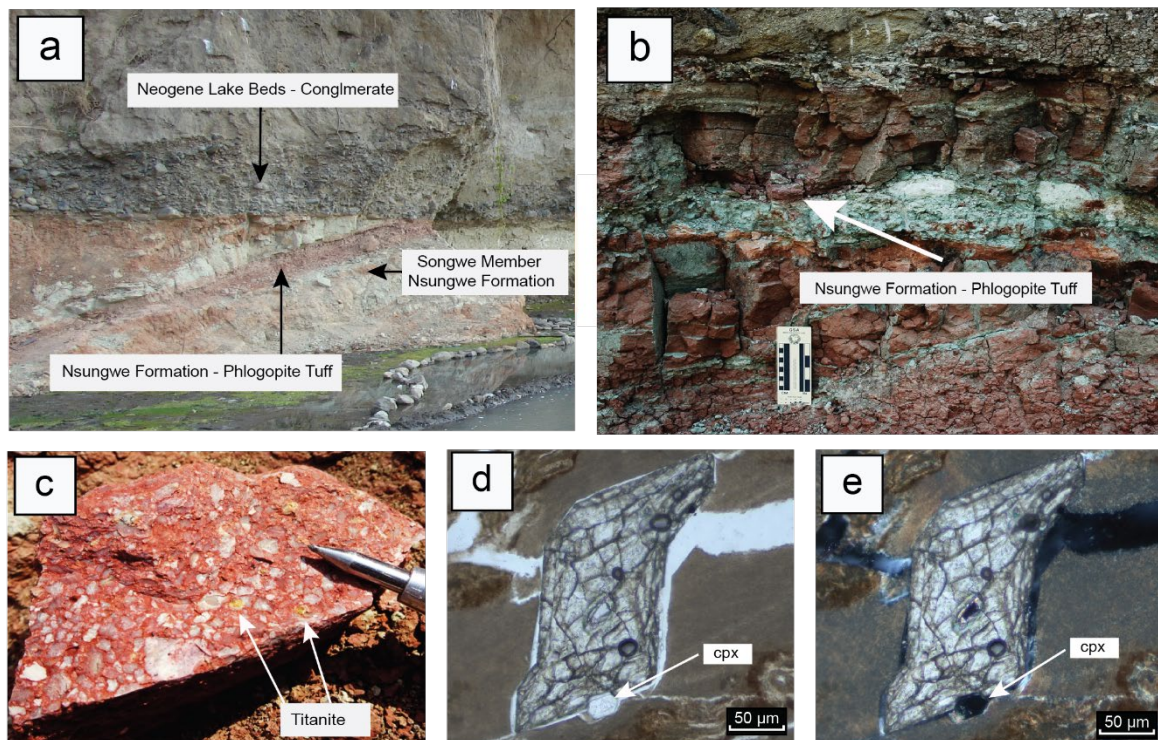


**Fig. 3.2** Field photos of the Songwe Member of the Nsungwe Formation and NFT. a) Nsungwe River outcrop with the Songwe Member sitting below an erosional unconformity with the overlying Neogene Lake Beds Group conglomerate. b) Close-up view of excavated NFT deposit (hand specimen shown in c). c) White relict tuffaceous textures of NFT in maroon matrix with large visible yellow titanite. d) Transmitted light image of NFT thin section showing euhedral titanite (looking down the c-axis) with intergrown clinopyroxene hosted in a fine clay matrix. e) Polarised light image of titanite shown in d).

For this study, a total of four samples (AS18, LL-05, BW4 and TZ-1) were collected from three Oligocene field localities (1. Nsungwe, 2. Songwe and, 3. Ikumbi river sections; Fig. 3.1c). Approximately 1kg of each sample was soaked overnight and washed thoroughly using an ultra-sonic bath prior to standard heavy liquid and Frantz magnetic separation procedures to produce titanite concentrates. Titanite grains containing large melt inclusions were hand-picked, mounted in epoxy and hand polished in a water-free environment (using a kerosene lubricant and diamond paste) to expose melt inclusions for petrographic and geochemical analysis. All inclusions were screened for evidence of post-entrapment modification (i.e. fractures in mineral host, devitrification textures, chemical alteration

or weathering to clay (see Appendix B3, Fig. S1) crystallisation at the melt-mineral host interface, etc.). Only unaltered glass inclusions (n=432) and host titanite grains were targeted for chemical analysis. Once polished, all mounts were stored under vacuum or in desiccators until analyses were conducted.

### 3.2.2 Petrography of titanite hosted primary inclusions

Titanites from these samples are distinctly yellow, have a tabular morphology (0.4 to 1.0 mm along the c-axis) and commonly host large (20 to >100  $\mu\text{m}$ ) rounded blobs or 3D wormy networks of primary silicate glass (formerly melt) inclusions (Fig. 3.3). Trapped silicate melts show no negative crystal shapes and, in most cases, polish to a clean homogenous glass. Vapour bubbles are common in inclusions larger than 30  $\mu\text{m}$ ; the volume of these bubbles can exceed 10% of the total inclusion volume.

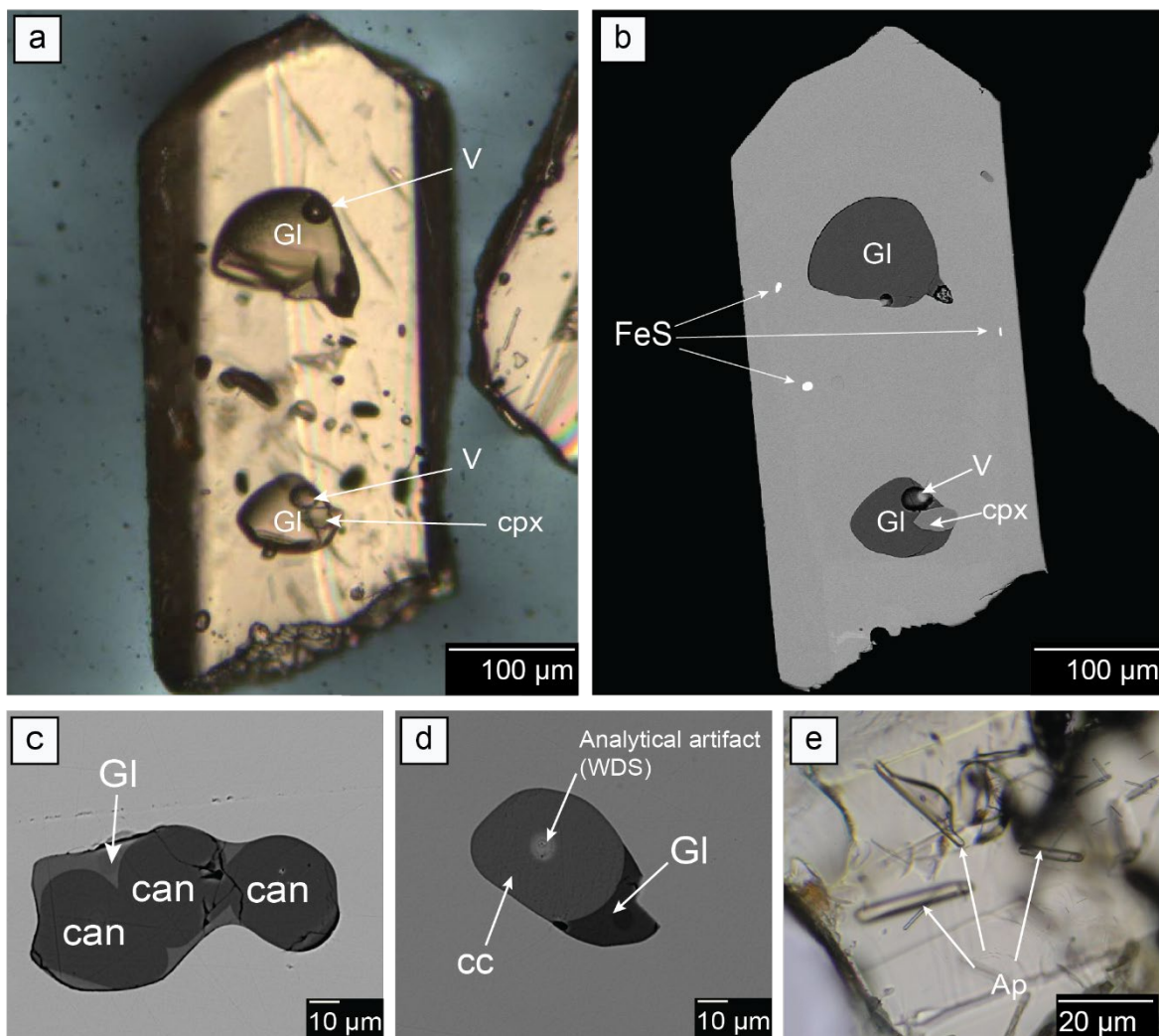


**Fig. 3.3** Mineral and melt inclusions within NFT titanite. a) Transmitted light and b) Backscattered electron images of euhedral titanite hosting large rounded glass inclusions [GI] with vapour bubbles [V], and a clinopyroxene [cpx] mineral inclusion, and iron sulphide (pyrrhotite) [FeS]. Backscattered electron images of titanite hosted phonolitic glass inclusions with c) cancrinite (can) and d) calcite [cc]. e) Transmitted light image of titanite hosting apatite [Ap] mineral inclusions.

Fluorapatite, clinopyroxene, Fe-sulphide (pyrrhotite), and less commonly nepheline, cancrinite and globular calcite are also present as inclusions in NFT titanite (Fig. 3.3a-e). Clinopyroxene and fluorapatite inclusions are most common and occur as either small (<10  $\mu\text{m}$ ) prismatic crystals trapped alongside or within melt inclusions, or as larger (up to 100  $\mu\text{m}$ ) euhedral crystals found near the outer domains of the titanite host. Fe-sulphide is also typically encapsulated within the rim zone of large titanite grains. Feldspathoid minerals nepheline and cancrinite occasionally occur trapped alongside silicate melt inclusions. Where observed, globular carbonate typically forms discrete menisci with the silicate glass in melt inclusions, although rare inclusions with only carbonate have also been recognised.

Some multi-phase inclusions do not preserve well during our polishing procedures. Some inclusions present with a porous texture (Fig. S1) and contain fine aggregates of clay minerals. These inclusions are interpreted to have undergone alteration via weathering and were not further investigated in this study. Qualitative raman spectroscopic analysis of other unexposed inclusions reveal that they have a large peak at raman shifts of between 1060-1095  $\text{cm}^{-1}$  which is consistent with high carbonate contents (Morizet et al. 2013). Similar multi-phase inclusions in associated fluorapatite are recognised to consist dominantly of Na-K-Ca-REE carbonates (Lawrence et al., 2020); these inclusions interpreted to represent an additional carbonate-rich melt phase.

### **3.2.3 Analytical methods**

#### **3.2.3.1 Electron microprobe analysis**

Pristine glass inclusions and their host titanite were analysed for major element contents by wavelength dispersive spectrometry using a JEOL JXA8200 superprobe housed at the Advanced Analytical Centre (AAC), James Cook University (JCU), Townsville. All analyses were standardised using well-characterised mineral standards (albite for Na and Al, olivine for Si and Mg, hematite for Fe, wollastonite for Ca, orthoclase for K, spessartite for Mn, tugtupite for Cl,  $\text{CePO}_4$  for P, rutile for Ti and F-TAP for F). The  $\phi\rho z$  corrections of Armstrong (1991) were applied to all analyses. Analyses were carried out using a 10 nA beam defocused to 10  $\mu\text{m}$  diameter, with acceleration voltage set to 15 kV. Analyses were done using a fixed peak and count times were 10s for Na and F, and 20s for Fe, Ca, Si, Al, K, Ti, Mg, Mn, P and Cl. The MPI-DING glass standards ML3B, ST-HS, TG-1 (Jochum et al., 2006) and the well characterised hydrous alkali-glass MQ#47963 (Kamenetsky et al., 2000) were routinely analysed as secondary check standards (Appendix B1). As hydrous silicate glass is susceptible to damage during electron beam analysis (e.g., Humphreys et al., 2006), extensive testing of analytical procedures was undertaken to minimise beam effects on the analytical results. Analytical conditions were carefully chosen to assess and avoid Na migration effects, which included measuring Na first in the analytical routine, and monitoring the time evolution of the Na signal alongside that of other major elements (i.e. Al, Si, K, Fe). This testing was done not only to ensure that the Na levels recorded reflect the primary Na content, but also to monitor rebound net increases in other major elements during their

longer and subsequent analysis times. No significant variation in these major constituents occurred during the time period they were individually analysed (Appendix B2, Fig. S2). The resulting data was screened for potential fluorescence and/or beam overlap from the host titanite. Inclusions displaying anomalously high (and positively correlated) CaO and TiO<sub>2</sub> contents were deemed affected and removed. After quantitative analyses, all titanite grains and inclusions were imaged using backscattered electron imaging (B3).

### **3.2.3.2 Trace element analysis**

Trace element analysis of the titanite and glass inclusions were conducted by laser ablation ICP-MS using a Geolas Pro 193 nm ArF excimer laser system coupled with a Bruker (formally Varian) 820-MS ICP-MS at the AAC, JCU, Townsville. Methods and instrumentation setup follow those outlined by Spandler et al. (2016). Spot sizes for the glass inclusions varied between 32 and 44 μm, depending on inclusion size and morphology. A 90 μm spot was used for all titanite analyses. All analyses were standardised using NIST SRM 610 reference glass, with MPI-DING glasses ML3B, ST-HS, TG-1 analysed as secondary reference standards. Data reduction was carried out using Iolite software, where Ca concentrations previously measured by WDS served as the internal standard.

### **3.2.3.3 In-situ Sm-Nd isotope microanalysis**

In-situ Sm-Nd isotopic analyses of titanite were carried out using a Geolas Pro 193nm ArF excimer laser system coupled with a ThermoScientific NEPTUNE multicollector ICP-MS at the AAC, JCU, Townsville. The <sup>147</sup>Sm/<sup>144</sup>Nd ratios were derived by calibration to a synthetic LREE-rich silicate glass (<sup>147</sup>Sm/<sup>144</sup>Nd = 0.2451; Fisher et al., 2011), which was routinely analysed throughout each session. Sample <sup>143</sup>Nd/<sup>144</sup>Nd ratios were further normalised to bracketing analyses of Nd-doped glass (JNdi-1, TIMS <sup>143</sup>Nd/<sup>144</sup>Nd = 0.512098 ± 13; Fisher et al., 2011). MKED1 titanite and Otter Lake apatite were also included in these brackets as secondary check standards (Yang et al., 2014; Spandler et al., 2016). The laser spot diameter used was between 60 and 90 μm. Initial isotope values (t = 25 Ma) for <sup>143</sup>Nd/<sup>144</sup>Nd were calculated using a present day CHUR reference value of 0.512638 (Goldstein et al., 1984). All additional methods and procedures follow those outlined by Spandler et al. (2016).

### **3.2.3.4 Raman Spectroscopy**

Raman spectroscopic analysis of the inclusions was conducted using a LabRAM HR800 Raman instrument from Horiba Jobin Yvon, housed at the Institute of Earth Sciences, University of Lausanne, Switzerland. Analyses were conducted on polished mounts under 100 times objective lens using a 532.1 nm laser. Additional analyses were conducted at the AAC, JCU using a WITec Alpha Access 300 Raman instrument connected to a modified Zeiss microscope with a 100 times objective. This Raman was equipped with a diode-generated 532 nm green laser. Raman spectra were collected over a wavenumber range from 200 cm<sup>-1</sup> up to 4000 cm<sup>-1</sup> to capture Raman spectral features of the silicate glass structure,

carbonate species ( $\sim 1060$  to  $1095\text{ cm}^{-1}$ ) and water ( $3100$  to  $3750\text{ cm}^{-1}$ ) (Fig.3.4). Baseline corrections to the spectrum were completed by subtracting an 8 point polynomial fit baseline, following similar procedures reported by Le Losq et al. (2012). Water contents were quantified using the calibrations of Le Losq et al. (2012) and Behrens et al., (2006), with both calibration returning comparable results (Appendix B1).  $\text{CO}_2$  contents were calculated using the method of Morizet et al. (2013) with peak deconvolution processing conducted using the peak fitting software Fityk. Examples of raman spectra and peak deconvolution are presented in Fig. 3.4 and Appendix B1.

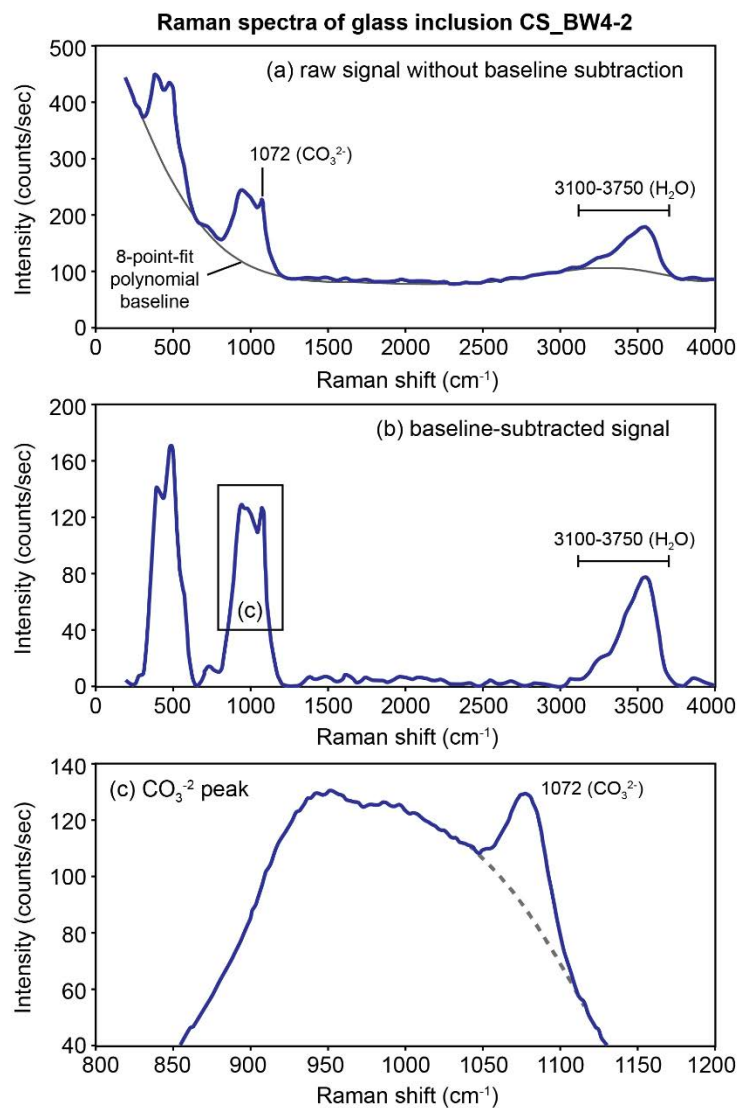


**Fig. 3.4** a) Raman spectra of inclusion CS\_BW4-2 showing both carbonate and water peaks prior to background subtraction. The peaks located between  $200$ - $600\text{ cm}^{-1}$  and  $800$ - $1200\text{ cm}^{-1}$  reflect the low and high frequency silicate glass bands respectively. The typical band for  $\nu_1\text{ CO}_3$  peak sits on top of the high frequency glass band as indicated here at  $1072\text{ cm}^{-1}$ . b) Baseline subtracted signal of CS\_BW-2 showing inset for panel (c). c) Prominent  $\text{CO}_3^{2-}$  peak sitting on top of projected high frequency glass band.

### 3.3 Results

Our geochemical and isotopic analyses reveal no notable differences between samples or localities of the Nsungwe Formation, which is consistent with results of previous studies in the area (Roberts et al., 2010, 2012; Spandler et al., 2016). We therefore consider these volcanic units to be of similar source, nature and magma type such that they can be evaluated collectively as the NFT magmas.

**Table 3.1** Normalised representative compositions of NFT glasses

Representative compositions Sample ID	Primitive NFT Gl. (BW4-7-71)	Av. NFT Phonolite Gl.	Evolved NFT Gl. (AS18-67)
SiO <sub>2</sub>	49.67	54.77	63.52
TiO <sub>2</sub>	0.81	0.43	0.30
Al <sub>2</sub> O <sub>3</sub>	19.30	21.90	24.43
FeO	6.28	3.52	4.03
MnO	0.25	0.17	0.11
MgO	0.99	0.18	0.15
CaO	5.94	2.10	1.80
Na <sub>2</sub> O	10.73	9.36	1.32
K <sub>2</sub> O	5.06	6.93	3.71
P <sub>2</sub> O <sub>5</sub>	0.08	0.03	0.00
Cl	0.37	0.39	0.38
F	0.52	0.23	0.24
Total	100.00	100.00	100.00
ASI: Al/(Ca+Na+K)	0.62	0.82	2.42

#### 3.3.1 Major elements and volatile contents

NFT titanite compositions approach the endmember CaTiSiO<sub>5</sub>, albeit with ~1.5 wt.% FeO, ~1 wt.% Al<sub>2</sub>O<sub>3</sub> and Nb<sub>2</sub>O<sub>5</sub>, and ~0.5 wt.% Ce and F (Appendix B1). These titanite compositions are comparable and consistent across all samples analysed (see Lawrence et al., 2020). Similarly, most of the NFT glass inclusions in all samples are of peralkaline (atomic Al/(Na+K) < 1) phonolite composition with between 52-57 wt.% SiO<sub>2</sub>, 14-18 wt.% Na<sub>2</sub>O + K<sub>2</sub>O, low FeO (3-5 wt.%) and relatively high Al<sub>2</sub>O<sub>3</sub> (20-23 wt.%) (Fig. 3.5). The high alumina contents are unusual for rift-related magmas, but not unprecedented (e.g., phonolites of the Cameroon Line (Nono et al., 1994), and the Gorringer Bank and southern Portugal (Cornen, 1982; Bernard-Griffiths et al., 1997) and phonolitic glasses identified in xenoliths/xenocrysts of the Edgar Graben, Germany (Loges et al., 2019)). A small number of the glasses are of nephelinite composition with comparatively lower silica (<50 wt.%) and alkali (Na<sub>2</sub>O + K<sub>2</sub>O = 11-14 wt.%) contents, and higher CaO (6-10 wt.%) and FeO (5-7 wt.%). Conversely, another suite of inclusions define a compositional trend of decreasing total alkali content with increasing SiO<sub>2</sub> (>57 wt.%) from phonolitic, through trachy-dacitic, trachy-andesitic to dacite compositions (Fig. 3.5a). These

high-silica, low-alkali glasses have remarkably high alumina contents (24 to 25 wt.%  $\text{Al}_2\text{O}_3$ ) and become increasingly peraluminous with increasing silica content (Fig. 3.5d; Appendix B1). CaO, FeO and MgO contents are highest in the most primitive nephelinite compositions and sharply decrease during the transition to phonolitic compositions before a more subtle decrease in the high-silica, low-alkali glass compositions (Fig. 3.4e-f). Representative compositions for the NFT glasses is presented in Table 1.

Calculated  $\text{H}_2\text{O}$  and  $\text{CO}_2$  contents for the phonolitic glass inclusions are in the range of 1.8 to 3 wt.%, and 0.4 to 0.9 wt.%, respectively. However, the  $\text{CO}_2$  values are considered to be minimum values for the melts at the time of entrapment, as these do not consider the proportion of  $\text{CO}_2$  that may have been lost to shrinkage bubbles, which has been demonstrated to commonly exceed 40% (Wallace et al., 2015). The high-silica glass analysed returned higher water contents of ~5.5%  $\text{H}_2\text{O}$  (Appendix B1). These high  $\text{H}_2\text{O}$  contents are consistent with low analytical totals returned from major-element analysis.

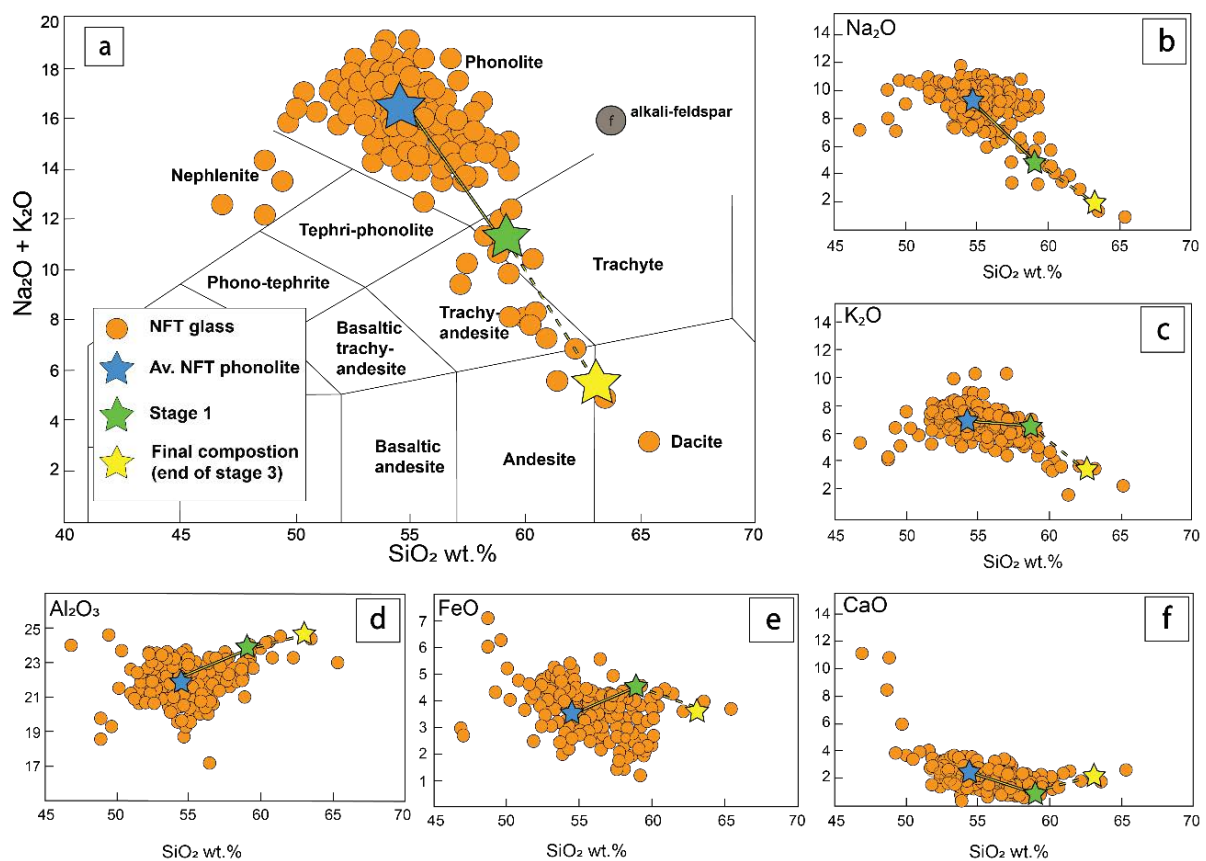


**Fig. 3.5** a) Total alkalis versus silica diagram after Le Bas et al. (1986) showing the composition of the NFT glass inclusions ( $n = 432$ ). Major element vs  $\text{SiO}_2$  Harker diagrams for b)  $\text{Na}_2\text{O}$  c)  $\text{K}_2\text{O}$  d)  $\text{Al}_2\text{O}_3$ , e)  $\text{FeO}$  and f)  $\text{CaO}$ . The coloured stars correspond to compositions modelled for the melt evolution (blue = average NFT phonolite; green = modelled composition after stage 1; yellow = composition at the end of stage 3).

### 3.3.2 Trace element and Sm-Nd isotope analysis

The titanite host grains have high REE contents (>8000 ppm total REE), with slightly concave upward REE patterns and feature a pronounced negative Y anomaly (Fig. 3.6). These titanites also contain elevated Nb, Zr and Sr concentrations that on average exceed >5000 ppm, >2000 ppm and >1700 ppm respectively. Samarium-Nd isotope analysis of titanite grains that host glass inclusions returned initial  $\epsilon\text{Nd}$  values of around +1.8 ( $2\sigma = 0.6$ ), irrespective of the composition of the associated glass inclusions (Fig. 3.7; Appendix B1). The phonolitic glasses return exceptionally high Ba (>3600 ppm) and Sr (>1600 ppm) contents and on average contain >300 ppm total REE. These glasses have a relative enrichment in light rare earth elements (REE) with comparatively flat heavy REE patterns (Fig. 3.6).

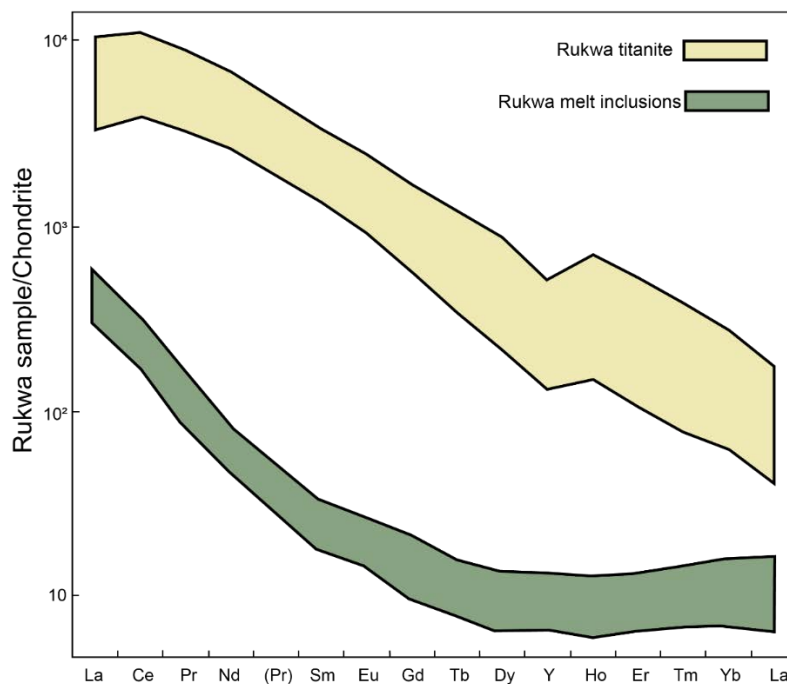


**Fig. 3.6** Chondrite normalised REE+Y plots of NFT titanite and glass inclusions (n=78 and n=73, respectively) (Lawrence et al., 2020 and This Study) chondrite values of McDonough and Sun (1995).

## 3.4 Discussion

### 3.4.1 Origin and source of the Nsungwe Formation Tuff deposits

The wealth of mixed lacustrine and terrestrial fossils preserved in the sand, muddy-sand, silt and claystone stratigraphy of the Songwe Member indicate that the NFT were likely deposited into a wetland environment proximal to the shores or at times within paleo-Lake Rukwa (Roberts et al., 2010, 2012; Stevens et al., 2013; Borths and Stevens, 2017). The high concentrations of phlogopite in the upper horizon of individual tuffs are consistent with airfall deposition into such an environment, given the susceptibility of mica to both aerodynamic and hydrodynamic fractionation from other mineral phases. The stratigraphically thin and intermittent deposition of the tuff units is interpreted to reflect the

low volume and punctuated nature of these explosive volcanic episodes, and although the depositional environment was not overtly hostile to preservation, the NFT units were clearly susceptible to chemical weathering and alteration.

With only alteration-resistant minerals persisting, conventional bulk-rock analysis is an unreliable indicator of magma source and composition. In fact, most conventional petrographic approaches are prohibitive given the extent to which these samples have been weathered (see also Lawrence et al., 2020). However, when placed in the geological context (incipient rifting), unravelling the source and nature of the NFT units is possible via geochemical and petrologic study of the resistant mineral assemblages.

The preserved minerals from the NFT and the mineral inclusions give a collective primary mineral assemblage of titanite, phlogopite, sanidine, Ti andradite, fluorapatite, nepheline, clinopyroxene, cancrinite, calcite, zircon and pyrochlore (Lawrence et al., 2020). This assemblage is characteristic of peralkaline phonolite-carbonatite magmatic systems, such as those documented in the EARS and many other intraplate localities throughout the geologic record (Kjarsgaard and Peterson, 1991; Haase et al., 2017; Balashova et al., 2018; Baudouin et al., 2018; Cooper, 2019). Due to their relatively low viscosity and low temperature, peralkaline-carbonatite magmas are considered to be excellent candidates for investigating mantle source characteristics as they have limited capacity to assimilate crustal material en-route to the surface (Bell and Tilton, 2001). The acquired Sm-Nd isotope data for NFT titanite can therefore provide useful insights into the source of these magmas.

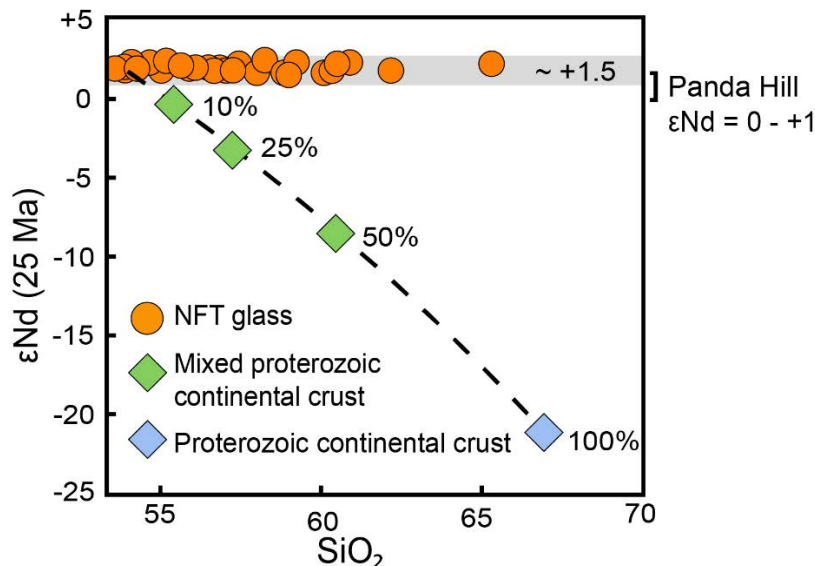


**Fig. 3.7 a)** Epsilon Nd (time = 25 Ma) versus SiO<sub>2</sub> content of NFT glass inclusions. Isotope values for the Proterozoic continental basement of the Rukwa rift are from Manyà (2011) and those for the Panda Hill carbonatite from (Bell and Tilton, 2001). Black dashed line tracks the shift in Nd isotope and SiO<sub>2</sub> composition that would occur with crustal contamination. Note the constancy of Nd isotope composition across the range of silica contents of the Nsungwe Formation melt inclusions is inconsistent with any notable assimilation of the basement crust.

The  $\epsilon\text{Nd}$  values returned for the NFT of +1.8 ( $2\sigma = 0.6$ ) are consistent with a genesis via partial melting of a fertile mantle source. Formation of peralkaline-carbonatite compositions via low-degree partial melting of an enriched lithospheric mantle has been proposed throughout the EARS (Bell and Tilton, 2001), and our Sm-Nd isotope data in combination with Ba, Sr and REE enrichment (Kampunzu and Lubala, 2012) suggests this is also likely the case here. Moreover, the similarity between the Nd isotopic signatures of the late Oligocene NFT and the nearby Cretaceous-aged Panda Hill carbonatite ( $\epsilon\text{Nd} \sim 0$  to +1; Bell and Tilton, 2001) indicates the persistence of common mantle source for alkaline magmatism in the region.

### **3.4.2 Origin of glass inclusions**

When small parcels of melt are trapped by their host minerals under (near) equilibrium conditions and are rapidly quenched, the resulting glasses are interpreted to record the physiochemical conditions of the larger magmatic system at the time of entrapment. In the case of the NFT, the host mineral titanite is critical, not only because of its capacity to preserve unmodified quenched glasses for study, but also because experimental studies and petrological models have shown that titanite is a stable mineral phase across a range of melt compositions from primitive nephelinite through phonolite, to dacite (Kjarsgaard and Peterson, 1991; Nakada, 1991). This range spans the melt inclusion compositions analysed here (Fig. 3.5a). Titanite can also incorporate high contents of trace elements into its crystal structure, which means conditions of equilibrium can be further evaluated using mineral-melt partitioning systematics.

We generated a set of partition coefficients for our Rukwa titanite/phonolitic melt pairs (Fig. 3.8) and found that they are very similar to those determined from the hydrous experiments of Tiepolo et al. (2002) and the natural titanite-matrix glass data of Olin and Wolff (2012). These results indicate that the Rukwa titanite and melt inclusions represent phases formed at, or near to, equilibrium conditions. This result is in accord with trace element compositions of other resistant minerals from the NFT, which also are indicative of derivation from phonolitic melt (Lawrence et al., 2020). Titanite has concave upward chondrite-normalised REE patterns and fractionated Y/Ho (negative Y anomaly; Fig. 3.6), which are artefacts of low-temperature fractionation as outlined by Olin and Wolff (2012). Similar partitioning behaviour was observed in the 850°C experiments of Tiepolo et al. (2002). A melt entrapment temperature of <900 °C is also consistent with the presence of low-temperature igneous phases assemblage associated with the melt inclusions, including calcite and cancrinite (Sirbescu and Jenkins, 1999) and titanite (Kjarsgaard and Peterson 1991), and the solidus conditions of comparable hydrous phonolitic melts (Andújar et al., 2008). Therefore, we assume inclusion entrapment temperatures in the range of 800 to 850 °C.

The pressure of melt entrapment is more difficult to constrain, however the  $\text{CO}_2$  contents of our silicate glasses can be used to estimate entrapment pressures within an acceptable degree of uncertainty.

We measure CO<sub>2</sub> contents up to 0.9 wt.% in our phonolitic glasses and infer higher (~1.6 wt.%) values based on qualitative analysis of volatile bubbles, petrographic observations and conditions of CO<sub>2</sub> saturation at the time of entrapment (Wallace et al., 2015) (Fig. S3). With this, we defer to the experiments of Brooker et al. (2001) and the best-fit CO<sub>2</sub> solubility curve. The solubility of CO<sub>2</sub> (and position of the curve) decreases in silicate melts with decreasing pressure and increasing temperature. Notably, the CO<sub>2</sub> solubility in melts with low NBO/T (<0.5; average Rukwa glass NBO/T = ~0.3) was found to be higher than predicted by the best fit curve. Given our inferred temperature (~850 °C) and magmatic CO<sub>2</sub> contents, we estimate the melt trapping pressure to be around 0.5 GPa.

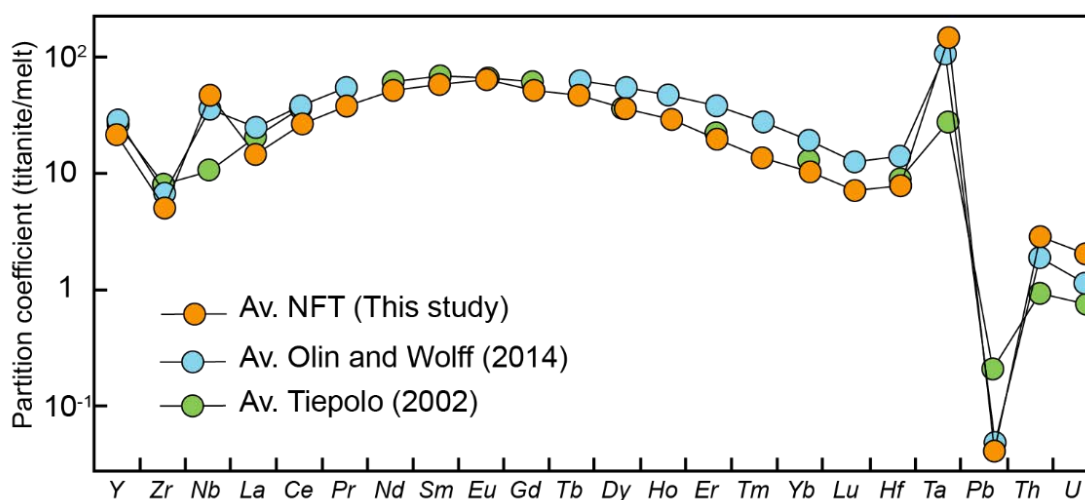


**Fig. 3.8** Comparison of the average titanite/melt trace element partition coefficients for the NFT and equilibrated titanite/melt pairs of Olin and Wolff (2012) and Tiepolo et al. (2002). The latter two cases are known to be in equilibrium at ca. 850 °C.

### 3.4.3 Melt evolution and a case for liquid immiscibility

The chemical evolution of magma is controlled *inter alia* by one or more of the following processes: fractional crystallisation; magma mixing; crustal assimilation; and/or liquid immiscibility (Wilson, 1993). The initial transition from relatively primitive nephelinitic melts to highly alkaline phonolite is consistent with fractional crystallisation experiments and modelling involving NFT feldspathoid minerals (e.g., cancrinite and/or nepheline), phlogopite and titanite ( $\pm$  minor clinopyroxene, magnetite and fluorapatite) of silica-undersaturated alkaline magma (Kjarsgaard and Peterson, 1991; Weidendorfer et al., 2016). The subsequent evolution from phonolitic to dacitic compositions (i.e. silica-undersaturated to silica-saturated compositions) defies typical closed system behaviour as this evolution traverses the thermal divide formed by feldspar in the quartz-nepheline-kalsilite system (Fig. 3.9). Therefore, this compositional trend cannot be reproduced via crystal fractionation alone (Bowen, 1937; Foland et al., 1993).

The Rukwa Rift Basin has developed within a Proterozoic mobile belt that has relatively unradiogenic Nd isotope compositions (Manya, 2011), therefore our Nd isotope data can be used to evaluate the effects of crustal contamination and (to some extent) magma mixing (Bell and Tilton, 2001), both of which may dramatically alter magma compositions (Foland et al., 1993; Wilson, 1993). The Nd isotopic data for our samples are consistent with magma derivation from a fertile mantle source, as outlined above, and show no significant variation with increasing silica content of the melt (Fig. 3.7). Such a trend is incompatible with even minor amounts of contamination of the magma by the basement crust. This result is also consistent with the limited thermal capacity of these magmas to induce anatexis or crustal assimilation (Bell and Tilton, 2001).

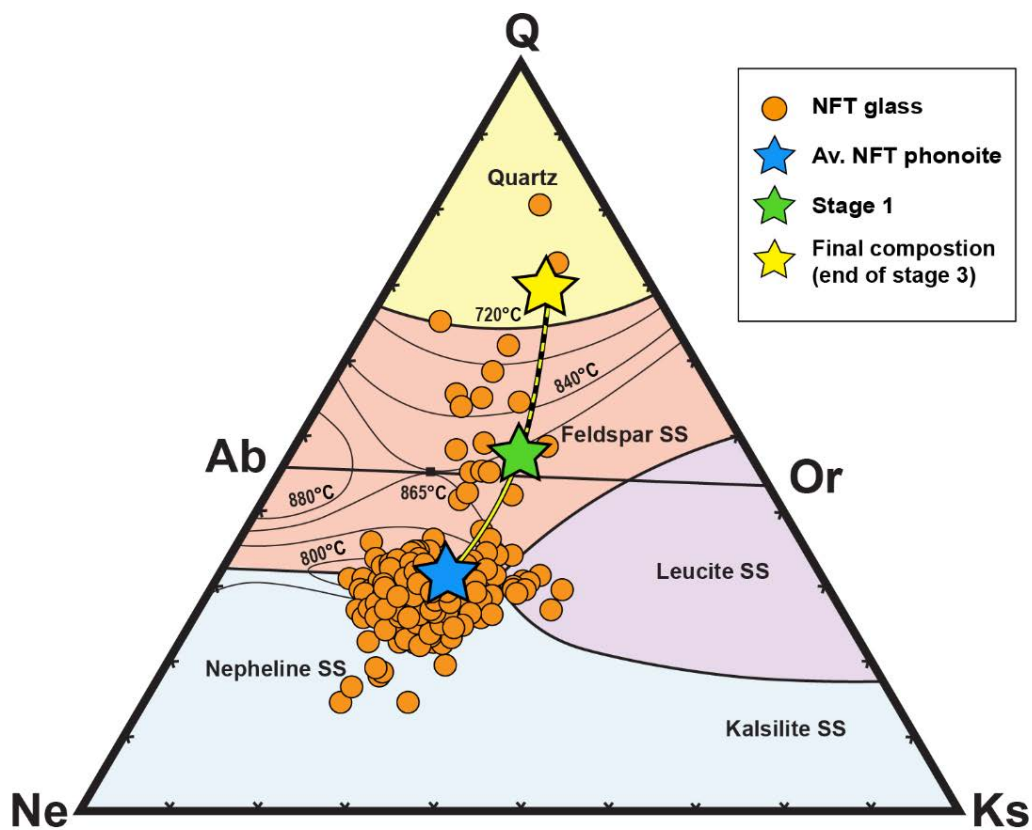


**Fig. 3.9** Melt compositions projected into the  $\text{SiO}_2\text{-NaAlSiO}_4\text{-KAlSiO}_4$  (quartz-nepheline-kalsilite, Q-Ne-Ks) ternary system. The albite-orthoclase join represents the feldspar thermal divide. Note the NFT glasses and modelled compositions traverse the feldspar thermal divide.

With closed-system crystal fractionation and crustal contamination unable to explain the observed melt compositions, we now examine magma evolution via liquid immiscibility. Liquid immiscibility has been presented as a crucial process in carbonatite genesis during the early stages of rifting in the EARS (Kjarsgaard and Peterson, 1991; Mitchell, 2009; Sharygin et al., 2012; de Moor et al., 2013; Guzmics et al., 2015). In addition to the proposed geologic setting of incipient rifting, a

carbonate-rich (CO<sub>2</sub>-saturated) magma source for the NFT is supported by their characteristic mineralogy and mineral chemistry; exceptionally high content of alkalis, Ba and Sr; the high CO<sub>2</sub> content of the glass inclusions, presence of multiphase Na-K-Ca-REE carbonate inclusions in fluorapatite (see Lawrence et al. 2020) and presence of magmatic carbonate and cancrinite inclusions that co-exist with the phonolitic glasses (Fig. 3.3d) (Kjarsgaard and Peterson, 1991; Kampunzu and Lubala, 2012; Guzmics et al., 2011, 2015; de Moor et al., 2013; Baudouin et al., 2018; Lawrence et al., 2020).

For unmixing of carbonatitic and silicate melt to take place, an alkali-rich parent magma must undergo chemical (e.g., via crystal fractionation) and/or physical (i.e., pressure or temperature changes) modification such that it intercepts the two-liquid solvus (Fig. 3.10), at which point a conjugate carbonatite melt will unmix (Kjarsgaard and Peterson, 1991; Veksler et al., 1998; Brooker and Kjarsgaard, 2010; Martin et al., 2013; Weidendorfer et al., 2016). Experiments reveal that the topology of the two-liquid solvus (Fig. 3.10) expands with reducing temperature and is widest in hydrous, CO<sub>2</sub>-saturated melts (Veksler et al., 1998; Brooker and Kjarsgaard, 2010; Martin et al., 2013). As such, the high content of alkali elements and volatiles (H<sub>2</sub>O+CO<sub>2</sub> ~4 wt.%) in the NFT phonolitic glasses renders these melts highly susceptible to unmixing (Fig. 3.10). Should it occur, unmixing of a conjugate carbonatite will greatly influence the composition of a silicate melt, and by default, its evolution thereafter (Veksler et al., 1998; Brooker and Kjarsgaard, 2010; Martin et al., 2013). Whereas Na<sub>2</sub>O, CaO and CO<sub>2</sub> will preferentially enter the carbonatite melt during unmixing, SiO<sub>2</sub>, Al<sub>2</sub>O<sub>3</sub> and H<sub>2</sub>O partition most strongly into the silicate melt component (Veksler et al., 1998; Brooker and Kjarsgaard, 2010; Martin et al., 2013). The net result of this unmixing is the production of a hydrous and silica-rich residual melt, which may account for the dacitic glass inclusion compositions.

#### **3.4.4 Melt evolution modelling**

We model this process using the average NFT phonolitic glasses with a conservative volatile content of 2 wt.% H<sub>2</sub>O and 1.6 wt.% CO<sub>2</sub> as a starting composition. These estimates are based on measured H<sub>2</sub>O and CO<sub>2</sub> contents of the glass inclusions and associated vapour bubbles, as well as the extrapolated CO<sub>2</sub> solubility expected for these glass compositions presented above (Brooker et al., 2001) (see Appendix B4 for additional modelling details). The carbonatite component is modelled based on the calculated values presented by Weidendorfer et al. (2016) and carbonatite melt inclusion compositions reported elsewhere (Mitchell, 2009; de Moor et al., 2013; Guzmics et al., 2015), and qualitative observations of the carbonate-rich multiphase inclusions in fluorapatite, interpreted to be crystallised carbonatite melts (Lawrence et al., 2020). As previously mentioned, temperature and pressure estimates of magma evolution are 850 °C or less and 0.5 GPa, respectively. The position of the two-liquid solvus at these conditions is extrapolated from previously-defined phase topologies (Kjarsgaard and Peterson, 1991; Brooker and Kjarsgaard, 2010; Martin et al., 2013; Weidendorfer et al., 2016).

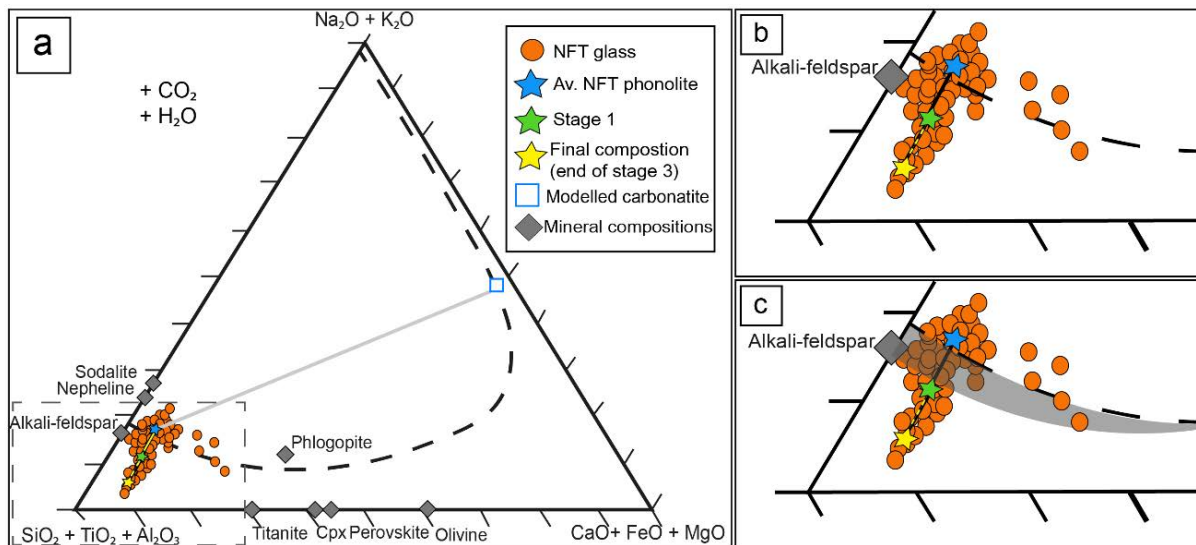


**Fig. 3.10** Magma evolution via liquid immiscibility. a) Hamilton diagram (after Hamilton et al. (1979)) showing the compositions of NFT glasses, modelled melt evolution and modelled carbonatite liquid composition. The silicate-carbonatite miscibility gap (i.e. two-liquid solvus) extrapolated from those previously-defined in the literature is indicated by the black dashed line (Kjarsgaard and Peterson, 1991; Weidendorfer et al., 2016). This solvus is the most appropriate for the conditions modelled here. b) Enlarged bottom left corner of the diagram highlighting the NFT glass compositions and starting composition (blue star - average NFT phonolite) used for the modelling. c) Expansion of the solvus with reducing temperature at near constant pressure (grey shaded area) allows carbonatite unmixing, and derivation of silicic magmas that traverse the feldspar thermal divide. Green star = the modelled composition arrived at after sodalite, feldspar and magnetite fractionation and carbonatite unmixing (Stage 1). The yellow star is the final composition after subsequent feldspar-dominated fractionation (Stages 2 & 3).

Our melt evolution model involves 3 stages of crystal fractionation, and one stage of carbonatite unmixing, from a phonolitic parent melt. The modelling procedures generally follow those of Weidendorfer et al. (2016) where a new stage is commenced when the modelled liquid no longer follows the observed evolution of the Rukwa melt inclusions. The mineral compositions used for fractionation modelling are based on mineral phases identified from the NFT, as outlined by Lawrence et al. (2020). The fractionating phase assemblages were also modelled with consideration to phase petrology of peralkaline phonolitic melts (stage 1) and peraluminous melts (stages 2 and 3) (Kjarsgaard and Peterson, 1991; Scaillet et al., 2016; Weidendorfer et al., 2016).

Beginning with the average NFT phonolite glass composition (blue star in Figs. 3.5, 3.9 & 3.10) a combination of feldspathoid fractionation (11% of the total mass) and carbonatite un-mixing (7%) acts to shift the melt composition from silica-undersaturated to silica-saturated compositions, whereupon feldspar crystallisation is stabilised. Stage 1 is completed by feldspar fractionation (30%) driving the melt to trachytic/trachy-andesitic compositions (green star in Figs. 3.5, 3.9 & 3.10) that closely resemble our glass inclusions. As predicted by element partitioning systematics and reflected in our data, an increase in alumina content shifts the melt from peralkaline to peraluminous compositions (Fig. 3.5).

Given that FeO is both a major and minor contributor to multiple phases of the NFT that are not modelled during stage 1 (i.e. Fe-sulphide, clinopyroxene, Ti-rich andradite, phlogopite, titanite etc.), modelled FeO concentrations project to the high-end range of natural NFT glass data in stage 1 (Fig 3.5e).

Once silica-saturated, no further immiscibility is required. Instead, successive-stages of alkali feldspar dominated fractionation (between 30-40%) accompanied by minor accessory phases (i.e. 1% phlogopite and 5% spinel in stage 2, and 2% phlogopite, 4% spinel and 1% titanite in stage 3) is sufficient to model the trend and compositions of the andesitic-dacitic glass inclusions (yellow star in Figs. 3.5, 3.9 & 3.10). Our model predicts a total accumulation of >5 wt.% H<sub>2</sub>O in the melt after the final stage of crystal fractionation, which is consistent with lower major element totals and high measured H<sub>2</sub>O (~5.5 wt.%) for the dacitic glass inclusions (Appendix B1). Magmas of this composition are not typically found in continental rift zones; rather, they archetypal magmas of supra-subduction zone environments.

### **3.4.5 Comparison to other EARS magma evolution models**

As previously stated, liquid immiscibility is widely recognised to be an important process in the evolution of alkaline magmas in the EARS (Kjarsgaard and Peterson, 1991; Guzmics et al., 2011, 2015; de Moor et al., 2013; Baudouin et al., 2018). Evidence for unmixing of carbonatite and peralkaline silicate liquids from a CO<sub>2</sub>-rich silicate parent magma, as predicted from experimental studies (Veksler et al., 1998; Brooker and Kjarsgaard, 2010; Martin et al., 2013), is preserved as melt inclusions in phenocrysts from a number of active volcanos in the eastern branch (Kjarsgaard and Peterson, 1991; Guzmics et al., 2011, 2015; de Moor et al., 2013; Baudouin et al., 2018). Of particular relevance to our study are the findings of Baudouin et al. (2018), who report evolved trachytic melt inclusions (SiO<sub>2</sub> >62 wt.%) coexisting with immiscible carbonatite and volatile phases within nepheline from Hanang Volcano, Tanzania (Fig. S4). These evolved melts are sub-alkaline, silica saturated, and were interpreted to be immiscibility products of a CO<sub>2</sub>- and alkali-rich phonolitic melt inclusion that underwent post entrapment unmixing while enclosed in nepheline during magma ascent (Baudouin et al., 2018). While we report a similar phenomenon, the absence of coexisting carbonatite melt phases in our high-silica glasses excludes post-entrapment processes as causative of unmixing. Instead, we suggest unmixing occurred within small volume magma chamber(s) at mid crustal levels (~0.5 GPa, or ~15 km depth) (Fadaie and Ranalli, 1990). Here, significant expansion of the two-liquid solvus is favourable with near isobaric cooling driving crystal fractionation and liquid immiscibility (Brooker and Kjarsgaard, 2010). Such conditions are consistent with the structures, processes and geodynamic models known to facilitate magmatism in the EARS (Corti et al., 2004; Chorowicz, 2005; Fagereng, 2013) (Fig. 3.11). The unmixed silicate melt would have had vastly different physical properties (e.g., wetting behaviour, viscosity) than the carbonatite liquids (Manga et al., 1998), which may have enabled effective separation and migration of the two melts, with limited trapping of the carbonatite melts by crystallising titanite due to their low viscosity.

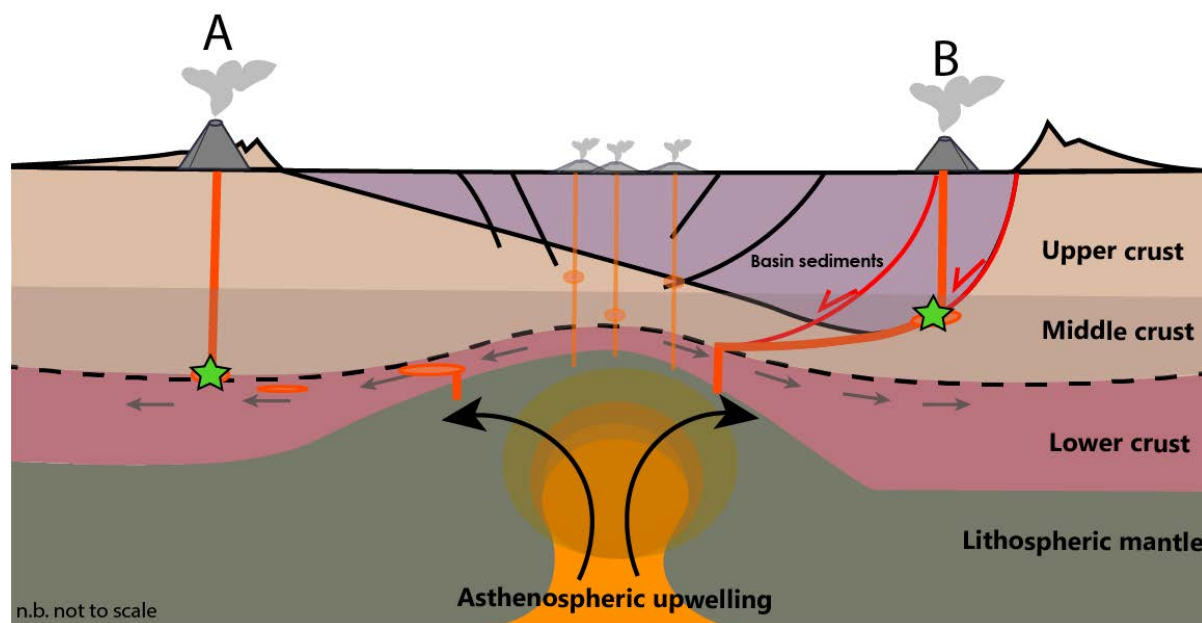


**Fig. 3.11** Schematic cross section of a continental rift depicting the generation of volatile rich melts via low degree partial melting of enriched lithospheric mantle or fertile asthenosphere. Two ways these melts may undergo near-isobaric cooling are represented by volcano A and volcano B. In case A, low degree melts are transported away from the rift axis hot zone at depth via ductile convection of the lower crust. In case B, low degree partial melts are injected along the sub-horizontal limb of a deep listric fault whereby they undergo cooling and unmixing (green star), followed by eruption. Both cases are consistent with geodynamic modelling of continental rift evolution (Corti et al., 2004; Chorowicz, 2005; Fagereng, 2013). Note, the figure is not drawn to scale.

### 3.4.6 Implications for explosive volcanism

In the case we present, the end stage andesitic-dacitic compositions produced after unmixing are expected to be around an order of magnitude more viscous than their phonolitic precursors (Manga et al., 1998; Andújar et al., 2008). This increase in viscosity is also accompanied by a significant rise in melt H<sub>2</sub>O content analogous to volcanic arc magmas (Kelley and Cottrell, 2009). Such physiochemical changes provide the necessary ingredients required for effective magma separation and migration from depth, followed by volatile exsolution and, ultimately, explosive volcanism and ash fallout at the surface (Andújar et al., 2008; Kamenetsky and Yaxley, 2015). The deposition of compositionally hybridised and chemically reactive (silicic-carbonatite) extrusive ashfall products and prevailing wetland depositional environment of the Rukwa Rift ~25 Ma, resulted in the formation of what are now narrow clay-rich horizons with alkaline magmatic mineral assemblages and relict tuffaceous textures. The magma evolution revealed here for multiple tuff horizons therefore provides a new determinant process for cyclical, highly-explosive volcanism in developing continental rifts. So far this magma evolution is only recognised from the late Oligocene of the Rukwa Rift Basin, although we note that cases of silicic melts coexisting with extrusive carbonatites have been reported, albeit rarely, in the EARS (e.g. trachyte-carbonatite immiscibility of the Suswa volcano, Kenya (Macdonald et al., 1993) and Hanang volcano,

Tanzania (Baudouin et al., 2018) and from other parts of the world (Woolley and Church, 2005) (Fig. S4). Further understanding of how explosive volcanic systems evolve in these settings is warranted, particularly considering the natural hazard implications to the vast populations living within or in close proximity to the EARS.

#### ***3.4.7 Titanite as a monitor for alkaline magmatism***

Although melt inclusions are commonly used to investigate alkaline-carbonatite systems, they are seldom reported (or sought after) in titanite. Our study demonstrates that titanite is not only a robust host for melt inclusions, but is also amenable to direct dating (in situ U/Pb dating; Spandler et al., 2016) and in-situ analysis for trace element and Sm-Nd isotopes to track aspects of melt composition (including volatiles) and magma source character. The wide stability of titanite in relatively evolved alkaline to silicic magma systems (Kjarsgaard and Peterson, 1991; Haase et al., 2017; Balashova et al., 2018; Baudouin et al., 2018; Cooper, 2019) and its resistance to weathering (Garzanti et al., 2013) mean it can be effective at trapping and preserving a diverse range of melts produced during magma evolution, as is the case here. The novelty of our approach and the distinctive nature of volcanism in the early Rukwa Rift showcases the research potential of this common, yet under-utilised accessory mineral phase, and we expect that the geological record of titanite will prove useful in the study of complex or poorly preserved intraplate alkaline magmas elsewhere.

#### ***3.4.8 Alkaline volcanism and the ecological evolution of East Africa***

The onset of rifting, regional uplift and alkaline magmatism in the EARS drastically changed the paleo-landscape of east Africa, and had profound effects on the adaptation, distribution, success and demise of local fauna (Sepulchre et al., 2006; Roberts et al., 2012; Stevens et al., 2013; Borths and Stevens, 2017). Explosive volcanism is intrinsically linked to the biosphere, and in the late Oligocene of eastern Africa, may have had the dual effect of allowing for the wide distribution of nutrient-rich volcanic ash to stimulate bio fertility (Frogner et al., 2001), as well as providing the catastrophic cause of mortality of flora and fauna, and ultimately, fossil preservation in the geological record. Significantly, today the volcanic terrains of the EARS are some of the most densely populated areas of eastern Africa (Small and Naumann, 2001), as volcanism has provided the rich soils and dynamic topography to facilitate life-sustaining agriculture and economic development. Understanding the volcanic character of these often-complex magmatic systems is essential to adequately assess their eruptive hazard potential and environmental impacts in the geologic past. Despite their cryptic preservation, this is well exemplified by the NFT and richly fossiliferous strata of the Rukwa Rift Basin.

### 3.5 Conclusions

- Our glass inclusion compositions and geochemical modelling support a premise that peraluminous silica-saturated melt compositions may be produced from peralkaline phonolitic precursors via a combination of closed-system carbonatite unmixing and crystal fractionation.
- The composition of both igneous minerals and silicate glass hosted in titanite indicate the pre-eruptive magma underwent near-isobaric cooling at mid-crustal conditions (approximately 850 °C and 0.5 GPa).
- The volatile-rich, silica-saturated magmas produced via unmixing of carbonatite have a highly explosive constitution. To our knowledge, this is the first report of what we propose is an entirely new and novel mode of explosive volcanism, yet to be recognised elsewhere in the geological record.
- Titanite and their enclosed silicate glass (formally melt) inclusions provide an unprecedented record of the earliest known incidence of alkaline-carbonatite volcanism of the Western Branch of the EARS. Titanite will likely prove to be a useful petrological tool for investigations of early rift sequences and carbonatite volcanism elsewhere, given the prevalence of accessory titanite in evolved alkaline magmas of the EARS.
- The coexistence of the NFT and extraordinary fossil archive hosted within the Oligocene strata of the Rukwa Rift highlights the intimate relationship between alkaline-carbonatite volcanism, rapid landscape evolution and ecological success in the geologic past.

### References

- Andújar, J., Costa, F., Martí, J., Wolff, J., Carroll, M., 2008. Experimental constraints on pre-eruptive conditions of phonolitic magma from the caldera-forming El Abrigo eruption, Tenerife (Canary Islands). *Chemical Geology*, 257(3-4): 173-191.
- Armstrong, J.T., 1991. Quantitative elemental analysis of individual microparticles with electron beam instruments, *Electron probe quantitation*. Springer, pp. 261-315.
- Bagley, B., Nyblade, A.A., 2013. Seismic anisotropy in eastern Africa, mantle flow, and the African superplume. *Geophysical Research Letters*, 40(8): 1500-1505.
- Balashova, A., Mattsson, H.B., Hirt, A.M., 2018. New tephrostratigraphic data from Lake Emakat (northern Tanzania): Implications for the eruptive history of the Oldoinyo Lengai volcano. *Journal of African Earth Sciences*, 147: 374-382.
- Baudouin, C., Parat, F., Michel, T., 2018. CO<sub>2</sub>-rich phonolitic melt and carbonatite immiscibility in early stage of rifting: Melt inclusions from Hanang volcano (Tanzania). *Journal of Volcanology and Geothermal Research*, 358: 261-272.

- Behrens, H., Roux, J., Neuville, D.R., Siemann, M., 2006. Quantification of dissolved H<sub>2</sub>O in silicate glasses using confocal microRaman spectroscopy. *Chemical Geology*, 229(1-3): 96-112.
- Bernard-Griffiths, J., Gruau, G., Cornen, G., Azambre, B., Mace, J., 1997. Continental lithosphere contributions to alkaline magmatism: Isotopic (Nd, Sr, Pb) and geochemical (REE) evidence from Serra de Monchique and Mount Ormonde Complexes. *Journal of Petrology*, 38: 115-132.
- Bell, K., Tilton, G., 2001. Nd, Pb and Sr isotopic compositions of East African carbonatites: evidence for mantle mixing and plume inhomogeneity. *Journal of Petrology*, 42(10): 1927-1945.
- Borths, M.R., Stevens, N.J., 2017. The first hyaenodont from the late Oligocene Nsungwe Formation of Tanzania: Paleoecological insights into the Paleogene-Neogene carnivore transition. *PloS one*, 12(10): e0185301.
- Bowen, N.L., 1937. Recent high-temperature research on silicates and its significance in igneous geology. *American Journal of Science*(193): 1-21.
- Brooker, R., Kjarsgaard, B., 2010. Silicate-carbonate liquid immiscibility and phase relations in the system SiO<sub>2</sub>-Na<sub>2</sub>O-Al<sub>2</sub>O<sub>3</sub>-CaO-CO<sub>2</sub> at 0.1-2.5 GPa with applications to carbonatite genesis. *Journal of Petrology*, 52(7-8): 1281-1305.
- Brooker, R., Kohn, S., Holloway, J., McMillan, P., 2001. Structural controls on the solubility of CO<sub>2</sub> in silicate melts: part I: bulk solubility data. *Chemical Geology*, 174(1-3): 225-239.
- Bruand, E., Storey, C., Fowler, M., 2016. An apatite for progress: Inclusions in zircon and titanite constrain petrogenesis and provenance. *Geology*, 44(2): 91-94.
- Campany, M. et al., 2015. Carbonatitic lavas in Catanda (Kwanza Sul, Angola): Mineralogical and geochemical constraints on the parental melt. *Lithos*, 232: 1-11.
- Chorowicz, J., 2005. The east African rift system. *Journal of African Earth Sciences*, 43(1-3): 379-410.
- Cooper, A.F., 2019. Petrology and petrogenesis of an intraplate alkaline lamprophyre-phonolite-carbonatite association in the Alpine Dyke Swarm, New Zealand. *New Zealand Journal of Geology and Geophysics*: 1-20.
- Cornen, G., 1982. Petrology of the alkaline volcanism of Gorringe Bank (southwest Portugal). *Marine Geology*, 47(1-2), pp.101-130.
- Corti, G. et al., 2004. Continental rift architecture and patterns of magma migration: A dynamic analysis based on centrifuge models. *Tectonics*, 23(2).
- de Moor, J.M. et al., 2013. Volatile-rich silicate melts from Oldoinyo Lengai volcano (Tanzania): Implications for carbonatite genesis and eruptive behavior. *Earth and Planetary Science Letters*, 361: 379-390.
- Ernst, R.E., Bell, K., 2010. Large igneous provinces (LIPs) and carbonatites. *Mineralogy and Petrology*, 98(1-4): 55-76.
- Fadaie, K.t., Ranalli, G., 1990. Rheology of the lithosphere in the East African Rift System. *Geophysical Journal International*, 102(2): 445-453.

- Fagereng, Å., 2013. Fault segmentation, deep rift earthquakes and crustal rheology: Insights from the 2009 Karonga sequence and seismicity in the Rukwa–Malawi rift zone. *Tectonophysics*, 601: 216-225.
- Foland, K., Landoll, J., Henderson, C., Chen, J., 1993. Formation of cogenetic quartz and nepheline syenites. *Geochimica et Cosmochimica Acta*, 57(3): 697-704.
- Frognier, P., Gíslason, S.R., Óskarsson, N., 2001. Fertilizing potential of volcanic ash in ocean surface water. *Geology*, 29(6): 487-490.
- Garzanti, E. et al., 2013. Weathering and relative durability of detrital minerals in equatorial climate: sand petrology and geochemistry in the East African Rift. *The Journal of Geology*, 121(6): 547-580.
- Goldstein, S., O'Nions, R., Hamilton, P., 1984. A Sm-Nd isotopic study of atmospheric dusts and particulates from major river systems. *Earth and Planetary Science Letters*, 70(2): 221-236.
- Guzmics, T. et al., 2011. Carbonatite melt inclusions in coexisting magnetite, apatite and monticellite in Kerimasi calciocarbonatite, Tanzania: melt evolution and petrogenesis. *Contributions to Mineralogy and Petrology*, 161(2): 177-196.
- Guzmics, T. et al., 2012. Liquid immiscibility between silicate, carbonate and sulfide melts in melt inclusions hosted in co-precipitated minerals from Kerimasi volcano (Tanzania): evolution of carbonated nephelinitic magma. *Contributions to Mineralogy and Petrology*, 164(1): 101-122.
- Guzmics, T., Zajacz, Z., Mitchell, R.H., Szabó, C., Wälle, M., 2015. The role of liquid–liquid immiscibility and crystal fractionation in the genesis of carbonatite magmas: insights from Kerimasi melt inclusions. *Contributions to Mineralogy and Petrology*, 169(2): 17.
- Haase, K.M., Beier, C., Regelous, M., Rappich, V., Renno, A., 2017. Spatial variability of source composition and petrogenesis in rift and rift flank alkaline lavas from the Eger Rift, Central Europe. *Chemical Geology*, 455: 304-314.
- Hamilton, D., Freestone, I.C., Dawson, J.B., Donsldson, C.H., 1979. Origin of carbonatites by liquid immiscibility. *Nature*, 279(5708): 52.
- Humphreys, M.C., Kearns, S.L., Blundy, J.D., 2006. SIMS investigation of electron-beam damage to hydrous, rhyolitic glasses: Implications for melt inclusion analysis. *American Mineralogist*, 91(4): 667-679.
- Jochum, K.P. et al., 2006. MPI-DING reference glasses for in situ microanalysis: New reference values for element concentrations and isotope ratios. *Geochemistry, Geophysics, Geosystems*, 7(2).
- Kamenetsky, M.B. et al., 2004. Kimberlite melts rich in alkali chlorides and carbonates: a potent metasomatic agent in the mantle. *Geology*, 32(10): 845-848.
- Kamenetsky, V.S. et al., 2000. Enriched end-member of primitive MORB melts: petrology and geochemistry of glasses from Macquarie Island (SW Pacific). *Journal of Petrology*, 41(3): 411-430.
-

- Kamenetsky, V.S., Yaxley, G.M., 2015. Carbonate–silicate liquid immiscibility in the mantle propels kimberlite magma ascent. *Geochimica et Cosmochimica Acta*, 158: 48-56.
- Kamunzu, A., Lubala, R., 2012. Magmatism in extensional structural settings: the Phanerozoic African plate. Springer Science & Business Media.
- Kelley, K.A., Cottrell, E., 2009. Water and the oxidation state of subduction zone magmas. *Science*, 325(5940): 605-607.
- Kjarsgaard, B., Peterson, T., 1991. Nephelinite-carbonatite liquid immiscibility at Shombole volcano, East Africa: petrographic and experimental evidence. *Mineralogy and Petrology*, 43(4): 293-314.
- Lawrence, L., Spandler, C., Roberts, E.M. and Hilbert-Wolf, H.L., 2020. Mineralogy and origin of the alkaline Nsungwe Formation tuffs of the Rukwa Rift Basin, southwestern Tanzania. *Lithos*, p.105885.
- Le Bas, M., Maitre, R.L., Streckeisen, A., Zanettin, B., Rocks, I.S.o.t.S.o.I., 1986. A chemical classification of volcanic rocks based on the total alkali-silica diagram. *Journal of petrology*, 27(3): 745-750.
- Le Losq, C., Neuville, D.R., Moretti, R., Roux, J., 2012. Determination of water content in silicate glasses using Raman spectrometry: Implications for the study of explosive volcanism. *American Mineralogist*, 97(5-6): 779-790.
- Loges, A., Schultze, D., Klügel, A. and Lucassen, F., 2019. Phonolitic melt production by carbonatite Mantle metasomatism: evidence from Eger Graben xenoliths. *Contributions to Mineralogy and Petrology*, 174(11), pp.1-24.
- Macdonald, R. et al., 1993. Liquid immiscibility between trachyte and carbonate in ash flow tuffs from Kenya. *Contributions to Mineralogy and Petrology*, 114(2): 276-287.
- Manga, M., Castro, J., Cashman, K.V., Loewenberg, M., 1998. Rheology of bubble-bearing magmas. *Journal of Volcanology and Geothermal Research*, 87(1-4): 15-28.
- Manya, S., 2011. Nd-isotopic mapping of the Archaean–Proterozoic boundary in southwestern Tanzania: Implication for the size of the Archaean Tanzania Craton. *Gondwana Research*, 20(2-3): 325-334.
- Martin, L.H., Schmidt, M.W., Mattsson, H.B., Guenther, D., 2013. Element partitioning between immiscible carbonatite and silicate melts for dry and H<sub>2</sub>O-bearing systems at 1–3 GPa. *Journal of Petrology*, 54(11): 2301-2338.
- Mitchell, R.H., 2009. Peralkaline nephelinite–natrocarbonatite immiscibility and carbonatite assimilation at Oldoinyo Lengai, Tanzania. *Contributions to Mineralogy and Petrology*, 158(5): 589.
- Morizet, Y., Brooker, R.A., Iacono-Marziano, G., Kjarsgaard, B.A., 2013. Quantification of dissolved CO<sub>2</sub> in silicate glasses using micro-Raman spectroscopy. *American Mineralogist*, 98(10): 1788-1802.

- Nakada, S., 1991. Magmatic processes in titanite-bearing dacites, central Andes of Chile and Bolivia. *American Mineralogist*, 76(3-4): 548-560.
- Nono, A., Déruelle, B., Demaiffe, D. and Kambou, R., 1994. Tchabal Nganha volcano in Adamawa (Cameroon): petrology of a continental alkaline lava series. *Journal of Volcanology and Geothermal Research*, 60(2), pp.147-178
- Olin, P.H., Wolff, J.A., 2012. Partitioning of rare earth and high field strength elements between titanite and phonolitic liquid. *Lithos*, 128: 46-54.
- Pik, R., Marty, B., Carignan, J., Yirgu, G., Ayalew, T., 2008. Timing of East African Rift development in southern Ethiopia: Implication for mantle plume activity and evolution of topography. *Geology*, 36(2): 167-170.
- Roberts, E.M. et al., 2010. Sedimentology and depositional environments of the Red Sandstone Group, Rukwa Rift Basin, southwestern Tanzania: New insight into Cretaceous and Paleogene terrestrial ecosystems and tectonics in sub-equatorial Africa. *Journal of African Earth Sciences*, 57(3): 179-212.
- Roberts, E.M. et al., 2012. Initiation of the western branch of the East African Rift coeval with the eastern branch. *Nature Geoscience*, 5(4): 289.
- Sepulchre, P. et al., 2006. Tectonic uplift and Eastern Africa aridification. *Science*, 313(5792): 1419-1423.
- Sharygin, V.V., Kamenetsky, V.S., Zaitsev, A.N., Kamenetsky, M.B., 2012. Silicate–natrocarbonatite liquid immiscibility in 1917 eruption combeite–wollastonite nephelinite, Oldoinyo Lengai Volcano, Tanzania: Melt inclusion study. *Lithos*, 152: 23-39.
- Small, C., Naumann, T., 2001. The global distribution of human population and recent volcanism. *Global Environmental Change Part B: Environmental Hazards*, 3(3): 93-109.
- Sobolev, A., 1996. Melt inclusions in minerals as a source of principle petrological information. *Petrology*, 4(3): 209-220.
- Spandler, C. et al., 2016. MKED1: a new titanite standard for in situ analysis of Sm–Nd isotopes and U–Pb geochronology. *Chemical Geology*, 425: 110-126.
- Stevens, N.J. et al., 2013. Palaeontological evidence for an Oligocene divergence between Old World monkeys and apes. *Nature*, 497(7451): 611.
- Tiepolo, M., Oberti, R., Vannucci, R., 2002. Trace-element incorporation in titanite: constraints from experimentally determined solid/liquid partition coefficients. *Chemical Geology*, 191(1-3): 105-119.
- Veizer, J.n., Bell, K., Jansen, S.L., 1992. Temporal distribution of carbonatites. *Geology*, 20(12): 1147-1149.
- Veksler, I., Petibon, C., Jenner, G., Dorfman, A., Dingwell, D., 1998. Trace element partitioning in immiscible silicate–carbonate liquid systems: an initial experimental study using a centrifuge autoclave. *Journal of Petrology*, 39(11-12): 2095-2104.
-

- Wallace, P.J., Kamenetsky, V.S., Cervantes, P., 2015. Melt inclusion CO<sub>2</sub> contents, pressures of olivine crystallization, and the problem of shrinkage bubbles. *American Mineralogist*, 100(4): 787-794.
- Weidendorfer, D., Schmidt, M.W., Mattsson, H.B., 2016. Fractional crystallization of Si-undersaturated alkaline magmas leading to unmixing of carbonatites on Brava Island (Cape Verde) and a general model of carbonatite genesis in alkaline magma suites. *Contributions to Mineralogy and Petrology*, 171(5): 43.
- Wilson, M., 1993. Magmatic differentiation. *Journal of the Geological Society*, 150(4): 611-624.
- Woolley, A., Church, A., 2005. Extrusive carbonatites: a brief review. *Lithos*, 85(1-4): 1-14.
- Yang, Y.-H. et al., 2014. Sr and Nd isotopic compositions of apatite reference materials used in U–Th–Pb geochronology. *Chemical Geology*, 385: 35-55.
- Zaitsev, A.N., Keller, J., 2006. Mineralogical and chemical transformation of Oldoinyo Lengai natrocarbonatites, Tanzania. *Lithos*, 91(1-4): 191-207.

## Chapter 4

# **Experimental investigation of the carbonatite trachyte association: phase relations and liquid immiscibility in evolved carbonatite-phonolite magmas**

### **Abstract**

The field association between carbonatites and silica-undersaturated alkaline rocks such as nephelinites and phonolites is well recognised in the geological record. Although less commonly observed, carbonatites associated with silica-saturated trachyte compositions have also been documented (e.g., The Nsungwe Formation tuffs of the Rukwa Rift Basin, Tanzania) yet the genesis and implications of this magma association remain poorly understood. To investigate this magma association further, we conducted a series of isobaric (0.5 GPa) piston cylinder experiments using a mixture of synthetic alkali-carbonate and natural syenite rock powder to investigate the mineralogy, paragenesis and melt evolution over a temperature range from 1000 °C to 700 °C. Phonolite – alkali-carbonate conjugate liquid pairs were produced at 1000 °C, 950 °C and 900 °C, the evolution of which is consistent with the predicted expansion of the two-liquid solvus with reducing temperature. The paragenetic sequence and overall mineralogy produced between 900 °C and 800 °C is strikingly similar to that observed for the Nsungwe Formation tuffs and in support of previously estimated P-T conditions implicated in their formation. Titanite is identified as a crucial fractionating phase in lower temperature runs and is the dominant Zr bearing phase above 800 °C. Whereas the Zr-K-silicate mineral wadeite and ZrO<sub>2</sub> baddeleyite accommodate the Zr budget in low temperature ( $\leq 800$  °C) and a single fluorine-rich run (respectively). Trachytic silicate melt compositions were not produced in this experimental series and the generation of such compositions via liquid immiscibility, though apparent in nature, remains experimentally unresolved. We highlight titanite as a key mineral of interest in the future investigation of immiscibility processes in low temperature peralkaline rocks elsewhere in the geological record.

### **4.1 Introduction**

The petrogenesis of the alkali-rich carbonatitic magmas observed in the peralkaline volcanos of the East African Rift have long been a source of intrigue and dispute to the igneous petrology community

---

(Wyllie and Tuttle, 1960; Hamilton et al., 1979; Bell et al., 1998; Mitchell, 2005). An influx of experimental and melt inclusion studies conducted over the past few decades has consolidated the role of both liquid immiscibility (i.e. un-mixing of alkali-carbonatite from a CO<sub>2</sub>-rich peralkaline silicate melt) and crystal fractionation (firstly to achieve liquid immiscibility and secondly drive the carbonatite portion to the extreme alkali-enrichment observed in the lavas of Oldoinyo Lengai) as key processes in their formation (Kjarsgaard and Peterson, 1991; Brooker and Kjarsgaard, 2010; de Moor et al., 2013; Weidendorfer et al., 2017; Baudouin et al., 2018; Guzmics et al., 2019). In light of this work, carbonatites accompanied by geochemical and/or textural evidence of liquid immiscibility are increasingly being recognised in the geological record (oftentimes via the extrusive pyroclastic deposits these systems produce), both within and outside of the East African Rift system (Bailey and Kearns, 2012; Campbell et al., 2012; Lawrence et al., 2020). In parallel, economic interest in carbonatites has also grown significantly given the melts and fluids associated with these systems can be powerful metasomatic agents and produce ore deposits rich in rare earth elements and critical metals (Elliott et al., 2018; Anenburg et al., 2020a).

Recently, Lawrence et al. (Chapter 3, *in review*) proposed a new model for explosive volcanism based on the magma evolution recorded in titanite-hosted silicate glass (formerly melt) inclusions from the 25 Ma Nsungwe Formation ashfall tuffs of the Rukwa Rift basin, southwestern Tanzania. The Nsungwe Formation tuffs preserve a characteristic assemblage of resistant minerals commonly observed in peralkaline-carbonatitic volcanic centres the East African Rift system (i.e. titanite, phlogopite, apatite, Ti-andradite, sanidine, pyrochlore, clinopyroxene, fluorapatite, nepheline, cancrinite, calcite, pyrrhotite, peralkaline silicate glass and Na-REE-carbonates) (Lawrence et al., 2020). The proposed magma evolution sees the formation of peraluminous silica-rich dacitic melt compositions (akin to those observed in arc environments) result from unmixing of an alkali-rich carbonatite melt from a CO<sub>2</sub>-rich phonolitic precursor (liquid immiscibility) and subsequent crystal fractionation at crustal pressures and temperatures (0.5 GPa and <900°C) (Chapter 3, *in review*). Given the highly explosive eruption dynamics associated with volatile-rich silica-saturated magmas, the mechanism proposed for the Nsungwe Formation tuffs has broad implications regarding the volcanic hazard potential of young volcanic provinces in the East African Rift (Manga et al., 1998; Fontijn et al., 2010).

The mineralogy and magma evolution proposed by Lawrence et al. (2020; Chapter 3, *in review*), are not a standalone observation, as similar observations at the Hanang volcano, northern Tanzania (Baudouin et al., 2018). Here alkali-carbonatite melt and silica-saturated compositions (ranging from trachyandesite to trachyte and dacite) form via unmixing from a CO<sub>2</sub>-rich phonolitic parent melt (Baudouin et al., 2018). In this instance however, un-mixing occurs en-route to the surface within silicate melt inclusions hosted in nepheline forming multi-phase immiscible trachyte-carbonatite-vapor inclusions through isobaric cooling (Baudouin et al., 2018). Although these authors recognise this as a purely post-entrapment process in their melt inclusions, carbonatites coexisting with silica-saturated

---

trachytic compositions are reported elsewhere in the EARS (Macdonald et al., 1993; Woolley and Church, 2005), yet mechanisms of this association remain poorly understood.

In order to investigate the formation of peraluminous silica-saturated compositions from evolved CO<sub>2</sub>-rich peralkaline precursors (and more specifically the mineralogy and melt evolution reported by Lawrence et al. (2020a, Chapter 3, *in review*) a series of isobaric immiscibility experiments were undertaken using piston cylinder apparatus at temperature intervals of 1000 °C, 950 °C, 900 °C, 850 °C, 800 °C and 700 °C and a fixed pressure of 0.5 GPa. The P-T conditions selected and starting compositions presented below are consistent with those inferred by Lawrence et al. (2020a; Chapter 3, *in review*) for the Nsungwe Formation tuffs and by others for the alkaline-carbonatite volcanos of the Northern Tanzanian Divergence zone (Kjarsgaard and Peterson, 1991). The isobaric nature of these experiments was adopted based on prior experimental work by Brooker and Kjarsgaard (2012) who demonstrate expansion of the two-liquid solvus (responsible for un-mixing) occurs with reducing temperature at stable pressures. Such conditions are common in the alkaline volcanism of young continental rifts (Kjarsgaard and Peterson, 1991; Kjarsgaard et al., 1995) and are thus most likely to mimic those inferred by the natural observations of Baudouin et al. 2018 and Lawrence et al. Chapter 3, *in review*.

## 4.2 Experimental and analytical methods

### 4.2.1 Starting materials

A single bulk composition (GSR-CNK) was prepared for experimental Runs 1-6 using a 7:3 mixture of the certified reference material GSR-7 natural syenite whole rock powder (see Appendix C1 for GSR-7 sample description and complete major and trace element composition) and a synthetic carbonatite mixture consisting of CaCO<sub>3</sub>, NaHCO<sub>3</sub>, and K<sub>2</sub>CO<sub>3</sub> (CNK) (Table 4.1). Additional fluorine was added to the GSR-CNK in the form of CaF and NaAlF for a single experimental Run-7 (GSR-CNK-F). All synthetic CNK and CNK-F components were mechanically mixed under acetone in an agate mortar and pestle, prior to mixing via the same procedure with the GSR-7 powder. Between 25-30 mg of powdered mixture and 0.5-1 mg of pure graphite were loaded into clean Ag-Pd capsules 6.5mm in length and 3.6mm in diameter. Each capsule was manually fabricated (crimped and arc-welded) and sealed prior to housing within piston-cylinder assemblies depicted in Fig. 4.1.

**Table 4.1** Bulk composition of starting materials in wt. %

	GSR-CNK	GSR-CNK-F
SiO <sub>2</sub>	38.31	38.18
Al <sub>2</sub> O <sub>3</sub>	12.46	12.46
Na <sub>2</sub> O	9.91	9.92
K <sub>2</sub> O	8.22	8.20
CaO	8.03	8.07
FeO	0.87	0.86
Fe <sub>2</sub> O <sub>3</sub>	4.25	4.23
MgO	0.46	0.46
TiO <sub>2</sub>	0.35	0.35
H <sub>2</sub> O	3.09	3.08
CO <sub>2</sub>	14.02	13.97
F	0.03	0.22
SUM	100.00	100.00

#### 4.2.2 Experimental techniques

Experimental runs were performed in an end-loaded piston cylinder apparatus at the Research School of Earth Sciences, Australian National University. All runs consisted of a 5/8" assembly with NaCl and MgO pressure mediums and a thin graphite foil as the heater (Fig. 4.1). Run conditions and duration for each experiment are summarised in Table 4.2. Rapid quenching to room temperature was done by shutting off the power supply to the heater which sees quenching of the experimental charge within ~ 10s. After each experimental run, the capsule was removed from the assembly and mounted in epoxy resin. After hardening, each capsule was manually cut and polished using 800 grit sandpaper and kerosene to expose experimental run products for analysis. Final polishing was conducted using 1200-, 2000-, and 4000-grit sandpaper, followed by 3-, 1-, and 0.25- $\mu$ m diamond paste. The samples were cleaned between polishing steps using hexane and stored in desiccators prior to microanalysis to preserve any reactive phases present.

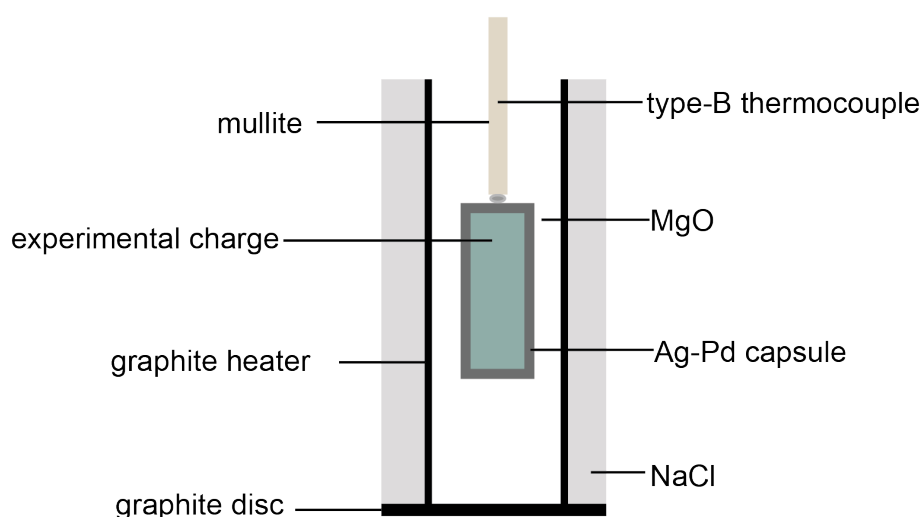


**Fig. 4.1** Schematic cross section of assembly design used in piston cylinder experiments for this study. Capsule dimensions are approximately 7 mm long and 3.6 mm wide

### 4.2.3 Microanalysis

Samples were studied in detail using a SU 5000 Hitachi field-emission gun scanning electron microscope equipped with an Oxford X-MAX Energy-dispersive X-ray spectrometer (EDS) at the Advanced Analytical Centre (AAC), James Cook University (JCU), Townsville, Australia. Textural analysis utilised secondary electron imaging (SEI), backscattered electron imaging (BSE) and EDS compositional element mapping of experimental run products. Mineral, glass and carbonate compositions (spot analysis) and element maps were carried out via EDS with the acceleration voltage set to 15keV.

## 4.3 Results

A summary of run products from each experiment is presented in Table 4.2. Representative compositions for liquid and solid phases for each run (as measured by EDS) presented in Tables 4.3-4.8. Representative back-scattered electron images and element maps for each run are shown in Figures 4.2-4.8. Mineral and quenched liquid compositions from all runs is presented in Appendix C1.

**Table 4.2** Experimental run conditions and products

	<i>P</i> (Gpa)	<i>T</i> (C)	Composition	Time (h)	Phase assemblage
<b>Run 1</b>	0.5	1000	GSR-CNK	19	LS + LC + Nph + Lct
<b>Run 2</b>	0.5	950	GSR-CNK	24	LS + LC + Nph + Lct + Sa + CCGM
<b>Run 3</b>	0.5	900	GSR-CNK	68	LS + LC + Nph + Lct + Sa
<b>Run 4</b>	0.5	850	GSR-CNK	96	LC + Nph + Lct + Sa + Cpx + Ttn + CCGM
<b>Run 5</b>	0.5	800	GSR-CNK	93	LC + Nph + Sa + Cpx + Ttn + Fe-Ti oxide + CCGM
<b>Run 6</b>	0.5	700	GSR-CNK	114	LC + Nph + Sa + Cpx + Ttn + Fe-Ti oxide + CCGM + Wadeite
<b>Run 7</b>	0.5	800	GSR-CNK-F	96	LC + Nph + Sa + Cpx + Fe-Ti oxide + Wadeite + Baddellyite

\*CCGM = cancrinite group minerals

Mineral abbreviations from Whitney and Evans (2010)

### 4.3.1 Run products

Experimental runs 1-3 (1000°C - 900°C) produce similar quenched melt textures and solid phases (feldspathoids and sanidine) albeit with varying liquid/solid proportions. Run 1 at 1000°C produced large spherical alkali-carbonatite globules ranging from 5 to >100 µm within alkali-silicate glass of phonolite composition (Fig. 4.2 A). At one end of the experimental charge of Run 1, this texture is reversed with alkali-silicate glass hosted within an alkali-carbonatite matrix (Fig. 4.2 B). A small number of open vesicles are present in both the silicate and carbonate matrixes, which may reflect excess volatiles or relict carbonate melt plucked/damaged during polishing. Nucleation of patchy-to-rounded leucite (Fig. 4.2) and nepheline crystals ranging from 10-25 µm are observed in the silicate glass whereas the alkali-carbonate quenched liquid is crystal free. Crystals form approximately 15-20% of the total volume, while silicate and alkali-carbonate quenched liquid comprise the remaining 80-85%. At 950°C alkali-carbonate globules ranging from 5-50 µm in diameter hosted in a silicate matrix consisting of subhedral (rounded) leucite and nepheline 5-35 µm, large tabular sanidine crystals up to 50 µm (along the c-axis) and phonolite silicate glass (Fig. 4.3). Alkali-carbonatite quenched liquid at 900°C forms

both small rounded globules and large wormy channels surrounded by silicate glass hosting > 60% subhedral sanidine, leucite and nepheline crystals. Rare cancrinite group minerals are produced in Run 2.

**Table 4.3** Major element composition of silicate glass and quenched carbonate liquids

Phase:	LC	LS	LC	LC-F	LS										
Run:	1	1	2	2	3	3	4	4	5	5	6	6	7	7	7
Starting composition:	GSR-CNK	GSR-CNK-F	GSR-CNK-F	GSR-CNK-F											
<i>P</i> (GPa)	0.5	0.5	0.5	0.5	0.5	0.5	0.5	0.5	0.5	0.5	0.5	0.5	0.5	0.5	0.5
<i>T</i> (°C)	1000	1000	950	950	900	900	850	850	800	800	700	700	800	800	800
<i>n</i>	8	11	8	10	5	7	2		9		9		6	3	
Na <sub>2</sub> O	26.16	8.91	24.81	9.54	19.49	7.51	26.64	-	20.38	-	19.56	-	23.34	17.57	-
MgO	1.05	0.56	1.06	0.75	1.41	0.72	1.31	-	0.42	-	0.35	-	0.45	0.59	-
Al <sub>2</sub> O <sub>3</sub>	0.66	16.85	1.01	16.26	0.68	17.89	0.99	-	2.44	-	4.93	-	1.48	0.70	-
SiO <sub>2</sub>	2.21	53.54	3.71	56.82	1.90	55.89	3.40	-	6.08	-	13.32	-	4.36	1.59	-
Cl	1.19	0.33	0.62	0.29	0.26	0.47	0.01	-	6.08	-	0.08	-	0.00	0.08	-
K <sub>2</sub> O	11.34	8.10	8.08	7.09	9.40	8.03	10.68	-	5.55	-	10.88	-	10.95	4.77	-
CaO	53.84	5.14	58.46	5.21	61.84	3.44	52.33	-	49.60	-	47.69	-	54.47	49.80	-
TiO <sub>2</sub>	n.d	0.71	n.d	0.84	n.d	1.84	n.d	-	n.d	-	-	-	n.d	n.d	-
MnO	0.13	0.09	0.09	0.08	0.52	0.14	n.d	-	0.48	-	0.69	-	0.36	0.23	-
FeO	3.42	6.28	2.17	3.37	4.48	4.14	4.66	-	9.55	-	3.20	-	4.46	3.69	-
Sr	n.d	-	n.d	-	n.d	-	n.d	0.75	-						
F	n.d	-	n.d	-	n.d	-	n.d	20.63	-						
Total	100	100	100	100	100	100	100		100		100		100	100	

\*Values reported are averages of multiple EDS analyses

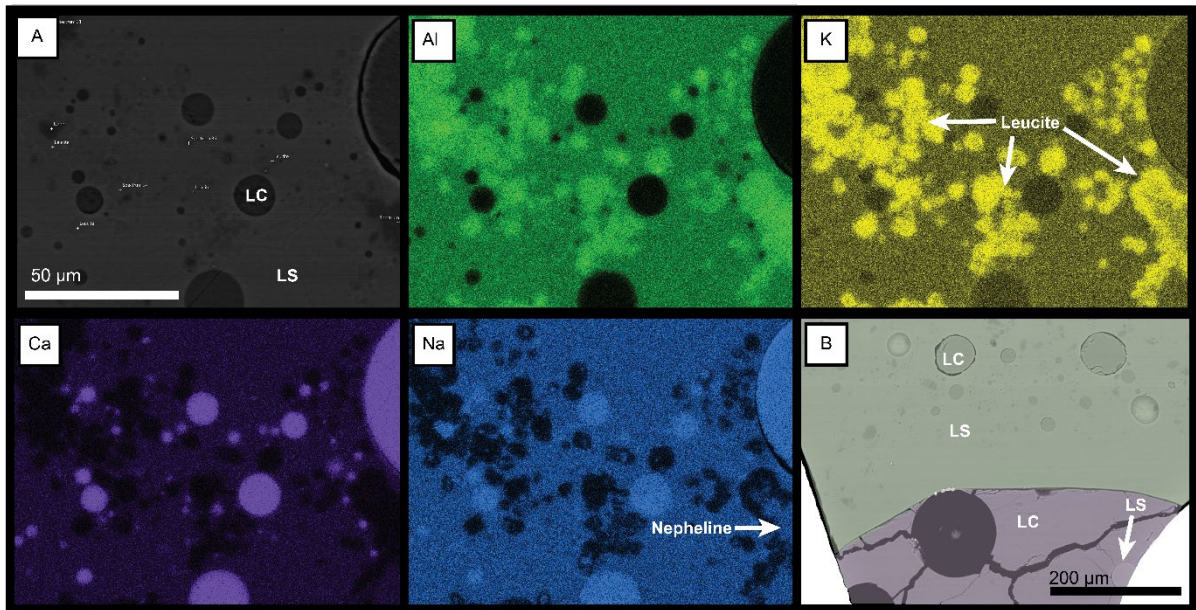


**Fig. 4.2** Run 1 (1000 °C) representative products and element maps : A) BSE image of element map panels Al, K, Ca and Na showing rounded spherules of quenched carbonate liquid (LC) hosted in phonolite silicate glass (LS). Nepheline and leucite are observed as patchy brighter Na and K zones correlative with Al (respectively). B) SEI image of Run 1 showing both quenched immiscible carbonate liquid hosted in phonolite silicate glass (green shaded area) and immiscible silicate glass hosted in carbonate liquid (purple shaded area; n.b. rounded immiscible silicate glass above the center of the scale bar).

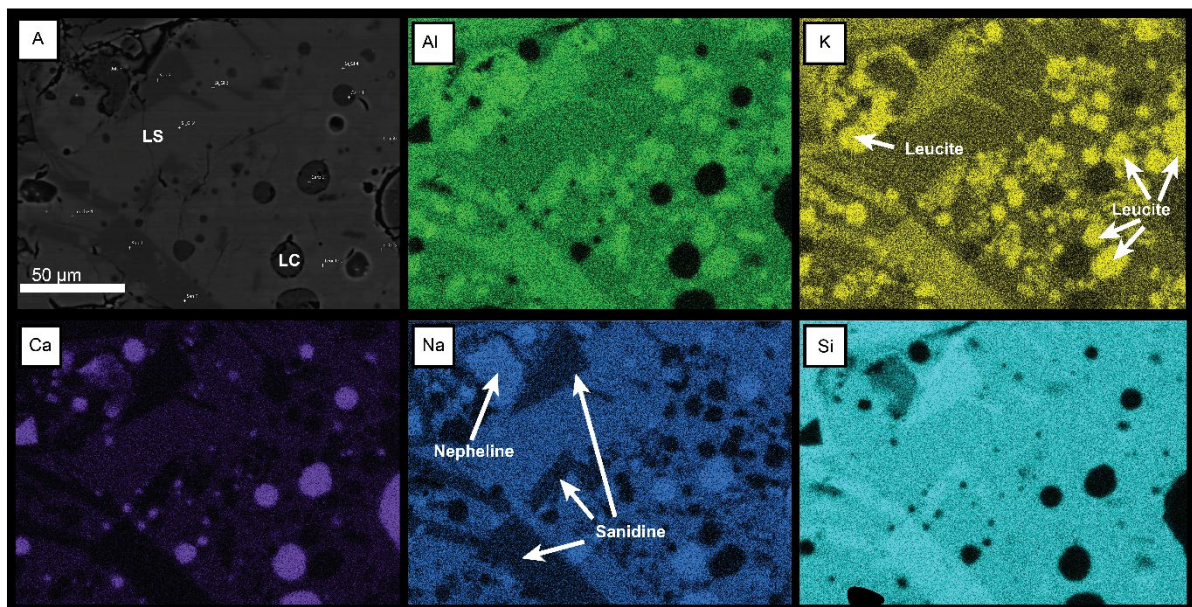


**Fig. 4.3** Run 2 (950 °C) representative products and element maps: A) BSE image of element map panels Al, K, Ca, Na and Si showing rounded- sub-rounded spherules of quenched carbonate liquid (LC) hosted in phonolite silicate glass (LS). Nepheline (high Na, low K and Si) and leucite (high K low Na) are observed as brighter Na and K zones correlative with Al. Euhedral sanidine register darker zones in Na with angular crystal borders correlative with brighter zones in Si and Al.

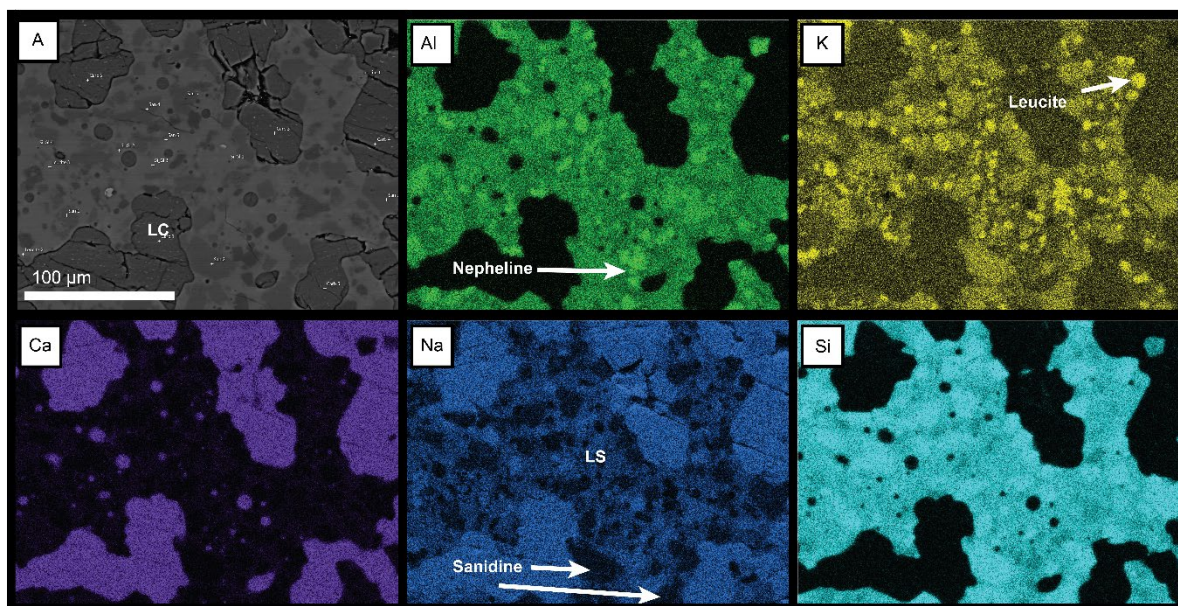


**Fig. 4.4** Run 3 (900 °C) representative products and element maps: A) BSE image of element map panels Al, K, Ca, Na and Si showing large wormy channels of quenched carbonate liquid (CL) hosted in fine phonolite network of silicate glass (LS) and crystals. Nepheline (high Na, Al and low K) and leucite (high K low Na) are observed as patchy brighter Na and K zones correlative with Al. Sanidine register darker zones in Na with sub-hederal crystal borders correlative with brighter zones in Si.

Runs 4-6 spanning 850°C – 700 °C see a significant reduction in both silicate and alkali-carbonatite liquids in favour of a diverse silicate crystal-rich mush hosted within interstitial alkali-carbonate quench. Runs 4 and 5 (850°C and 800°C) are dominated by large (>50 µm) blocky sanidine and smaller needle-like sanidine laths, as well as subhederal nepheline with leucite overgrowths. Euhedral titanite, 30-50 µm in size and subhederal clinopyroxene form high contrast phases in backscattered electron images (Fig. 4.5). Notably, small clinopyroxene inclusions form within sanidine, and elsewhere anhedral clinopyroxene is present interstitially between other silicate crystal phases. Alkali-carbonate remains present as an interstitial quenched liquid observed in areas of low relief in-between solid silicate phases. Alkali-silicate glass is rarely found as narrow (<5 µm) worm-like pools between silicate crystals, which renders both identification and analyses dubious. Cancrinite group minerals and Fe-Ti oxides form minor phases at, and below 850°C, and 800°C (respectively). At 700°C, run products consist of euhedral to subhederal sanidine, nepheline, clinopyroxene, titanite, Fe-Ti oxide Zr-rich phases (i.e. wadeite) (Fig. 4.7).

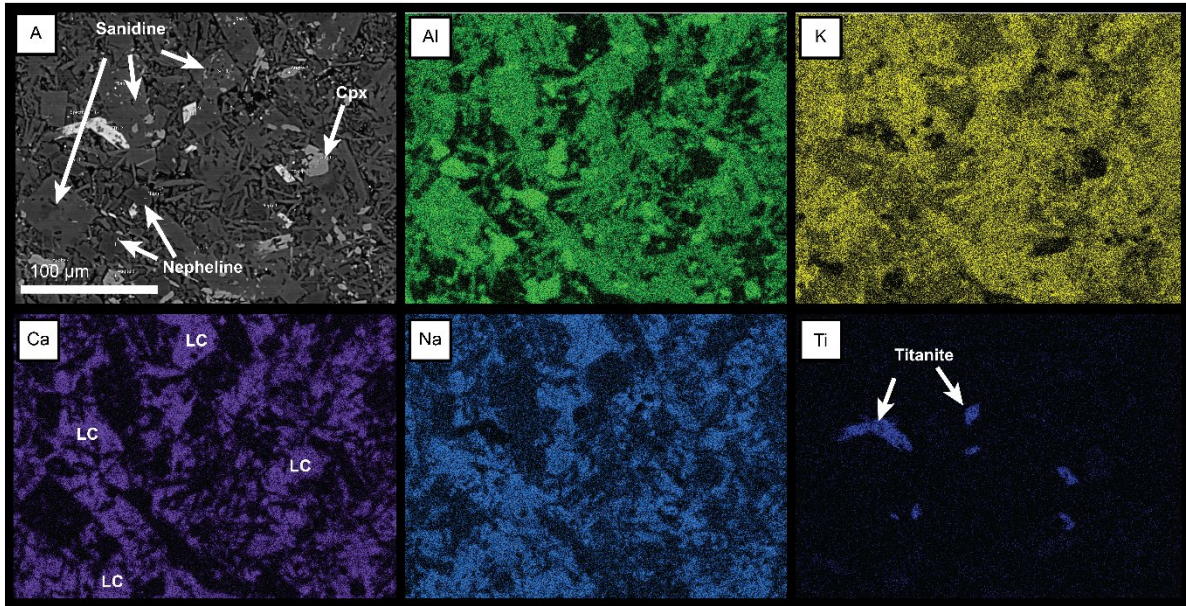


**Fig. 4.5** Run 4 (850 °C) representative products and element maps: A) BSE image of element map panels Al, K, Ca, Na and Ti showing large euhedral blocky/tabular sanidine and smaller need-like sanidine, titanite and clinopyroxene in a quenched skeletal carbonate matrix (brighter zone in panel Na and Ca). Titanite are observed as bright grey crystals in panel A correlative with bright areas in panel Ti. Clinopyroxene appear as medium-grey sub-hederal crystals in panel A correlative with dark regions in panels Al and K.

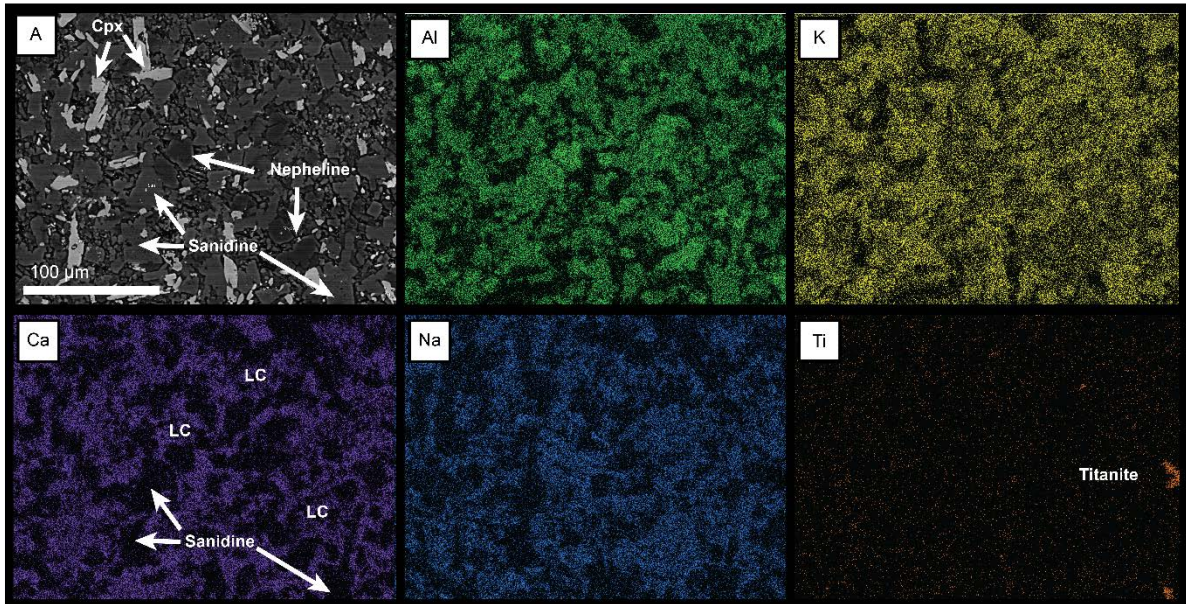


**Fig. 4.6** Run 5 (800 °C) representative products and element maps: A) BSE image of element map panels Al, K, Ca, Na and Ti showing large euhedral to sub-hederal clinopyroxene (light-grey), sub-hederal nepheline (very dark-grey correlative with brightest zones in panel Al) and sanidine (dark grey) crystals in a quenched interstitial alkali-carbonate matrix. Small titanite crystals are shown in panel Ti and correlate with very bright zones in panel A.

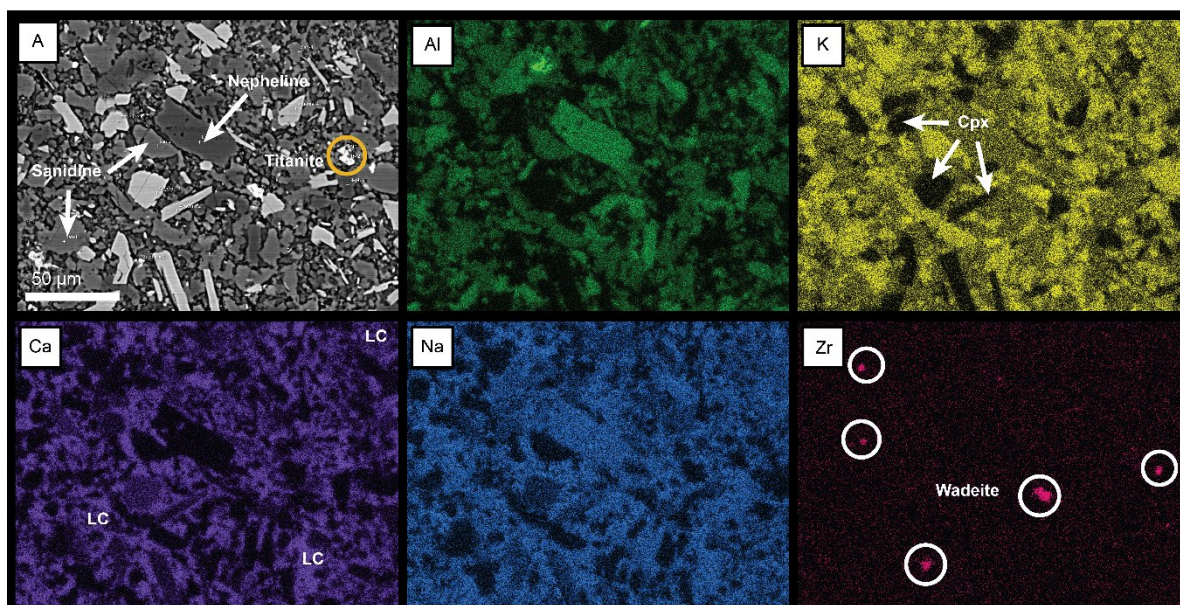


**Fig. 4.7** Run 6 (700 °C) representative products and element maps: A) BSE image of element map panels Al, K, Ca, Na and Ti showing euhedral clinopyroxene (light-grey), nepheline (very dark-grey correlative with brightest zones in panel Al) and sanidine (medium grey correlative with bright zones in panel K) crystals in a quenched interstitial alkali-carbonate matrix. Small wadeite crystals are shown in panel Zr and appear extremely bright in panel A. Titanite is also observed as extremely bright, diamond-shaped euhedral crystals in panel A not seen in panel Zr.

Experimental products from the GSR-CNK-F starting composition at 800°C are dramatically different in texture from those observed for the GSR-CNK experiments (Fig. 4.8). Alkali-carbonate forms characteristic high-low contrast skeletal quench textures. Brighter high-contrast regions are correlated with higher fluorine and chlorine contents as measured via EDS. Silicate crystal phases have well-formed crystal habits (i.e. 20-40 μm tabular sanidine, and < 20μm euhedral baddeleyite, ilmenite and clinopyroxene) and are overall less needle-like than the low fluorine runs. Solid phases present include liquid alkali-carbonate (high and low Cl/F) quenched liquid, nepheline, sanidine, Fe-Ti oxide, clinopyroxene, wadeite and baddeleyite. Silicate glass was not identified in the products of this experiment.

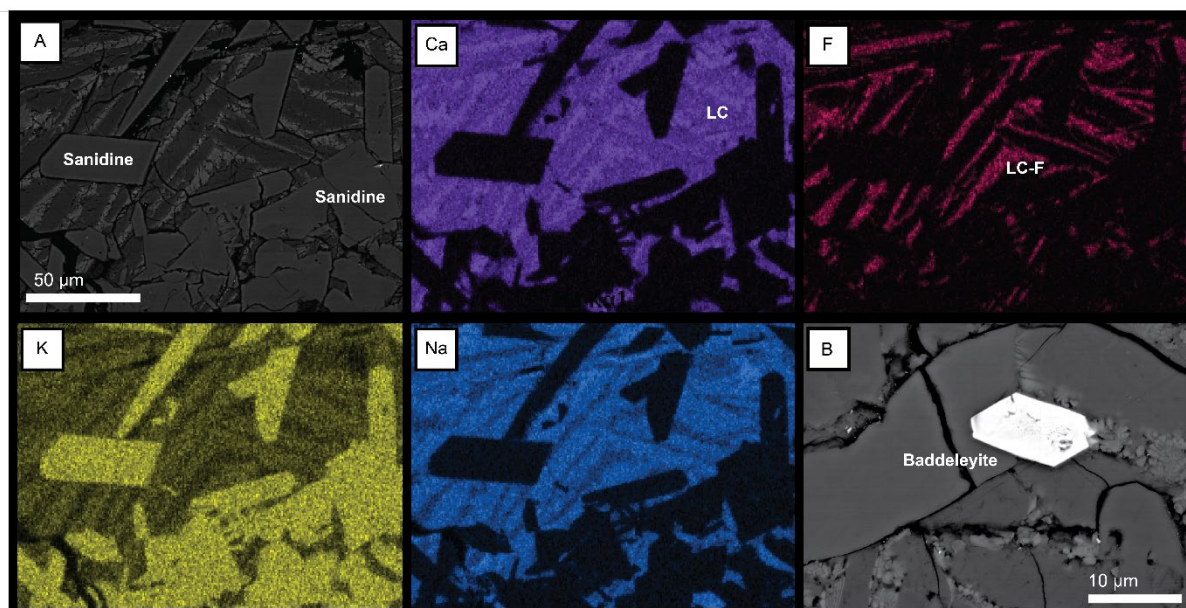


**Fig. 4.8** Run 7 (800 °C; GSR-CNK-F) representative products and element maps: A) BSE image of element map panels Ca, F, K and Na showing euhedral sanidine crystals (correlative with brightest zones in panel K) in a skeletal textured, multi-phase, quenched alkali-carbonate liquid(s) (LC and LC-F). Lighter quench zone in panel A correspond to high fluorine contents shown in panel F. Representative small euhedral baddeleyite crystal shown in panel B. Other phases mentioned in text not shown here (i.e. nepheline, ilmenite wadeite and clinopyroxene) see supplementary materials.

### 4.3.2 Liquid compositions

Semi-quantitative analyses (as sample averages) for silicate glass and conjugate carbonate quenched liquid generated in this study are listed in Table 4.3 and presented in Fig. 4.10. Silicate liquid measured from Runs 1-3 (1000-900°C) is phonolitic in composition (Table 4.3). In general, with reducing temperature glass FeO, CaO, Na<sub>2</sub>O contents decrease, whereas K<sub>2</sub>O remains constant and Al<sub>2</sub>O<sub>3</sub>, TiO<sub>2</sub> and SiO<sub>2</sub> contents increase. The exsolved conjugate carbonate liquids measured in Runs 1-3 are rich in alkalis (Na<sub>2</sub>O + K<sub>2</sub>O = 26 - 39 wt%) and see a decrease in Na<sub>2</sub>O, K<sub>2</sub>O and increase in FeO, MnO and MgO relative to CaO with reducing temperatures (Fig. 4.10). Silica contents are notably variable in the carbonate liquids ranging from 1.0 – 4.6 wt.%. Below 900°C analyses of what may be silicate liquid is problematic and unreliable given the size and dimensions (i.e. narrow wormy glass pools, as described above). Interstitial carbonate liquid quench persists at temperatures below 900°C evidenced by element mapping and textural analysis; however, semi-quantitative analyses of interstitial carbonate quench is compromised by interference with surrounding silicate mineral phases. As a result, a negative correlation is observed between SiO<sub>2</sub> and CaO contents (and an increased variability with respect to other element oxides) in the carbonates analysed in lower temperature runs. For the purposes of clarity, the composition of silicate and carbonate liquids from Runs 1-3 will be later discussed as conjugate liquids; in lower temperature runs liquids will discussed as either present or absent.

### 4.3.3 Solid phase compositions

The semi-quantitative analyses (as sample averages) for experimental solid phases are presented in Tables 4.4-4.9. Leucite ( $\text{KAlSi}_2\text{O}_6$ ) produced in Runs 1-4 (1000 – 850°C) is of similar composition with 54.5 – 55.2 wt.%  $\text{SiO}_2$ , 18.3 – 19.6 wt.%  $\text{K}_2\text{O}$ , 21.3 – 23.7 wt.%  $\text{Al}_2\text{O}_3$  and minor amounts of FeO (0.5-2.4 wt.%) and  $\text{Na}_2\text{O}$  (1.2 – 2.0 wt.%). With the exception of Run 2 (950°C), experimental nepheline ( $[\text{Na},\text{K}]\text{AlSiO}_4$ ) are also compositionally consistent with average  $\text{SiO}_2$  and  $\text{Al}_2\text{O}_3$  of 42.0 – 43.4 wt.% and 32.2 – 34.6 wt.% respectively across all temperatures (1000-700°C) and compositions (GSR-CNK and GSR-CNK-F). The  $\text{Na}_2\text{O}$  (14.2 – 15.9 wt.%) and  $\text{K}_2\text{O}$  (6.2 – 7.7 wt.%) contents of nepheline are inversely related, with generally higher  $\text{Na}_2\text{O}$  (and lower  $\text{K}_2\text{O}$ ) contents are found in lower temperature experiments. The two nepheline analyses of Run 2 (950°C) are markedly different with respect to all oxides measured, which may reflect interference of surrounding silicate glass or feldspar (i.e. higher  $\text{SiO}_2$  and  $\text{K}_2\text{O}$  and lower  $\text{Na}_2\text{O}$  and  $\text{Al}_2\text{O}_3$ ). Given the scarcity of analyses, the nepheline compositions from Run 2 will be omitted from further interpretation. Like leucite compositions, minor amounts of FeO is present in all nepheline analyses (ranging from 0.4 – 2.2 wt.%), although there is notably high variability in FeO contents of nepheline within each experiment, which in some cases may reflect interference; however, small amounts of FeO are inferred to be present in these crystals.

**Table 4.4** Average leucite compositions

Run	Av. Leucite (n = 8)	Av. Leucite (n = 13)	Av. Leucite (n = 7)	Leucite n = 1
<i>P</i> (Gpa)	0.5	0.5	0.5	0.5
<i>T</i> (°C)	<b>1000</b>	<b>950</b>	<b>900</b>	<b>850</b>
$\text{Na}_2\text{O}$	2.08	1.27	2.04	1.74
$\text{MgO}$	0.16	0.15	0.21	0.20
$\text{Al}_2\text{O}_3$	22.70	23.71	23.32	21.36
$\text{SiO}_2$	54.49	54.62	54.60	55.20
$\text{K}_2\text{O}$	18.28	19.64	19.48	19.06
$\text{CaO}$	0.24	n.d.	n.d.	n.d.
$\text{MnO}$	0.03	0.02	0.01	n.d.
$\text{FeO}$	1.72	0.59	0.90	2.44
Total	99.17	99.51	99.98	100.00

**Table 4.5** Average nepheline compositions

Run	Av. Neph (n = 6)	Av. Neph (n = 2)	Av. Neph (n = 11)	Av. Neph (n = 6)	Av. Neph (n = 5)	Av. Neph (n = 5)	Av. Neph (n = 8)
<i>P</i> (Gpa)	0.5	0.5	0.5	0.5	0.5	0.5	0.5
<i>T</i> (°C)	<b>1000</b>	<b>950</b>	<b>900</b>	<b>850</b>	<b>800</b>	<b>700</b>	<b>800</b>
$\text{Na}_2\text{O}$	14.24	11.22	15.47	15.92	14.67	15.17	15.59
$\text{MgO}$	0.05	0.05	0.11	0.17		0.11	0.09
$\text{Al}_2\text{O}_3$	33.52	29.92	34.45	34.62	32.85	33.14	32.26
$\text{SiO}_2$	42.87	48.80	42.81	42.01	43.39	42.81	43.36
$\text{Cl}$	0.00	n.d.	n.d.	n.d.	n.d.	n.d.	n.d.
$\text{K}_2\text{O}$	7.72	9.70	6.21	6.50	7.29	7.15	6.43
$\text{CaO}$	0.57	n.d.	0.52	0.91	0.97	1.01	n.d.
$\text{MnO}$	0.04	0.01	0.01	n.d.	n.d.	n.d.	n.d.
$\text{FeO}$	1.31	0.33	0.42	1.20	1.60	1.10	2.26
Total	100.32	100.01	100.00	101.34	100.77	100.49	99.98

Sanidine ( $[\text{K},\text{Na}][\text{SiAl}]_4\text{O}_8$ ) compositions show a reduction in  $\text{SiO}_2$  (64.6 wt.% to 59.6 wt.%) contents, increase in  $\text{K}_2\text{O}$  (12.2 wt.% to 14.7 wt.%) contents and relatively stable  $\text{Al}_2\text{O}_3$  (19.4 wt.% to 20.4 wt.%) with decreasing temperature (i.e. from 950°C to 800°C). Overall a minor reduction in  $\text{Na}_2\text{O}$  (3.6 wt.% to 2.2 wt.%) contents is observed from 850 to 700°C with limited amounts of MnO and FeO also present at lower temperatures (i.e. <850°C). CaO contents are low (<<0.8 wt%) in all runs.

**Table 4.6** Average sanidine compositions

Run	Av. Sanidine (n = 6)	Av. Sanidine (n = 10)	Av. Sanidine (n = 6)	Av. Sanidine (n = 4)	Av. Sanidine (n = 7)	Av. Sanidine (n = 7)
Run	<b>2</b>	<b>3</b>	<b>4</b>	<b>5</b>	<b>6</b>	<b>7</b>
<i>P</i> (Gpa)	0.5	0.5	0.5	0.5	0.5	0.5
<i>T</i> (°C)	<b>950</b>	<b>900</b>	<b>850</b>	<b>800</b>	<b>700</b>	<b>800</b>
Na <sub>2</sub> O	3.22	3.48	3.63	2.98	2.28	2.43
MgO	0.05	0.09	0.11	0.07	0.08	0.10
Al <sub>2</sub> O <sub>3</sub>	19.48	19.19	18.98	20.41	18.83	18.99
SiO <sub>2</sub>	64.68	63.52	61.77	59.65	62.49	63.00
Cl	0.00	0.00	0.00	0.00	0.00	0.00
K <sub>2</sub> O	12.20	11.63	12.55	14.76	14.43	13.06
CaO	n.d.	0.15	n.d.	0.82	n.d.	0.05
MnO	0.04	0.00	2.20	0.32	1.77	1.69
FeO	0.32	0.57	1.90	1.41	2.09	0.80
Total	99.98	98.61	99.99	99.98	100.00	99.17

Clinopyroxene from Runs 4-6 (850-700 °C) have consistent  $\text{Al}_2\text{O}_3$  contents of between 3.2 and 2.8 wt.% whereas a slight increase in  $\text{SiO}_2$  contented is observed with reducing temperature (49.7 wt.% to 53.3 wt.%) from 850 °C to 700 °C. The most dramatic shift in composition from 850 °C to 700°C occurs via a steep reduction in CaO and Mg contents (from 17.0 wt.% to 6.4 wt% and 4.4 to 2.1 wt.% respectively) and sharp increase in FeO and Na<sub>2</sub>O contents (from 19.0 wt.% to 22.6 wt%; and 4.9 to 10.8 wt.% respectively). In this sense, clinopyroxene compositions see an increase in aegirine and Fe-essentite components and a reduction in diopside and wollastonite components with reducing temperature. Little variance is observed with respect to the F-bearing (Run-7) versus F-absent (Run-5) experiments at 800 °C; however, the highest FeO clinopyroxenes are produced in F-bearing Run-7.

**Table 4.7** Average titanite and clinopyroxene compositions

Run	Av. TTN (n=5)	Av. TTN (n=2)	Av. TTN (n=3)	Av. Cpx (n = 8)	Av. Cpx (n = 4)	Av. Cpx (n = 8)	Av. Cpx (n = 6)
Run	<b>4</b>	<b>5</b>	<b>6</b>	<b>4</b>	<b>5</b>	<b>6</b>	<b>7</b>
<i>P</i> (Gpa)	0.5	0.5	0.5	0.5	0.5	0.5	0.5
<i>T</i> (°C)	<b>850</b>	<b>800</b>	<b>700</b>	<b>850</b>	<b>800</b>	<b>700</b>	<b>800</b>
Na <sub>2</sub> O	1.11	2.06	3.00	4.96	5.43	10.82	6.22
MgO	0.05		0.01	4.39	2.72	2.13	3.56
Al <sub>2</sub> O <sub>3</sub>	1.69	2.91	2.69	3.26	2.80	2.81	2.29
SiO <sub>2</sub>	30.26	32.84	32.08	49.78	50.04	53.37	48.69
K <sub>2</sub> O	1.31	1.02	0.66	1.22	0.82	3.85	0.26
CaO	24.34	25.04	25.04	16.99	16.03	6.41	14.23
TiO <sub>2</sub>	24.72	32.35	33.15	0.30		0.61	
MnO	0.88	0.09		0.10		0.27	0.32
FeO	0.88	1.29	1.24	19.02	22.17	22.64	24.42
ZrO <sub>2</sub>	15.50	2.43	1.19				
Total	100.74	100.00	99.06	100.00	100.00	102.91	99.96

Titanites from Runs 4-6 (850-700°C) show a systematic shift in composition with SiO<sub>2</sub>, TiO<sub>2</sub> and Al<sub>2</sub>O<sub>3</sub> contents increasing from 30.2 wt.% to 32.0 wt.%; 24.7 to 33.1 wt.%; and 1.6 to 2.7 wt.% (respectively). A sharp reduction in the ZrO<sub>2</sub> content of titanite (from 15.5 wt.% to 1.1 wt.%) occurs between Runs 5 and 6 (i.e. 850°C to 800°C). The CaO contents of titanite remain stable between 24.3 – 25.0 wt. % across Runs 4-6. At 800°C the Zr-rich phase wadeite (K<sub>2</sub>ZrSi<sub>3</sub>O<sub>9</sub>) forms from the GSR-CNK-F composition of Run-7 and contains 31.4 wt.% ZrO<sub>2</sub>, 20.6 wt.% K<sub>2</sub>O and 45.2 wt% SiO<sub>2</sub> with minor amounts of Na<sub>2</sub>O (1.86 wt.%). Baddeleyite (ZrO<sub>2</sub>) is also produced from the fluorine-rich composition in Run-7. Wadeite is produced at 700°C from the GSR-CNK starting composition (Run-6); however, measured K<sub>2</sub>O and ZrO<sub>2</sub> contents are lower in favour of higher SiO<sub>2</sub> and minor contributions of Na<sub>2</sub>O, Al<sub>2</sub>O<sub>3</sub>, CaO and FeO compared to those produced from the fluorine rich composition of Run-7 (Table 4.8).

**Table 4.8** Representative analyses of Zr-rich phases

Run	Wadeite 6	Wadeite 6	Wadeite 6	Wadeite 7	Baddelyite 7	Baddelyite 7	Baddelyite 7
<i>P</i> (Gpa)	0.5	0.5	0.5	0.5	0.5	0.5	0.5
<i>T</i> (°C)	<b>700</b>	<b>700</b>	<b>700</b>	<b>800</b>	<b>800</b>	<b>800</b>	<b>800</b>
Na <sub>2</sub> O	3.38	3.47	7.15	1.86	0.54	0.4	2.06
MgO	1.24	0.05		0.08	0.11	0.06	0.25
Al <sub>2</sub> O <sub>3</sub>	1.87	1.68	3.24	0.39	0.3	0.35	0.14
SiO <sub>2</sub>	47.04	42.03	41.08	45.28	n.d.	n.d.	0.6
P <sub>2</sub> O <sub>5</sub>	n.d.	n.d.	n.d.	n.d.	6.77	6.83	0
K <sub>2</sub> O	16.48	17.04	18.6	20.67	0.3	0.17	0.58
CaO	2.45	1.58	6.36	0.05	0.37	n.d.	1.94
TiO <sub>2</sub>	n.d.	n.d.	n.d.	n.d.	2.76	7.54	2.96
FeO	4.78	0.81	1.32	0.29	0.98	1.44	1.48
ZrO <sub>2</sub>	22.75	26.51	22.25	31.37	86.51	80.25	87.03
BaO	n.d.	n.d.	n.d.	n.d.	1.32	2.86	n.d.
HfO <sub>2</sub>	n.d.	n.d.	n.d.	n.d.	n.d.	n.d.	1.66
Total	99.98	99.95	100	100	99.96	99.91	98.71

**n.b.** the P<sub>2</sub>O<sub>5</sub> contents shown in Baddelyite likely an artifact of overlapping Zr and P peaks in EDS spectra.

Runs 5-7 (800°C -700°C) contain Fe-oxides with 80-90 wt% FeO with minor (6-20 wt.%) TiO<sub>2</sub> are produced. A single ilmenite Fe-Ti oxide (49 wt% TiO<sub>2</sub>; 47 wt.% FeO) was identified in Run-7. In runs 2 and 4,5 and 6, what appear to be cancrinite group minerals are produced. However, given the limitations of EDS analyses (inability to account for volatile species) it is difficult to discern which variant of this mineral group is likely present. Representative analyses of what are referred to hereafter as cancrinite-group minerals are shown in Table 4.9.

**Table 4.9** Representative analyses of cancrinite group minerals

Run	2	4	5	6
<i>P</i> (Gpa)	0.5	0.5	0.5	0.5
<i>T</i> (°C)	<b>950</b>	<b>850</b>	<b>800</b>	<b>700</b>
Na <sub>2</sub> O	16.49	15.54	9.02	8.27
MgO	0.1	0.38	0.26	0.16
Al <sub>2</sub> O <sub>3</sub>	32.3	29.98	20.35	22.54
SiO <sub>2</sub>	36.64	43.45	44.02	46.56
K <sub>2</sub> O	7.09	6.22	14.01	15.29
CaO	6.79	2.06	8.79	5.25
FeO	0.48	2.37	3.55	1.94
Total	99.89	100	100	100

#### 4.4 Discussion

Polythermal, isobaric experiments are considered a useful methodological approach in determining the crystallisation sequence and position/topology of the two-liquid solvus governing liquid immiscibility within subvolcanic-volcanic CO<sub>2</sub>-rich peralkaline magmatic systems (Kjarsgaard and Peterson, 1991; Kjarsgaard et al., 1995; Brooker and Kjarsgaard, 2010). This is largely because the geological conditions often encountered in nature facilitate near-isobaric cooling (following magma recharge/emplacement) prior to either: (1) magma migration to shallower reservoirs (2) eruption or (3) solidification in the crust. Hence, this experimental design may provide critical insights into melt evolution of conjugate silicate-carbonate liquid pairs (and potentially effusive vs explosive volcanic regimes) that results from crystal fractionation and mimic liquid immiscibility in natural systems. In the case presented here, we are able to describe a paragenetic sequence for a hydrous, CO<sub>2</sub>-saturated nephelinite-phonolite melt subjected to cooling at a fixed pressure of 0.5 GPa, which corresponds to mid-crustal conditions of the more ancient terrains of the EARS (Fadaie and Ranalli, 1990). Such conditions and processes are thought to be relevant to the formation of the Nsungwe Formation tuffs of the early Rukwa Rift, as well as other alkali-carbonatite volcanic systems during the incipient stages of continental rift development (Kjarsgaard and Peterson, 1991; Kjarsgaard et al., 1995; Baudouin et al., 2016; Baudouin et al., 2018; Lawrence et al., 2020).

##### 4.4.1 Crystallisation sequence for experimental CO<sub>2</sub> saturated nephelinite-phonolite GSR-CNK

The paragenetic crystallisation sequence recorded for the GSR-CNK composition is shown in Table 4.2 and the T-X diagram of Fig. 4.9. At 1000°C leucite and nepheline crystallise from a phonolite silicate melt in equilibrium with alkali-carbonatite. Sanidine and cancrinite group minerals join the assemblage at 950°C and 900°C. Below 900°C liquid silicate is insignificant (not easily identified) in favour of a crystal mush consisting of leucite, nepheline, sanidine, cancrinite, clinopyroxene and Zr-rich titanite with interstitial alkali-carbonate liquid. At 800°C Fe-Ti oxides form, titanite contains



with previous experiments and an expansion of the two-liquid solvus. The phonolite composition of the silicate liquid becomes progressively enriched in  $\text{SiO}_2$ ,  $\text{Al}_2\text{O}_3$  and  $\text{TiO}_2$  relative to  $\text{CaO}$ ,  $\text{FeO}$ ,  $\text{MgO}$  and  $\text{MnO}$ ; and  $\text{Na}_2\text{O}$  and  $\text{K}_2\text{O}$ . The alkali-carbonate liquid also sees a minor reduction in  $\text{Na}_2\text{O}$  and  $\text{K}_2\text{O}$  and increase in  $\text{CaO}$ ,  $\text{FeO}$ ,  $\text{MgO}$  and  $\text{MnO}$  with reducing temperature.

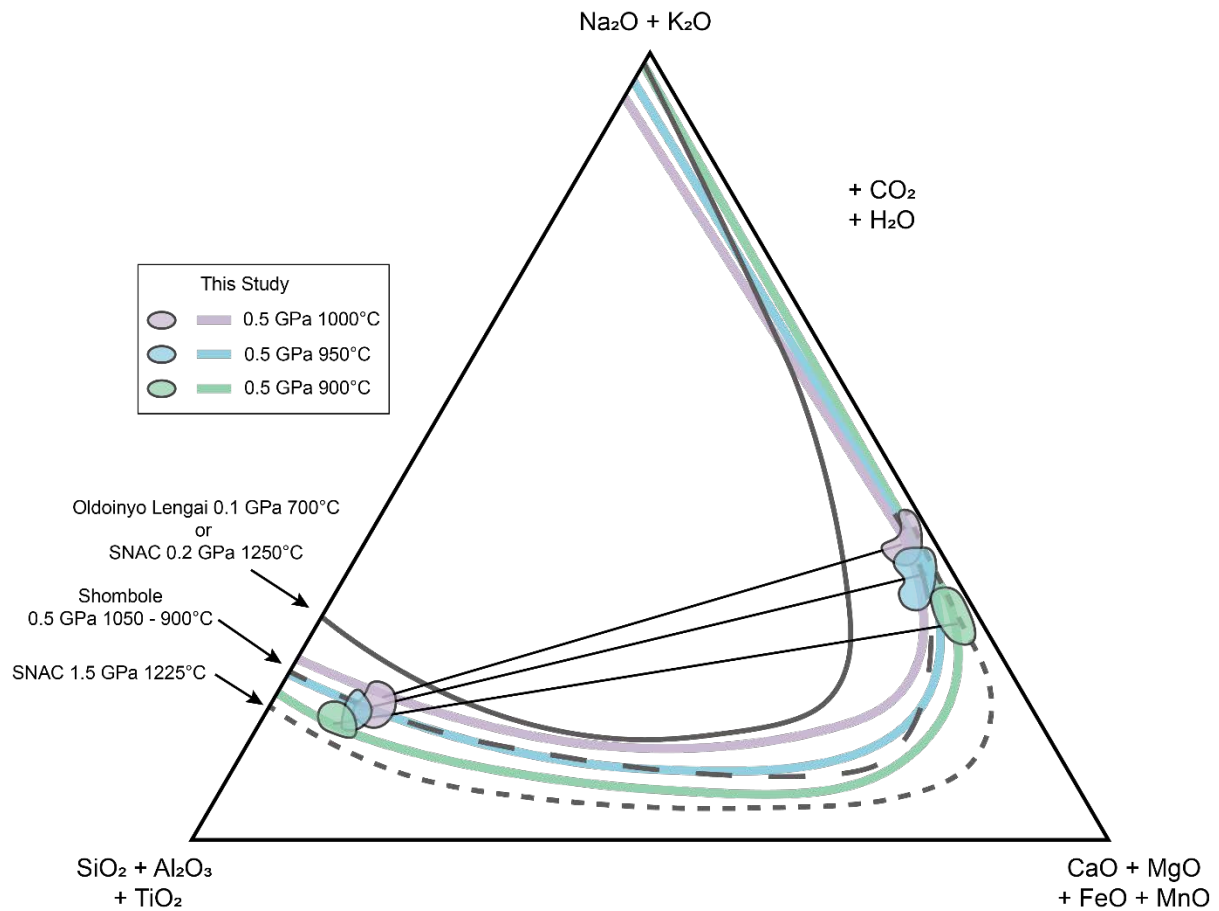


**Fig. 4.10** Hamilton projection of the experimentally derived silicate-carbonate conjugate liquid pairs onto the adapted Hamilton diagram of Brooker and Kjarsgaard (2010). Purple, blue and green fields and solvi correspond to 1000°C, 950°C and 900°C experiments (respectively). The shape of projected solvi follow previously defined topologies. Experimentally derived two-liquid solvi (solid and dashed grey lines) are shown for Oldoinyo Lengai (Kjarsgaard et al., 1995), Shombole (Kjarsgaard and Peterson, 1991) and the SNAC experimental system (Brooker and Kjarsgaard, 2010).

An important consideration in the series of experiments presented in this study is the appreciable  $\text{H}_2\text{O}$  contents of the GSR-CNK starting composition (3.09 wt.%). Martin et al. (2013) made the first order observation that the addition of  $\text{H}_2\text{O}$  in immiscible peralkaline silicate-carbonate systems acts to widen the miscibility gap, which sees the silicate melt become more enriched in network forming elements  $\text{SiO}_2$  and  $\text{Al}_2\text{O}_3$  and poorer in the network modifiers  $\text{CaO}$ ,  $\text{FeO}$  and  $\text{MgO}$  (i.e. greater degree of melt polymerisation) than is otherwise typical of immiscible anhydrous systems. This effect may in

part be responsible for the apparent wider solvus observed in in this study compared to solvi experimentally derived by Kjarsgaard and Peterson (1991) for Shombole using similar compositions and run conditions, and for Oldoinyo Lengai (albeit at lower P-T conditions) (Kjarsgaard et al., 1995) (Fig. 4.10). Additionally, a widening of the solvus significantly effects the partitioning behaviour of both major and trace elements between conjugate silicate-carbonate melt pairs. A relevant finding of the partitioning experiments of Martin et al. (2013) is that the partitioning behaviour of  $K_2O$  shifts from strongly favouring the carbonate liquid to favouring the silicate liquid in the presence of  $H_2O$  and with increased polymerisation of the silicate melt (i.e. increase in  $SiO_2$  and  $Al_2O_3$ ; widening of the miscibility gap). Evidence of such partitioning behaviour may be inferred via the abundance and dominance of K-rich alumina-silicate phases in the run products and the formation of exotic Zr-K-rich phases in lower temperature runs. Such observations are suggestive of abundant  $K_2O$  in a highly polymerised, hydrous, silicate-melt system.

The reduction in alkalis observed in the carbonate liquids with reducing temperature is a curious one. Undoubtedly the reduced partitioning of  $K_2O$  in the carbonatite melt will partially contribute, however it does not fully account for the simultaneous apparent reduction in  $Na_2O$  content. Given the aforementioned influence of  $H_2O$  and lack of hydrous mineral phases produced in these experiments (e.g. mica and amphibole; minor cancrinite group minerals notwithstanding) we may consider that an accumulation of water in the experimental system was also a by-product of combined cooling and fractionation. As with any other magmatic environment,  $H_2O$  may exist as a standalone volatile/aqueous phase (capable of sequestering alkalis and/or other element ions), partition into the silicate melt and/or partition into the carbonatite melt depending on degree of saturation (solubility/partial pressure) in the system. Although textural evidence of an aqueous fluid phase (i.e. vugs/vesicles) is limited, the low-relief and interstitial nature of the carbonate liquid in lower temperature runs may reflect the presence of a fluid/fluid condensate rather than purely be a polishing phenomenon of the alkali-carbonate. To the extent an aqueous phase may be present as a run product (as reported in similar experiments i.e. Anenburg et al. (2020b)), the sequestration of some alkalis (as well as some halogens and excess carbonate) away from both silicate and carbonate liquids remains a possibility. The inference and influence of an aqueous residua is in agreement with observed natural systems, given the alkali-enriched fenitising fluids associated with syenite and carbonatite intrusive bodies (Elliott et al., 2018) and alkali-fluid-condensates reported from inclusion studies (Bühn and Rankin, 1999; Guzmics et al., 2019; Lawrence et al., 2020).

A noticeable feature of the carbonate liquids produced in this study (and possible explanation for why extreme alkali-carbonate liquids i.e.  $Na_2O+K_2O > 50\%$  are not produced) is the scant evidence indicating that fractionation of the carbonate liquid occurred post-immiscibility. Weidendorfer et al. (2017) demonstrated that the subsequent fractionation of alkali-free phases (namely calcite and apatite) from a moderately alkali-rich carbonatite liquids crucially acts to increase the alkali-content of the

carbonatite liquid towards the archetypal natro-carbonatite magmas of Oldoinyo Lengai. Contrary to the long-running narrative that Oldoinyo Lengai is a predominantly anhydrous system, de Moor et al. (2013) revealed extremely high water contents (up to 10 wt% H<sub>2</sub>O) in silicate melt inclusions from the volcanic centre. Consistent with first order partitioning behaviour observed by Martin et al. (2013) (also apparent in this study), the presence of H<sub>2</sub>O at the time of unmixing appears to contribute to the dominance of Na<sub>2</sub>O (over K<sub>2</sub>O) in the carbonatite melt, that may later become amplified with calcite (and/or apatite) fractionation to form the iconic natro-carbonatite produced in nature and absent in this study.

#### 4.4.3 Comparisons with natural peralkaline-carbonatite immiscible systems

Based on the characteristic mineral assemblage present, the unusual melt evolution recorded in glass inclusions trapped within titanite crystals, and the volatile contents of trapped silicate glass; Lawrence et al., (Chapter 3, *in-review*) proposed a carbonatite association and inferred mid-crustal P-T conditions of ~ 850 °C and 0.5 GPa for the genesis of the Nsungwe Formation tuffs of the Rukwa Rift Basin. In comparing the paragenetic sequence of Runs 1-6 and the composition of key indicator minerals such as titanite, clinopyroxene and sanidine, we can evaluate the P-T conditions previously inferred conditions for Nsungwe Formation tuffs with reference to our experimental run products.

The co-crystallisation of titanite, clinopyroxene, nepheline, cancrinite and sanidine from a phonolitic melt composition between 900-850 °C (Runs 3 and 4) agrees with the observations and analysis of natural minerals of the Nsungwe Formation tuffs and inclusions (Lawrence et al. 2020; Chapter 3, *in-review*). Importantly, the temperature of 850 °C is shown to be a minimum for this assemblage given the temperature range to which it persists at a pressure of 0.5 GPa (850 °C – 700 °C). The composition of clinopyroxene (namely high Fe and Na contents) as well as extremely Ca-poor sanidine is also in agreement with those reported for natural NFT mineral compositions (Lawrence et al., 2020). Similarly titanite produced from the 800 °C and 700 °C experiments contain noteworthy (but not extreme) amounts of Zr (1-2 wt%) which is also a feature of natural Nsungwe Formation tuff titanite (0.25-0.75 wt%). The extreme Zr concentrations reported in titanite from Run-5 at 850 °C, re-affirm the governing role early titanite fractionation and temperature may have on the Zr budget of alkaline rocks, whereby Zr-phases such as zircon, baddeleyite or wadeite are not present (Seifert and Kramer, 2003; Hayden et al., 2008).

Expansion of the two-liquid solvus and progressive evolution towards peraluminous silicate melt compositions with reducing temperature was presented a powerful new possible mechanism for explosive volcanism in alkali-carbonatite systems (Chapter 3, *in-review*). Given the silicate melt evolution produced in Runs 1-3 (and general vector towards peraluminous corner of the ternary diagram) this mechanism is partially substantiated and in agreement with previous studies, albeit without crossing the thermal divide (Brooker and Kjarsgaard, 2010). Whereas melt inclusions from the Nsungwe Formation tuffs and Hanang volcanoes of Tanzania (as well as trachyte-carbonatite tuffs of the Suswa

volcano in Kenya) demonstrate an apparent capacity to cross the thermal divide to produce trachytic compositions via unmixing alkali-carbonate from a CO<sub>2</sub>-rich phonolitic parent melt, without identifying and measuring the composition of the silicate melt in lower temperature runs, experimentally crossing the feldspar thermal divide via this process remains theoretically plausible, but not yet demonstrated (Macdonald et al., 1993; Brooker and Kjarsgaard, 2010; Baudouin et al., 2018; Lawrence et al., 2020). Notwithstanding, the compositions and geological conditions replicated by our experiments appear to favour volatile enrichment and melt polymerisation, which is known to have critical implications for the explosive character of arc-magmas and Plinian-style eruptions observed in highly fractionated phonolites (Manga et al., 1998; Andújar et al., 2008). Furthermore, with increasing H<sub>2</sub>O contents in the liquid system, the possibility of three-phase immiscibility i.e. silicate liquid, carbonate liquid and alkali-carbonate fluid or fluid condensate (as observed in nepheline hosted inclusions from the Kermasi volcano of Tanzania; (Guzmics et al., 2019)) presents an additional repository for alkali-elements and pathway to peraluminous silicate melt compositions with continued fractionation.

#### ***4.4.4 Zirconium and fluorine in immiscible peralkaline igneous systems***

Fluorine has long been acknowledged as a consequential element in the formation of alkali-carbonatite magmas, particularly for its capacity to lower the liquidus of carbonatite melt in the Na<sub>2</sub>CO<sub>3</sub>-CaCO<sub>3</sub> system (Jago and Gittins, 1991; Weidendorfer et al., 2017). It is also recognised to have an important role in REE complexation (as well as other economic metals) and the formation of REE deposits (Elliott et al., 2018; Anenburg et al., 2020a). The GSR-CNK-F starting composition of experimental Run-7 contained appreciable F contents, which significantly influenced the texture, morphology and to a limited extent mineralogy of the run products (Fig. 4.8; Table 4.2). There are generally greater proportions of the carbonate liquid present in the products of Run-7 compared to Run-5, which is consistent with a lowering of the liquidus. Furthermore, the carbonate liquid quenched into two discrete alkali-rich compositions, one of which contains appreciable fluorine contents (> 20 wt%). A further clear point of difference observed in Run-7, is the formation and relative prevalence of baddeleyite (ZrO<sub>2</sub>) as the dominant Zr-bearing phase suggesting that, like REE's, fluorine exerts some influence over the complexation and solubility of Zr within this experimental system (Keppler, 1993; Aseri et al., 2015).

An unexpected feature of the experimental runs 4-7 is the enrichment of Zr, initially in titanite at 850 °C and subsequently in wadeite at 700 °C and both baddeleyite and wadeite at 800 °C from the GSR-CNK-F composition. Where present in immiscible silicate-carbonate systems, Zr (like other network forming elements Si, Al) strongly partitions and becomes enriched in the silicate liquid over the carbonatite liquid upon unmixing (Martin et al., 2013). Silica-undersaturated silicate and carbonatitic melts rich in alkalis have characteristically low SiO<sub>2</sub> activities, which favours the formation of exotic Zr-rich phases such as wadeite and baddeleyite (as well as Na-REE eudialyte group minerals) over zircon (Marr et al., 1998; Marks et al., 2011; Gervasoni et al., 2017). Experimental studies and

observations in natural samples have shown that the crystallization and stability of alkali-zirconosilicates is also sensitive to fluid activity, alkali-contents and fluorine contents of the melt as these (to varying degrees) are suggested to destabilise alkali-zirconium complexation in favour of alkali-fluorine complexation resulting in  $ZrO_2$  precipitation (Marr et al., 1998; Wu et al., 2015). With reference to the experiments in this study, the effect of fluorine on alkali-complexation (evidenced by the F-rich alkali-carbonate quench of Run-7) may account for the prevalence of baddeleyite in the GSR-CNK-F composition over other zirconosilicate phases and dominance of Zr complexed with K to form wadeite in the comparatively low-F Run-6. The preferential formation of wadeite over other exotic Na-REE eudialyte group minerals likely reflects the highly-potassic nature of this experimental system, given that the Na/K ratio exerts a strong influence over the dominant alkali-Zr-SiO<sub>2</sub> species forming (Marr et al., 1998; Wu et al., 2015). The formation of the K-Zr-silicate wadeite over dyalite provides some added insight into the formative melt composition. Namely, that the SiO<sub>2</sub> concentration in the crystallising experimental melt is lesser than those encountered in peralkaline granitic systems, which sees dalyite crystallise as the dominant Zr species (Marr et al., 1998; Marks et al., 2011).

#### 4.5 Conclusions

Experimental investigation of phase relations in evolved phonolite-carbonatite liquid systems from 1000 °C to 700 °C at 0.5 GPa reveal:

- The position and behaviour (i.e. predicted expansion) of the two-liquid solvus with reducing temperature shown in this experimental series from 1000°C - 900°C is consistent with inferences made from previous experimental studies conducted at higher pressures and temperatures, and petrographic observations in natural rocks (the Nsungwe Formation tuffs).
- The P-T ranges previously inferred for the formation of the Nsungwe Formation tuffs largely reproduce the assemblages and compositions previously reported for these deposits. Furthermore, unmixing alkali-carbonatite at, and en-route, to these conditions is clearly demonstrated. In agreement with previous work, this supports the characterisation of the Nsungwe Formation tuffs as the eruptive products of phonolite-carbonatite liquid immiscibility.
- Above 850 °C titanite is the dominant Zr bearing mineral in this experimental phonolite-carbonatite system. At lower temperatures the Zr-K-SiO<sub>2</sub> wadeite forms, sequestering both K and Zr from low-F melt compositions. When significant F is present, alkali complexation with F sees the formation of the K-free Zr-phase baddeleyite. Further geochemical analyses of trace element bearing phases may provide insights regarding the respective influence titanite, clinopyroxene, fluorine, H<sub>2</sub>O and alkali complexation have on REE and HFSE behaviour in low temperature evolved alkaline magmatic systems.

- Titanite is a key fractionating phase in peralkaline-carbonatite systems. The P-T conditions under which titanite crystallises are of significant interest pertaining to both the eruptive behavior of volcanic systems and the formation of critical mineral systems of economic interest. This series of experiments highlights titanite as an exceptional monitor of magma evolution and petrological tool in natural rocks.
- Although silica-saturated (trachytic) melt compositions were not produced in this experimental series, the principles demonstrated and the formation of the carbonatite trachyte association warrants further investigation. Firstly as a means of generating explosive volcanic eruptions, but also to better understand the trace element partitioning behaviour and phase assemblages of low-temperature, evolved peralkaline systems.

## References

- Andújar, J., Costa, F., Martí, J., Wolff, J., Carroll, M., 2008. Experimental constraints on pre-eruptive conditions of phonolitic magma from the caldera-forming El Abrigo eruption, Tenerife (Canary Islands). *Chemical Geology*, 257(3-4): 173-191.
- Anenburg, M., Mavrogenes, J.A., Bennett, V.C., 2020a. The fluorapatite P–REE–Th vein deposit at Nolans Bore: genesis by carbonatite metasomatism. *Journal of Petrology*.
- Anenburg, M., Mavrogenes, J.A., Frigo, C., Wall, F., 2020b. Rare earth element mobility in and around carbonatites controlled by sodium, potassium, and silica. *Science advances*, 6(41): eabb6570.
- Aseri, A.A., Linnen, R.L., Che, X.D., Thibault, Y., Holtz, F., 2015. Effects of fluorine on the solubilities of Nb, Ta, Zr and Hf minerals in highly fluxed water-saturated haplogranitic melts. *Ore Geology Reviews*, 64: 736-746.
- Bailey, D., Kearns, S., 2012. New forms of abundant carbonatite–silicate volcanism: recognition criteria and further target locations. *Mineralogical Magazine*, 76(2): 271-284.
- Baudouin, C., Parat, F., Denis, C.M., Mangasini, F., 2016. Nephelinite lavas at early stage of rift initiation (Hanang volcano, North Tanzanian Divergence). *Contributions to Mineralogy and Petrology*, 171(7): 64.
- Baudouin, C., Parat, F., Michel, T., 2018. CO<sub>2</sub>-rich phonolitic melt and carbonatite immiscibility in early stage of rifting: Melt inclusions from Hanang volcano (Tanzania). *Journal of Volcanology and Geothermal Research*, 358: 261-272.
- Bell, K., Kjarsgaard, B., Simonetti, A., 1998. Carbonatites—into the twenty-first century. *Journal of Petrology*, 39(11-12): 1839-1845.
- Brooker, R., Kjarsgaard, B., 2010. Silicate–carbonate liquid immiscibility and phase relations in the system SiO<sub>2</sub>–Na<sub>2</sub>O–Al<sub>2</sub>O<sub>3</sub>–CaO–CO<sub>2</sub> at 0.1–2.5 GPa with applications to carbonatite genesis. *Journal of Petrology*, 52(7-8): 1281-1305.
-

- Bühn, B., Rankin, A., 1999. Composition of natural, volatile-rich Na–Ca–REE– Sr carbonatitic fluids trapped in fluid inclusions. *Geochimica et Cosmochimica Acta*, 63(22): 3781-3797.
- Campbell, L., Dyer, A., Williams, C., Lythgoe, P., 2012. The masquerade of alkaline–carbonatitic tuffs by zeolites: a new global pathfinder hypothesis. *Mineralium Deposita*, 47(4): 371-382.
- de Moor, J.M. et al., 2013. Volatile-rich silicate melts from Oldoinyo Lengai volcano (Tanzania): Implications for carbonatite genesis and eruptive behavior. *Earth and Planetary Science Letters*, 361: 379-390.
- Elliott, H. et al., 2018. Fenites associated with carbonatite complexes: A review. *Ore Geology Reviews*, 93: 38-59.
- Fadaie, K.t., Ranalli, G., 1990. Rheology of the lithosphere in the East African Rift System. *Geophysical Journal International*, 102(2): 445-453.
- Fontijn, K. et al., 2010. Holocene explosive eruptions in the Rungwe Volcanic Province, Tanzania. *Journal of volcanology and geothermal research*, 196(1-2): 91-110.
- Gervasoni, F., Klemme, S., Rohrbach, A., Grützner, T., Berndt, J., 2017. Experimental constraints on the stability of baddeleyite and zircon in carbonate-and silicate-carbonate melts. *American Mineralogist*, 102(4): 860-866.
- Guzmics, T. et al., 2019. Natrocarbonatites: A hidden product of three-phase immiscibility. *Geology*, 47(6): 527-530.
- Hamilton, D., Freestone, I.C., DAWSON, J.B., DONALDSON, C.H., 1979. Origin of carbonatites by liquid immiscibility. *Nature*, 279(5708): 52-54.
- Hayden, L.A., Watson, E.B., Wark, D.A., 2008. A thermobarometer for sphene (titanite). *Contributions to Mineralogy and Petrology*, 155(4): 529-540.
- Jago, B.C., Gittins, J., 1991. The role of fluorine in carbonatite magma evolution. *Nature*, 349(6304): 56-58.
- Keppler, H., 1993. Influence of fluorine on the enrichment of high field strength trace elements in granitic rocks. *Contributions to Mineralogy and Petrology*, 114(4): 479-488.
- Kjarsgaard, B., Hamilton, D., Peterson, T., 1995. Peralkaline nephelinite/carbonatite liquid immiscibility: comparison of phase compositions in experiments and natural lavas from Oldoinyo Lengai, *Carbonatite Volcanism*. Springer, pp. 163-190.
- Kjarsgaard, B., Peterson, T., 1991. Nephelinite-carbonatite liquid immiscibility at Shombole volcano, East Africa: petrographic and experimental evidence. *Mineralogy and Petrology*, 43(4): 293-314.
- Lawrence, L., Spandler, C., Roberts, E., Hilbert-Wolf, H., 2020. Mineralogy and origin of the alkaline Nsungwe Formation tuffs of the Rukwa Rift Basin, southwestern Tanzania. *Lithos*: 105885.
- Macdonald, R. et al., 1993. Liquid immiscibility between trachyte and carbonate in ash flow tuffs from Kenya. *Contributions to Mineralogy and Petrology*, 114(2): 276-287.
- Manga, M., Castro, J., Cashman, K.V., Loewenberg, M., 1998. Rheology of bubble-bearing magmas. *Journal of Volcanology and Geothermal Research*, 87(1-4): 15-28.

- Marks, M.A., Hettmann, K., Schilling, J., Frost, B.R., Markl, G., 2011. The mineralogical diversity of alkaline igneous rocks: critical factors for the transition from miaskitic to agpaitic phase assemblages. *Journal of Petrology*, 52(3): 439-455.
- Marr, R.A., Baker, D.R., Williams-Jones, A.E., 1998. Chemical controls on the solubility of Zr-bearing phases in simplified peralkaline melts and application to the Strange Lake Intrusion, Quebec-Labrador. *The Canadian Mineralogist*, 36(4): 1001-1008.
- Martin, L.H., Schmidt, M.W., Mattsson, H.B., Guenther, D., 2013. Element partitioning between immiscible carbonatite and silicate melts for dry and H<sub>2</sub>O-bearing systems at 1–3 GPa. *Journal of Petrology*, 54(11): 2301-2338.
- Mitchell, R.H., 2005. Carbonatites and carbonatites and carbonatites. *The Canadian Mineralogist*, 43(6): 2049-2068.
- Seifert, W., Kramer, W., 2003. Accessory titanite: an important carrier of zirconium in lamprophyres. *Lithos*, 71(1): 81-98.
- Weidendorfer, D., Schmidt, M.W., Mattsson, H.B., 2017. A common origin of carbonatite magmas. *Geology*, 45(6): 507-510.
- Woolley, A., Church, A., 2005. Extrusive carbonatites: a brief review. *Lithos*, 85(1-4): 1-14.
- Wu, B. et al., 2015. Wadeite (K<sub>2</sub>ZrSi<sub>3</sub>O<sub>9</sub>), an alkali-zirconosilicate from the Saima agpaitic rocks in northeastern China: Its origin and response to multi-stage activities of alkaline fluids. *Lithos*, 224: 126-142.
- Wyllie, P., Tuttle, O., 1960. The System CaO-CO<sub>2</sub>-H<sub>2</sub>O and the Origin of Carbonatites. *Journal of Petrology*, 1(1): 1-46.

## Chapter 5

# **Radiogenic isotope record of magma genesis and lithospheric geodynamics of the Rukwa Rift, Tanzania: ca. 165 Ma to present**

### **Abstract**

The Rukwa Rift of southwestern Tanzania has experienced multiple episodes of tectonic reactivation, leading to renewed basin development and intraplate alkaline volcanism since the Late Jurassic, however the geodynamic processes and lithospheric evolution involved in this protracted geological history remains poorly defined. Here, we present Sm-Nd, Lu-Hf, and Rb-Sr isotopic data of igneous minerals and mineral concentrates for three magmatic episodes known to coincide with basin activation, respectively represented by: (1) the Late Jurassic to Cretaceous Panda Hill carbonatite; (2) the late Oligocene phonolitic-carbonatitic Nsungwe Formation tuffs; and (3) Miocene-recent bi-modal volcanism of the Rungwe Volcanic Province. Of these, the Oligocene-aged Nsungwe Formation tuffs fill a critical temporal gap as they offer a discrete window into the early phases of lithospheric disturbance associated with modern rifting and a renewed temporal framework for the geodynamic evolution of the Western Branch of the East African Rift.

Our data show that alkaline magmas erupted prior to the Miocene are isotopically distinct ( $\epsilon\text{Nd} +1.5$  and  $^{87}\text{Sr}/^{86}\text{Sr}$  0.7041) from modern Rungwe lavas ( $\epsilon\text{Nd} -3.5$  and  $^{87}\text{Sr}/^{86}\text{Sr}$  0.7069) and likely originate from a lithospheric mantle that experienced enrichment during the Pan-African orogeny (~550-700 Ma). Consistent with previous studies, our results indicate that Rungwe Volcanic Province magmas were generated from a mixed, isotopically-enriched component of the lithospheric mantle that may have developed during the ca. 1.0 Ga Irumide Orogeny. Collectively, the progressive enrichment in the source region of rift lavas through time, observed in our data, is consistent with melting of a compositionally layered lithosphere. Combined with existing geophysical and sedimentological data, we hypothesise that the lithosphere beneath Rukwa-Malawi-Usangu junction of the Western Branch experienced an episode of destabilisation and foundering (lithospheric drip) near the onset of East African Rift (30-25 Ma), coincident with basin development.

## 5.1 Introduction

The interconnected tectonic basins, flanking escarpments and intra-plate volcanism of the East African Rift System (EARS) serve as a natural laboratory for the study of continental break-up. Over the past few decades, a key focus in this area has been linking deep geophysical observations of the lithospheric and deep mantle, with geochemical observations (namely, trace element and isotopic data) of rift lavas at the surface to discern lithospheric processes that govern continental break-up in Eastern Africa (Morley et al., 1992a; Furman and Graham, 1999; Nyblade, 2011; Castillo et al., 2014;; Furman et al., 2016; Tepp et al., 2018; Rooney, 2020; Mesko et al., 2020). Collectively, this work has generated numerous models that describe the temporal evolution of the sub-continental lithospheric mantle (SCLM) with reference to the magmatic products being produced at the surface (Furman, 1995; Furman and Graham, 1999; Bagley and Nyblade, 2013; Castillo et al., 2014; Furman et al., 2016; Rooney, 2019). Given the vast spatial and temporal extent of the EARS (>4000 km and >40 m.y., respectively) and the diverse nature of rift lavas across these parameters, discrepancies between models are commonplace. However, some clarity is emerging with regards to the key ingredients involved in the formation and evolution of the EARS, and continental breakup more generally. These include: the presence and involvement of the African Large Low Shear Velocity Province (LLSVP); also referred to as African Superplume (Pik et al., 2008; Nyblade, 2011; Bagley and Nyblade, 2013; Castillo et al., 2014); a significant reduction in northward motion of the African plate between 30-19 Ma (O'Connor et al., 1999); and inherited metasomatic heterogeneities (i.e. mantle metasomes) within the lithospheric mantle of eastern Africa (Rogers et al., 1998; Furman and Graham, 1999; Rooney, 2020).

Like the gates of Hades, the break-up of eastern Africa is suggested by many to be governed by a beast with many heads; more commonly referred to as the African Superplume (LLSVP hereafter) (Bagley and Nyblade, 2013; Castillo et al., 2014). The African LLSVP is a deep mantle feature interpreted through a series of connected low-velocity seismic anomalies suggested to contribute both heat and material across the 660 km discontinuity beneath the entire EARS (Nyblade, 2011; Bagley and Nyblade, 2013; Castillo et al., 2014). From a geophysical standpoint, magmatism in the EARS arises from a single plume, or many heads stemming from single deep mantle source. Isotopically, the African LLSVP termed “Plume-V” by Castillo et al. (2014) is characterised by  $^{87}\text{Sr}/^{86}\text{Sr} \sim 0.7045$ ,  $^{143}\text{Nd}/^{144}\text{Nd} \sim 0.5127$ ,  $^{206}\text{Pb}/^{204}\text{Pb} > 19$ , and  $^3\text{He}/^4\text{He} > 15 R_A$  isotopic ratios. Using these ratios, contribution of the Plume-V source has been inferred (albeit to varying degrees) in the products of the Kivu, Virunga and Rungwe volcanic provinces in the Western Branch and Ethiopian and Kenyan rift lavas in the Eastern Branch of the EARS (Halldórsson et al., 2014). The isotopic variability across and within sections of the EARS is suggested to be a function of degree of metasomatic overprint and/or degree of mixing with locally heterogenous “common lithospheric mantle” en-route to the surface. (Furman and Graham, 1999; Bell and Tilton, 2001; Castillo et al., 2014; Furman et al., 2016; Rooney, 2020). The variably enriched “common-lithospheric mantle” as described by Furman and Graham (1999) broadly reflects a

period of regional carbonatite metasomatism that impacted the lithospheric mantle beneath the EARS between 1000 – 500 Ma.

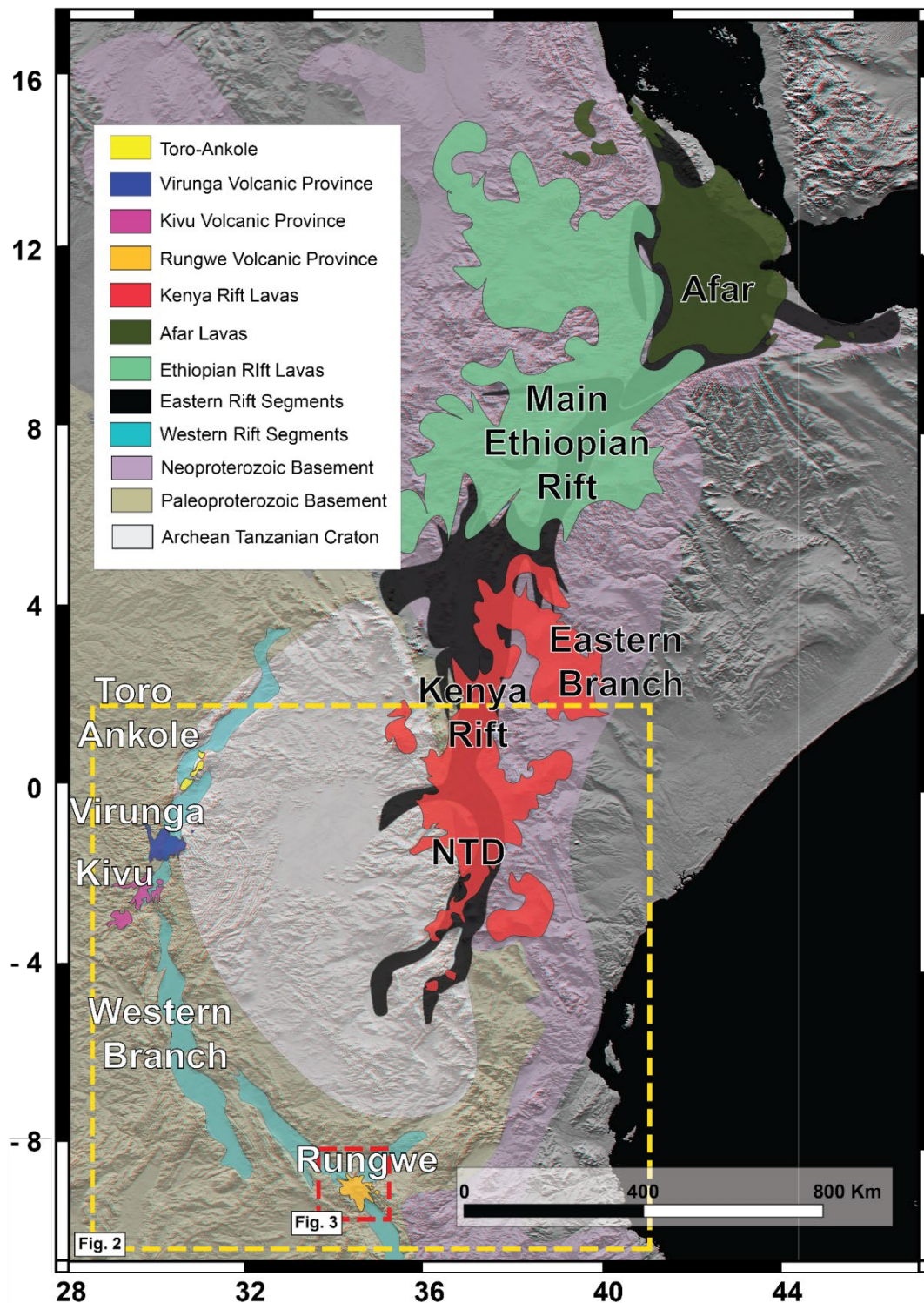


**Fig. 5.1** Image of the EARS showing rift segments, basement rocks and Cenozoic volcanic rocks as presented by Rooney (2020), base image modified from the NASA Shuttle Radar Topography Mission collection. The dashed yellow box indicates the field of view shown in Fig. 5.2. The dashed red box indicates field of view of Fig. 5.3

An important distinction is often made between the Eastern and Western branches of the EARS regarding the timing and nature of magmatism in the respective branches. Namely, that magmatism in the Eastern Branch is older, more voluminous and less isotopically variable than the younger Western Branch, which is host to some of the most alkaline-rich, silica-undersaturated and isotopically variable lavas known (Ebinger, 1989; Rogers et al., 1998; Furman and Graham, 1999; Muravyeva et al., 2014; Rooney, 2020). In contrast to the >35 m.y. along-axis bimodal volcanism of the Eastern Branch, magmatism in the Western Branch occurs in concentrated, young (<12 Ma) intra-basinal volcanic provinces that bridge some of the deepest rift lakes in the world (Ebinger, 1989; Kampunzu and Lubala, 2012; Ring, 2014) (Fig. 5.1). Geochemical complexity in the composition of rift magmas, as especially reflected in the occurrence and isotopic character of East African carbonatites, increase nearer to the Archean Tanzanian craton (Van Straaten and Bell, 1989; Bell and Tilton, 2001; Foley et al., 2012; Rooney, 2020).

The extensive orogenic history preserved along the southern and western margins of the Tanzanian craton has been suggested to influence the geochemical character of Western Rift lavas (Fig. 5.2; Rogers et al., 1998; Furman and Graham, 1999). Here, subduction-related metasomatic processes are implicated in the development of heterogeneities in the lithospheric mantle and marked spatial and temporal isotopic variability within the volcanic provinces of the Western Branch (Furman, 1995; Rogers et al., 1998; Furman and Graham, 1999; Rosenthal et al., 2009; Rooney, 2020). Given the poor preservation capacity and notable scarcity of early rift lavas in surface outcrop, uncovering a complete magmatic history for the western rift segments, is inherently restricted. Additionally, the complex nature of the mantle lithosphere and short window of time through which to observe variation (<12 Ma) has impeded modelling of the source region for Western Rift lavas (Furman, 1995; Rogers et al., 1998; Furman and Graham, 1999; Rosenthal et al., 2009; Foley et al., 2012; Castillo et al., 2014).

By adopting a single-crystal approach in the isotopic analysis of volcanic tuffs and intrusive units from the Rukwa Rift, we may capably generate a time-integrated mineral-scale isotopic framework for the evolution of the lithosphere beneath at the Rukwa-Malawi-USangu junction. With this, the Rukwa-Malawi-USangu region now offers a unique opportunity to study the role of mantle sources in the rifting of Eastern Africa and continental breakup more generally, given; (1) the long-lived orogenic and metasomatic history of the local lithosphere (2) the comprehensive geological record preserved during periods of basin infill (Morley et al., 1992a; Roberts et al., 2010; Hilbert-Wolf et al., 2017); (3) the discrete sample intervals offered by local episodes of rift-related alkaline magmatism (Ebinger et al., 1989; Van Straaten and Bell, 1989; Roberts et al., 2010; Hilbert-Wolf et al., 2017; Mesko et al., 2020); (Fig. 5.3), and; (4) intensive high-resolution geophysical study of the lithosphere beneath the Rungwe Volcanic Province and northern Malawi Rift makes this one of the most interpreted sections of lithosphere in the EARS (Morley et al., 1992a; Laó-Dávila et al., 2015; Borrego et al., 2018; Grijalva et al., 2018; Tepp et al., 2018; Njinju et al., 2019).

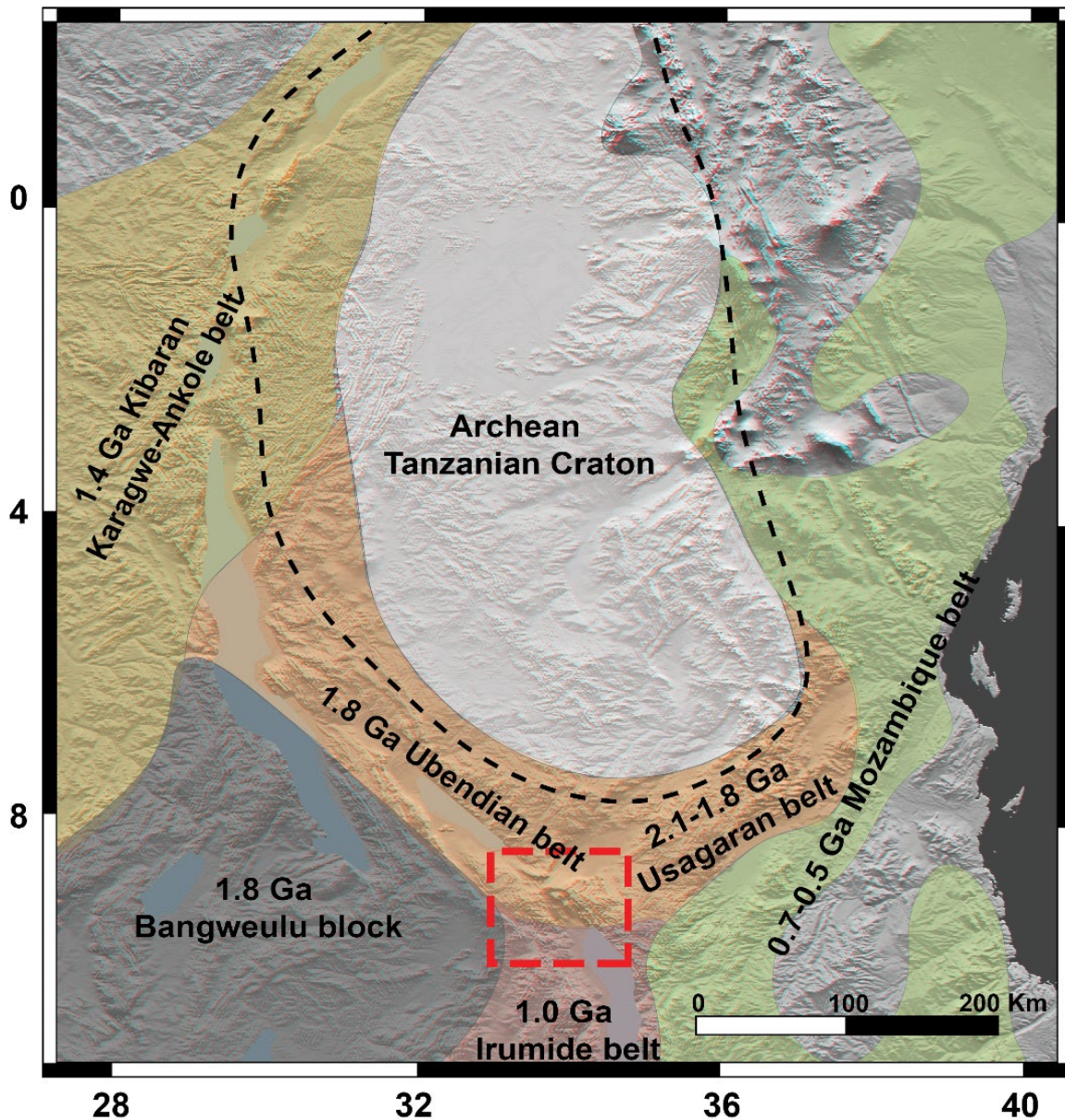


**Fig. 5.2** Regional map showing the approximate ages and distribution orogenic basement terrains surrounding the Tanzanian craton (adapted from Roberts et al. (2012)). The red dashed box indicates area shown in Fig. 5.3.

In this work, we utilise Rb-Sr, Sm-Nd and Lu-Hf isotope chemistry of igneous minerals and mineral concentrates sourced from the Panda Hill carbonatite, the NFT and the Rungwe Volcanic Province to establish the isotopic evolution of the magmatism in the Rukwa-Malawi-Usangu junction from 165 Ma to the present. By linking the isotopic evolution of the regional lithosphere with existing geological data, a conceptual tectono-magmatic model can be considered for the Oligocene-recent history of the long-lived Rukwa Rift Basin. Such a model may have broader implications for the break-up of complex ancient terrains elsewhere, particularly in the Western Branch and southernmost Eastern Branch of the EARS.

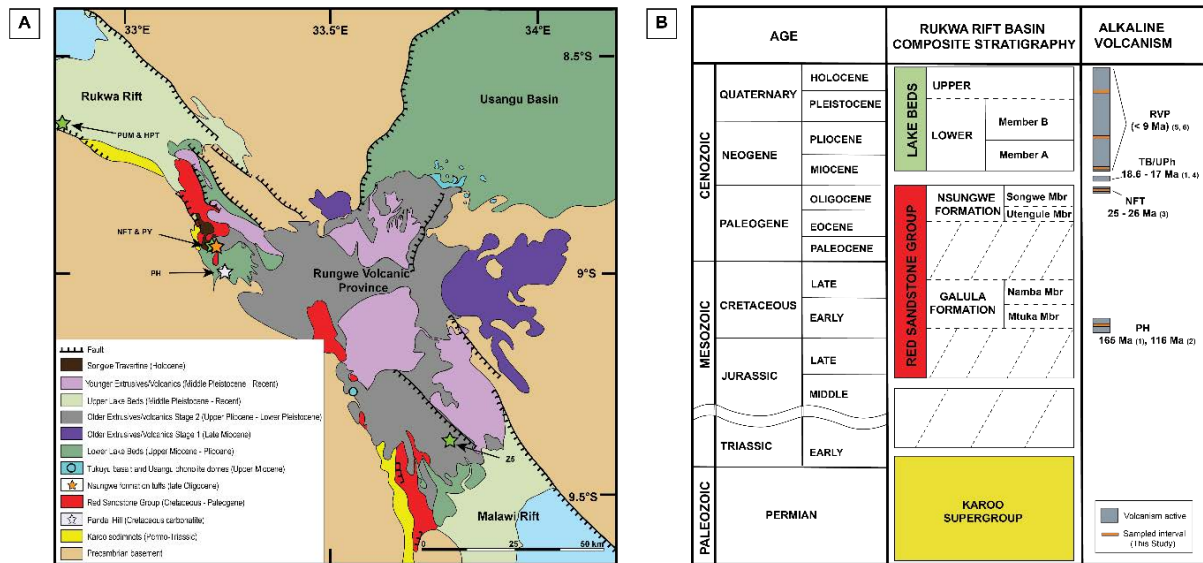


**Fig. 5.3** The Rukwa-Malawi-Usangu junction and simplified stratigraphy of the Rukwa Rift Basin A) Geological map of the Rukwa-Malawi-Usangu junction and Rungwe Volcanic Province (adapted from Fontijn et al. (2012) and Rasskazov et al. (2003)). The orange marks the sample locality for the NFT and PY samples, green stars marks the sample locality for the HPT, PUM and Z5 Lake Bed tuffs (Roberts et al., 2010; Hilbert-Wolf et al., 2017). Base topography and co-ordinates for b) and c) were generated using the Global Multi-Resolution Topography base map of Ryan et al. (2009). B) Simplified stratigraphy of the Rukwa Rift Basin and volcanic episodes of the Rukwa-Malawi-Usangu Junction. PH = Panda Hill carbonatite, NFT = Nsungwe formation Tuffs, TB = Tikuyu Basalt, UPH = Usangu phonolites, RVP = Rungwe volcanic province. Reported ages are from: (1) Mesko et al. (2020); (2) Morisset (1993); (3) Roberts et al. (2012); (4) Rasskazov et al. (2003); (5) Ebinger et al. (1989); (6) Fontijn et al. (2012). Volcanic intervals sampled in this study are shown in orange.

## 5.2 Geological setting

### 5.2.1 The East African Rift System

The EARS is an interconnected series of graben and half-graben basins hosted within a Precambrian tectonic framework surrounding the Archean-aged Tanzanian Craton (Chorowicz, 2005; Begg et al., 2009). The EARS is divided into Eastern and Western branches that run either side of the Tanzanian craton. The Eastern Branch extends from the Afar triple junction in northern Ethiopia, through Kenya and into Northern Tanzania (Fig. 5.1). Rift development follows pre-existing weaknesses in the Pan-African Mozambique belt that formed during the collision between East and West Gondwana (ca. 650-580 Ma) (Chorowicz, 2005; Fritz et al., 2005; Ring, 2014). The Eastern Branch is characterised by voluminous, on-axis bimodal volcanism that follows a general north to south progression of rift development and initiated at ca. 40 – 35 Ma in northern Kenya near Lake Turkana (MacDonald et al., 2001; Furman, 2007), at ca. 30 Ma in other parts of northern Kenya (Morley et al., 1992b), at ca. 15 Ma in central Kenya, at ca. 12 Ma in southern Kenya (Morley et al., 1992b) and at 8 Ma in northern Tanzania (Dawson, 1992).

The Western Branch runs from western Uganda to southern Malawi and central Mozambique and is hosted in a complex series of basement terrains (i.e. the Rwenzori, Kibaran, Ubendian, and Irumide mobile belts) accreted along the western margins of the Tanzanian craton between ca. 2.1 Ga and 1 Ga (Fig. 5.1 & 5.2) (Yoshida et al., 2003; Begg et al., 2009; Delvaux et al., 2012). Many of the Rift basins in the Western Branch have undergone more than one period of activation, with Cenozoic rifting being associated with the reactivation of pre-existing Karoo-aged structures (Kilembe and Rosendahl, 1992; Morley et al., 1992a; Delvaux et al., 2012). Magmatism in the Western Branch is considerably less voluminous and occurs in a series of intra-basinal volcanic provinces initiating at ca. 25 Ma in the Rukwa-Malawi-Usangu junction (proximal to the Rungwe Volcanic Province) followed by both the Virunga Volcanic Province (ca. 12 Ma), Kivu Volcanic Province (ca. 8 Ma) and Toro Ankole Volcanic Field (ca. 50 Ka) to the north (Fig. 5.1; (Ebinger, 1989a; Ebinger et al., 1989b; Kampunzu and Lubala, 2012; Roberts et al., 2012).

### **5.2.2 Local geology**

The Rukwa-Malawi-Usangu junction is hosted within the Paleoproterozoic Ubendian belt between the Archean Tanzanian Craton to the NE and the Paleoproterozoic Bangweulu Block (1.8 Ga) to the SW. The Ubendian shear zone developed via the ~1.8 Ga deformation of ~2.1 Ga Usagaran belt, the NW-SW trending fabric of which continues to govern basin development in the Cenozoic Rukwa Rift (Morley et al., 1992a; Delvaux et al., 2012). Basement rocks to the north of the Bangweulu Block beneath the Tanganyika Rift (and sections of the Western Branch further north) are associated with the Kibaran Orogeny (ca. 1.4 Ga) (Ring, 2014). Crustal basement between the Bangweulu Block and Malawi Rift are associated with the ca. 1 Ga the Irumide orogeny (Hauzenberger et al., 2014; Ring, 2014). East of the Tanzanian Craton and the Malawi Rift, is dominated by the Mozambique belt (650-550 Ma) that also makes up the vast majority crustal rocks in the Eastern Branch (Fig. 5.2.) (Yoshida et al., 2003; Ring, 2014).

The Rukwa Rift has witnessed several episodes of activation during the Permian (Karoo), Cretaceous, Paleogene and Neogene, each of which is preserved in the 8-10 km thick package of sedimentary infill (Kilembe and Rosendahl, 1992; Roberts et al., 2010). Alkaline magmatism has accompanied the three most recent episodes of activity resulting in the Panda Hill and Mbalizi carbonatites (ca. 165-120 Ma; Morisset, 1993; Mesko et al., 2020) associated with deposition of the Cretaceous Galula Formation, the Nsungwe Formation tuffs associated with deposition of the Oligocene Nsungwe Formation (ca. 25 Ma; Roberts et al., 2012; Lawrence et al., 2020) and modern (ca. 9 Ma-recent) Rungwe Volcanic Province associated with deposition of the Lake Beds Group (Fig. 5.3) (Ebinger et al., 1989; Fontijn et al., 2012; Hilbert-Wolf et al., 2017). Three stages of volcanic activity are described for the Rungwe Volcanic Province; (1) Late Miocene: ca. 9.2–5.4 Ma, (2) Late Pliocene–Early Pleistocene: ca 3–1.6 Ma, (3) Mid-Pleistocene–Recent: since ca 0.6 Ma (Fig. 5.3). However, analysis of both primary igneous crystals from volcanic tuff beds and detrital volcanic grains in outcrop

and drill core from the Lake Beds Group suggests this activity may have been more continuous than previously recognised (Mtelela et al., 2016; Hilbert-Wolf et al., 2017; Mtelela et al., 2017).

Geophysical studies describe the local lithosphere beneath Rungwe-Malawi-Usangu junction and Rungwe Volcanic Province as being significantly thinned, which has been attributed elsewhere in the EARS to be a consequence of stagnation of the northward African plate motion between 30-19 Ma (Ebinger and Sleep, 1998; O'Connor et al., 1999; Njinju et al., 2019; Hopper et al., 2020). This coincides with an episode of thermal perturbation beneath the Rukwa-Malawi-Usangu junction, potentially resulting from long-lived flow stagnation and pooling of upwelling material against the cratonic root of the Tanzanian Craton (Grijalva et al., 2018; Tepp et al., 2018; Hopper et al., 2020). This feature is suggested to exert an effect on the flow direction and extent of magmatism in the Western Branch (Tepp et al., 2018).

An additional volcanic episode is recorded along the north-east boundary of the Rungwe Volcanic Province in the Usangu Basin during the early-mid Miocene (ca. 19-13 Ma) in the form of phonolitic cones and edifices (Rasskazov et al., 2003). However, no correlative rift-fill deposition or volcanic tephra is known in the Rukwa or Malawi Rifts during this time (Fig. 5.3) (Kilembe and Rosendahl, 1992; Rasskazov et al., 2003; Roberts et al., 2010; Mesko et al., 2020). Previous studies of the 9 Ma-recent activity of the Rungwe Volcanic Province observed a strong relationship between the inherited NW-SE trending tectonic fabric of the underlying basement with the activation normal faults and volcanism at the surface (Fontijn et al., 2010a; Fontijn et al., 2012). Such tectonic controls were not observed for the older vents in the Usangu Basin. However, these outcrops, along with the NFT, clearly demonstrate an early period of lithospheric disturbance and Cenozoic magmatism prior to the development of the modern Rungwe Volcanic Province.

### **5.2.3 Sample description and rationale**

Samples of the Panda Hill carbonatite (PH), NFT (AS18, TZ-1, BW-4, CM, WT) and Lake Beds Group tuffs (Pumice tuff [PUM], Hippo tuff [HPT] Pyro tuff [PY] and Z5 tuff, originating from the Rungwe Volcanic Province) were collected from known outcrops in the Rukwa Rift Basin during the 2014-2018 field seasons (Fig. 5.3). Age data for the NFT is presented in Roberts et al. (2012), Stevens et al. (2013) and Spandler et al. (2016), and in-depth petrographic descriptions and mineral chemistry are presented in Lawrence et al. (2020). Age data and descriptions for the Lake Beds Group tuffs are presented in Hilbert-Wolf et al. (2017), Mtelela et al. (2017) and in the supplementary materials.

The NFT represent an isolated, early manifestation of phonolite-carbonatite volcanism and rift development in the Rukwa Rift at ca. 25 Ma (Roberts et al., 2012; Lawrence et al., 2020). The selected samples of Lake Bed tuffs cover the three recognised periods of increased volcanic activity in the Rungwe Volcanic Province at 8.7 Ma (PUM), 3.5 Ma (HPT) and <1Ma (PY and Z5). The Cretaceous Panda Hill carbonatite represents an earlier (ca. 165 – 116 Ma) period of alkaline volcanism and basin

development in the Rukwa Rift (Morisset, 1993; Mesko et al., 2020). Collectively, these samples provide a robust temporal framework for monitoring the lithospheric source of rift-associated magmatism in the Rukwa Rift over ca. 165 Ma.

Volcanic tuffs of the Rukwa Rift (particularly the NFT) are pervasively altered and dominated by devitrified clay matrixes, which makes them unsuitable for conventional whole rock analysis. Furthermore, no vent or source is known for the NFT. Lawrence et al. (2020) utilised resistant igneous mineral separates and their inclusions to identify an igneous assemblage for the NFT that includes titanite, phlogopite, fluorapatite, clinopyroxene, Ti-rich andradite, sanidine, pyrochlore, nepheline, cancrinite, pyrrhotite, zircon, calcite, Na-REE-carbonate and phonolite silicate glass, which characteristically represent the volcanic products of an early rift phonolite-carbonatite system (Lawrence et al., 2020). Of these, titanite, apatite, pyrochlore and zircon were shown to be significantly enriched in rare-earth elements (REE) (with light- and middle-REE concentrations in excess of  $10^4$  times chondritic values) and are thus deemed excellent candidates for in-situ isotopic analysis (Lawrence et al., 2020).

In-situ isotopic analysis of individual crystals has the capacity to trace mineral-scale variations that cannot be monitored via whole-rock analysis (Hammerli et al., 2014; Spandler et al., 2018). For this reason, an in-situ approach was taken for all samples in order to generate a high resolution and internally comparable isotopic data set spanning 165 Ma – present. This also serves to test the reliability and compatibility of our in-situ results for Panda Hill and the Lake Beds Group tuff samples against previous whole-rock isotope analyses of Panda Hill and the Rungwe Volcanic Province, respectively. We also undertook bulk Sm-Nd and Rb-Sr isotope analyses of titanite crystal concentrates from two NFT samples and one Lake Beds Group tuff sample to allow comparisons to be made between bulk and in-situ Sm-Nd isotope analysis of the samples utilised in this study, and also an additional point of isotopic comparison with existing whole rock data via the Rb-Sr system.

### **5.3 Analytical procedures**

#### ***5.3.1 Sample Preparation***

Each of the samples underwent heavy liquid and magnetic separation processes, as previously described in (Lawrence et al., 2020), to produce clean mineral separates. Primary igneous minerals selected for in-situ isotopic analysis include titanite, apatite, pyrochlore and zircon. Mounted crystals used in this study were previously studied in detail using scanning electron imaging, backscattered electron imaging and cathodoluminescence imaging to inspect variability in mineral zonation. Complimenting the in-situ analysis were Sm-Nd and Rb-Sr isotope analysis of pure titanite separates analysed by solution TIMS analysis, as outlined below.

#### ***5.3.2 Bulk Sm-Nd and Rb-Sr isotope analysis***

Bulk Sm-Nd and Rb-Sr isotope analysis of clean titanite separates was performed at the University of Adelaide with a Finnigan MAT262 thermal ionisation mass spectrometer (TIMS), in static and quadruple cup dynamic measurement modes following the routine described in Wade et al. (2006). Between 5 and 15 mg of the samples were digested in PARR acid (HNO<sub>3</sub>-HF acid mix) digestion bombs at 190 °C for 96 hours, then evaporated to dryness and bombed with 6M HCl overnight. The samples were then spiked with a <sup>150</sup>Nd/<sup>147</sup>Sm spike. The measurements were corrected for mass fractionation by normalisation to <sup>146</sup>Nd/<sup>144</sup>Nd = 0.7219. Neodymium and Sm concentrations were calculated by isotope dilution and were corrected for 100 pg and 50 pg blanks, respectively. Reference material JNdi-1 was 0.512107 ± 9 (2σ) and <sup>143</sup>Nd/<sup>144</sup>Nd ratios were normalised to the TIMS value of the JNdi-1 glass (0.512098 ± 13; Fisher et al. 2011). Strontium isotope analyses follow the same digestion procedures as for Sm-Nd isotope analysis, followed by Sr separation carried out using 200 μL eichrom 50-100μ Sr resin in Micro Bio-spin columns. The measurements underwent normalisation to <sup>86</sup>/<sup>88</sup>Sr = 0.1194, using exponential mass fractionation correction. The <sup>87</sup>Sr/<sup>86</sup>Sr ratios were normalised to the measured NIST SRM 987 TIMS value of 0.710238 ± 0.000011 (Appendix D1).

### 5.3.3 *In-situ Sm-Nd isotope analysis*

In situ Sm-Nd isotope analysis of titanite, apatite and pyrochlore was undertaken at the Advanced Analytical Centre, James Cook University, using a Coherent GeoLasPro 193 nm Excimer laser ablation system coupled with a Thermo-Scientific NEPTUNE multicollector ICP-MS. The NEPTUNE Faraday cup configuration is the same set up used by McFarlane and McCulloch (2007) with interference and mass bias corrections made according to Fisher et al. (2011). Laser spot sizes of between 40 and 90 μm were used for titanite, apatite and pyrochlore depending on size and morphology of individual grains. Each analysis consisted of 60s on background and 60s data acquisition with a 60s washout time between analyses. Samples were ablated in a large volume cell (Fricker et al., 2011) using a repetition rate of 4 Hz and surface energy density (measured at the site of ablation) of 4 J/cm<sup>2</sup>. The ablated material was carried via He gas (flow rate of 2.5 l/min) to a bulb with a volume of 2.5 cm<sup>3</sup> where it was mixed with Ar (flow of 0.95 l/min) and N<sub>2</sub> (0.01 l/min) before being carried to the MC-ICP-MS. A synthetic LREE-doped glass (ID-TIMS; <sup>147</sup>Sm/<sup>144</sup>Nd = 0.2451 ± 7) and a Nd-doped glass (JNdi-1; ID-TIMS <sup>143</sup>Nd/<sup>144</sup>Nd = 0.512098 ± 13) were used as primary standards to monitor and correct for drift in unknown <sup>147</sup>Sm/<sup>144</sup>Nd and <sup>143</sup>Nd/<sup>144</sup>Nd values (Fisher et al., 2011). Our results for JNdi-1 glass are <sup>143</sup>Nd/<sup>144</sup>Nd = 0.512092 ± 6 (n = 43) and for LREE glass are <sup>147</sup>Sm/<sup>144</sup>Nd = 0.2453 ± 6 (n = 39). As a quality control measure, Otter Lake apatite and MKED-1 titanite were used as secondary standards. Our results for Otter Lake apatite (n = 17; <sup>143</sup>Nd/<sup>144</sup>Nd = 0.511915 ± 24 and <sup>147</sup>Sm/<sup>144</sup>Nd = 0.0809 ± 6) align with the average values (<sup>143</sup>Nd/<sup>144</sup>Nd = 0.511942 ± 45 and <sup>147</sup>Sm/<sup>144</sup>Nd = 0.0827 ± 21) reported for Otter Lake (Yang et al., 2014). Our results for MKED-1 titanite (n = 7; <sup>143</sup>Nd/<sup>144</sup>Nd = 0.511624 ± 25 and <sup>147</sup>Sm/<sup>144</sup>Nd = 0.1267 ± 20) agree with those published by Spandler et al. (2016); <sup>143</sup>Nd/<sup>144</sup>Nd = 0.5116303 ± 25 and <sup>147</sup>Sm/<sup>144</sup>Nd = 0.0127. Some analyses returned errors >1 εNd unit due to low

Nd concentrations or analyses compromised by inclusions. These analyses were excluded from the final dataset.

### 5.3.4 *In-situ Lu-Hf isotope analysis*

In situ Lu-Hf isotope micro-analysis of zircon was conducted using the laser ablation and multicollector ICP-MS instrumentation as outlined above. The NEPTUNE Faraday cup configuration and isobaric interference corrections are carried out according to Woodhead et al. (2004) and Kemp et al. (2009). Each analysis consisted of 60s on background and 60s data acquisition with a 60s washout time between analyses. Samples were ablated using a repetition rate of 4 Hz, a surface energy density of 6 J/cm<sup>2</sup>, and a spot size of 65 µm. FC1 zircon was used as a secondary standard for quality assurance. We obtained average values of  $^{176}\text{Hf}/^{177}\text{Hf} = 0.282483 \pm 8$  for Mud Tank and  $^{176}\text{Hf}/^{177}\text{Hf} = 0.282175 \pm 9$  for FC1 zircon. These values are within error of the solution value of FC1 of  $0.282184 \pm 16$  (Woodhead and Hergt, 2005), and indistinguishable from the  $^{176}\text{Hf}/^{177}\text{Hf}$  values determined by LA-MC-ICP-MS of  $0.282499 \pm 17$  and  $0.282176 \pm 22$  for Mud Tank and FC1, respectively (Kemp et al., 2009). As with the Sm-Nd isotope analyses, values with errors >1 εHf unit were deemed unreliable and excluded from the dataset.

## 5.4 Results

### 5.4.1 *Sm-Nd and Rb-Sr isotopes of bulk titanite separates*

Bulk Sm-Nd and Rb-Sr isotopes of titanite separates from four samples are presented in Table 5.1. The 25 Ma NFT samples AS18 and BW4 return similar measured  $^{143}\text{Nd}/^{144}\text{Nd}$  values of 0.512727 and 0.512726 respectively, whereas NFT sample TZ-1 returned a  $^{143}\text{Nd}/^{144}\text{Nd}$  value of 0.512647. This corresponds to εNd (t = 25 Ma) values of + 2.05, + 2.02 and + 0.49 respectively, which is in good agreement with the previous in-situ analysis of Spandler et al. (2016). The Pleistocene sample PY (<1 Ma) returned a  $^{143}\text{Nd}/^{144}\text{Nd}$  value of 0.512456 and εNd of -3.54. NFT samples AS18, BW4 and TZ-1 return near indistinguishable measured  $^{87}\text{Sr}/^{86}\text{Sr}$  ratios of 0.704171, 0.704175 and 0.704303 respectively, whereas PY returned a  $^{87}\text{Sr}/^{86}\text{Sr}$  ratio of 0.706985. The Rb contents of NFT titanite is exceedingly low < 0.07 ppm and <0.4 ppm for PY titanite, therefore the measured  $^{87}\text{Sr}/^{86}\text{Sr}$  ratio is in this case interpreted to represent the initial ratio.

**Table 5.1** Bulk Sm-Nd and Rb-Sr

Sample	$^{87}/^{86}\text{Sr}$	Nd ppm	Sm ppm	$^{147}\text{Sm}/^{144}\text{Nd}$	$^{143}/^{144}\text{Nd}$	$\epsilon\text{Nd} (T=0)$	$\epsilon\text{Nd} (T=\text{age})$	Age
AS18	0.704171	1439	231	0.0972	0.512727	1.73	2.05	25
BW4	0.704175	1434	233	0.0983	0.512726	1.71	2.02	25
TZ1	0.704303	1471	237	0.0972	0.512647	0.17	0.49	25
PY	0.706985	9194	1361	0.0895	0.512456	-3.55	-3.54	1

### 5.4.2 In-situ Sm-Nd isotopes

Average isotopic analyses of igneous titanite, apatite and pyrochlore are presented in Table 2 (see Appendix D1 for individual and standard analyses). Initial  $\epsilon\text{Nd}$  values have been calculated using the most recent 165 Ma age reported for Panda Hill by Mesko et al. (2020), the 25 Ma ages of Roberts et al. (2012) for the NFT, 8.7 Ma and 3.5 Ma ages of Hilbert-Wolf et al. (2017) for the PUM and HPT tuff, respectively, and 0.84 Ma for Z5 tuff (Roberts et al. *Pers. Comm.*).

Both Panda Hill apatite ( $n = 7$ ) and pyrochlore ( $n = 5$ ) return similar  $\epsilon\text{Nd}_{(i)}$  values ranging between 0 and 1.5 (average =  $0.76 \pm 0.75$ ; Fig. 5.4). Due to the similarity in Sm/Nd of Panda Hill pyrochlore and apatite, a meaningful isochron cannot be calculated from these two minerals. Analyses of NFT titanite from samples AS18 ( $n = 15$ ), WT ( $n = 10$ ) and BW4 ( $n = 14$ ) show some variance in  $\epsilon\text{Nd}_{(i)}$  range between  $\sim 0$  and + 2.4. Analyses of NFT sample TZ-1 ( $n=16$ ) titanite return two distinct  $\epsilon\text{Nd}_{(i)}$  populations, the first in agreement with other NFT samples  $\epsilon\text{Nd}_{(i)}$  0.6 to 2.2 ( $n = 9$ ) and the second returning significantly lower  $\epsilon\text{Nd}_{(i)}$  values between -2.2 to -4.7 ( $n = 8$ ) Fig 5.5. Younger samples from the Lake Beds sequence form tight groups around average  $\epsilon\text{Nd}_{(i)}$  values of -4.1, -3.4 and -1.5 for the PUM ( $n = 9$ ), HPT ( $n = 9$ ) and Z5 ( $n = 7$ ) samples respectively (Fig. 5.6).

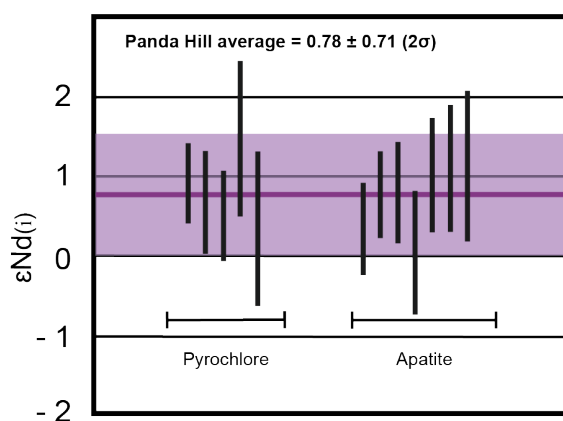


**Fig. 5.4** In-situ Sm-Nd isotopes of Panda Hill. Epsilon Nd values of individual Panda Hill pyrochlore and apatite analyses (vertical bars). Length of the vertical bars represents  $2\sigma$  error range. The purple horizontal line and shaded field represents the average value and  $2\sigma$  error, respectively.

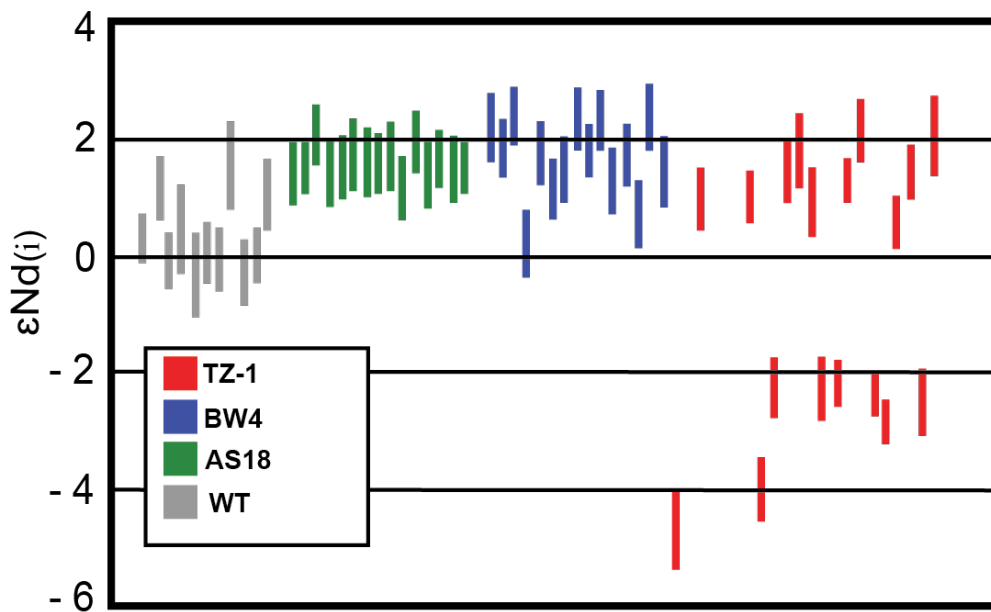


**Fig. 5.5** In-situ Sm-Nd isotopes of NFT titanite Epsilon Nd values of individual titanite analyses for the NFT. Length of the vertical bars represents  $2\sigma$  error range.

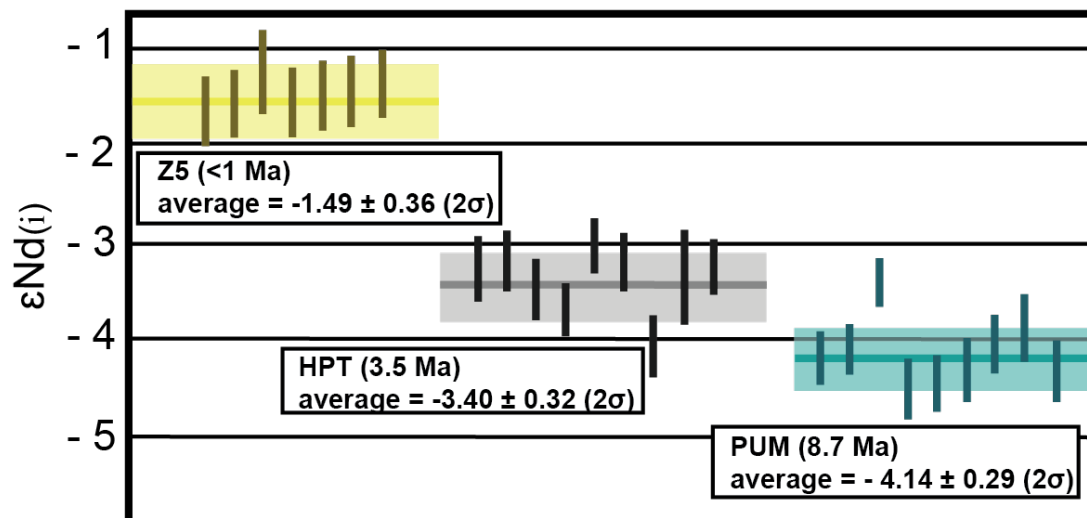


**Fig. 5.6** In-situ Sm-Nd isotopes of Lake Beds titanite Epsilon Nd values of individual titanite analyses for the Lake Bed tuffs. Length of the vertical bars represents  $2\sigma$  error range for each analysis. The yellow, grey and light blue horizontal lines and shaded fields correspond to the sample average and  $2\sigma$  error for the Z5, HPT and PUM tuffs, respectively.

Table 5.2 In-situ Sm-Nd isotopes

Sample	Mineral	$^{147}\text{Sm}/^{144}\text{Nd}$	$\pm 2\sigma$	$^{143}\text{Nd}/^{144}\text{Nd}$	$\pm 2\sigma$	Age (Ma)	CHUR (at 'i')	$^{143}\text{Nd}/^{144}\text{Nd}(i)$	$\epsilon \text{Nd}(i)$	$\pm 2\sigma$	Age DM (Ma)
<b>Panda Hill</b>											
Av. Pcl.	Pyrochlore	0.0851	0.0013	0.512563	0.000037	165	0.512426	0.512471	0.89	0.72	702
Av. Ap.	Apatite	0.0886	0.0013	0.512565	0.000036	165	0.512426	0.512469	0.85	0.71	709
<b>Nsungwe Formation Tuffs</b>											
Av. BW4	Titanite	0.1015	0.0003	0.512708	0.000028	25	0.512606	0.512692	1.68	0.54	599
Av. AS18	Titanite	0.0938	0.0004	0.512702	0.000028	25	0.512606	0.512687	1.58	0.54	571
Av. WT	Titanite	0.0952	0.0003	0.512640	0.000029	25	0.512606	0.512624	0.35	0.57	655
Av. TZ*	Titanite	0.0926	0.0003	0.512693	0.000027	25	0.512606	0.512678	1.41	0.54	577
<b>Lake Bed Tuffs</b>											
Av. PUM	Titanite	0.0956	0.0015	0.512420	0.000015	8.7	0.512627	0.512415	-4.14	0.29	936

\* TZ average excludes outlier data (i.e.  $\epsilon\text{Nd}$  below -2; Fig. 4)

\*\* Depleted mantle (DM) enrichment ages have been calculated using  $^{143}\text{Nd}/^{144}\text{Nd DM}_{(t=0)}$  of 0.51315 and  $^{147}\text{Sm}/^{144}\text{Nd DM}_{(t=0)}$  of 0.2145 and  $^{147}\text{Sm} \lambda = 6.54 \times 10^{-12}$  values of Goldstein et al. (1984)

Table 5.3 In-situ Lu-Hf isotopes

Sample		$^{176}\text{Lu}/^{177}\text{Hf}$	$\pm 2\sigma$	$^{176}\text{Hf}/^{177}\text{Hf m}$	$^{176}\text{Hf}/^{177}\text{Hf n}$	$\pm 2\sigma$	Age (Ma)	$^{176}\text{Lu}/^{177}\text{Hf}(i)$	$\epsilon\text{Hf}(t=0)$	$\epsilon\text{Hf}(t=\text{age})$	$\pm$ in $\epsilon\text{Hf}$ units	*Age DM (Ma)
<b>Nsungwe Formation Tuff</b>												
CM	Min	0.000189	0.000002	0.282683	0.282731	0.000013	25	0.282729	-1.91	-1.41	0.45	636
	Max	0.003249	0.000052	0.282746	0.282794	0.000026	25	0.282794	0.31	0.86	0.92	785
	Av	0.001130	0.000016	0.282716	0.282763	0.000020	25	0.282763	-0.77	-0.23	0.70	696
<b>Lake Bed Tuffs</b>												
PUM	Min	0.002356	0.000004	0.282611	0.282606	0.000014	8.7	0.282605	-6.35	-6.17	0.50	914
	Max	0.005642	0.000159	0.282650	0.282645	0.000020	8.7	0.282644	-4.97	-4.80	0.71	1029
	Average	0.004152	0.000030	0.282633	0.282627	0.000017	8.7	0.282626	-5.59	-5.42	0.60	967
<b>HPT</b>												
	Min	0.001723	0.000009	0.282528	0.282522	0.000010	3.5	0.282522	-9.29	-9.22	0.35	957
	Max	0.004998	0.000062	0.282594	0.282589	0.000015	3.5	0.282588	-6.95	-6.87	0.52	1151
	Av	0.002982	0.000032	0.282554	0.282548	0.000012	3.5	0.282548	-8.39	-8.32	0.42	1053

\* Depleted mantle (DM) enrichment ages have been calculated using  $^{176}\text{Lu}/^{177}\text{Hf DM}(t=0)$  of 0.0384 and  $^{176}\text{Hf}/^{177}\text{Hf DM}(t=0)$  of 0.28325 values of Griffin et al (2004) and  $\lambda = 1.87 \times 10^{-5}$  of Soderlund (2004)

### 5.4.3 In-situ Lu-Hf isotopes of zircon

Lutetium-Hf isotope analyses of previously-dated zircon from the NFT sample CM (Roberts et al., *in-prep*), and the Lake Beds samples PUM and HPT (Hilbert-Wolf et al., 2017) are presented in Table 3. Isotopic ratios of zircon from the NFT and HPT show greater variance with respect to measured  $^{176}\text{Lu}/^{177}\text{Hf}$  and  $^{176}\text{Hf}/^{177}\text{Hf}$ , with values ranging from  $0.000189 \pm 2$  to  $0.003249 \pm 52$ , and  $0.282683 \pm 13$  and  $0.282794 \pm 26$  respectively for the NFT, and between  $0.001723 \pm 9$  to  $0.004998 \pm 62$ , and  $0.282528 \pm 10$  to  $0.282594 \pm 15$ , respectively for the HPT. The  $^{176}\text{Lu}/^{177}\text{Hf}$  and  $^{176}\text{Hf}/^{177}\text{Hf}$  for the PUM sample are less variable with values between  $0.002356 \pm 4$  and  $0.005642 \pm 11$ , and  $0.282611 \pm 14$  and  $0.282650 \pm 20$ , respectively. Calculated  $\epsilon\text{Hf}_{(i)}$  values for the NFT zircon ( $n = 5$ ) are between 0.86 and -1.41 with an average of  $-0.23 (\pm 0.7)$ . The Lake Beds samples PUM ( $n=9$ ) and HPT ( $n=8$ ) return respective average  $\epsilon\text{Hf}_{(i)}$  values of  $-5.5 (\pm 0.6)$  and  $-8.3 (\pm 0.42)$ . All analyses shown in Fig. 5.7 are presented in Appendix D1.

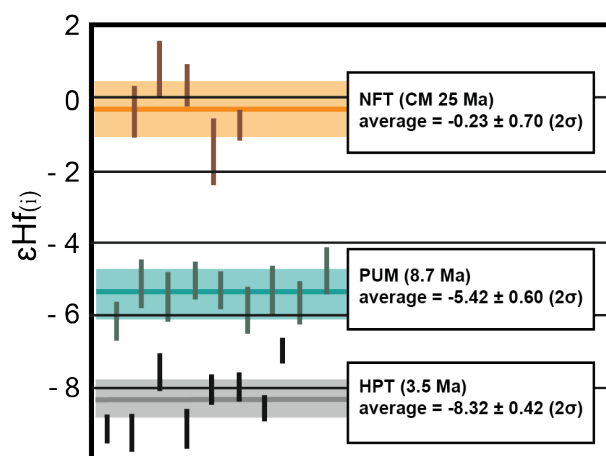


**Fig. 5.7** Epsilon Hf values of NFT and Lake Beds zircon. Epsilon-Hf values of individual zircon analyses for the NFT (sample CM; orange), PUM (light-blue), HPT (grey) Lake Bed Tuffs. Length of the coloured vertical bars represents  $2\sigma$  error range for each analysis. The orange, light-blue and grey horizontal lines and shaded fields correspond to the sample average and  $2\sigma$  error for the CM, PUM and HPT tuffs, respectively.

### 5.4.4 Model enrichment age calculations

Depleted mantle (DM) enrichment ages have been calculated using  $^{143}\text{Nd}/^{144}\text{Nd}$   $\text{DM}_{(t=0)}$  of 0.51315 and  $^{147}\text{Sm}/^{144}\text{Nd}$   $\text{DM}_{(t=0)}$  of 0.2145 and  $^{147}\text{Sm}$   $\lambda = 6.54 \times 10^{-12}$  values of Goldstein et al. (1984) and  $^{176}\text{Lu}/^{177}\text{Hf}$   $\text{DM}_{(t=0)}$  of 0.0384 and  $^{176}\text{Hf}/^{177}\text{Hf}$   $\text{DM}_{(t=0)}$  of 0.28325 values of Griffin et al (2004) and  $\lambda = 1.87 \times 10^{-5}$  of Soderlund (2004) (Appendix D1). The NFT samples return enrichment ages between 495 Ma and 770 Ma with an overall average of 613 Ma, whereas Sm-Nd data from bulk titanite crystal concentrates return model enrichment ages of 551 Ma, 557 Ma and 665 Ma for AS18, BW4 and TZ-1, respectively. The Lu-Hf isotope data of NFT zircon return DM enrichment ages between 785 Ma and

635 Ma (average = 685 Ma). The Sm-Nd isotope DM ages for Panda Hill and the Lake Bed Tuff samples are 706 Ma (PH), 932 Ma (PUM), 889 Ma (HPT) and 676 Ma (Z5), whereas model Lu-Hf isotope ages of 974 Ma (PUM) and 1053 Ma (HPT) are produced from in-situ zircon analyses. The single bulk Lake Beds Group sample PY produces a Sm-Nd isotope model age of 847 Ma.

## 5.5 Discussion

Alkaline and carbonatite rocks of the EARS are considered excellent geochemical probes of mantle source regions. This is largely attributed to a general enrichment in trace elements, low magma temperatures and geologically rapid ascent rates associated with their parental magmas, all which can provide resistance against chemical and isotopic contamination (Bell and Tilton, 2001). The NFT have a characteristic mineral assemblage that is consistent with a phonolite-carbonatite source (Lawrence et al., 2020). Within this assemblage, trace element rich mineral phases (such as titanite, apatite and pyrochlore used in this study) offer the best opportunity to investigate the lithospheric source of the NFT, and an alternative approach for previously studied volcanic episodes in the region. The Panda Hill carbonatite and alkaline lavas of the Rungwe Volcanic Province have been shown previously (via whole-rock analysis) to retain the isotopic character of their mantle source (Furman, 1995; Bell and Tilton, 2001; Castillo et al., 2014). Therefore, the single crystal in-situ methods adopted for the Panda Hill and the Lake Bed tuff mineral separates presented in this study can be used to test the compatibility between conventional whole rock and in-situ isotope data in the Rukwa-Malai-Usangu region and, by extension, the accuracy and reliability of our results for the NFT.

Bell and Tilton (2001) provide  $^{143}\text{Nd}/^{144}\text{Nd}$  and  $^{87}\text{Sr}/^{86}\text{Sr}$  data for the Panda Hill carbonatite (including the data of Morisset (1993)) where initial  $\epsilon\text{Nd}$  values are between 0 and +0.6 ( $t = 116$  Ma, Cahen et al. (1984)). Recalculated using the new age for Panda Hill of 165 Ma as reported by Mesko et al. (2020) increases the  $\epsilon\text{Nd}$  values to between +1.2 to +1.8. Although  $^{87}\text{Sr}/^{86}\text{Sr}$  analyses were not conducted for Panda Hill in our work, we defer to the  $^{87}\text{Sr}/^{86}\text{Sr}$  values presented by Bell and Tilton (2001) (who consider these initial ratios due to exceedingly low Rb) of between 0.7037 and 0.7042 (Fig. 5.9) as representative. For the Cenozoic lavas of the Rungwe Volcanic Province, Furman and Graham (1994) report  $\epsilon\text{Nd}$  values between -0.4 and -4.5, and  $^{87}\text{Sr}/^{86}\text{Sr}$  of between 0.7046 and 0.7055. These values have since been corroborated by Castillo et al. (2014) who report  $^{143}\text{Nd}/^{144}\text{Nd}$  values between 0.512619 and 0.512417 ( $\epsilon\text{Nd}$  between -0.16 and -4.1;  $t = 0$  calculated here) and slightly extend the  $^{87}\text{Sr}/^{86}\text{Sr}$  range of Rungwe lavas to between 0.704603 and 0.706920 (Fig. 5.9).

Our measured in-situ data of Panda Hill apatite and pyrochlore ( $^{143}\text{Nd}/^{144}\text{Nd} = 0.512527 - 0.512594$ ;  $\epsilon\text{Nd}_{(i)} = +0.4$  to +1.6; Fig. 5.4) conform reasonably well with previous whole rock analyses (provide range; Fig. 5.8). Similarly, the reported sample averages and individual Sm-Nd isotope spot analyses of titanite ( $^{143}\text{Nd}/^{144}\text{Nd} = 0.512401 - 0.512573$ ;  $\epsilon\text{Nd} = -4.3$  to -0.7; Fig. 5.6) from the Lake Beds Group tuff samples are in agreement with ranges previously defined by Castillo et al. (2014) for whole-

rock analysis of uncontaminated lavas of the Rungwe Volcanic Province (Fig. 5.8). This is also the case for our bulk titanite Sm-Nd-Sr isotope results of Lake Bed tuff sample PY ( $^{143}\text{Nd}/^{144}\text{Nd} = 0.512456$ ;  $\epsilon\text{Nd} = -3.55$  and  $^{87}\text{Sr}/^{86}\text{Sr} = 0.706985$ ; Figs. 5.8 & 5.9), which returned values similar to the most isotopically enriched TAZ09-12 ( $^{143}\text{Nd}/^{144}\text{Nd} = 0.512417$  and  $^{87}\text{Sr}/^{86}\text{Sr} = 0.706920$ ) sample presented by Castillo et al. (2014). The average  $\epsilon\text{Hf}$  of -5.42 and -8.32 for the 8.7 Ma PUM and 3.5 Ma HPT Lake Bed Group tuffs (respectively) fall within range of those reported from whole-rock analysis of uncontaminated lavas elsewhere in the Western Branch ( $\epsilon\text{Hf} = -8.8$  to  $-0.1$ ) (Rosenthal et al., 2009).

Together, the high degree of compatibility between our in-situ data and the published bulk-rock data not only provide a robust temporal framework of the local lithosphere, but also demonstrate the capacity for in-situ analyses of single minerals to accurately reflect the magma source region in this locality, and hence to constrain the lithospheric source of primary igneous rocks even in cases where the rocks are altered and/or surface outcrop is unknown (e.g. for the NFT).

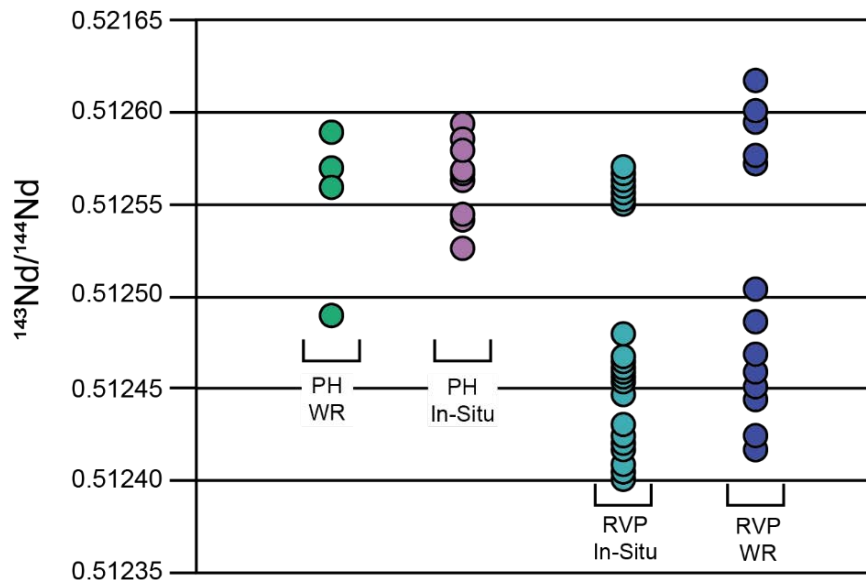


**Fig. 5.8** Comparison between whole rock (WR) and in-situ Sm-Nd isotopes  $^{143}\text{Nd}/^{144}\text{Nd}$  for Panda Hill (PH; Bell and Tilton (2001) and the Rungwe Volcanic Province (RVP; Castillo et al. (2014)). Note the general consistency in the ranges and values returned for both the PH and RVP, irrespective of method.

### 5.5.1 Isotopic constraints of the NFT

The resolution provided by our in-situ Sm-Nd isotope data capably resolves the observed discrepancy between bulk Sm-Nd-Sr isotope data of sample TZ-1 ( $\epsilon\text{Nd} = +0.49$ ) and those of BW4 and AS18 ( $\epsilon\text{Nd} = +2.02$  and  $+2.05$ , respectively). Where in-situ data of AS18 and BW4 agrees with bulk analyses, in-situ analyses of TZ-1 reveals the presence of two clearly distinct populations ( $\epsilon\text{Nd} = +0.6$  to  $+2.2$ ; and  $\epsilon\text{Nd} = -2$  to  $-4.7$ ) (Fig. 5.5). Our results for sample TZ-1 provides a resolution not attainable using bulk analyses whereby more than one population is present in a sample. Specifically, that single crystal analysis reliably detects individual populations, whereas bulk analysis may return a mixed

isotopic result. Notwithstanding, bulk analysis of NFT samples form a restricted array around values of  $\epsilon\text{Nd} +2$  to 0 (consistent with Spandler et al. (2016)) and  $^{87}\text{Sr}/^{86}\text{Sr}$  of 0.704171 to 0.704303 (Figs. 5.8 & 5.9). Although a slight variation observed within the representative in-situ Sm-Nd data of the NFT may reflect two overlapping yet discrete populations (i.e. at  $\epsilon\text{Nd} +1.5$  and  $+0.5$  respectively; Figs. 5.5 & 5.8), they remain well within values previously reported for East African carbonatites including the nearby Panda Hill (Bell and Tilton, 2001; Rooney, 2020 and references therein; Fig. 5.9) and are thus considered representative of their mantle origin.

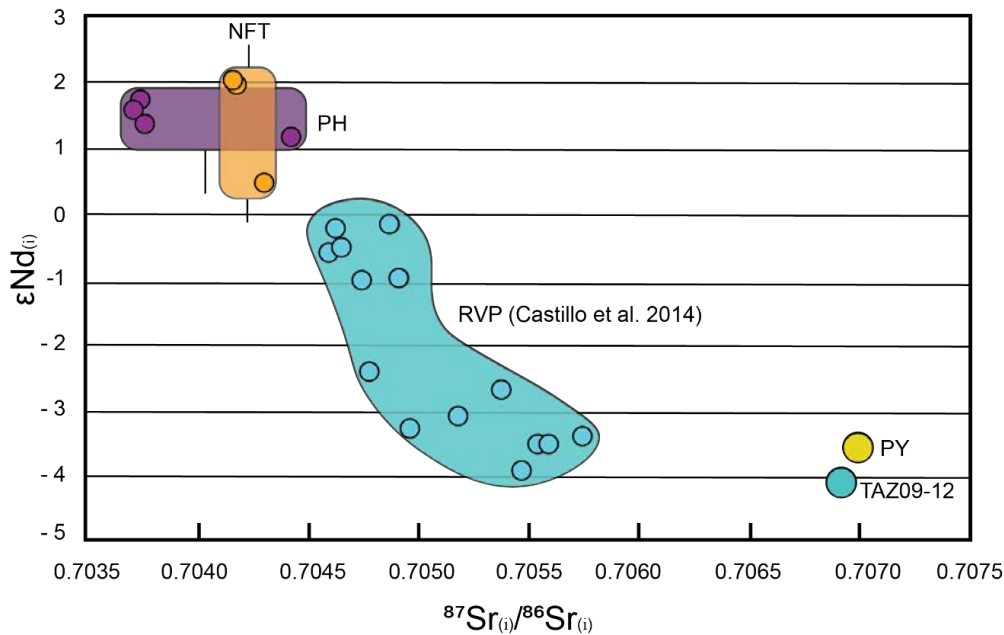


**Fig. 5.9**  $^{87}\text{Sr}/^{86}\text{Sr}$  vs initial  $\epsilon\text{Nd}$  diagram. for Panda Hill (PH; purple), the NFT (orange) and the Rungwe Volcanic Province (blue/yellow). Circle symbols correspond to whole rock data points, while the fields represent hypothetical isotopic space based on the variation in whole rock data. N.B. whiskers on PH and NFT fields represent the total variations in  $\epsilon\text{Nd}$  returned via in-situ analysis. Samples PY (yellow; this study) and TAZ09-12 of Castillo et al. (2014) are the most isotopically enriched analyses of the RVP.

While the trace element enrichment observed in alkaline magmas (and in this case igneous crystals) is considered beneficial in buffering against isotopic contamination, discriminating between possible causes of isotopic variability (i.e. crustal contamination/mixing of mantle sources) can prove difficult (i.e. in the case of TZ-1). The outlying TZ-1 population with respect to in-situ Sm-Nd isotopes ( $\epsilon\text{Nd} = -2$  to  $-4.7$ ) is notably different to both bulk and in-situ NFT analyses in this study and elsewhere (Spandler et al., 2016, Lawrence et al., Chapter 3, *in review*). Our data shows scant evidence of an apparent gradual mixing (i.e. progressive range between endmembers), rather two distinct populations are present. Crustal assimilation (of Proterozoic basement) and/or primary generation from a more radiogenic lithospheric source are competing possibilities that may be considered in order to account for the observed outliers

The Ubendian Proterozoic basement traversed by NFT magmas en-route to the surface is significantly enriched ( $\epsilon\text{Nd} > -21$ ; Manyá et al., 2011). Previously, Lawrence et al., (Chapter 3, *in review*) utilised the Sm-Nd isotopic values of NFT titanite and  $\text{SiO}_2$  content of entrapped melt inclusions to generate a crustal assimilation model and investigate closed vs open system magma evolution in their genesis. Here, no link was found between increasing silica content of the melt and radiogenic  $\epsilon\text{Nd}$ , as would be expected to occur during crustal assimilation. Furthermore, trace element analyses of NFT titanite and melt inclusions (including samples AS18, BW4 and TZ-1) did not find any notable indicators of crustal assimilation such as the emergence of an Eu anomaly, a prominent feature of both Proterozoic and Archean crust beneath the Rukwa Rift (Manyá et al., 2011; Lawrence et al., 2020; Lawrence et al., Chapter 3, *in review*). Nevertheless, assuming a primary mantle value of  $\epsilon\text{Nd} +1.5$  for the NFT the crustal assimilation model indicates approximately 15-25% of the Proterozoic must be incorporated to account for the enriched values of TZ-1 ( $\epsilon\text{Nd} -2.2 - 4.7$ ) (Lawrence et al., Chapter 3, *in review*).

An alternative consideration is that the more radiogenic TZ population are within the total range of uncontaminated lavas of the Rungwe Volcanic Province and thus may represent the contribution of additional lithospheric mantle (rather than crustal) component present locally (Furman, 1995; Castillo et al., 2014; Mesko, 2020). Given the inability to investigate this more carefully (due to the limited and extensively altered nature of the sample), for the purposes of this study we defer to the coherent  $\epsilon\text{Nd}$  population ( $\epsilon\text{Nd} = +0.6$  to  $+2.2$ ) as representative for TZ-1 and an overall mantle source value of  $\epsilon\text{Nd} = 1.5 \pm 1$  for the NFT, which is consistent with previous investigations (Spandler et al., 2016; Lawrence et al., Chapter 3, *in review*) and the bulk analyses of this study.

Our in-situ Hf isotope analyses of NFT zircon (average  $\epsilon\text{Hf} = -0.23$ ) are limited making it difficult to integrate these data with already limited published literature. Lutetium-Hf isotopic data for whole rock ( $\epsilon\text{Hf} = -10.9$ ) and non-carbonate fractions ( $\epsilon\text{Hf} = +6.6$ ) of Panda Hill samples are reported by Bizimis et al. (2003); however, the large discrepancy and scarcity of these data provide little context for the NFT. Moreover, these data highlight the potential disequilibrium of Lu-Hf isotopes shown to occur in mixed silicate-carbonatite sources, melts and products (Bizimis et al., 2003). Given that our Lu-Hf data is of in-situ zircon and analysis the carbonate or whole rock fractions is not possible (due to the nature of the samples), disequilibrium remains an important consideration for these data. Nonetheless, our data for the NFT are within range of the upper limits reported by Rosenthal et al. (2009) for Western Rift lavas.

### ***5.5.2 Isotopic evolution through time***

The Sm-Nd-Sr isotopic data of the NFT overlap values previously reported for the Panda Hill carbonatite and are less enriched with respect to both Nd and Sr isotopes than values reported for the uncontaminated lavas of the Rungwe Volcanic Province (Fig. 5.9). These data suggest that the lithospheric source region responsible for local carbonatite magmatism from 165 Ma – 25 Ma may be

isotopically distinct from that of late Miocene – recent magmatism in the Rungwe Volcanic Province for which there is no known carbonatite association. Temporally, the in situ Sm-Nd isotope data of Panda Hill, NFT, and Lake Beds Group tuff samples (and the bulk Sm-Nd-Sr isotope data of Castillo et al. (2014) and Bell and Tilton (2001) of the modern Rungwe lavas and Panda Hill, respectively) are consistent with the contribution of a more isotopically enriched lithospheric source in modern Rungwe lavas. In this sense, the isotopic signature of magmatic products locally from 25 Ma, becomes increasingly enriched, with reducing  $\epsilon_{\text{Nd}}$  and increasing  $^{87}\text{Sr}/^{86}\text{Sr}$  through time (Figs. 5.9 & 5.10). Similarly,  $\epsilon_{\text{Hf}}$  of NFT zircon are comparatively more positive than both the Lake Bed tuff zircon and whole-rock samples from elsewhere in the Western Branch (Rosenthal et al., 2009). Consistent with Sr-Nd isotope data, a progressive enrichment through time is also reflected in the Lu-Hf isotopic system with  $\epsilon_{\text{Hf}} = -0.23$  (25 Ma),  $\epsilon_{\text{Hf}} = -5.42$  (8.7 Ma) and  $\epsilon_{\text{Hf}} = -8.32$  (3.5 Ma) for the NFT and Lake Bed tuffs, respectively (Figs. 5.7 & 5.10).

### 5.5.3 Isotopic characteristics and possible lithospheric sources for the NFT

In synthesising the isotopic data collected from Cenozoic rift lavas of the EARS over the past few decades, Rooney (2020) condensed proposed models for rift magmatism into those that emphasise: the presence of a plume, the absence of a plume (i.e. predominantly lithospheric), or a hybrid (influence of both plume and lithosphere components). Within these models, potential isotopic reservoirs (source regions) of rift lavas include the convecting (depleted) upper mantle, enriched metasomatic assemblages i.e. amphibole-, phlogopite- and carbonate-bearing metasomes within the continental lithosphere (lithospheric source) and Plume-“C” (linked to the African LLSVP, high  $^3\text{He}/^4\text{He}$  ratios and otherwise isotopically typified in the Afar; Fig. 5.11) (Rooney, 2020).

The similarity between in-situ and bulk-rock Sm-Nd-Sr isotope analyses of Panda Hill and the NFT indicates they may share a common lithospheric source and/or process of formation. Unlike the majority of available Rungwe data, the NFT (and Panda Hill) data reside within a field previously defined for the Rungwe Volcanic Province by (Castillo et al., 2014) as Plume-V (Fig. 5.11). The proposed Plume-V source is isotopically constrained via the Nd-Sr-Pb isotopic signatures of the Nyiragongo volcano of the Virunga Volcanic Province (Chakrabarti et al., 2009); and via elevated  $^3\text{He}/^4\text{He}$  ratios ( $>9 R_A$ ) measured throughout the EARS (Castillo et al., 2014) (Fig 5.11). Importantly, while the presence of high  $^3\text{He}/^4\text{He}$  ratios in young Rungwe lavas and ubiquity of this signature extending throughout the Eastern Branch to the Afar substantiates the presence and contribution of a deeply-sourced mantle plume, the  $^3\text{He}/^4\text{He}$  ratios and modelled isotopic mixing between Plume-V and lithospheric reservoirs (as suggested by Castillo et al. (2014)) are inconsistent with the Sr-Nd isotope data. As shown in Fig. 5.11, the Sr-Nd isotope data of Castillo et al. (2014) sees the highest  $^3\text{He}/^4\text{He}$  ratios (proposed greatest plume influence) plot further away from the proposed “Plume-V” endmember in Sm-Nd isotopic space. Rooney (2020) also notes discrepancies in the  $^3\text{He}/^4\text{He}$  with respect to the Pb isotopic data presented of the proposed Plume-V. Thus, the enrichment we observe in local magmatism

from 25 Ma to 8.7 Ma (i.e. a reduction in  $^{143}\text{Nd}/^{144}\text{Nd}$  and increase in  $^{87}\text{Sr}/^{86}\text{Sr}$  ratios, as well as decrease in  $\epsilon\text{Hf}$  in our data), and the mixture of isotopic ratios for the Rungwe Volcanic Province (presented in this study and by Castillo et al., (2014)), is independent of the deep “Plume” source that is likely responsible for elevated  $^3\text{He}/^4\text{He}$  ratios measured at this locality.

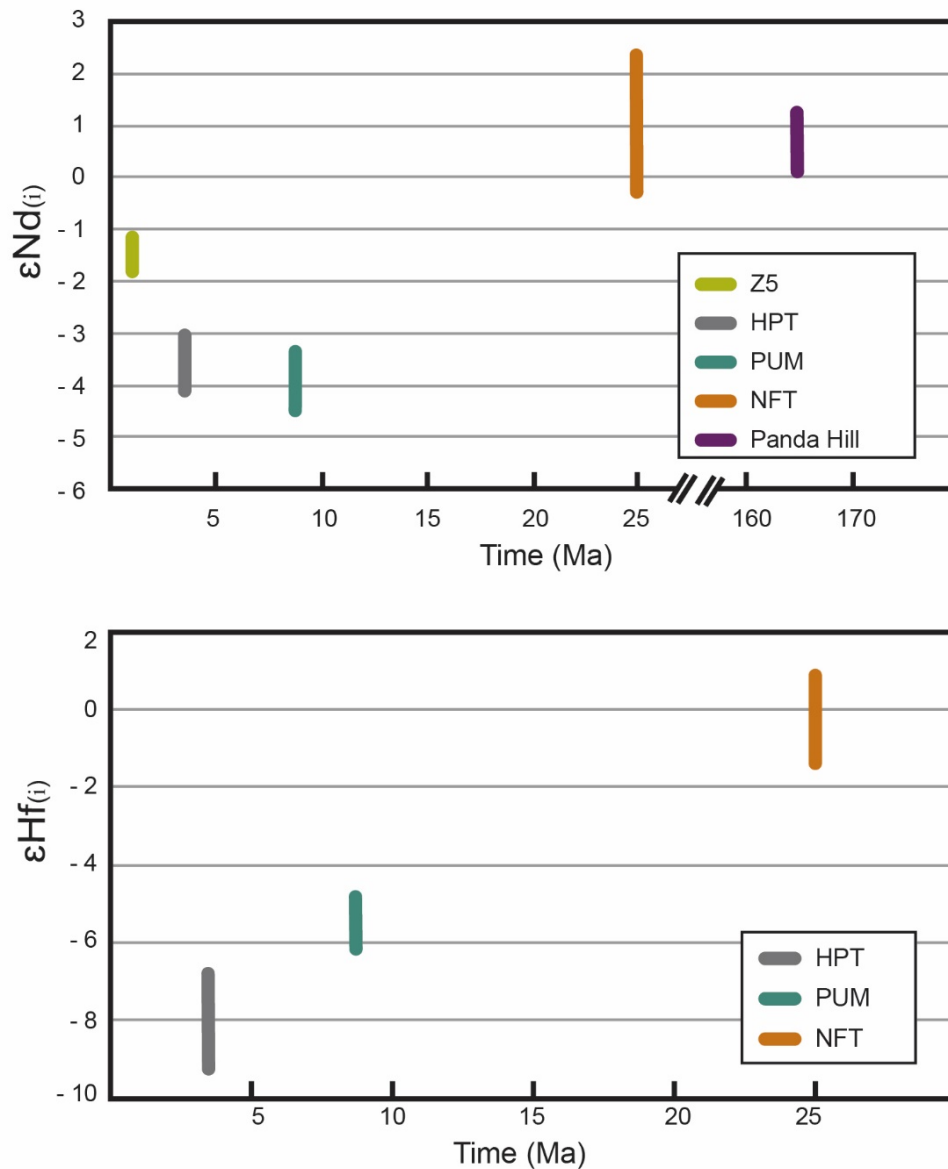


**Fig. 5.10** Epsilon Nd and Hf variation with time. In-situ Sm-Nd isotope (presented as epsilon Nd) and Lu-Hf isotope (presented as epsilon Hf) compositions for alkaline magmas of the Rukwa Rift and Rungwe volcanic province versus time (Ma).

An alternative offered by (Rooney, 2020) is that the Sr-Nd isotopic composition of the plume reservoir responsible for high  $^3\text{He}/^4\text{He}$  throughout the EARS reflects that of the Afar Plume (Plume “C”; Fig. 5.11) and the region termed Plume-V (where the NFT reside, Fig. 5.11) more likely represents the “common lithospheric mantle”. As described by Furman and Graham (1999), this reservoir formed as a

result of regional carbonatite metasomatic events impacting the base of the lithosphere surrounding the Tanzanian Craton (between 1000 – 500 Ma). In such a model, the trace element and isotopic expression of rift lavas is intimately linked to the presence and melt-contribution of volatile-rich assemblages in the mantle source (i.e. carbonate-, amphibole- and/or phlogopite-bearing mantle metasomes). Herein, isotopic variance observed within (and between) volcanic regions of the EARS reflects localised lithospheric heterogeneity. The heterogeneity itself reflects the metasomatic (orogenic) and/or melting histories of individual volcanic provinces.

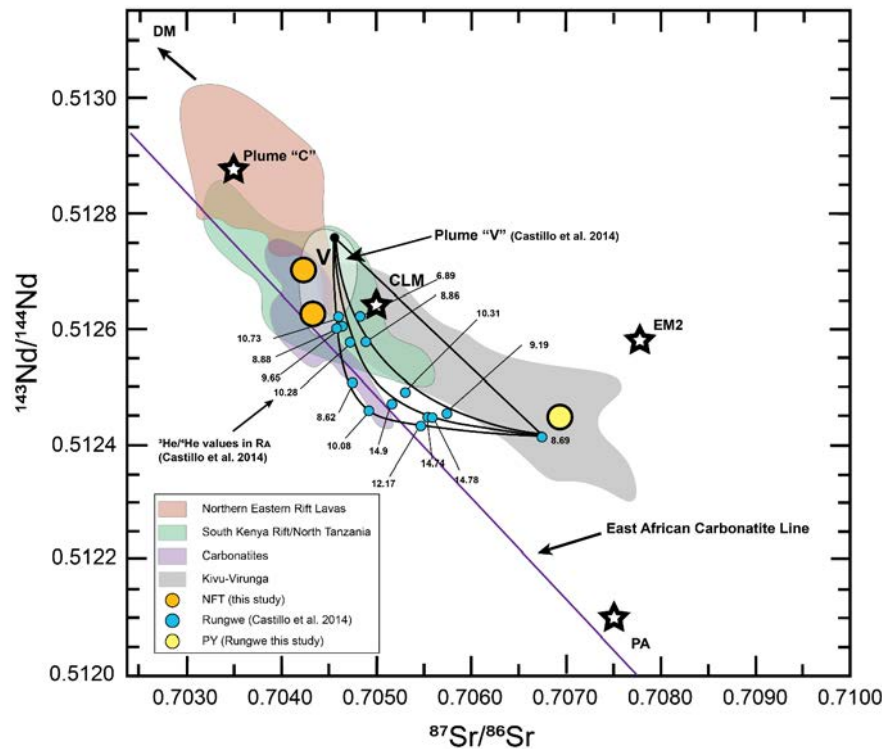


**Fig. 5.11**  $^{87}\text{Sr}/^{86}\text{Sr}$ - $^{143}\text{Nd}/^{144}\text{Nd}$  data of mafic Quaternary rocks throughout East Africa (adapted from Rooney (2020)) with the addition of bulk isotopic data of the NFT and PY (this study) and the individual points for whole rock isotopic data of Castillo et al. (2014). The Pan African lithosphere (PA), Depleted Mantle (DM) and Afar Plume “C” endmembers are from Rooney et al., (2012), CLM component is that of Furman and Graham (1999) and the East African Carbonatite line is from Bell and Tilton (2001). Note, the Plume-V component and proposed mixing curves (from Castillo et al. (2014)) for Rungwe samples are inconsistent with the reported  $^3\text{He}/^4\text{He}$  ratios for each respective sample (shown in  $R_A$ ). The NFT (significantly older than data fields shown for Quaternary rocks) isotopic reservoir is consistent with other East African carbonatites and youngest rocks of the South Kenya/North Tanzania rift lavas emplaced on cratonic lithosphere subjected to the Pan-African orogeny. The isotopic evolution and variation observed in modern Rungwe lavas more closely resembles that of the Kivu-Virunga western rift volcanic provinces whereby more complex and ancient lithospheric mantle components proposedly exist.

The convergent-margin orogens surrounding the Tanzanian Craton represent a mechanism to create local, isotopically-enriched assemblages in the lithosphere via subduction-related metasomatism. As highlighted by previous studies, successive orogenic events may have produced multiple distinct metasomatic reservoirs that persist in the continental lithosphere of the Western Branch (Furman, 1995; Rogers et al., 1998; Furman and Graham, 1999). Isotopic studies within the East African Rift and continental rifts elsewhere (e.g. the Labrador Sea) conceptualise this as a layered lithosphere (Furman, 1995; Rogers et al., 1998; Furman and Graham, 1999; Tappe et al., 2007). In such a model the youngest and least isotopically-enriched reservoir exists at the base and is the first to contribute melt at the onset of rift development. Where the lithospheric mantle is metasomatised by mafic silicate melts (producing Fe-Ti-, pyroxene- and garnet-rich assemblages) and/or volatile-rich fluids (producing phlogopite-, amphibole- and carbonate-rich veins) it retains a lower melting temperature than the surrounding asthenosphere (Furman, 2016). When thermo-mechanically perturbed, volatile-rich assemblages produce low viscosity melts that contribute disproportionately to early magma genesis. Consequently, the remnant denser metasomatic assemblages are gravitationally unstable and prone to foundering in the surrounding mantle asthenosphere (Furman, 2016). With continued melting, destabilisation and lithospheric thinning, more ancient and isotopically-enriched regions become exposed to melting (and/or thermally perturbed) and contribute to the isotopic character of lavas erupting at the surface.

If we consider this model of a layered lithosphere, the earliest-formed (i.e., oldest) local magmas (Panda Hill and the NFT) will incorporate the most recently-formed metasomatic assemblages (i.e. youngest lithospheric reservoirs) with the contribution of more ancient and isotopically enriched regions being expressed in the younger lavas. With reference to our calculated depleted mantle (DM) enrichment ages of between 785 Ma and 495 Ma from both Sm-Nd and Lu-Hf isotope data, both the NFT and Panda Hill magmas appear to be the melt products of an enriched lithospheric source that coincides with the Pan-African orogeny (550-700 Ma). The respective Sm-Nd and Lu-Hf isotope mantle enrichment ages calculated for the Lake Beds Group tuff samples (889 Ma and 1053 Ma) reflect a of period lithospheric enrichment that broadly coincides with the Irumide orogeny at ~1 Ga. Collectively, these data are generally consistent with melting of a layered lithosphere, with local removal of the Pan-African aged enriched base occurring between 25 Ma and 8.7 Ma.

The hypothesis that the enriched signatures observed for the Rungwe Volcanic Province are indeed that of exposure and melting of more ancient lithospheric assemblages, necessitates that the local lithosphere beneath the Rungwe has experienced a degree of thinning. Until very recently, this prediction of the layered lithosphere concept was unsubstantiated. However, recent geophysical studies focused on the northern Malawi Rift extending to the Rungwe Volcanic Province now reveal a mantle lithosphere that is indeed anomalously thinned and suggest that this occurred prior (or during) the very early stages of EARS development (Laó-Dávila et al., 2015; Borrego et al., 2018; Grijalva et al., 2018; Tepp et al., 2018; Njinju et al., 2019; Hopper et al., 2020).

Geophysical evidence of a thinned lithosphere beneath the Rungwe Volcanic province and discovery of the NFT in the Oligocene sedimentary archive of the early Rukwa Rift are indeed supportive of early lithospheric perturbation and rift development (Roberts et al., 2012; Hopper et al., 2020). The radiogenic isotope data presented here provide useful temporal constraints as to when such an event may have occurred, which appears to be coeval with rift development in the Eastern Branch (~30-25 Ma). In continuing to draw on evidence across the geosciences, a more complete hypothesis and conceptual model for geological history for the Rukwa Rift is presented for future consideration (Fig. 5.12).

Fig. 5.12 see next page for caption.

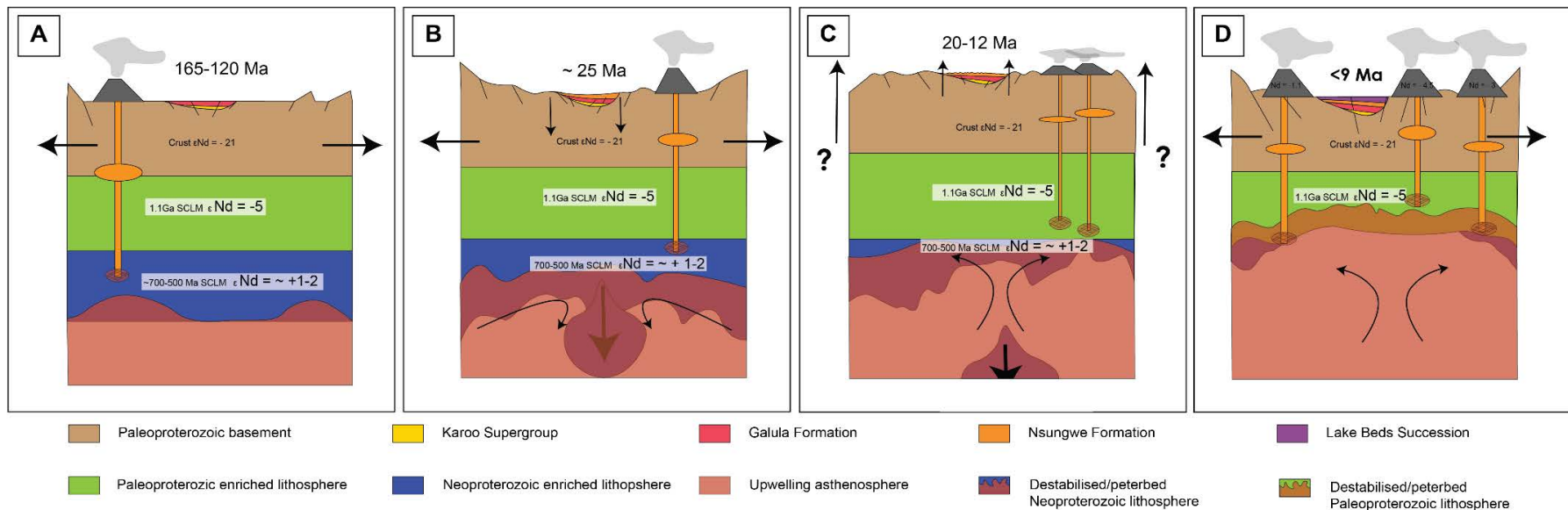


**Fig. 5.12** Geological evolution of the Rukwa Rift and Rungwe Volcanic Province. **A)** Stage 1: Late Jurassic to Cretaceous: Crustal extension, basin subsidence and deposition accompanied by decompression melting produces carbonatite volcanism at Panda Hill from Pan-African-aged metasomatised lithosphere. **B)** Stage 2: Late Oligocene: Slowing of the African plate over the LLSVP causes chemical and mechanical destabilisation (shown here as a drip) of the Pan-African metasomatised lithospheric mantle beneath the Rukwa-Malawi-Usangu junction. This produces an early punctuated episode of basin subsidence and deposition of the Nsungwe Formation accompanied by the phonolite-carbonatite volcanism of the NFT. Lithospheric foundering (sagging of the crust) sees the structural reactivation of the Rukwa Rift and a shift in paleo-drainage pattern towards and inwardly draining basin (Roberts et al., 2010, 2012). The thermo-chemical destabilisation of the lithospheric mantle produced the accompanying carbonatite magmatism of the NFT; the isotopic signatures of which reflects production from dominantly Pan-African metasomatised mantle lithosphere (metasomes). **C)** Stage 3: Early-mid Miocene: Isostatic rebound of the crust after lithospheric detachment. Continual melting of remnant Pan-African and newly exposed Irumide lithosphere produces magmatism. Devolatilisation of sinking drip and melt interaction produces hybridised Pan-African/Irumide isotopic reservoirs (metasomes) in the heterogeneous continental lithosphere. No basin subsidence or deposition is known during this time, instead the Red Sandstone Group likely underwent denudation/erosion due to regional uplift. **D)** Stage 4: Late Miocene to present: Continued heating of exposed ancient mantle lithosphere throughout the Miocene facilitates extension, thermal uplift of rift flanks and basin formation accompanied by more voluminous bi-modal magmatism in the RVP. The isotopic character of accompanying voluminous magmatism in RVP reflects the incorporation and mixing between newly-exposed Irumide-aged enriched lithosphere (and/or metasomes) and hybridised lithosphere (and/or metasomes) produce via prior melting of Pan-African lithosphere

#### ***5.5.4 Model of the geological evolution of the Rukwa Rift Basin and Rungwe Volcanic Province***

The Late Jurassic to recent volcanic and sedimentary history of the Rukwa Rift Basin can be summarised into four stages: (1) depositional regime accompanied by carbonatite volcanism at Panda Hill during the Late Jurassic-Cretaceous (Morisset, 1993; Roberts et al., 2010; Mesko et al., 2020); (2) an early punctuated episode of deposition accompanied by the alkaline-carbonatite volcanism of the NFT in the late-Oligocene (26-25 Ma) (Roberts et al., 2010, 2012); (3) a period of Miocene volcanism in the Usangu Basin and Rungwe Volcanic Province (19-14 Ma) during which the sedimentary archive records an erosional discontinuity (Rasskazov et al., 2003; Roberts et al., 2010; Mtelela et al., 2017; Mesko et al., 2020); followed by (4) late-Miocene to recent extension and deposition accompanied by more voluminous bimodal magmatism in the Rungwe Volcanic Province (ca. 9 Ma to present) (Fontijn et al., 2012; Hilbert-Wolf et al., 2017; Mtelela et al., 2017). In addition, sedimentary provenance and paleo-drainage analysis of the Rukwa Rift Basin records a shift from NW-SE sediment supply and drainage regime to an inwardly draining basin at the onset of stage 2 (Roberts et al., 2010). Geophysical (Hopper et al., 2020) and isotopic investigations (this study) indicate the mantle lithosphere experienced thinning in the time between stage 2 and 3 (25 to 9Ma) during which the Rukwa Rift Basin experienced uplift, tilting and erosion of the Nsungwe Formation (evidenced by a significant basal conglomerate at the base of the Lake Beds Group) prior to the modern extension regime of stage 4 (Roberts et al., 2012; Mtelela et al., 2017).

A significant reduction in the northward motion of the African plate resulted in a stagnation of Eastern Africa over the African LLSVP coincided with the initiation phases of rift development in both the Eastern and Western Branches of the EARS between 30-25 Ma (O'Connor et al., 1999; Roberts et al., 2012; Rooney, 2017). In the Rukwa Rift, stagnation of the African plate over the LLSVP contributed to the relative pooling of upwelling material against the southernmost cratonic root of the Tanzanian Craton and the destabilisation of the lower lithospheric mantle beneath the Rungwe Volcanic Province (Tepp et al., 2018; Hopper et al., 2020). Physical destabilisation resulted in the structural reactivation and sagging of the Rukwa Rift Basin, as evidenced by a shift in paleo-drainage (draining inwardly) and the development of a lacustrine depositional regime at 26-25 Ma (Roberts et al., 2010, 2012). The thermo-chemical destabilisation of the lower lithospheric mantle produced the accompanying carbonatite magmatism of the NFT; the isotopic signatures of which reflects production from Pan-African aged metasomatised mantle lithosphere.

The above geological observations and subsequent period of basin inversion and erosion (ca. 23-9 Ma) recorded in the stratigraphy of the Rukwa Rift Basin, and persistent magmatism throughout the Miocene in and around the Rungwe Volcanic Province (Rasskazov et al., 2003; Mesko et al., 2020) is consistent with isostatic rebound and continued melt contribution to surface volcanism following detachment of a foundering lithosphere (drip; shown in Fig. 5.12) (Furman et al., 2016). Heating of exposed ancient mantle lithosphere throughout the Miocene facilitated the extensional regime in the

present day Rukwa Rift Basin. As shown here, the isotopic character of accompanying voluminous magmatism in the Rungwe Volcanic Province reflects the incorporation and potential mixing between newly-exposed Irumide-aged enriched lithosphere and that responsible for the NFT (i.e. peripherally exposed or sinking Pan-African mantle). In agreement with the suggestions of Furman et al. (2016), the occurrence of lithospheric detachments may be essential in the evolution of magmatism elsewhere in the EARS, but particularly in the Western Branch where volcanism is most prevalent in isolated inter-basinal volcanic provinces superimposed on ancient and complex lithospheric terrains. The progressive isotopic enrichment and increased variability of localised intraplate magmas, as observed here may offer an additional line of evidence for such a process.

## 5.6 Conclusions

The lithospheric foundations of the Western Branch record a complex and long-lived metasomatic history that has a profound influence on the isotopically-enriched and variable character of western rift lavas. Evidently, the timing and nature of processes governing continent formation exert a strong influence on these same parameters during continental-scale tectonic stress and ultimately break-up. Single crystals from heavily-altered volcanogenic strata of the Rukwa Rift Basin capably record and preserve the character and evolution of the lithospheric mantle in the RMU region. With these data we conclude that:

- The earliest manifestation of magmatism associated with the development of the Western Branch at 25 Ma (NFT) appear to be generated from a long-lived and common lithospheric component that may have persisted or replenished beneath the Rungwe-Malawi-USangu locality since the Mid-Mesozoic. These compositions are observed in the carbonatite and uncontaminated Quaternary lavas of Southern Kenya and Northern Tanzania, proximal to the Tanzanian Craton and Pan-African aged Mozambique Belt suture zone.
- The isotopic variability observed in lavas from the mid Miocene-Recent Rungwe Volcanic Province (combined with geophysical and sedimentological data), enable the hypothesis of a layered lithosphere that experienced thinning (via lithospheric foundering) at the end of the Oligocene to be presented for the Rungwe-Malawi-USangu region. In such a scenario, the presence and mixing between eroded Pan-African- and recently exposed Irumide-aged enriched lithosphere is the primary influencing factor on the isotopic fingerprint of Rungwe lavas.
- The concept of drip magmatism and a layered lithosphere may play an important role in the evolution of the Kivu, Virunga and Toro-Ankole volcanic provinces of the Western Rift. This hypothesis warrants further consideration and testing.

**References**

- Bagley, B., Nyblade, A.A., 2013. Seismic anisotropy in eastern Africa, mantle flow, and the African superplume. *Geophysical Research Letters*, 40(8): 1500-1505.
- Begg, G. et al., 2009. The lithospheric architecture of Africa: Seismic tomography, mantle petrology, and tectonic evolution. *Geosphere*, 5(1): 23-50.
- Bell, K., Tilton, G., 2001. Nd, Pb and Sr isotopic compositions of East African carbonatites: evidence for mantle mixing and plume inhomogeneity. *Journal of Petrology*, 42(10): 1927-1945.
- Bizimis, M., Salters, V.J., Dawson, J.B., 2003. The brevity of carbonatite sources in the mantle: evidence from Hf isotopes. *Contributions to Mineralogy and Petrology*, 145(3): 281-300.
- Borrego, D. et al., 2018. Crustal structure surrounding the northern Malawi rift and beneath the Rungwe Volcanic Province, East Africa. *Geophysical Journal International*, 215(2): 1410-1426.
- Cahen, L. et al., 1984. The geochronology and evolution of Africa.
- Castillo, P.R., Hilton, D.R., Halldórsson, S.A., 2014. Trace element and Sr-Nd-Pb isotope geochemistry of Rungwe Volcanic Province, Tanzania: implications for a superplume source for East Africa Rift magmatism. *Frontiers in Earth Science*, 2: 21.
- Chakrabarti, R., Basu, A.R., Santo, A.P., Tedesco, D., Vaselli, O., 2009. Isotopic and geochemical evidence for a heterogeneous mantle plume origin of the Virunga volcanics, Western rift, East African Rift system. *Chemical Geology*, 259(3-4): 273-289.
- Chorowicz, J., 2005. The east African rift system. *Journal of African Earth Sciences*, 43(1-3): 379-410.
- Dawson, J., 1992. Neogene tectonics and volcanicity in the North Tanzania sector of the Gregory Rift Valley: contrasts with the Kenya sector. *Tectonophysics*, 204(1-2): 81-92.
- Delvaux, D., Kervyn, F., Macheyeky, A., Temu, E., 2012. Geodynamic significance of the TRM segment in the East African Rift (W-Tanzania): Active tectonics and paleostress in the Ufipa plateau and Rukwa basin. *Journal of Structural Geology*, 37: 161-180.
- Ebinger, C.J., 1989. Tectonic development of the western branch of the East African rift system. *Geological Society of America Bulletin*, 101(7): 885-903.
- Ebinger, C.J., Deino, A.L., Drake, R., Tesha, A., 1989. Chronology of volcanism and rift basin propagation: Rungwe volcanic province, East Africa. *Journal of Geophysical Research: Solid Earth*, 94(B11): 15785-15803.
- Ebinger, C.J., Sleep, N., 1998. Cenozoic magmatism throughout east Africa resulting from impact of a single plume. *Nature*, 395(6704): 788-791.
- Foley, S., Link, K., Tiberindwa, J., Barifaijo, E., 2012. Patterns and origin of igneous activity around the Tanzanian craton. *Journal of African Earth Sciences*, 62(1): 1-18.
- Fontijn, K. et al., 2010a. Tectonic control over active volcanism at a range of scales: Case of the Rungwe Volcanic Province, SW Tanzania; and hazard implications. *Journal of African Earth Sciences*, 58(5): 764-777.

- Fontijn, K. et al., 2010b. Holocene explosive eruptions in the Rungwe Volcanic Province, Tanzania. *Journal of volcanology and geothermal research*, 196(1-2): 91-110.
- Fontijn, K., Williamson, D., Mbede, E., Ernst, G.G., 2012. The Rungwe volcanic province, Tanzania—a volcanological review. *Journal of African Earth Sciences*, 63: 12-31.
- Fritz, H. et al., 2005. Central Tanzanian tectonic map: a step forward to decipher Proterozoic structural events in the East African Orogen. *Tectonics*, 24(6).
- Furman, T., 1995. Melting of metasomatized subcontinental lithosphere: undersaturated mafic lavas from Rungwe, Tanzania. *Contributions to Mineralogy and Petrology*, 122(1-2): 97-115.
- Furman, T., 2007. Geochemistry of East African Rift basalts: an overview. *Journal of African Earth Sciences*, 48(2-3): 147-160.
- Furman, T., Graham, D., 1994. Chemical and isotopic variations in volcanic rocks from the Rungwe Province: constraints on the development and scales of source heterogeneity beneath the African Western Rift. *Mineralogical Magazine*, 58(1): 297-298.
- Furman, T., Graham, D., 1999. Erosion of lithospheric mantle beneath the East African Rift system: geochemical evidence from the Kivu volcanic province, *Developments in Geotectonics*. Elsevier, pp. 237-262.
- Furman, T., Nelson, W.R., Elkins-Tanton, L.T., 2016. Evolution of the East African rift: Drip magmatism, lithospheric thinning and mafic volcanism. *Geochimica et Cosmochimica Acta*, 185: 418-434.
- Grijalva, A. et al., 2018. Seismic evidence for plume-and craton-influenced upper mantle structure beneath the northern Malawi rift and the Rungwe volcanic province, East Africa. *Geochemistry, Geophysics, Geosystems*, 19(10): 3980-3994.
- Halldórsson, S.A., Hilton, D.R., Scarsi, P., Abebe, T., Hopp, J., 2014. A common mantle plume source beneath the entire East African Rift System revealed by coupled helium-neon systematics. *Geophysical Research Letters*, 41(7): 2304-2311.
- Hammerli, J., Kemp, A., Spandler, C., 2014. Neodymium isotope equilibration during crustal metamorphism revealed by in situ microanalysis of REE-rich accessory minerals. *Earth and Planetary Science Letters*, 392: 133-142.
- Hauzenberger, C. et al., 2014. Termination of the southern irumide belt in Tanzania: zircon U/Pb geochronology. *Precambrian Research*, 255: 144-162.
- Hilbert-Wolf, H. et al., 2017. Application of U–Pb detrital zircon geochronology to drill cuttings for age control in hydrocarbon exploration wells: A case study from the Rukwa Rift Basin, Tanzania. *AAPG Bulletin*, 101(2): 143-159.
- Hilton, D.R. et al., 2011. Helium isotopes at Rungwe Volcanic Province, Tanzania, and the origin of East African plateaux. *Geophysical Research Letters*, 38(21).
- Hopper, E. et al., 2020. Preferential localized thinning of lithospheric mantle in the melt-poor Malawi Rift. *Nature Geoscience*, 13(8): 584-589.

- Kampunzu, A., Lubala, R., 2012. Magmatism in extensional structural settings: the Phanerozoic African plate. Springer Science & Business Media.
- Kilembe, E.A., Rosendahl, B.R., 1992. Structure and stratigraphy of the Rukwa rift. *Tectonophysics*, 209(1-4): 143-158.
- Laó-Dávila, D.A., Al-Salmi, H.S., Abdelsalam, M.G., Atekwana, E.A., 2015. Hierarchical segmentation of the Malawi Rift: The influence of inherited lithospheric heterogeneity and kinematics in the evolution of continental rifts. *Tectonics*, 34(12): 2399-2417.
- Lawrence, L., Spandler, C., Roberts, E., Hilbert-Wolf, H., 2020. Mineralogy and origin of the alkaline Nsungwe Formation tuffs of the Rukwa Rift Basin, southwestern Tanzania. *Lithos*: 105885.
- MacDonald, R., Rogers, N., Fitton, J., Black, S., Smith, M., 2001. Plume–lithosphere interactions in the generation of the basalts of the Kenya Rift, East Africa. *Journal of Petrology*, 42(5): 877-900.
- Mesko, G.T., 2020. Magmatism at the southern end of the east african rift system: Origin and role during early stage rifting. Columbia University.
- Morisset, N., 1993. Stable isotope and radioisotope geochemistry of the Panda Hill carbonatite, Tanzania.
- Morley, C., Cunningham, S., Harper, R., Wescott, W.A., 1992a. Geology and geophysics of the Rukwa rift, East Africa. *Tectonics*, 11(1): 69-81.
- Morley, C.K., Wescott, W.A., Stone, D.M., Harper, R.M., Wigger, S.T. and Karanja, F.M., 1992b. Tectonic evolution of the northern Kenyan Rift. *Journal of the Geological Society*, 149(3), pp.333-348.
- Morley, C., Vanhauwaert, P., De Batist, M., 2000. Evidence for high-frequency cyclic fault activity from high-resolution seismic reflection survey, Rukwa Rift, Tanzania. *Journal of the Geological Society*, 157(5): 983-994.
- Mtelela, C., Roberts, E.M., Downie, R., Hendrix, M.S., 2016. Interplay of structural, climatic, and volcanic controls on late quaternary lacustrine–deltaic sedimentation patterns in the Western Branch of the East African Rift System, Rukwa Rift Basin, Tanzania. *Journal of sedimentary research*, 86(10): 1179-1207.
- Mtelela, C. et al., 2017. Sedimentology and paleoenvironments of a new fossiliferous late Miocene–Pliocene sedimentary succession in the Rukwa Rift Basin, Tanzania. *Journal of African Earth Sciences*, 129: 260-281.
- Muravyeva, N., Belyatsky, B., Senin, V., Ivanov, A., 2014. Sr–Nd–Pb isotope systematics and clinopyroxene–host disequilibrium in ultra-potassic magmas from Toro-Ankole and Virunga, East-African Rift: Implications for magma mixing and source heterogeneity. *Lithos*, 210: 260-277.
- Njinju, E.A. et al., 2019. Lithospheric Structure of the Malawi Rift: Implications for Magma-Poor Rifting Processes. *Tectonics*, 38(11): 3835-3853.

- Nyblade, A.A., 2011. The upper-mantle low-velocity anomaly beneath Ethiopia, Kenya, and Tanzania: Constraints on the origin of the African superswell in eastern Africa and plate versus plume models of mantle dynamics. *Geological Society of America Special Papers*, 478: 37-50.
- O'Connor, J., Stoffers, P., van den Bogaard, P., McWilliams, M., 1999. First seamount age evidence for significantly slower African plate motion since 19 to 30 Ma. *Earth and Planetary Science Letters*, 171(4): 575-589.
- Pik, R., Marty, B., Carignan, J., Yirgu, G., Ayalew, T., 2008. Timing of East African Rift development in southern Ethiopia: Implication for mantle plume activity and evolution of topography. *Geology*, 36(2): 167-170.
- Rasskazov, S. et al., 2003. A magmatic episode in the Western Rift of East Africa (19-17 Ma). *Geologiya i Geofizika*, 44(4): 317-324.
- Ring, U., 2014. THE EAST AFRICAN RIFT SYSTEM. *Austrian Journal of Earth Sciences*, 107(1).
- Roberts, E.M. et al., 2010. Sedimentology and depositional environments of the Red Sandstone Group, Rukwa Rift Basin, southwestern Tanzania: New insight into Cretaceous and Paleogene terrestrial ecosystems and tectonics in sub-equatorial Africa. *Journal of African Earth Sciences*, 57(3): 179-212.
- Roberts, E.M. et al., 2012. Initiation of the western branch of the East African Rift coeval with the eastern branch. *Nature Geoscience*, 5(4): 289.
- Rogers, N., James, D., Kelley, S., De Mulder, M., 1998. The generation of potassic lavas from the eastern Virunga province, Rwanda. *Journal of Petrology*, 39(6): 1223-1247.
- Rooney, T.O., 2017. The Cenozoic magmatism of East-Africa: Part I—flood basalts and pulsed magmatism. *Lithos*, 286: 264-301.
- Rooney, T.O., 2020. The Cenozoic magmatism of East Africa: part V—magma sources and processes in the East African Rift. *Lithos*, 360: 105296.
- Rosenthal, A., Foley, S., Pearson, D.G., Nowell, G.M., Tappe, S., 2009. Petrogenesis of strongly alkaline primitive volcanic rocks at the propagating tip of the western branch of the East African Rift. *Earth and Planetary Science Letters*, 284(1-2): 236-248.
- Spandler, C., Hammerli, J., Pirard, C., 2018. Neodymium isotope disequilibria in subducted sediments, and potential consequences for subduction-zone recycling. *Geology*, 46(9): 815-818.
- Spandler, C. et al., 2016. MKED1: a new titanite standard for in situ analysis of Sm–Nd isotopes and U–Pb geochronology. *Chemical Geology*, 425: 110-126.
- Stevens, N.J. et al., 2013. Palaeontological evidence for an Oligocene divergence between Old World monkeys and apes. *Nature*, 497(7451): 611.
- Tappe, S. et al., 2007. Craton reactivation on the Labrador Sea margins:  $^{40}\text{Ar}/^{39}\text{Ar}$  age and Sr–Nd–Hf–Pb isotope constraints from alkaline and carbonatite intrusives. *Earth and Planetary Science Letters*, 256(3-4): 433-454.

- Tepp, G. et al., 2018. Seismic anisotropy of the upper mantle below the Western rift, East Africa. *Journal of Geophysical Research: Solid Earth*, 123(7): 5644-5660.
- Van Straaten, P., Bell, K., 1989. Nature and structural relationships of carbonatites from Southwest and West Tanzania. *Carbonatites: Genesis and Evolution*. Unwin Hyman, London: 177-199.
- Yoshida, M., Windley, B.F., Dasgupta, S., 2003. Proterozoic East Gondwana: supercontinent assembly and breakup. Geological Society of London.

## Chapter 6

### **Thesis summary and future work**

Detailed mineralogical and geochemical investigations of volcanic products deposited into the Rukwa Rift Basin throughout the Cenozoic has greatly enhanced knowledge and understanding of rifting, volcanism and lithospheric evolution in the Western Branch of the East African Rift System. The variety of mineral-scale geochemical approaches utilised in this research have demonstrated the effectiveness of using individual igneous crystals, particularly titanite, to overcome the pervasive alteration inherent to alkaline tuff deposits and to monitor the timing, nature and source character of alkaline magmatism in developing continental rifts. Collectively, this work has provided; 1. advancements in field-, petrographic- and laboratory-based tools for discovering new carbonatites in the global geological record; 2. the discovery of an entirely new process of explosive rift volcanism driven by silicate-carbonatite liquid immiscibility; 3. an experimental record of phase relations and melt evolution in highly-fractionated, volatile-rich and low-temperature immiscible peralkaline-carbonatite systems; and 4. an integrated and protracted isotopic record of alkaline magmatism with applied geological data, to develop a conceptual geodynamic model for the evolution of the Rukwa Rift Basin and nearby Rungwe Volcanic Province.

The four studies that comprise this thesis independently explore and garner fresh insights into the nature of Nsungwe Formation tuff deposits, and by extension the enigmatic nature of incipient volcanism and rift development in the Western Branch. In first instance, the petrographic and geochemical study of igneous mineral separates presented in Chapter 2, reveals a characteristic mineral assemblage that retain the geochemical hallmarks of a carbonatite-phonolite magmatic system. Consistent with uniformitarianism, this volumetrically rare expression of volcanism is also observed in the youngest modern-day sections of the East African Rift. Given the low volume, dominantly young and isolated nature of Cenozoic volcanism in the Western Branch, re-examining the sedimentary archives with a focus on identifying volcanogenic deposits rich in resistant minerals such as titanite, may provide renewed temporal insights regarding the onset of volcanism and rift development. The methodology and approach outlined in this work has redefined the initiation and evolution of the Rungwe Volcanic Province and will greatly enhance similar undertakings elsewhere.

The melt evolution recorded in titanite and subsequent model for generating explosive volcanism presented in Chapter 3 (and subsequent experimental investigations of Chapter 4) is an entirely new contribution to the field of volcanology and igneous petrology. Despite being geologically rare, these results provide grounds to re-examine the hazard potential of some young alkaline volcanoes in densely populated regions of the East African Rift. Unmixing carbonatite from evolved peralkaline melts may be implicated in the carbonatite-trachyte association as well as spatially related peralkaline and peraluminous igneous bodies elsewhere in the geological record. More broadly, there is a prominent and now well documented spatiotemporal relationship between explosive alkaline volcanism and diversity of fauna in the Oligocene Rukwa Rift. Consolidating the co-dependent, causal or correlative interplay between the emergence of alkaline-carbonatite volcanism, C3/C4 grasslands and ecologically diverse biotas elsewhere in Eastern Africa remains an important and ongoing area of focus worthy of continued multi-disciplinary collaboration.

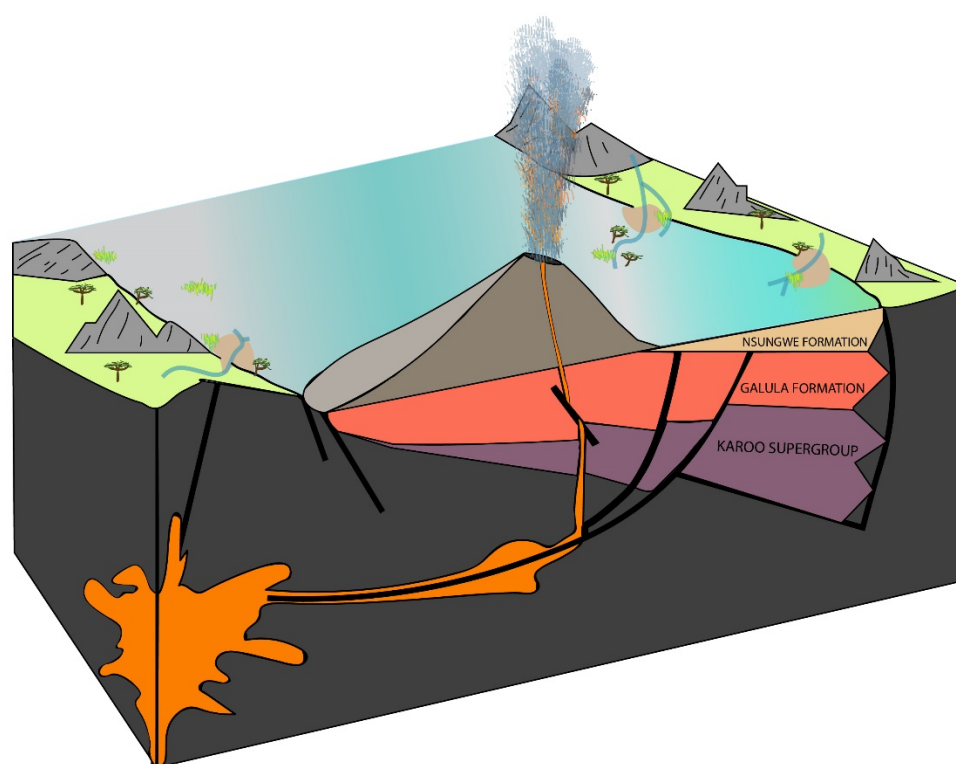


**Fig. 6.1** The emergence of active alkaline volcanism and fertile lake-shore environments in the Oligocene Rukwa Rift.

Although designed to examine explosive volcanism, the low temperature immiscibility experiments utilising natural whole rock powder (as opposed to simplified synthetic component systems) were shown to closely mimic the natural systems for which they were designed to understand. Highly evolved alkaline magmas and their metasomatising fluids produce some of the most strategically important mineral systems of the 21st century. Such an approach, geared towards mimicking nature rather than simplifying it, may be well applied in understanding the paragenesis and economic

mineralisation of magmatic critical metal (i.e., Zr, Nb, Ta) and rare earth element deposits. Furthermore, examining the element partitioning behaviour between immiscible melt/fluid phases and both economic and non-economic minerals in low temperature, volatile-rich experimental alkaline systems are warranted to better understand rare earth element and critical metal endowment in their natural counterparts. Comprehensive trace element analysis of the experimental series presented are an obvious and readily available starting point.

The Nsungwe Formation tuffs offer the only isotopic window into the lithospheric mantle at the onset of East African Rift development in the Western Branch. A key outcome of the work presented in Chapter 4 is demonstrating that in-situ isotope analysis of igneous crystals reliably records primary lithospheric source characteristics and integrates well with existing whole rock data. Collectively, this resulted in an unprecedented and complete isotope record of alkaline magmatism for the Rukwa Rift and Rungwe Volcanic Province. In consulting the literature throughout undertaking this research, unavoidable conjecture and in-some-cases contradiction is prevalent within the tangled the minutia of geochemical rift models. Yet, consideration of well evidenced macro-scale processes such as basin dynamics occurring in response to lithospheric evolution, are notably absent. For these reasons, the model presented sought to inclusively weigh and consider our newly generated in-situ data; the geochemical composition of rift lavas and contemporary models of lithospheric development presented elsewhere; alongside, the stratigraphic record of Rukwa Rift Basin dynamics and emerging geophysical interpretations of the lithospheric mantle beneath the Rungwe Volcanic Province. In doing so, the model presented offers a first pass at conceptualising the geological evolution of the Rukwa Rift and Rungwe Volcanic Province via drip magmatism of an isotopically layered lithosphere. This model offers a viable mechanism that may account for the geomorphological expression of the amagmatic Western Branch, which warrants consideration and further testing.

It is hypothesised that, like the Rungwe, some of the other isolated volcanic provinces in the Western Branch (i.e. Virunga and Kivu) are likely longer-lived than their exposed volcanic rock record would suggest. Given the rich history preserved in the Rukwa Rift, exploring the stratigraphic record surrounding isolated intra-basinal volcanic provinces of the Western Branch may yield fresh insights into the temporal development of Cenozoic rifting and magmatism in these localities. Absent this, the geodynamic model presented for the Rukwa Rift offers predictable ramifications resulting from lithospheric detachment, which is also hypothesised to influence rifting elsewhere in the Western Branch. Re-examining the tectonic histories of sedimentary basins and/or uplift histories of the immediate surrounds may extend the Cenozoic rift histories of Western Rift segments beyond that presented in the young volcanic provinces. Given the remote and isolated nature of these locations and current geopolitical climate, it may be some time before these questions can be better explored on the ground.

The significance of the Nsungwe Formation cannot be overstated. Since their discovery, these Paleogene sediments, and volcanic tuffs along with the rich fossil archive have challenged and re-defined the conventional narrative regarding the geological and biological evolution of sub-equatorial Eastern Africa. It is hoped that the research presented here is a meaningful addition to the ever-evolving knowledge regarding the geological processes that govern the expression of continental alkaline magmatism and rift development locally in the Rukwa Rift, Eastern Africa more broadly, and ultimately in the global geological record.

## Appendix A

### A1 Major element and trace element analyses of NFT minerals

(Supplementary Data file: Lawrence\_L\_2021\_Digital\_Appendix\_A1.xlsx)

### A2 REE+Y distribution and modelling

(Supplementary Data file: Lawrence\_L\_2021\_Digital\_Appendix\_A2.xlsx)

### A3 Supplementary Figures

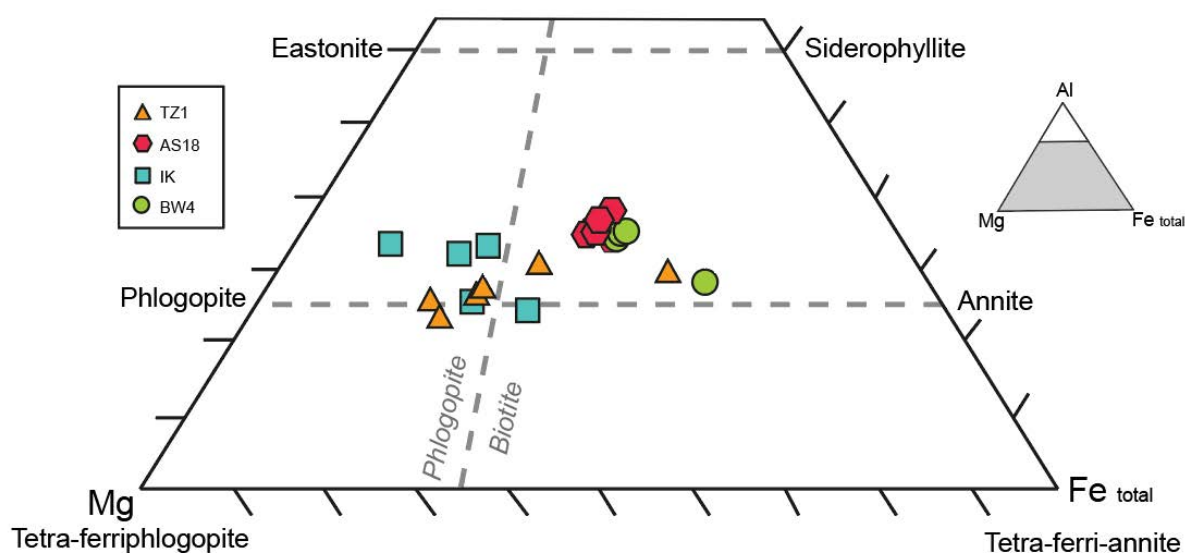


**Fig. S1.** Mica compositions (a.p.f.u) shown in the ternary classification scheme of Mitchell (1995). Here, the Fe and Mg contents of phlogopite-annite series mica are used to arbitrarily delineate phlogopite  $\text{Fe}/(\text{Fe}+\text{Mg}) < 0.33$  from other biotite compositions  $\text{Fe}/(\text{Fe}+\text{Mg}) > 0.33$  in the series (i.e. phlogopite containing Mg-Fe ratio of  $> 2:1$ ). Mica from samples AS18 and BW4 contain intermediate Mg-Fe ratios and form a tight cluster in the biotite field. Mica from samples TZ1 and IK show greater variance with compositions traversing from biotite to phlogopite compositions. Notably, this variance is observed in the form of phlogopite cores with biotite overgrowth.

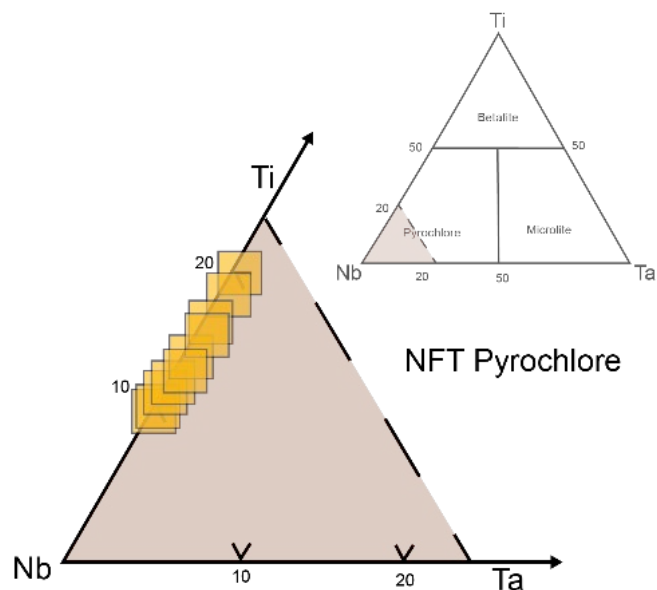


**Fig. S2.** Classification of NFT pyrochlore in the Ti-Ta-Nb (a.p.f.u) system of Hogarth (1977). All analyses incorporate moderate amounts of Ti, lack appreciable Ta, and plot in the pyrochlore field.

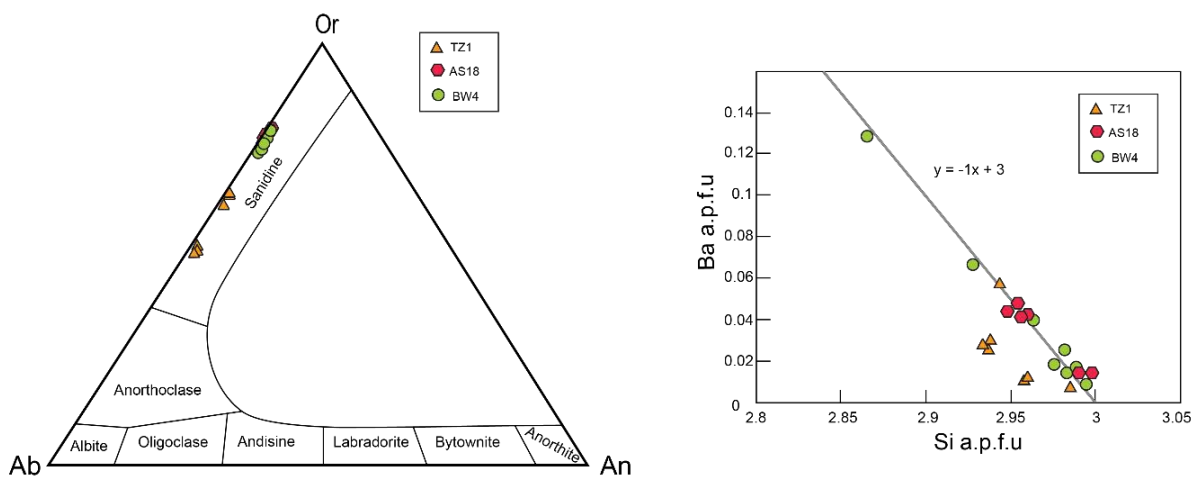


**Fig. S3.** (a) Feldspar classification diagram showing a variation in the Na component of the sanidine analysed. (b) Ba substitution into sanidine via the  $\text{Ba}+\text{Al} \rightarrow \text{Si}+\text{Na}$  typically used by  $\text{Ca}^{2+}$  to form anorthoclase.

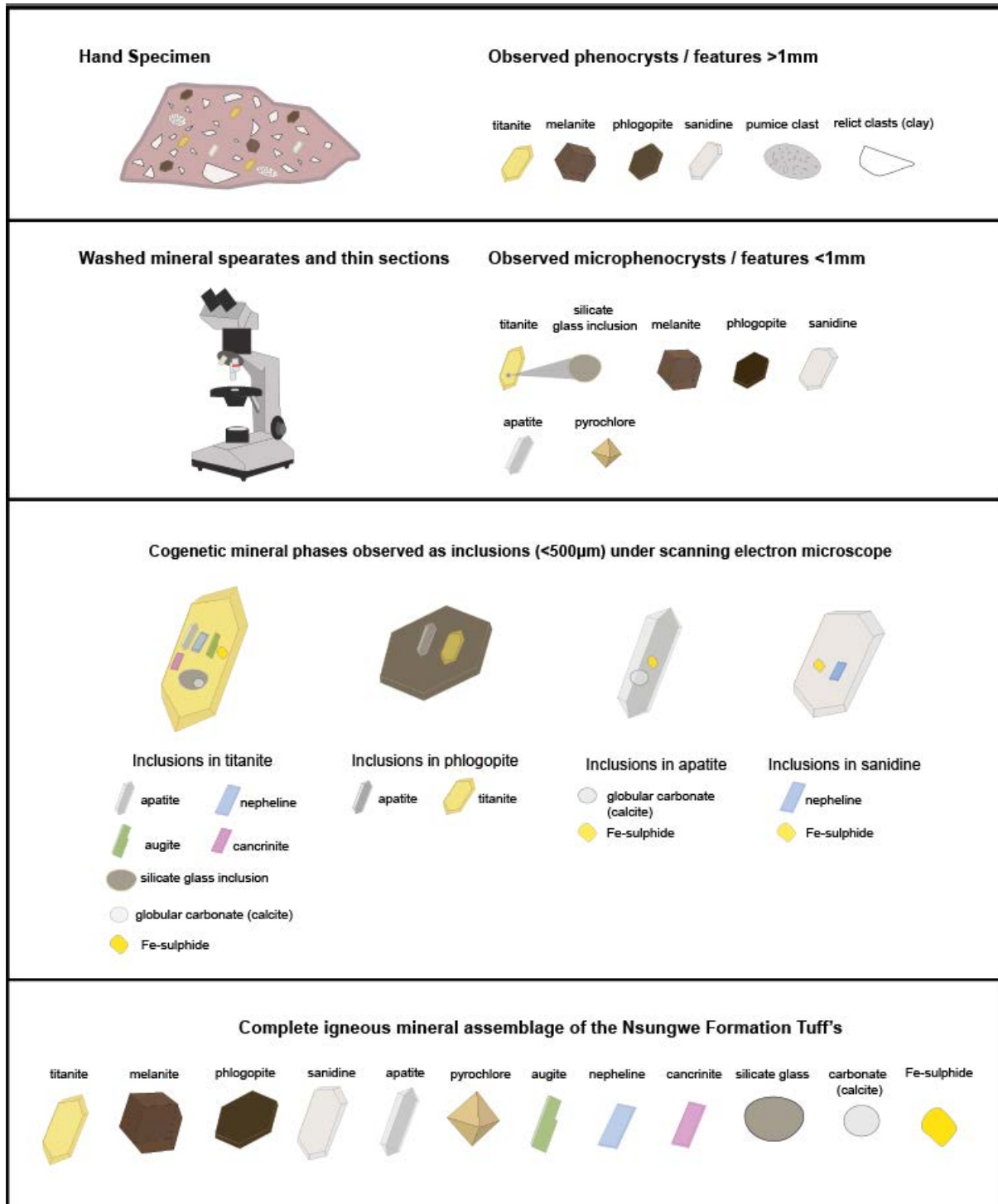


**Fig. S4.** Cogenetic igneous mineral assemblage arrived at via the multi-stage processing and petrographic observations of NFT mineral separates.

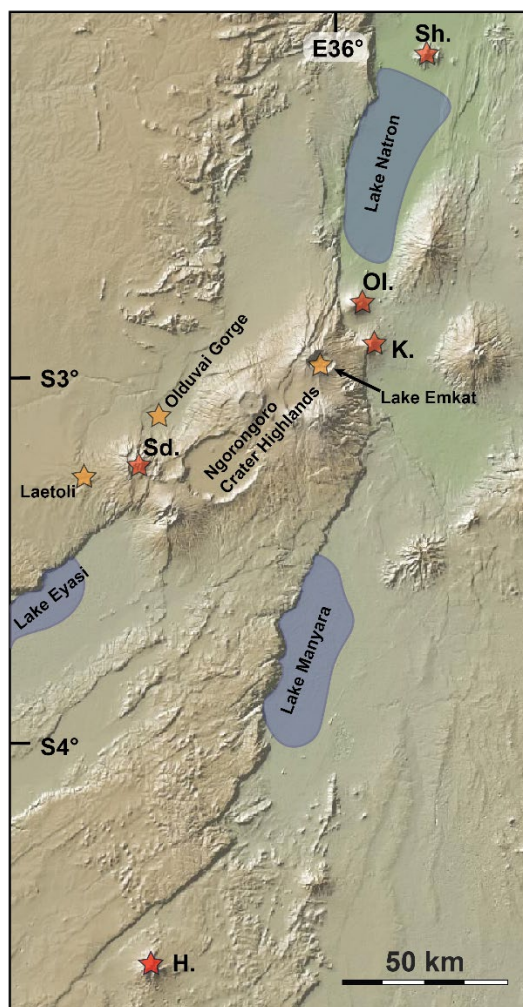


**Fig. S6.** Map of the North Tanzanian Divergence zone adapted from Le Gall et al. (2008) and using the Global Multi-Resolution Topography base map of Ryan et al. (2009). Alkaline volcanoes (red stars) and tuff deposits (orange stars) are discussed in text; Oldoinyo Lengai (Ol), Kermasi (K), Sadiman (Sd.) Hanag (H) and Shombole (Sh.).

### References (A3)

- Hogarth, D., 1977. Classification and nomenclature of the pyrochlore group. *American Mineralogist*, 62(5-6): 403-410.
- Le Gall, B. et al., 2008. Rift propagation at craton margin.: Distribution of faulting and volcanism in the North Tanzanian Divergence (East Africa) during Neogene times. *Tectonophysics*, 448(1-4): 1-19.
- Mitchell, R., 1995. *Kimberlites, Orangeites and Related Rocks* Plenum Press, New York, pp. 410.
- Ryan, W.B. et al., 2009. Global multi-resolution topography synthesis. *Geochemistry, Geophysics, Geosystems*, 10(3).

## Appendix B

### B1 Supplementary Data and Tables referred to in text

(Supplementary Data file: Lawrence\_L\_2021\_Digital\_Appendix\_B1.xlsx)

### B2 Additional analyses of Rukwa glass inclusions and host titanite.

(Supplementary Data file: Lawrence\_L\_2021\_Digital\_Appendix\_B2.xlsx)

### B3 Supplementary images of Rukwa glasses

(Supplementary image files: B3)

### B4 Supplementary figures and modelling details

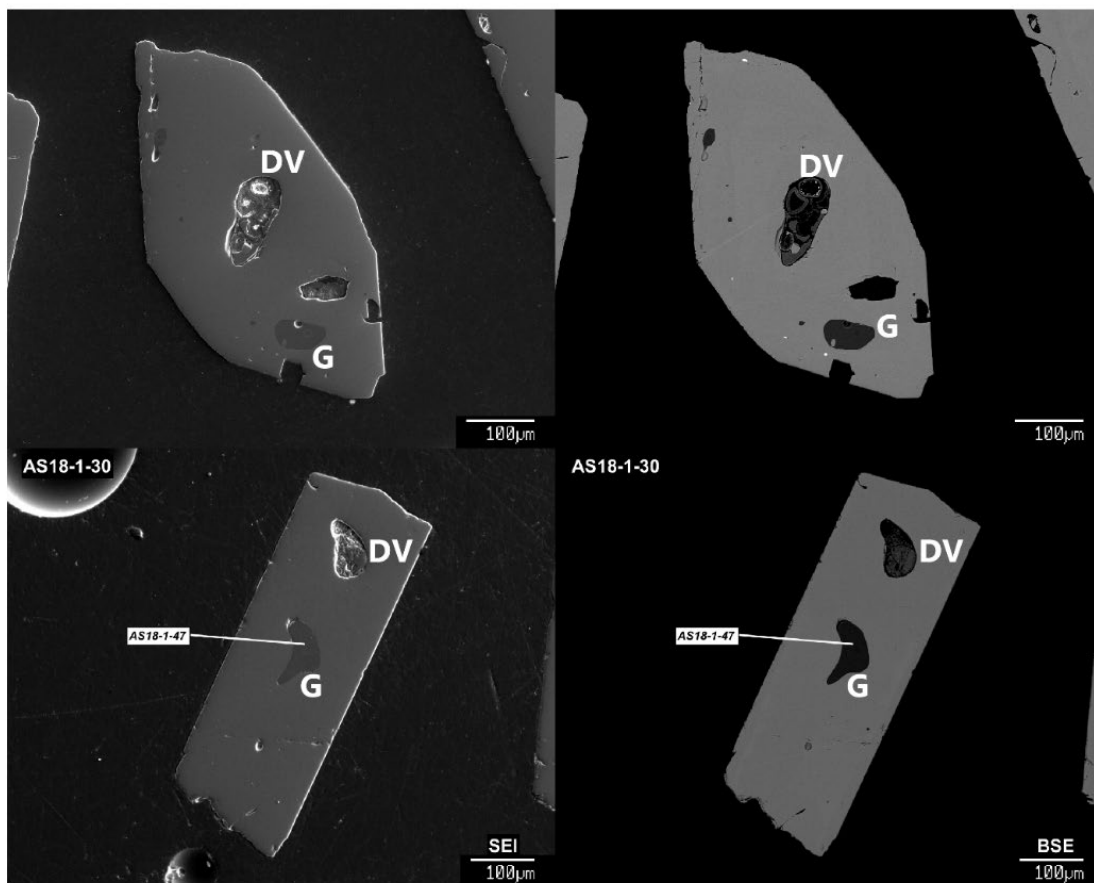


**Fig. S1.** Scanning and backscattered electron images of NFT titanite hosting both unaltered silicate melt inclusions (glasses – G) and devitrified or altered inclusions (DV).

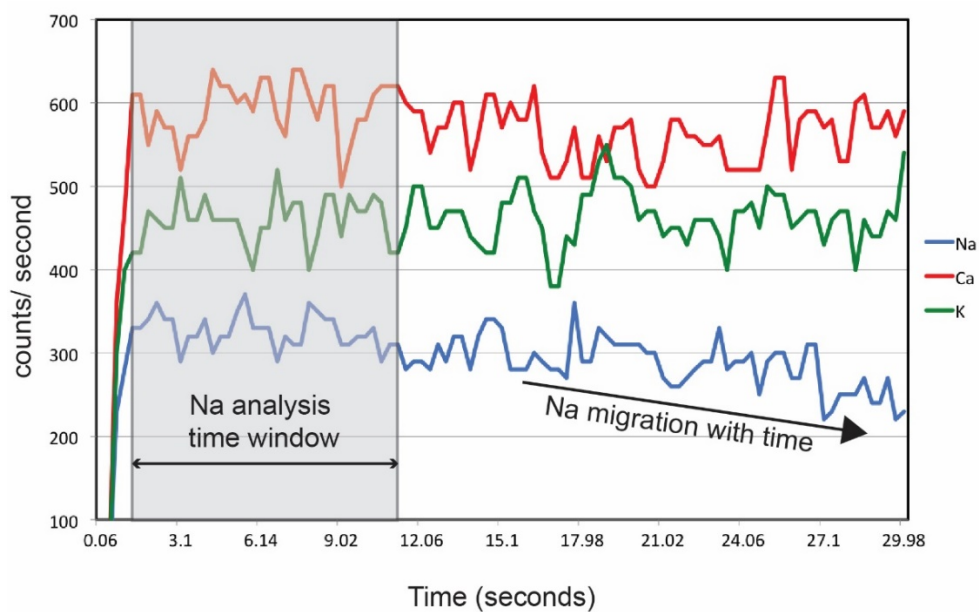


**Fig. S2.** WDS X-ray count rate for Na, Ca and K during a long duration (30 seconds) analysis of a phonolitic melt inclusion. Note, significant Na loss only comes into effect well after the 10 second analytical timeframe used in our methods for quantitative analysis.

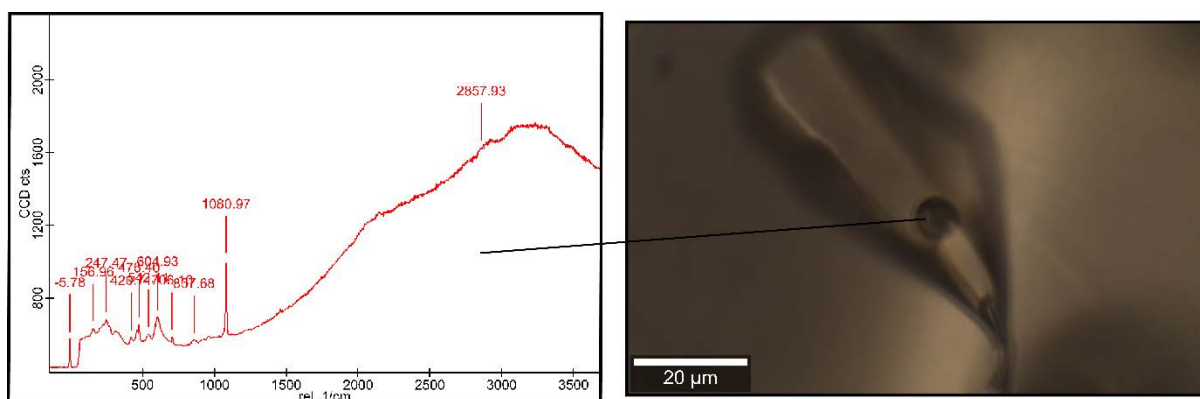


**Fig. S3.** Raman spectra of bubble phases within titanite hosted phonolite glasses showing the presence of CO<sub>2</sub> as carbonate (1080) peak.

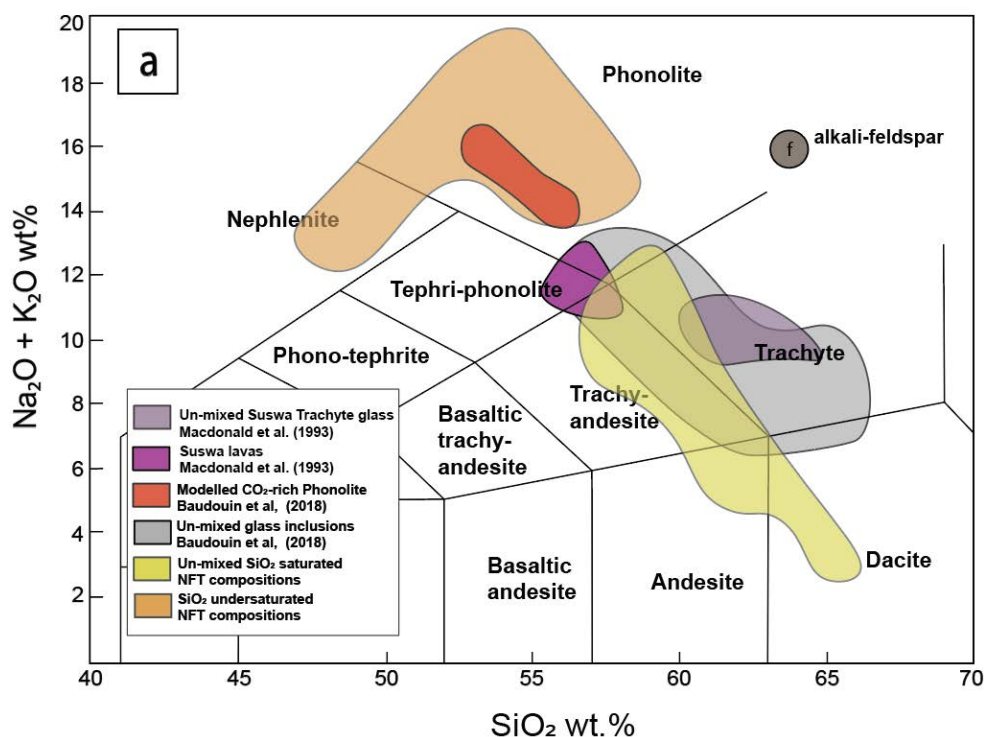


**Fig. S4.** TAS diagram depicting coeval silica saturated and undersaturated melt compositions associated with carbonatites. Grey shaded area represents the silicate melt compositions co-existing with immiscible carbonatite trapped within nepheline crystals from Hanang Volcano, Tanzania (Baudouin et al., 2018). Red shaded area is the modelled CO<sub>2</sub>-rich phonolitic melt prior to post-entrapment unmixing (Baudouin et al., 2018). Purple shaded field is the lava compositions from the Suswa volcano and the purple/grey field is the trachyte glass compositions associated with carbonatite ashflows, globules and tuffs of the Suswa volcano, Kenya (Macdonald, 1993). Orange and yellow shaded areas are the silica-undersaturated and silica-saturated fields (respectively) for the NFT that have been modelled here via combined carbonatite immiscibility and crystal fractionation.

## Supplementary modelling details

### Magma evolution modelling

To model the observed compositional evolution of the Rukwa melt inclusions, we conducted a relatively simple melt evolution model involving 3 stages of crystal fractionation, and one stage of carbonatite unmixing, from a phonolitic parent melt. The modelling procedures generally follow those of Weidendorfer et al. (2016) where a new stage is commenced when the modelled liquid no longer follows the observed evolution of the Rukwa melt inclusions.

### Starting melt composition

The initial composition for the melt was calculated by taking the average of all Rukwa melt inclusions that plot within the phonolite field (Table S1). The H<sub>2</sub>O contents of the initial melt composition was conservatively set to 1.8 wt.%, based on the quantitative Raman analyses of Rukwa phonolitic glasses (Supplementary text; Supplementary Data). Extrapolations based on the CO<sub>2</sub> solubility experiments in silicate melts of varying composition (including phonolite) presented by

Brooker et al. (2001), suggest CO<sub>2</sub>-saturation in the range of ~1.6 wt.%. Raman analyses of phonolitic glasses returned values up to ~1 wt.% CO<sub>2</sub> (Supplementary Data), and CO<sub>2</sub> has also been qualitatively identified in vapour bubbles within glass inclusions (Fig. S3) indicating CO<sub>2</sub>-saturation in the melt at, or shortly after, the time of entrapment. Saturation with CO<sub>2</sub> is also supported by the presence of magmatic carbonate phases as inclusions trapped alone alongside silicate melt inclusions (Supplementary Fig. S2). Hence, we consider 1.6 wt.% CO<sub>2</sub> at the time of entrapment a conservative estimate for our initial melt composition.

### **Composition of fractionating mineral phases, unmixed carbonatite and representative evolved NFT glasses**

The mineral compositions used for fractionation modelling is based on mineral phases identified as inclusions within titanite, as well as those found with titanite as mineral components of the weathered tuffs (i.e. phlogopite and feldspar). The fractionating phase assemblages were also modelled with consideration to phase petrology of peralkaline phonolitic melts (stage 1) and peraluminous melts (stages 2 and 3) (Kjarsgaard and Peterson, 1991; Scaillet et al., 2016; Weidendorfer et al., 2016). Mineral compositions are presented in Table S2. The modelled carbonatite melt component (Table S1) is constructed based on the analysed carbonatite melt inclusions of Mitchell (2009), Guzmics et al. (2015) and de Moor et al. (2013), in conjunction with the calculations of Weidendorfer et al. (2016) and projections of Schmidt and Weidendorfer (2018). This melt composition is a natrocarbonatite of comparable compositions to Oldoinyo Lengai (Mitchell, 2009). The evolved NFT glass compositions (Table S3) plot within (and have been selected to represent) small clusters of evolved NFT glasses that sit along the compositional array between phonolite and dacite compositions.

### **Model**

The model uses 3 stages to reproduce the trend observed for the NFT glasses. The fractionating minerals/unmixed carbonatite component, along with their proportions for each stage, are listed below. The modelling simply involved the subtraction of the fractionating/unmixing phases in their respective proportion at each stage, with the derivative melt composition being the residual melt after phase subtraction. At the end of each stage, elemental values are normalised to produce the starting composition for the next stage [i.e. values shown for stage 1 (Table S3) become the starting composition for stage 2]. To compare the modelled values with the Rukwa data, the H<sub>2</sub>O content is subtracted from the total (equivalent to the WDS data and low totals returned for the NFT glasses) and then re-normalised for comparison [indicated as **Stage\_x** (Table S3)]. Minor elements Mn, Ti, P, Cl and F are considered negligible for the model, and hence are not included here.

## Modelled stages

Stage 1 – Fractionate 11% sodalite, 30% feldspar, 0.8% magnetite and unmix 7% carbonatite.

Stage 2 – Fractionate 40% feldspar, 1% phlogopite and 5% hercynite spinel.

Stage 3 – Fractionate 30% feldspar, 4% hercynite spinel, 2% phlogopite and 1% titanite.

## Summary

As shown in Table S3, our model accurately reproduces the observed trends with respect to major element compositions ( $\text{Na}_2\text{O}$ ,  $\text{K}_2\text{O}$ ,  $\text{Al}_2\text{O}_3$  and  $\text{SiO}_2$ ) and volatiles ( $\text{H}_2\text{O}$ ) throughout each stage (n.b. inclusion AS18-67 returned a WDS total of ~88.2 wt.% indicating ~10 wt.%  $\text{H}_2\text{O}$ ). The most noteworthy shift in melt composition occurs in stage 1, modelled here to be the result of unmixing. At this stage, a total increase of 4 wt.%  $\text{SiO}_2$  and 2 wt.%  $\text{Al}_2\text{O}_3$  occurs in both the natural NFT glasses and the modelled melt evolution. Where crystal fractionation alone will serve to shift the melt either towards, along, or away from the feldspar thermal divide, the modelled unmixing acts to bypass this affect and saturate the system with respect to silica, while simultaneously increasing the alumina content (i.e., the melts become peraluminous). This shift mirrors what is predicted by element partitioning experiments and agrees with previously determined partition coefficients for silicate and carbonatite liquids during immiscibility (Olin and Wolff, 2012; Tiepolo et al., 2002). As  $\text{Na}_2\text{O}$ ,  $\text{CaO}$  and  $\text{CO}_2$  are preferentially lost to the carbonatite melt (and  $\text{SiO}_2$ ,  $\text{Al}_2\text{O}_3$  and  $\text{H}_2\text{O}$  preferably remain within the silicate liquid), a net increase in  $\text{SiO}_2$ ,  $\text{Al}_2\text{O}_3$  and  $\text{H}_2\text{O}$  is expected for the silica melt, as is observed in the modelled and natural glasses during stage 1. Once on the high silica side of the thermal divide, two stages (stage 2 and 3) of fractionation are required to reproduce the evolution of the NFT glass inclusions. As with other peraluminous systems, feldspar dominates these stages with minor accessory phases [in this case phlogopite, titanite and hercynite] acting to buffer  $\text{FeO}$ ,  $\text{Al}_2\text{O}_3$  and  $\text{CaO}$  contents to that observed for the NFT glasses.

## Table S1.

Table 1. Projected composition of carbonatite melt (wt%)

	Na2O	FeO	CaO	SiO2	K2O	Al2O3	MgO	H2O	MnO	Cl	P2O5	TiO2
Model carbonatite	25.00	5.00	30.00	1.33	10.00	0.30	0.60	-	0.30	-	3.74	0.08
*Rukwa average	9.00	3.39	2.46	52.67	6.66	21.06	0.17	1.80	0.16	0.37	0.03	0.41

## Table S2.

Table 2. Mineral compositions (wt%) used for model

Mineral	Na2O	FeO	CaO	SiO2	K2O	Al2O3	MnO	Cl	MgO	TiO2	H2O
Sodalite	25.58	-	-	37.2	-	31.56	-	7.3	-	-	-
Feldspar 1	7	-	-	64	9	19	-	-	-	-	-
Phlogopite	-	23	-	40	4.4	15.1	0.5	-	11	-	4
Titanite	-	-	28	30	-	-	-	-	-	38	-
Spinel (hercynite)	-	41.34	-	-	-	58.66	-	-	-	-	-
Magnetite	-	100	-	-	-	-	-	-	-	-	-

**Table S3.**

Table 3. Major element compositions (wt%) of both calculated [fractionation/immiscibility model] and measured melts.

	Na2O	FeO	CaO	SiO2	K2O	Al2O3	MgO	H2O	MnO	TiO2	F	Cl	P2O5
*Rukwa average	9.0	3.4	2.5	52.7	6.7	21.1	0.2	1.8	0.2	0.4	0.2	0.4	0.0
Interval 1	4.5	4.3	0.7	56.8	6.3	23.0	0.3	3.9	0.3	0.8	0.4	-0.8	-0.4
Interval 1x	4.7	4.5	0.7	59.1	6.6	23.9	0.3		0.3	0.8	0.4	-0.9	-0.5
TZBW-R1-LL6018-i **	4.8	3.9	1.8	59.3	5.0	23.1	0.2		0.1	0.6	0.6	0.4	0.0
Interval 2	3.1	4.1	1.3	56.4	4.9	22.6	0.5	7.0	0.5	1.4	0.7	-1.5	-0.8
Interval 2x	3.4	4.7	1.3	60.4	5.3	24.1	0.5		0.5	1.5	0.8	-1.6	-0.9
AS18-6-184 **	4.6	4.1	2.2	60.0	3.6	24.0	0.2		0.2	0.5	0.1	0.4	0.1
Interval 3	1.6	3.1	1.9	56.6	3.3	22.1	0.4	10.8	0.7	2.2	1.2	-2.4	-1.2
Interval 3x	1.8	3.5	2.2	63.2	3.7	24.7	0.4		0.8	2.4	1.3	-2.6	-1.4
AS18-67 **	1.3	4.0	1.8	63.5	3.7	24.4	0.1		0.1	0.3	0.2	0.4	0.0

\* = average of all rukwa Phonolitic glass inclusions + CO2 (ca. 1.6 wt%)

\*\* Normalised WDS values of Rukwa glasses

x = re-normalised values (minus H2O contents i.e. Rukwa glass equivalent)

**References (B3)**

- Brooker, R., Kohn, S., Holloway, J., McMillan, P., 2001. Structural controls on the solubility of CO2 in silicate melts: part I: bulk solubility data. *Chemical Geology*, 174(1-3): 225-239.
- Baudouin, C., Parat, F., Michel, T., 2018. CO2-rich phonolitic melt and carbonatite immiscibility in early stage of rifting: Melt inclusions from Hanang volcano (Tanzania). *Journal of Volcanology and Geothermal Research*, 358: 261-272.
- de Moor, J.M. et al., 2013. Volatile-rich silicate melts from Oldoinyo Lengai volcano (Tanzania): Implications for carbonatite genesis and eruptive behavior. *Earth and Planetary Science Letters*, 361: 379-390.
- Guzmics, T., Zajacz, Z., Mitchell, R.H., Szabó, C., Wälle, M., 2015. The role of liquid–liquid immiscibility and crystal fractionation in the genesis of carbonatite magmas: insights from Kerimasi melt inclusions. *Contributions to Mineralogy and Petrology*, 169(2): 17.
- Kjarsgaard, B., Peterson, T., 1991. Nephelinite-carbonatite liquid immiscibility at Shombole volcano, East Africa: petrographic and experimental evidence. *Mineralogy and Petrology*, 43(4): 293-314.
- Macdonald, R. et al., 1993. Liquid immiscibility between trachyte and carbonate in ash flow tuffs from Kenya. *Contributions to Mineralogy and Petrology*, 114(2): 276-287.
- Mitchell, R.H., 2009. Peralkaline nephelinite–natrocarbonatite immiscibility and carbonatite assimilation at Oldoinyo Lengai, Tanzania. *Contributions to Mineralogy and Petrology*, 158(5): 589.
- Olin, P.H., Wolff, J.A., 2012. Partitioning of rare earth and high field strength elements between titanite and phonolitic liquid. *Lithos*, 128: 46-54.
- Scaillet, B., Holtz, F., Pichavant, M., 2016. Experimental constraints on the formation of silicic magmas. *Elements*, 12(2): 109-114.
- Schmidt, M.W., Weidendorfer, D., 2018. Carbonatites in oceanic hotspots. *Geology*, 46(5): 435-438.
- Tiepolo, M., Oberti, R., Vannucci, R., 2002. Trace-element incorporation in titanite: constraints from experimentally determined solid/liquid partition coefficients. *Chemical Geology*, 191(1-3): 105-119.

Weidendorfer, D., Schmidt, M.W., Mattsson, H.B., 2016. Fractional crystallization of Si-undersaturated alkaline magmas leading to unmixing of carbonatites on Brava Island (Cape Verde) and a general model of carbonatite genesis in alkaline magma suites. *Contributions to Mineralogy and Petrology*, 171(5): 43.

## Appendix C

### **C1 Synthesis of starting compositions and EDS analysis of run products**

(Supplementary Data file: Lawrence\_L\_2021\_Digital\_Appendix\_C1.xlsx)

## Appendix D

### **D1 Bulk Sm-Nd-Sr and in-situ Sm-Nd & Lu-Hf isotope analyses**

(Supplementary Data file: Lawrence\_L\_2021\_Digital\_Appendix\_D1.xlsx)